

Thèse de doctorat

Pour obtenir le grade de Docteur de l'Université de VALENCIENNES ET DU HAINAUT-CAMBRESIS et de L'ECOLE DES MINES DE DOUAI

Discipline, spécialité selon la liste des spécialités pour lesquelles l'Ecole Doctorale est accréditée :
Mécanique et Énergétique

Présentée et soutenue par Bruno, Furieri.

Le 01/10/2012, à Valenciennes

Ecole doctorale :

Sciences Pour l'Ingénieur (SPI)

Erosion éolienne de tas de stockage de matières granulaires sur sites industriels : Amélioration des méthodes de quantification des émissions

JURY

Président du jury

- Peerhossaini, Hassan. Professeur, Laboratoire de Thermocinétique. Polytech'Nantes.

Rapporteurs

- Ould El Moctar, Ahmed. Maître de Conférences, HDR, Laboratoire de Thermocinétique. Université de Nantes.
- Naaim, Mohamed. Directeur de Recherche, Institut National de Recherche en Sciences et Technologies pour l'Environnement et l'Agriculture (IRSTEA ETNA). Centre de Grenoble.

Examineurs

- Valance, Alexandre. Directeur de Recherche CNRS, Institut de Physique de Rennes. Université de Rennes 1.
- Milliez, Maya. Titre, Ingénieur/Chercheur. EDF R&D. Chatou.
- Russeil, Serge. Maître-Assistant, École des Mines. Douai.

Directeur de thèse

- Harion, Jean-Luc. Professeur des École des Mines. Douai.

Co-directeur de thèse : Santos, Jane Meri. Professeur, Federal University of Espirito Santo. Brésil.

Membres invités

- Pons, Anne. Responsable Environnement, ArcelorMittal. Saint-Denis.

If someone does just what is known, never will go
forward a step

Clarice Lispector

Remerciements

Les travaux de recherche présentés dans cette thèse ont été réalisés au sein du Département Énergétique Industrielle à l'École des Mines Douai.

J'exprime ma gratitude à M. Hassan Peerhossaini, Professeur à l'Institut des Énergies de Demain, pour avoir accepté d'être le président de mon jury de thèse. De même, j'exprime ma reconnaissance aux rapporteurs de cette thèse : M. Ahmed Ould El Moctar, Maître de Conférences HDR au Laboratoire Thermocinétique de Nantes et M. Mohamed Naaïm, Directeur de Recherche à l'IRSTEA ETNA. Ils ont examiné avec attention le contenu de mon rapport de thèse et formulé des remarques intéressantes ayant contribué à améliorer les analyses présentées dans ce mémoire. Mes remerciements vont aussi à l'ensemble des examinateurs de mon jury de thèse: M. Alexandre Valance, Directeur de Recherche CNRS à l'Institut de Physique de Rennes et Mme Anne Pons, Responsable Environnement à ArcelorMittal.

Je tiens à remercier mes co-directeurs de thèse et mes co-encadrants. Tout d'abord, mes remerciements s'adressent à Mme Jane Meri Santos, Professeure à l'Université Fédérale de l'Espírito Santo au Brésil, pour avoir été co-directrice de cette thèse. Malgré l'éloignement elle a pu répondre aux questionnements, proposer ses corrections et soumettre ses idées, fondamentales pour l'avancement de la thèse. Je remercie tout particulièrement M. Jean-Luc Harion, Professeur des Écoles de Mines, co-directeur de cette thèse. Tout d'abord pour avoir accepté ma venue en France pour réaliser cette thèse de doctorat. Deuxièmement, pour sa grande compréhension, sa patience et son amitié lors de ces années de travail en commun. Enfin, je remercie Jean-Luc pour avoir partagé et transmis ses connaissances sur la problématique étudiée, tout en me laissant libre pour réaliser la recherche. J'ai fortement apprécié sa façon de travailler et de diriger cette thèse.

Ma grande reconnaissance va à M. Serge Russeil, Maître-Assistant à Mines Douai. Depuis mon arrivée au département, Serge a été la personne qui a suivi au plus près l'avancement de mes travaux. Toujours sympathique et disponible pour mes questions liées au travail et même pour mes difficultés personnelles. Ses corrections et ses analyses très détaillées et précises m'ont beaucoup apporté et ont été décisives pour la qualité finale de mon travail. De plus, sa façon de travailler avec les doctorants m'a positivement impressionné. Ensuite, je tiens à remercier Mme Maya Milliez, Ingénieur-Chercheur à EDF R&D CEREa, pour toute son aide lors des développements liés à l'utilisation du code de calcul *Code_Saturne*. Je remercie également EDF R&D pour le soutien financier de la thèse.

Je remercie l'ensemble du personnel du Département Énergétique Industrielle pour la façon dont j'ai été accueilli et toute l'aide apportée au long de ces années de travail: Marie-Françoise et Nadine pour leur sympathie et leur aide sur les tâches administratives, Chrystèle, Jean-Luc et Claude pour leur disponibilité et leur réponse à mes besoins pendant les expériences. À ce niveau, je remercie, tout particulièrement, Daniel Jacquart pour ses conseils précieux et son aide lors des montages expérimentaux liés à la soufflerie.

Je remercie profondément mes amis à Douai. J'ai eu l'occasion de faire de très belles rencontres et tiens notamment à rester en contact avec Cyril Bruhier, Charbel Habchi, Sébastien Vintrou, Amor Mlayeh, Vânia Oliveira, Vitor Zonta et Felipe Brasil: merci d'avoir, chacun à votre façon, contribué à rendre mes jours à Douai plus agréables, comme si j'étais en famille. La ville de Douai va beaucoup me manquer.

À ma famille et à mes amis au Brésil je me permets de faire un petit paragraphe en portugais pour qu'il soit compréhensible à tous: *à minha esposa linda, obrigado pela sua "presença à distância" e sua vinda à Douai. Foram momentos inesquecíveis e um aprendizado enorme para nós dois, profissionalmente e principalmente pessoalmente. Seu amor e sua confiança me sustentaram nessa distância. A minha mãe e meu pai por terem me apoiado sem hesitar nessa aventura com a maior torcida do mundo. A meu irmão pelo seu apoio incondicional desde minha vinda e durante todos esses anos. Muito obrigado!*

Contents

Résumé en français - Introduction générale	1
Introduction	5
1 Bibliographic Study	9
1.1 Wind erosion: a general introduction	9
1.2 Modelling of turbulent flows	13
1.3 Turbulent wall flow properties	17
1.3.1 Velocity profile	17
1.3.2 Roughness effects	18
1.3.3 Fluid flow around wall-mounted obstacles	18
1.4 Dust emission quantification and physics	21
1.4.1 USEPA model for dust emission quantification from diffuse sources	21
1.4.2 Non-erodible particles and their influence on dust emission quantification	24
1.5 Conclusions of the literature review	30
2 Experimental details	33
2.1 Wind-tunnel description	33
2.2 Surface flow visualization: oil-film technique	34
2.3 Dust emission investigation in wind-tunnel	37
3 Influence of non-erodible particles on dust emissions	43
3.1 Investigation of non-erodible particles effects by wind-tunnel simulations	43
3.1.1 Effects of non-erodible particles on aeolian erosion: wind-tunnel simulations of a sand oblong storage pile	43
3.1.2 Influence of stockpile orientation on the non-erodible particles effects on dust emission	66
3.1.2.1 Comparison of non-erodible particles distribution pattern with CFD contours	66
3.1.2.2 Influence of cover rate and wind flow velocity on the temporal evolution of emitted mass flux of sand	68
3.1.2.3 Conclusions	75
3.2 Local analysis of the influence of non-erodible particles on dust emissions by means of numerical simulation approach	76
3.2.1 Numerical modelling of aeolian erosion over a surface with poly-dispersed roughness elements	76
3.3 Non-erodible particles effects on the methodology of dust emission quantification	101
4 Analysis of aeolian erosion over oblong stockpiles: experimental and numerical approaches for turbulent fluid flow featuring and dust emission quantification	105
4.1 Investigation of isolated oblong stockpiles	105
4.1.1 Experimental surface flow visualization and numerical investigation of flow structure around an oblong stockpile	105
4.1.2 Aeolian erosion of storage piles yards: contribution of the surrounding areas	128

4.1.3	Analysis of a rounded crest stockpile: influence on dust emissions	146
4.1.3.1	Tested configurations	146
4.1.3.2	Near wall flow topology over a rounded crest of an oblique and perpendicular stockpiles	148
4.1.3.3	Dust emission quantification	152
4.1.3.4	Conclusions	153
4.2	Investigation of various arrangements of two successive stockpiles	154
4.2.1	Aeolian erosion of isolated and successive arrangements of oblong storage piles	154
4.2.2	Analysis of dust re-emission from the ground region surrounding successive stockpiles	174
4.2.2.1	Wall and air flow topology around successive stockpiles	174
4.2.2.2	Dust emission quantification	180
4.2.2.3	Conclusions	182
	Résumé en français - Conclusions	185
	Conclusions and Perspectives	187
	Bibliography	191

List of Figures

1	Organigramme de la thèse	4
2	Flowchart of the thesis	8
1.1	Scheme showing the forces acting upon a granular particle submitted to wind erosion. Adapted from Merrison (2012) [51]	11
1.2	Scheme of the three main modes of particle movement as an effect of aeolian erosion: suspension, saltation and reptation. Adapted from Duran et al. (2011) [25]	12
1.3	Take-off criterion curve. Adapted from Turpin (2010) [70]	13
1.4	Chart correlating the wall variables u^+ and y^+ . Adapted from Chassaing (2000) [14]	19
1.5	Shift in the logarithmic profile zone. Adapted from Cousteix (1989) [19]	20
1.6	Main flow features observed around an isolated cubical obstacle. Adapted from Hosker (1980) [36]	20
1.7	Numerical simulation of fluid flow around a stockpile perpendicular to the main wind flow direction: (a) Contours of thermodynamic pressure at the wall over and around the stockpile and (b) Coloured pathlines of fluid particles released from a line on the ground upstream the obstacle. Adapted from Turpin (2010) [70]	21
1.8	Contours of normalized surface windspeeds, u_s/u_r [75]	24
1.9	(c) Cylindrical roughness element. Evolution of the drag coefficient C_d for isolated cylindrical and spherical roughness elements as a function of: (b) h_{NEP}/b and (c) $S_{frontal}/S_{floor}$ [70]	26
1.10	Evolution of $1-R_{fric}$ in function of the value of $S_{frontal}/S_{floor} \cdot TDC$ [71]	27
1.11	Number of taking-off possibilities at the bed surface. Adapted from Descamps (2004) [21]	28
1.12	Balance of forces exerted on a particle and the effect of pavement on particle take-off [22]	29
1.13	Principle of the emitted mass flux simulation [22]	29
1.14	Results obtained by the model of a wide size distribution for several values of cover rate, by numerical and experimental approaches [22]	30
2.1	Wind-tunnel facilities: (a) original wind-tunnel and main dimensions and (b) configuration for oil-film surface flow visualization	34
2.2	Validation of the incoming wind profile at the entrance of the test section by literature data [63]: (a) linear and log laws of the velocity profile and (b) turbulence intensity. Adapted from Turpin (2010) [70]	35
2.3	Three compounds used in the oil-film mixture: (a) paraffin oil, (b) yellow powder and (c) oleic acid	36
2.4	Typical photograph of oil-film surface flow visualization	37
2.5	Temporal evolution of oil-film mixture at wall in wind-tunnel around the stockpile oriented 90° to the wind flow direction	38
2.6	Wind-tunnel configurations: dust emission quantification	39
2.7	Numerical contours of static pressure and the delimitation of the wind-tunnel circular plate	40
2.8	Hopper and mold used for the construction of the sand stockpile model	40
2.9	Oblong stockpile made with sand: shape and dimensions. (a) top view and (b) side view	41

3.1	Qualitative comparison of erosion for an oblong stockpile oriented 30°: (a) experimental photographs representing a top view of the pile and some highlighted zones and (b) contours of u_s/u_r values from CFD calculations	67
3.2	Qualitative comparison of erosion near the surface of an oblong stockpile oriented 60°: (a) experimental photographs representing a top view of the pile and some highlighted zones and (b) contours of u_s/u_r values from CFD calculations	69
3.3	Temporal evolution of surface covering in wind-tunnel experiments of a stockpile oriented 30°, cover rate 10% and wind velocity 7 m/s: (a) plot of emitted mass flux and (b) experimental photographs of sand stockpile top view in which dashed lines show the evolution of non-erodible particles agglomeration	70
3.4	Influence of the cover rate on the temporal decrease of the emitted mass flux of a stockpile oriented 30° and wind velocity equal to 8 m/s: (a) plot of emitted mass flux and (b) experimental photographs of sand stockpile top view in which dashed lines show the evolution of non-erodible particles agglomeration	71
3.5	Influence of the wind velocity on the temporal decrease of the emitted mass flux of a stockpile oriented 30° and cover rate equal to 10%: (a) plot of emitted mass flux and (b) experimental photographs of sand stockpile top view in which dashed lines show the evolution of non-erodible particles agglomeration	72
3.6	Temporal evolution of surface covering in wind-tunnel experiments of a stockpile oriented 60°, cover rate 10% and wind velocity 7 m/s: (a) plot of emitted mass flux and (b) experimental photographs of sand stockpile top view in which dashed lines show the evolution of non-erodible particles agglomeration	73
3.7	Influence of the cover rate on the temporal decrease of the emitted mass flux of a stockpile oriented 60° and wind velocity equal to 8 m/s: (a) plot of emitted mass flux and (b) experimental photographs of sand stockpile top view in which dashed lines show the evolution of non-erodible particles agglomeration	74
3.8	Influence of the wind velocity on the temporal decrease of the emitted mass flux of a stockpile oriented 60° and cover rate equal to 10%: (a) plot of emitted mass flux and (b) experimental photographs of sand stockpile top view in which dashed lines show the evolution of non-erodible particles agglomeration	75
3.9	Results obtained by the wind-tunnel measurements for one wind velocity	102
3.10	Plots of the correlation between emitted mass calculated in wind-tunnel and the values of $M_{balance}$ by the Equation 3.3	103
3.11	Steps of data management carried out to propose modifications in the USEPA methodology of diffuse dust quantification	103
3.12	Plots of the correlation between emitted mass calculated in wind-tunnel and the values of $M_{balance}$ by the Equation 3.3	104
4.1	Tested configurations and different shapes of stockpile crests: (a) sharpened crest, (b) rounded crest with radius $r_{pile} = 1$ and (c) rounded crest with radius $r_{pile} = 5$	147
4.2	Definition of r_{pile}	148
4.3	Numerical simulation results of the near wall flow distribution by means of the ratio u_s/u_r of a stockpile oriented 30°: (a) sharpened crest, (b) rounded crest with radius $r_{pile} = 1$ and (c) rounded crest with radius $r_{pile} = 5$	149
4.4	Numerical simulation results of the near wall flow distribution by means of the ratio u_s/u_r of a stockpile oriented 90°: (a) sharpened crest, (b) rounded crest with radius $r_{pile} = 1$ and (c) rounded crest with radius $r_{pile} = 5$	150
4.5	Numerical simulation results of the near wall flow distribution: ratio u_s/u_r of a stockpile oriented 60°: (a) sharpened crest, (b) rounded crest with $r_{pile} = 1$ and (c) rounded crest with $r_{pile} = 5$	151
4.6	Contours of longitudinal wind velocity plotted over a XZ plane located at the computational domain center line for the stockpile oriented 60° (at right, detail of separation on the crest): (a) sharpened crest, (b) rounded with radius $r_{pile} = 0.5$, (c) rounded with radius $r_{pile} = 1$ and (d) rounded with radius $r_{pile} = 5$	152

4.7	Numerical and experimental approaches of the wall shear stress evaluation on the ground region surrounding two successive stockpiles oriented 30° with a gap equal to $1e$ ($e = 0.9h$, h is the stockpile height): (a) numerical contours of normalized wall shear stress magnitude ($\tau_{ref} = 0.07Pa$) and (b) photograph of oil-film surface flow visualization	175
4.8	Numerical results of the air flow topology surrounding the successive stockpiles oriented 30° : (a) streamlines over a transversal (YZ) plane and (b) plot of normalized spanwise wall shear stress ($\tau_{ref} = 0.07Pa$)	176
4.9	Near wall flow velocity distribution in terms of the ratio u_s/u_r of the configuration 30° : (a) isolated stockpile, (b) two successive stockpiles with a gap $1e$, (c) two successive stockpiles with a gap $2e$ ($e = 0.9h$, h is the stockpile height)	177
4.10	Numerical and experimental approaches of the wall shear stress evaluation on the ground region surrounding two successive stockpiles oriented 60° with a gap equal to $1e$ ($e = 0.9h$, h is the stockpile height): (a) numerical contours of normalized wall shear stress magnitude ($\tau_{ref} = 0.07Pa$) and (b) photograph of oil-film surface flow visualization	178
4.11	Numerical results of the air flow topology surrounding the successive stockpiles oriented 60° : (a) streamlines over a transversal (YZ) plane and (b) plot of normalized spanwise wall shear stress ($\tau_{ref} = 0.07Pa$)	179
4.12	Near wall flow velocity distribution in terms of the ratio u_s/u_r of the configuration 60° : (a) isolated stockpile, (b) two successive stockpiles with a gap $1e$, (c) two successive stockpiles with a gap $2e$ ($e = 0.9h$, h is the stockpile height)	179
4.13	Numerical and experimental approaches of the wall shear stress evaluation on the ground region surrounding two successive stockpiles perpendicular to the incoming wind flow with a gap equal to $1e$ ($e = 0.9h$, h is the stockpile height): (a) numerical contours of normalized wall shear stress magnitude ($\tau_{ref} = 0.07Pa$) and (b) photograph of oil-film surface flow visualization	180
4.14	Numerical results of the air flow topology surrounding the perpendicular successive stockpiles: (a) streamlines over a transversal (YZ) plane and (b) plot of normalized spanwise wall shear stress ($\tau_{ref} = 0.07Pa$)	181
4.15	Near wall flow velocity distribution in terms of the ratio u_s/u_r of the perpendicular configuration: (a) isolated stockpile, (b) two successive stockpiles with a gap $1e$, (c) two successive stockpiles with a gap $2e$ ($e = 0.9h$, h is the stockpile height)	182
4.16	New particle size distribution to be tested in future works	189
4.17	Instantaneous contours of wall shear stress on the underlying surface surrounding cylindrical roughness elements.	190

List of Tables

1.1	$K - \epsilon$ standard model constants [42]	15
1.2	Particle size multiplier (k) for several aerodynamic particle sizes	22
1.3	Threshold friction velocity for several material and conditions as reported by the USEPA (2006) [75]	23
3.1	Summary of emitted mass balance [g]	76
3.2	Mass balance for a perpendicular oriented stockpile and various percentage values of non-erodible particles	102
4.1	Dust emission quantification of two shapes of stockpile's crest: sharpened and rounded	153
4.2	Dust emissions per perturbation in g/m^2 for the tested cases: on and around the stockpiles	181
4.3	Contribution in percent of the ground region surrounding stockpiles	183

List of Symbols

Variable	Definition	[SI unit]
Latin characters		
A	Activity rate	[depends on the activity]
b	Roughness element diameter	[mm]
C_R	Roughness element drag coefficient	[-]
C_S	Surface drag coefficient	[-]
D_p	Particle diameter	[mm]
D_{pref}	Reference particle diameter	[mm]
\tilde{D}_p	Normalized particle diameter	[-]
E	Estimated dust emission	[g]
EF	Emission factor	[g/m ²]
ER	Overall emission reduction efficiency	[-]
h_{NEP}	Roughness element height	[mm]
h_s	Mean roughness elements height	[mm]
K	Turbulent kinetic energy	[m ² /s ²]
k	Particle size multiplier	[-]
M	Number of isosurfaces of the velocity distribution over the surface of interest	[-]
m	Surface shear stress inhomogeneity parameter	[-]
$M_{balance}$	Wind-tunnel experimental mass balance	[g]
N	Number of perturbations in the USEPA methodology	[-]
N_p	Number of roughness elements	[-]
P_i	Erosion potential	[g/m ²]
P_{fric}	Roughness element geometrical parameter ($S_{floor}/S_{frontal} \cdot TDC$)	[-]
R_{fric}	Friction velocity ratio	[-]
R_t	Threshold friction velocity ratio	[-]
R	Correlation coefficient	[-]
S_{floor}	Roughness element basal surface	[mm ²]
$S_{frontal}$	Roughness element frontal surface	[mm ²]
S_{NEP}	Computational domain basal surface	[mm ²]
TDC	Cover rate	[-]
u_R^*	Friction velocity for an erodible surface protected by roughness elements	[ms ⁻¹]
u_S^*	Friction velocity for a smooth erodible surface	[ms ⁻¹]
u_t^*	Threshold friction velocity	[ms ⁻¹]
u_{t-R}^*	Threshold friction velocity for an erodible surface protected by roughness elements	[ms ⁻¹]

u_{t-S}^*	Threshold friction velocity for a smooth erodible surface	$[ms^{-1}]$
u_t^*	Threshold friction velocity value	$[m/s]$
u_{ref}^*	Reference friction velocity	$[m/s]$
\tilde{u}^*	Normalized threshold friction velocity	$[-]$
u_i	Velocity components (i varies between 1 to 3)	$[m/s]$
\bar{u}	Mean value of a flow variable (for instance, u corresponds to the velocity)	
u'	Fluctuation value of a flow variable (for instance, u corresponds to the velocity)	
u_s	Velocity magnitude at a plane distant 25 cm to a surface	$[m/s]$
u_r	Velocity magnitude at 10 m to a surface	$[m/s]$
u_{10}^+	Fastest mile of the wind velocity in a period between perturbations	$[m/s]$
u_t^*	Threshold friction velocity	$[m/s]$
x, y and z	Streamwise, spanwise and vertical coordinates	$[m]$
x^+, y^+, z^+, u^+ and h_S^+	Coordinates, streamwise wind velocity and mean roughness height in wall units	$[-]$

Greek characters

α	Angle of repose of a granular material	$[^\circ]$
β	Ratio of roughness element to surface drag coefficients	$[-]$
δ	Turbulent boundary layer thickness	$[m]$
ϵ	Kinetic energy dissipation	$[m^2/s^3]$
γ_p	Apparent gravity	$[m/s^2]$
κ	Von Kármán constant	$[-]$
λ	Roughness density	$[-]$
μ	Dynamic viscosity	$[Pa \cdot s]$
μ_t	Eddy viscosity	$[Pa \cdot s]$
ν	Kinematic viscosity	$[m^2/s]$
ω	Specific turbulence dissipation rate	$[1/s]$
ρ_p	Particle density	$[kg/m^3]$
ρ_{air}	Air density	$[kg/m^3]$
ρ	Density	$[kg/m^3]$
σ	Ratio of roughness element basal to frontal area ($S_{floor}/S_{frontal}$)	$[-]$
τ_w	Wall shear stress	$[Pa]$
τ	Total shear stress	$[Pa]$
τ_R	Roughness element shear stress	$[Pa]$
τ_S	Surface shear stress	$[Pa]$
τ_{ref}	Reference shear stress computed over an erodible surface without roughness elements	$[Pa]$

Résumé en français - Introduction générale

Les tas de stockage de matières granulaires érodés par le vent sont considérés comme des sources diffuses d'émissions de particules. Cette catégorie de sources peut être l'une des causes significatives de l'altération de la qualité de l'air sur certains sites industriels, comme par exemple sur les sites sidérurgiques. Ces effets peuvent s'étendre au voisinage et à des zones plus éloignées des sources principales par la dispersion atmosphérique. Par conséquent, la présente étude s'inscrit dans le cadre d'une investigation de la pollution atmosphérique dans laquelle les résultats et les discussions ont pour objectif de satisfaire aux exigences environnementales et de contribuer au contrôle de la qualité de l'air, par exemple, par la quantification plus précise des pollutions particulières émises.

Les difficultés dans le processus de quantification des émissions de particules provenant de sources diffuses sont principalement associées à la très grande taille des sources exposées à des conditions météorologiques atmosphériques. Ainsi, des mesures précises étant quasi inaccessibles car rapidement prohibitives en termes de coûts, ces émissions sont généralement estimées par des modèles numériques qui reposent souvent sur des variables telles que : la composition des matériaux, les conditions atmosphériques, l'exposition à l'écoulement du vent et la topographie du terrain. Les principaux objectifs du travail réalisé et présenté dans ce mémoire portent sur l'amélioration des méthodes de quantification des émissions de particules provenant de sources diffuses générées par érosion éolienne de matières granulaires.

Un modèle largement utilisé et reconnu dans le monde est proposé par l'Agence Américaine pour la Protection de l'Environnement (US EPA) [75]. Ce modèle est basé sur des facteurs d'émission. Plusieurs études ont déjà été menées concernant la quantification des émissions de particules provenant des tas de stockage. Toutefois, une partie des paramètres du modèle nécessite encore une analyse et des investigations plus approfondies. Parmi les analyses et recherches complémentaires pour améliorer les modèles de quantification des émissions, on peut citer notamment : les caractéristiques de l'écoulement du vent proche paroi, les structures tridimensionnelles de l'écoulement d'air autour des sources diffuses, des techniques expérimentales visant la validation des modèles numériques et la quantification expérimentale de l'envol des particules.

Le Chapitre 1 expose une revue de la littérature, notamment: une introduction générale sur l'érosion éolienne, la modélisation des écoulements turbulents, la physique de l'écoulement de fluides autour d'obstacles, les méthodologies de quantification des émissions de particules et l'influence des particules non-érodibles. Le Chapitre 2 est consacré à la présentation des installations expérimentales: la technique du film d'huile de visualisation de la contrainte en surface et la mesure continue des émissions d'un modèle de tas de stockage oblong constitué de sable de granulométrie bimodale. Les deux techniques expérimentales ont été mises en œuvre dans une soufflerie. Les mesures en continu de masse permettent d'évaluer l'évolution temporelle du flux massique émis. La technique de visualisation par film d'huile a pour objectif l'étude des structures de l'écoulement proche de la paroi. La méthode consiste à enduire un mélange d'huile sur une paroi exposée aux frottements d'un écoulement de vent.

Les résultats sont ensuite présentés dans deux chapitres. Le Chapitre 3 se concentre sur l'influence des particules non-érodibles sur l'érosion éolienne des tas de stockage de matières granulaires. En bref, l'érodibilité d'une particule est principalement basée sur sa granulométrie et la vitesse de frottement du vent. Pour une vitesse de vent donnée, les particules au delà d'un certain diamètre ne s'envolent

pas et sont donc non-érodibles, en raison de leur inertie. Le Chapitre 3 présente quatre sections. Des approches expérimentales et numériques sont utilisées pour obtenir les résultats.

La première section présente les résultats sous forme d'une publication en revue scientifique, **qui sera soumise à la revue « Atmospheric Environment »**, et intitulée **« Effects of non-erodible particles on aeolian erosion: wind-tunnel simulations of a sand oblong storage pile »**. Cette section est dédiée aux techniques expérimentales mises en œuvre en soufflerie afin de déterminer l'influence des particules non-érodibles sur l'érosion éolienne des tas de stockage oblongs, notamment sur l'évolution temporelle du flux de masse émise et la quantité de particules émises. Des expériences en soufflerie sur un tas de sable oblong (granulométrie bimodale) ont été effectuées sur la base des travaux antérieurs. La vitesse du vent et le ratio de la masse de particules non-érodibles (taux de couverture) ont défini les configurations testées. Les tas de stockage testés sont perpendiculaires à la direction principale de l'écoulement incident. La deuxième section du Chapitre 3 présente des discussions similaires à celles de la première section. L'orientation du vent incident est modifiée. Deux orientations obliques ont été testées dans la soufflerie. En effet, l'orientation de l'écoulement du vent exerce une forte influence sur la configuration de l'écoulement autour du tas de stockage.

Une approche numérique locale de l'influence des particules non-érodibles est présentée dans la troisième section. Les résultats sont présentés sous forme d'une publication, **qui sera soumise à la revue « Earth Surface Processes and Landforms »**, intitulée **« Numerical modelling of aeolian erosion over a surface with poly-dispersed roughness elements »**. Elle traite de l'évaluation locale de l'influence des particules non-érodibles. Les grosses particules sont prises en compte dans les simulations numériques comme des éléments de rugosité sur une surface lisse. Une étude de référence a défini une relation mathématique pour l'analyse de l'évolution de la vitesse de frottement sur la surface érodible associée à la géométrie des éléments de rugosité [71]. Cette formulation caractérise la diminution de la vitesse de frottement moyennée sur la surface lisse, c'est-à-dire, une atténuation de l'érosion éolienne des surfaces érodibles due à l'accumulation de particules non-érodibles. La corrélation vise à modifier l'utilisation de la vitesse de frottement dans les modèles mathématiques de quantification des émissions de particules. Pour les simulations numériques initiales [71], des particules avaient des diamètres et des hauteurs de sortie du lit égales, correspondant à une configuration monodispersée de particules non-érodibles, ce qui n'est jamais le cas dans une situation réelle, par exemple pour les matières présentes sur sites industriels (par exemple minerais ou charbons). Par conséquent, cette section vise à réaliser des simulations numériques de plusieurs configurations poly-dispersées : les diamètres et hauteurs de sortie du lit des particules non-érodibles sont variables. L'objectif principal est de vérifier la validité de la formulation précédemment proposée pour toute distribution de particules.

La dernière section du Chapitre 3 décrit une proposition de modification du modèle d'estimation des émissions de particules développé par l'USEPA. Les modifications proposées sont fondées sur les données de masses émises obtenus par mesures expérimentales en soufflerie. Une modification de la formulation du facteur d'émission est présentée. A l'origine, la méthode USEPA ne transcrit pas explicitement dans sa formulation, l'influence d'un paramètre prenant en compte la quantité de particules non-érodibles présente dans la matière considérée. En effet, il a été montré par ces mesures expérimentales que l'émission totale d'un tas de stockage est fortement réduite en raison de la présence de particules non-érodibles.

Le Chapitre 4 est consacré à l'estimation de l'érosion éolienne de tas de stockage sur sites industriels disposés dans plusieurs configurations. Le chapitre est divisé en deux sections: tas de stockage isolés et divers arrangements de deux tas de stockage successifs. L'analyse la plus originale et récente menée dans cette section porte sur l'investigation de la contribution des émissions sur la région qui entoure les tas de stockage et la quantification de l'influence de tas successifs sur l'écoulement du vent, la structuration de l'écoulement et les émissions associées. La revue de la littérature réalisée n'a pas montré de travaux de recherche antérieurs sur ce sujet.

Deux publications résument les principaux résultats obtenus pour les configurations testées avec un tas de stockage isolé. La première, **publiée dans « Environmental Fluid Mechanics »** est intitulée **«Experimental surface flow visualization and numerical investigation of flow structure around an oblong stockpile»**. Cette publication présente les principaux résultats et les comparaisons

effectuées sur la base de la technique expérimentale de visualisation de l'écoulement de surface mise en œuvre dans ce travail. La section se concentre sur la région qui entoure les tas de stockage. Sur les sites industriels, ces régions sont fortement couvertes par des particules fines. La technique expérimentale aide l'analyse de la topologie d'écoulement en paroi et permet aussi une validation partielle des simulations numériques. L'écoulement d'air qui entoure le tas est également décrit de façon à déterminer les structures d'écoulement du fluide conduisant éventuellement à la réémission de particules.

La deuxième publication concerne la quantification de la réémission de particules provenant de la région autour d'un tas de stockage **soumise à la revue « Environmental Fluid Mechanics »**, intitulée **« Aeolian erosion of storage piles yards: contribution of the surrounding areas »**. Les émissions provenant du tas et de la région autour de celui-ci sont comparées à fin d'étudier la contribution de la réémission aux émissions globales.

Une dernière section considère la modification de la crête du tas. Des travaux antérieurs ont montré que la zone proche de la crête est la zone la plus exposée sur un tas et est par conséquent d'une grande importance pour la quantification des émissions. En se basant sur des études antérieures ayant étudié d'autres formes de crêtes, et sur les travaux expérimentaux qui ont mis en évidence cette forme pour les tas réalisés en soufflerie, l'influence du rayon de la crête a été analysée par simulations numériques.

La deuxième partie du Chapitre 4 traite de l'influence de tas de stockage successifs sur la structuration de l'écoulement du vent près de la paroi et donc sur les émissions estimées. L'analyse de l'érosion éolienne sur le tas et sur la région environnante est présentée séparément dans cette section. La section est également présentée sous la forme d'une publication, **qui sera soumise à « Applied Mathematical Modelling »** et intitulée **« Aeolian erosion of isolated and successive arrangements of oblong storage piles »**. Les résultats de simulations numériques sur plusieurs arrangements successifs de deux tas de stockage oblongs y sont discutés. L'objectif de cette section est de qualifier l'érosion éolienne sur la surface des tas. Une configuration oblique a indiqué l'augmentation des émissions globales pour les deux tas de stockage. La section suivante présente une analyse similaire pour les régions avoisinantes de plusieurs dispositions de deux tas de stockage successifs: la technique expérimentale de visualisation de l'écoulement, la quantification des émissions par la méthode USEPA et l'analyse de la topologie de l'écoulement de l'air par des simulations numériques.

L'organigramme de la Figure 1 présente de façon synthétique les chapitres et sections de cette thèse. Certaines sections, comme indiqué précédemment, sont présentées sous forme de publications. En outre, l'organigramme précise comment chaque résultat est relié à un manque de connaissances identifié lors de la revue bibliographique ainsi que la relation de chaque méthode d'analyse (expérimentale et numérique) avec les résultats.

Les principaux objectifs de cette thèse sont les suivants:

- l'analyse expérimentale (soufflerie) de l'influence des particules non-érodibles sur les émissions de particules avec une configuration géométrique de tas de stockage oblong;
- l'analyse locale de l'influence de la présence d'éléments de rugosité (particules non-érodibles) dans une couche limite turbulente par simulations numériques;
- amélioration du modèle mathématique USEPA de la quantification d'émission de particules en vue de la prise en compte de particules non-érodibles dans les paramètres du modèle;
- investigation de l'écoulement de vent (près de la paroi et la topologie de l'écoulement tridimensionnel) sur la surface du sol entourant les tas de stockage oblongs à l'aide d'expériences en soufflerie et de simulations numériques;
- évaluation de la réémission de particules retombées autour de tas de stockage;

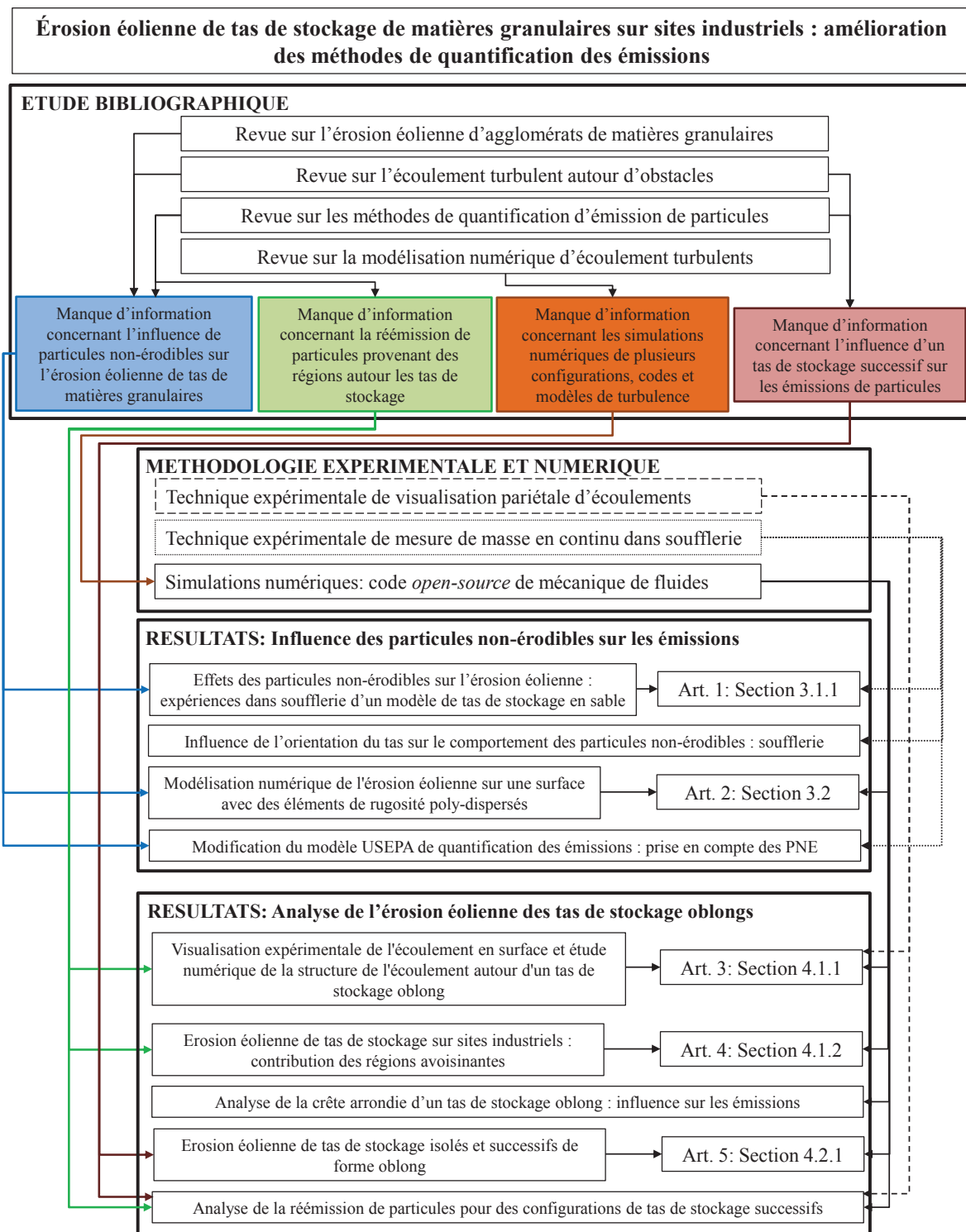


Figure 1: Organigramme de la thèse

- simulations numériques de différentes configurations de tas de stockage oblongs : divers aménagements successifs de deux tas de stockage et qualification de l'impact de la modification de la forme de crête sur les émissions à l'aide de la méthode USEPA.

Introduction

Aeolian eroded storage piles of granular materials are classified as diffuse sources of dust emissions. This class of source can be one of the important causes of air quality decrease on some industrial sites, as example on steel plants sites. These effects may extend to the vicinity and even zones far away the main source due to the atmospheric dispersion. Hence, the present study is part of an atmospheric pollution investigation in which the results and discussions may fulfill environmental requirements and assist the air quality control by, for instance, the quantification of emitted pollutant rates.

The difficulties in the process of quantification of particles emissions from diffuse sources are primarily associated to their large size. Therefore, these emissions are usually estimated by models which are often based on variables such as: material composition, atmospheric conditions, wind flow exposure and structure, topography of the land, etc. The main objectives arise from the need to improve the methods for estimating dust emissions from diffuse sources.

A widely used model is proposed by the United States Environmental Protection Agency (US EPA) [75] which is based on emission factors. Several studies have been already done about dust emission quantification from stockpiles [1,2,24,69,70,72,73]. However, some of the model parameters still require further analysis. Among the analysis that can be developed to improve the models of emissions quantification there are: wind flow features on the near wall, three-dimensional air flow structures around the diffuse sources, experimental techniques aiming the validation of numerical models and experimental quantification of particles take-off.

Chapter 1 exposes the literature review including: wind erosion general introduction, modelling of turbulent flows, physics of fluid flow around obstacles, methodologies of dust emission quantification and influence of non-erodible particles. Chapter 2 is devoted to the experimental facilities: oil-film surface flow visualization and continuous emissions measurement of an oblong stockpile model made of sand. Both experimental techniques were carried out in a wind-tunnel. The measurements in wind-tunnel allow the evaluation of the temporal evolution of emitted mass flux. The oil-film visualization technique aims to investigate the fluid flow pattern over a given wall surface. The method consists in coating an oil mixture over a given wall exposed to flow friction.

The results are divided into two chapters. Chapter 3 is focused on the influence of non-erodible particles on the aeolian erosion of granular materials storage piles. Briefly, the erodibility of a particle is mainly based on its granulometry and on the friction velocity of the eroding wind. Larger particles are often categorized as non-erodible due to their inertia. Chapter 3 presents four sections. Experimental and numerical approaches are employed to obtain the results.

The first section presents the results as an article **to be submitted to the "Atmospheric Environment" journal**, and entitled **"Effects of non-erodible particles on aeolian erosion: wind-tunnel simulations of a sand oblong storage pile"**. The section deals with experimental works performed in wind-tunnel to determine the influence of non-erodible particles on the aeolian erosion of oblong stockpiles, notably on the temporal evolution of the emitted mass flux and on the amount of emitted particles. Wind-tunnel experimentations of an oblong stockpile made of a bimodal granulometry sand were carried out based on previous works. Wind velocity and ratio in mass of non-erodible particles (cover rate) defined the tested configurations. The tested stockpiles are perpendicular to the incoming wind flow.

The second section of Chapter 3 performed similar discussions than those presented in the first section. The incoming wind flow orientation was changed. Two oblique orientations were tested in the wind-tunnel. Indeed, the wind flow orientation has a strong influence on the flow pattern around

the stockpile.

A numerical approach of the influence of non-erodible particles is presented in the third section. The results, presented as an article, **to be submitted to the "Earth Surface Processes and Landforms" journal**, entitled **"Numerical modelling of aeolian erosion over a surface with poly-dispersed roughness elements"**, refers to local evaluation of the influence of non-erodible particles. The coarse particles are considered in the numerical simulations as roughness elements over a smooth surface. A previous reference work has defined a mathematical relation between the evolution of the friction velocity over the erodible surface and the geometry of the roughness elements [71]. In fact, the formulation is a correlation that indicates the decrease of the mean friction velocity, i. e., an attenuation of the wind erosion of erodible surfaces, with the accumulation of non-erodible particles. The correlation aims to change the use of friction velocity in mathematical models of dust emission quantification. A condition set in reference numerical simulations [71] is never accomplished in nature: roughness particles have equal diameters and emerging heights. Therefore, this section aimed to carry out numerical simulations of several configurations with poly-dispersed configurations of diameters and emerging heights of non-erodible particles. The main objective was to check the validity proposed formulation for any distribution of particles.

The last section of Chapter 3 shows initial propositions of modifications in the USEPA mathematical model of dust emission estimation. The modifications are based on the data of emitted mass obtained after wind-tunnel experimental works. A modification on the emission factor formulation is presented. Originally, the USEPA methodology does not have in its formulations the description of the amount of non-erodible particles contained in the storage pile. Indeed, it was shown by these experimental measurements that the total emission from a stockpile is strongly reduced due to the presence of non-erodible particles.

Chapter 4 is devoted to the aeolian erosion of open yards of oblong storage piles in its several possible configurations. The chapter is divided into two sections: isolated stockpile and various arrangements of two successive stockpiles. The most original and recent analysis carried out in this part are the investigation of the ground region surrounding the stockpiles and the quantification of the influence of a successive pile on the surrounding fluid flow. No previous research work has carried out investigations about it.

Two publications summarizes the main results obtained for the configurations tested with one isolated stockpile. The first, **published in the "Environmental Fluid Mechanics" journal** is entitled **"Experimental surface flow visualization and numerical investigation of flow structure around an oblong stockpile"**. It shows the main results and comparisons carried out about an experimental technique of surface flow visualization. The section focuses on the ground region surrounding the stockpiles. On industrial sites, these regions are strongly covered by silt particles. The experimental technique assists the analysis of the wall flow topology on the ground region as well as a partial validation of numerical simulation of similar configurations. The air flow surrounding the stockpile is also described to determine the fluid flow structures possibly leading to dust re-emission.

The second **submitted to the "Environmental Fluid Mechanics" journal**, entitled **"Aeolian erosion of storage piles yards: contribution of the surrounding areas"**, presents the quantification of dust re-emission with the USEPA methodology. The dust emission quantification concerns the ground region surrounding the stockpile. The emissions from the stockpile and from the surrounding ground are compared to investigate the contribution of dust re-emission to global emissions.

A final subsection considers the modification of the pile crest. Previous works have shown that the crest is the most eroded zone over the stockpile and consequently is of great significance on the quantification of dust emissions. Based on previous studies, which studied other crest shapes, and on the experimental works which showed this form, the rounded crest was analysed by the means of numerical simulations.

The second section deals with the influence of a successive stockpile on the near wall fluid flow pattern and consequently the dust emissions. The analysis of the aeolian erosion on the pile and on the surrounding region is separately presented in this section. The section also presented as an article, **to be submitted to the "Applied Mathematical Modelling" journal** and entitled **"Aeolian erosion of isolated and successive arrangements of oblong storage piles"** shows the

results of numerical simulations about several arrangements of two successive oblong stockpiles. The focus of this section is the aeolian erosion over the pile surface. An oblique configuration has indicated the increase of overall emissions for two nearby stockpiles. The next section shows similar analysis for the surrounding regions of several arrangements of two successive stockpiles: experimental technique of surface flow visualization, USEPA dust emission quantification and air flow topology by numerical simulations.

The flowchart shown in Figure 2 presents the chapters and sections of this thesis. In some sections, as previously stated, will be presented the articles on the developed subject. Also, the flowchart shows the reader how each outcome is related to a lack of knowledge diagnosed in the literature review as well as the relationship of each methodology (experimental and numerical) with the results.

The main objectives of this thesis are:

- experimental analysis (wind-tunnel) of the influence of non-erodible particles on dust emissions with a stockpile geometry configuration;
- local analysis of roughness elements (non-erodible particles) in a turbulent boundary layer by means of numerical simulations;
- improvement of the mathematical model of dust emission quantification aiming the consideration of non-erodible particles in the model parameters;
- investigation of the fluid flow (near wall and air flow topology) on the ground surface surrounding an oblong stockpile by means of wind-tunnel experiments and numerical simulations;
- evaluation of re-emission of dust settled around stockpiles;
- numerical simulations of remaining configurations of oblong stockpiles: various arrangements of two successive stockpiles and impact of the modification of the crest shape on dust emission by using the USEPA methodology.

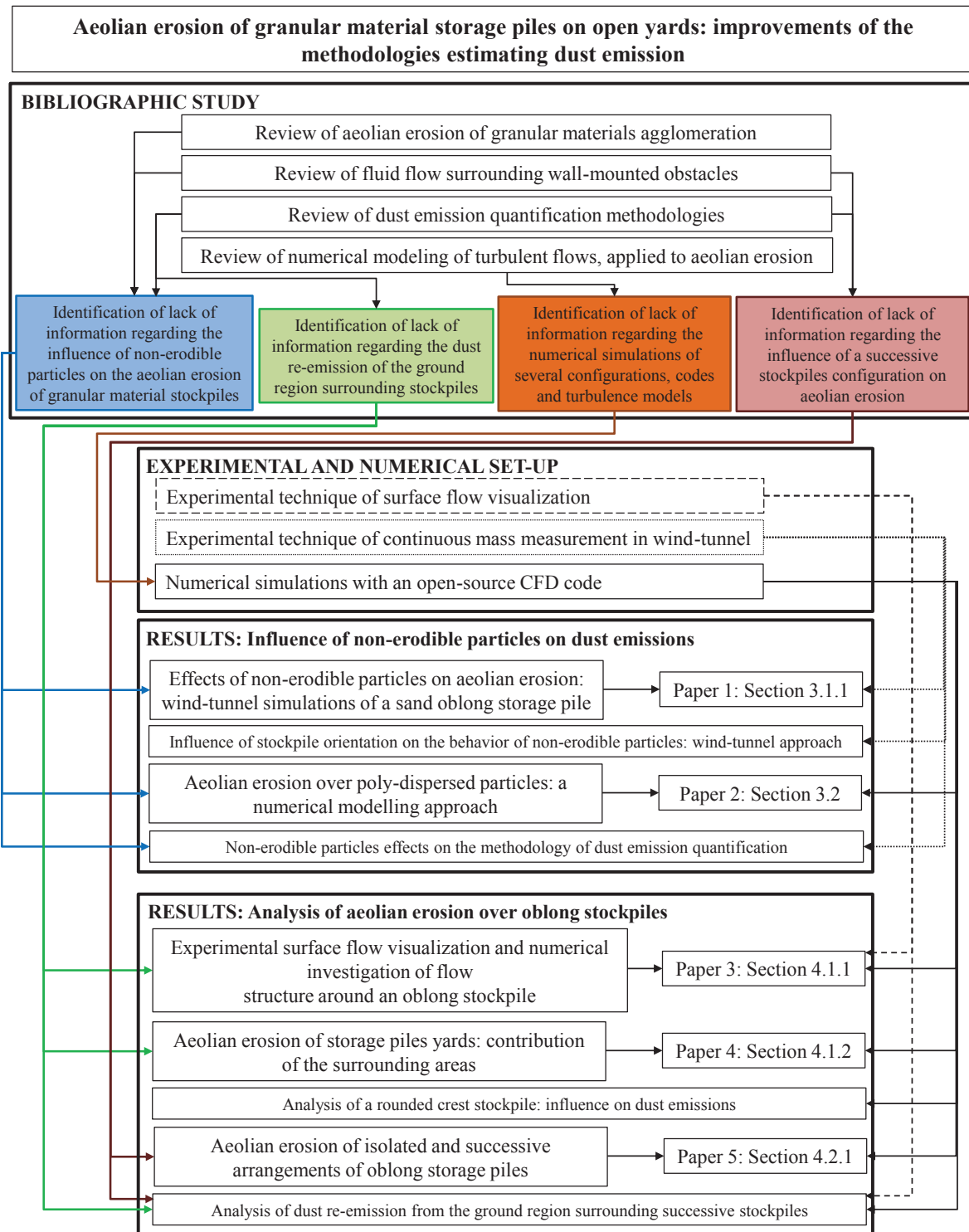


Figure 2: Flowchart of the thesis

Chapter 1

Bibliographic Study

This literature review provides in three sections some concepts about aeolian erosion on industrial sites, numerical modelling and experimental investigations on dust emission quantification. In general, wind erosion leads to a negative impact on air quality. The physics of wind erosion is complex as it involves atmospheric and land-surface processes [66]. The review article written by Merrison (2012) [51] states that the research in aeolian transport involves two inter-related fields: fluid mechanics and granular materials which are both discussed in this chapter.

The first section considers the wind erosion phenomena involving particles erodibility and particles take-off from the agglomeration. The next section is devoted to mathematical approaches, formulations and turbulence models employed to model the fluid flow around obstacles. The last section details the mathematical modelling of dust emissions quantification which is dependent on the fluid flow around an obstacle and the particles being eroded.

Some of the concepts and literature works necessary to support the work are presented later in the related sections of the papers included in this thesis.

1.1 Wind erosion: a general introduction

The aeolian erosion is a natural process which disturbs a given surface originating the movement of particles towards the atmosphere. As reported by Duran et al. (2011) [25], if the wind blowing over a surface of agglomerated particles, such as soil, sand, minerals or coal, exceeds a velocity threshold, the particles are set into motion and transported elsewhere. Wind erosion depends on the granular material chemical composition, density, atmospheric conditions (such as wind speed, precipitation, air moisture and temperature) and the eroded surface characteristics (such as topography, roughness, surface moisture, vegetation cover and presence of non-erodible particles).

The investigation concerning diffuse sources performed by the United States Environmental Protection Agency (USEPA) [75] states that the generation of dust may be caused by two main phenomena: pulverization or abrasion of the surface material by mechanical force and entrainment of dust particles (removed from the surface by the wind shear) by turbulent air currents, which is the condition for wind erosion events.

Diffuse sources are categorized by USEPA (2006) [75] as: (i) agriculture operations, (ii) construction, (iii) mining, (iv) paved and unpaved roads and (v) open storage yards of granular material. Dust emissions from agricultural operations result from soil disturbances that occur during land preparation for seeding which may be included as mechanical disturbances. Dust emissions from this category exhibit a seasonal pattern. Construction operations can cause a temporary acute impact on local air quality. Dust emissions from construction sites or roads are associated with land clearing, drilling and blasting, ground excavation, and cut and fill operations. A vehicle travelling over an unpaved road causes the pulverization of surface material due to the impact of the wheels on the road surface. Particles are lifted and dropped from rolling wheels and the turbulent wake behind the vehicle continues moving the particles from and to the road surface after the vehicle has passed. Open storage yards are wide areas found out on some industrial sites used for the storage of granular materials. An essential aim concerning the atmospheric pollution of these diffuse sources is the sig-

nificant amount of pollutant particles emitted due to aeolian erosion events. Particles take-off, and the dust emissions associated, is a main action of the incoming wind flow on industrial sites. The aeolian erosion of sand dunes, and their transport, is another field of study deserving attention in this review. The works about sand dunes mobility appeared in the 1970s [10, 81]. The previous works about sand dunes were concentrated on measurements of wind flow and sand flux by the means of numerical and experimental simulations [26, 45, 62, 77]. A wide variety of dune shapes can be found in deserts or sea-bottom, for instance. The study of sand dunes is of great significance for the understanding of the aeolian erosion mechanisms.

First investigations concerning aeolian erosion, which started in 1941 with Bagnold [4], focused on the movement of individual particles in the wind flow. After that, some works have discussed the implications of the wind flow structure around a given source on the aeolian transport. For instance, the studies of Lancaster et al. (1996) [41], Wiggs et al. (1996) [79], McKenna et al. (1997) [48] and Parson et al. (2004) [57] have largely improved the description of the interactions between the fluid flow around complex obstacle and the aeolian erosion. Recently, several experimental and numerical works have been carried out to simulate the aeolian erosion over granular material agglomeration, for instance, Ferreira and Oliveira (2009) [28], Ferreira and Lambert (2011) [27], Cong et al. (2011) [18] and Faria et al. (2012) [26] carried out the analysis of pile protection by wind barriers using numerical simulations of the fluid flow around the pile and wind-tunnel experiments.

Badr and Harion (2005) [2] have also described that the presence of piles, acting like obstacles to the wind flow, causes flow streamlines to diverge and generates pressure gradients in flow field near surfaces. Hence, the complex shape of these obstacles upsets the flow dynamics and changes the near-field uptake force of the wind. The magnitude and extent of the modifications are essentially controlled by the configurations of the piles and wind conditions. Later studies carried out by the same research group aims to evaluate the influence of oblong stockpiles geometries on aeolian transport [3, 72, 73].

Badr and Harion (2007) [3] performed numerical simulations and results provided evidence to suggest that modifications on piles arrangement may sensibly modify dust emissions. Carrying on this subject, Turpin and Harion (2009) [72] investigated the effect of changing the shape of the crest. The objective was the assessment of dust emission for various forms of crest. The main conclusion is based on the fact that flat-topped piles are in fact more pollutant contrarily to the first thought. The last study carried out by Turpin and Harion (2010) [73] promotes an important practical application for industrial sites of these previously presented investigations, i.e., the simulation of the entire domain including all the main buildings on the industrial site. Numerical simulations associated with the USEPA model for the dust emission quantification showed the great influence of the surrounding buildings on the overall fluid flow in the domain and, therefore, on the quantification of aeolian dust emissions.

The present thesis corresponds to a next step on the investigations in this specific domain of aeolian erosion which consists in testing new configurations taking into account parameters not yet considered in dust emission quantification. Moreover, this work aims to enhance the knowledge about particles take-off, re-emission from the ground region surrounding piles and non eroded coarse particles. New experimental techniques and open-source numerical simulations are performed in this study to achieve the objectives.

The understanding of particle entrainment mechanisms is of major importance for accurate predictions of particle transport rates and mobility and, as a consequence, for accurate quantification of dust emission aiming the implementation of dust emission abatement strategies. The processes of particle entrainment, transport and deposition involve a set of particle-to-flow, particle-to-surface and particle-to-particle interactions. The physical properties of individual particles, such as shape, size and density, play an important role in these interactions [66]. Moreover, the mechanisms of entrainment of aeolian eroded particles are dependent on the parameters mentioned hereafter:

- particle mass which is associated to density and size,
- density ratio, between the particles and the fluid and

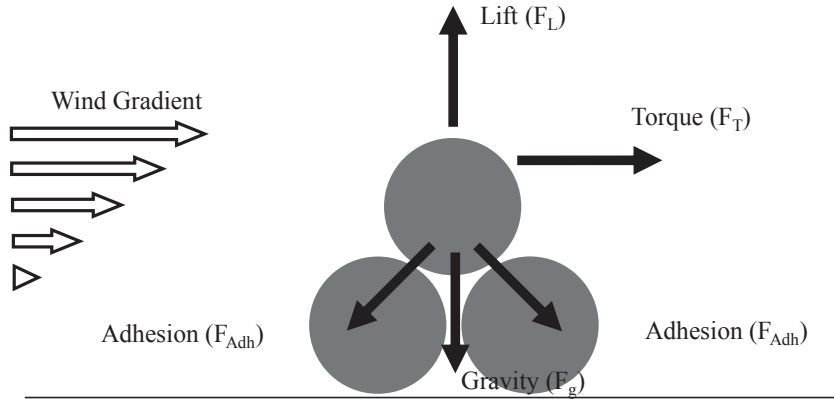


Figure 1.1: Scheme showing the forces acting upon a granular particle submitted to wind erosion. Adapted from Merrison (2012) [51]

- viscosity of the air.

These parameters will then define the forces components acting upon a granular particle being eroded by a wind flow. A scheme is shown in Figure 1.1 representing such forces: lift (F_L), torque (F_T), adhesion (F_{Adh}) and gravity (F_g) [51]. Lift and torque forces are associated to density ratio and air viscosity. Gravity force is associated to the mass of the granular particle. Finally, for adhesion forces, previous works (Zhao et al. (2003) [82] and Bowling (1988) [8]) have defined a dependence on the particle diameter and the effective contact area between adjacent particles. These forces (except for the gravity) are only known in an empirical or semi-empirical way.

Moreover, the work of Merrison (2012) [51] presents the force balance approach. The forces acting on an individual particle are compared to define its threshold condition: $F_L + F_T$ and $F_g + F_{Adh}$.

Figure 1.2 introduces the three categories (modes) of particles transport by wind erosion: suspension (pure or modified), saltation (pure or modified) and reptation.

Suspension

When aerodynamical forces are dominant (lift and torque) the particles may perform a pure or modified suspension movement. Suspension movements are associated to small particles. For pure suspension the particles are weightless and small enough to be entrained towards the free stream flow. These particles are taken-off from the wall by lift forces and they are entrained by the turbulent movements of the air flow. The modified suspension movements correspond to slightly heavier particles and do not follow the small scale turbulent eddies because of their inertia. Particles eroded with pure suspension movements reach distances from the take-off point further than those under modified suspension movements.

Saltation

A second mode of particle movement, called saltation, indicates grains that rebound and expel other grains when hitting a bed of particles. It is the principal mechanism for the transport of large quantities of soil particles in the direction of the wind [66]. Saltation occurs if the lift force is greater than the particle weight (gravity) and adhesion force, if existent. After take-off, gravity force becomes more important than the lift force. Thus, the particle rise is interrupted and it falls back onto the bed. The fate of this particle, can, then, be: rebounding and remaining as a saltation particle or integrating the group of particles on the surface. A saltation particle can disturb the surface during its rebounds causing an extra emission. As for the modified suspension, the modified saltation is caused by the slightly heavier particles. This condition may leave the particles further in the pure saltation than the modified saltation.

Reptation

Reptation is the third mode of particles movement and occurs if the density of the fluid is much smaller than that of the grains. In fact, if the particles are too heavy to be lifted, they roll or

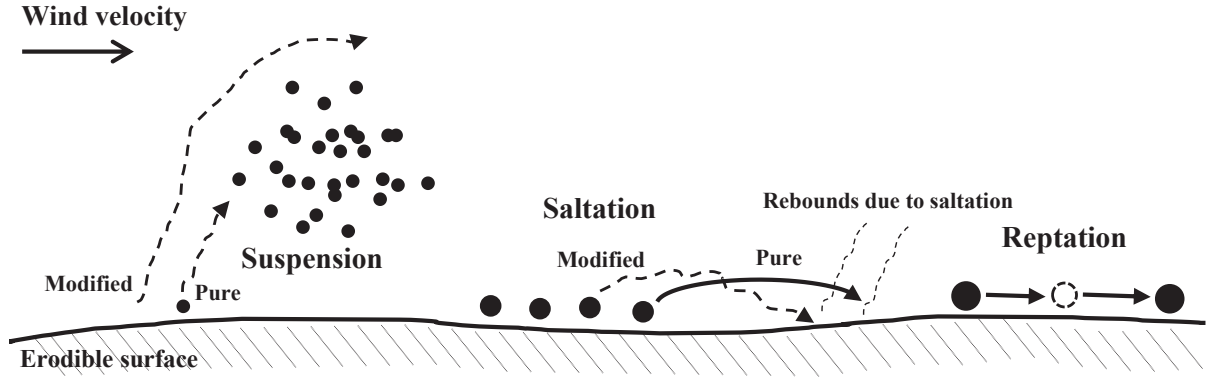


Figure 1.2: Scheme of the three main modes of particle movement as an effect of aeolian erosion: suspension, saltation and reptation. Adapted from Duran et al. (2011) [25]

slide along the surface under the effect of aerodynamic forces. According to some authors, this phenomenon often occurs as a result of the impact of saltation particles. The momentum provided to reptation particles by the impact of saltation particles is large enough for them to roll but not to take-off. It is also noticed that one particle in reptation transmits momentum to other particles.

Some works on aeolian erosion have observed and worked on the fact that an agglomeration of particles with large size distribution may be partly erodible and an another part non-erodible [9,33,54]. An erodible particle is defined, in simply words, as the particle displaced from a bed of particles under a wind erosion event. Non-erodible particles have a very important effect on the quantification of particles emission where, erodibility is easy to see on a curve representing the threshold velocity as a function of the particle diameter.

The threshold friction velocity (u_t^*) is the friction velocity from which wind erosion is initiated. u_t^* is affected by surface and soil properties. It is a function of the particle size for idealized soils, but also, in real cases, a function of material moisture. Earlier investigations carried out by Bagnold (1941) [4] and Chepil (1942) [15] proposed a non-dimensional approach to group fluid flow velocity and particle granulometry. The authors pointed out that if the mixed particles have a large amount of very small particles or very large ones, the threshold friction velocity increases. These two conditions are interesting to be analysed as the increase of the threshold friction velocity indicates an aeolian erosion less efficient in terms of emitted particles. In this framework, later studies (for instance, Iversen and White (1982) [37] and Foucaut [30]) established formulations associating non-dimensional values of friction velocity and particle diameter. Foucaut [30] determined the formulation from the experimental data and the correlation proposed by White (1982) [78]. The take-off velocity threshold is introduced by Iversen and White (1982) [37] in Equations 1.1 and 1.2 and by Foucaut (1994) [30] in Equation 1.3.

$$\widetilde{D}_p = \frac{D_p}{D_{pref}} \quad \widetilde{u}^* = \frac{u^*}{u_{ref}^*} \quad (1.1)$$

where,

$$D_{pref} = \left(\frac{\nu^2}{\gamma_p} \right)^{\frac{1}{3}} \quad u_{ref}^* = (\gamma_p \nu)^{\frac{1}{3}} \quad (1.2)$$

$$\gamma_p \text{ being the apparent gravity: } \gamma_p = \frac{\rho_p g}{\rho_{air}}$$

$$\widetilde{u}_t^* = 22,71 \widetilde{D}_p^{0,043} + 10,23 \widetilde{D}_p^{-0,118} - 32,5 \quad (1.3)$$

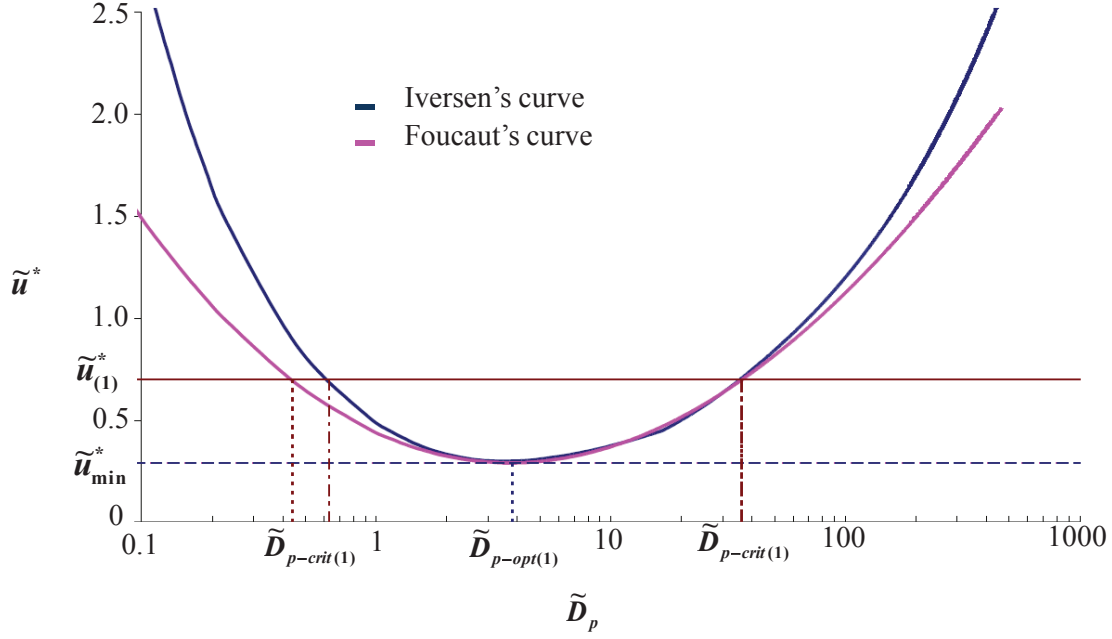


Figure 1.3: Take-off criterion curve. Adapted from Turpin (2010) [70]

where: D_p is the particle diameter [m], u^* is the friction velocity [m/s], $D_{p_{ref}}$ is the reference diameter particle [m], u_{ref}^* is the reference friction velocity [m/s], ν is the kinematic viscosity of air [m^2/s], γ_p is the apparent gravity [m/s^2], ρ_p is the particle density [kg/m^3], ρ_{air} is the air density [kg/m^3] and g is the gravity [m/s^2].

After presenting the formulations above, an analysis tool, called take-off criterion (Figure 1.3) may be shown. It is an interesting alternative to assess the erodibility of a particle. The referred tool intends to associate the threshold friction velocity of a material to its granulometry. The take-off criterion plot presented in Figure 1.3 aims to determine the ranges of diameters of erodible and non-erodible particles, for a given threshold friction velocity. The minimum value of \tilde{u}_{min}^* (highlighted in the plot as a dashed blue line) represents the velocity required to cause the first particle take-off. There will be a range of critical diameters ($[\tilde{D}_{p-crit(1)}, \tilde{D}_{p-crit(2)}]$) in which particles are emitted. Outside of this range, particles remain on the surface caused mainly by, respectively, particle weight for large particles and high adhesion force for small ones.

The wind velocity is directly linked to dust emissions. High wind velocity can cause particle suspension from a surface and are related to high turbulence levels which influence particle transport over long distances.

The aeolian transport takes place in a turbulent flow and the mathematical models of aeolian erosion phenomena must take into account the effects of atmospheric turbulence on the wind flow. The conditions and details of the turbulent approach are presented in section 1.2.

1.2 Modelling of turbulent flows

This section presents the governing equations of the atmospheric fluid flow and the turbulence models usually employed to take into account the turbulence effects on momentum and mass transfer. Equations 1.4 and 1.5 represent the transient and three dimensional form of the mass and momentum conservation for a fluid:

$$\frac{\partial \rho}{\partial t} + \frac{\partial}{\partial x_i}(\rho u_i) = 0 \quad (1.4)$$

$$\frac{\partial}{\partial t}(\rho u_i) + \frac{\partial}{\partial x_j}(\rho u_i u_j) = -\frac{\partial p}{\partial x_i} + \frac{\partial}{\partial x_j} \left[\mu \left(\frac{\partial u_i}{\partial x_j} \right) \right] \quad (1.5)$$

where:

ρ represents density [kg/m^3], u_i corresponds to the component of velocity in direction i [m/s] and μ is the dynamic viscosity [$Pa.s$].

Equations 1.4 and 1.5 are valid for both laminar and turbulent flows. As reported by Versteeg and Malasekera (2007) [76], a complete and direct numerical solution of these equations, for all scales of turbulent motion, would require very fine mesh resolution for the spatial discretization, requiring an enormous computational effort. Thus, several turbulence models have been developed and presented in the literature [16, 39, 42, 49]. Wilcox (1998) [80] enunciates that an ideal model should introduce the minimum amount of complexity while capturing the essence of the relevant physics.

The random nature of a turbulent flow property leads to a decomposition of each flow variable into two main parts: a mean value (\bar{u}) and a fluctuating component (u'). This decomposition was proposed by Osborne Reynolds in the late 19th century:

$$u = \bar{u} + u' \quad (1.6)$$

After the substitution of all variables in the mass and momentum conservation equations by their mean values and fluctuations resulting in Equations 1.7 and 1.8:

$$\frac{\partial}{\partial t}(\rho) + \frac{\partial}{\partial x_i}(\rho \bar{u}_i) = 0 \quad (1.7)$$

$$\frac{\partial}{\partial t}(\rho \bar{u}_i) + \frac{\partial}{\partial x_j}(\rho \bar{u}_i \bar{u}_j) = -\frac{\partial p}{\partial x_i} + \frac{\partial}{\partial x_j} \left[\mu \left(\frac{\partial \bar{u}_i}{\partial x_j} + \frac{\partial \bar{u}_j}{\partial x_i} - \frac{2}{3} \delta_{ij} \frac{\partial \bar{u}_l}{\partial x_l} \right) \right] + \frac{\partial}{\partial x_j}(-\rho \overline{u_i' u_j'}) \quad (1.8)$$

These equations called the Reynolds Averaged Navier-Stokes (RANS) equations, yield to an extra term ($-\rho \overline{u_i' u_j'}$), the turbulent momentum flux, called Reynolds Stress tensor. Thus, after the substitution of Reynolds decomposed variables there are more variables than equations to solve the fluid flow field and a closure problem emerges. The main task of modelling turbulence is to develop computational procedures of sufficient accuracy and generality to predict the Reynolds stresses.

Boussinesq (1887) introduced the eddy viscosity concept. According to Boussinesq, the Reynolds stress can be treated as the laminar shear stress replacing the dynamic viscosity by the eddy viscosity (the Boussinesq analogy) as shown in Equation 1.9. This analogy is accurate for many flows and simplifies their mathematical description and solution.

$$\tau_{ij} = (-\rho \overline{u_i' u_j'}) = \mu_t \left(\frac{\partial \bar{u}_i}{\partial x_j} + \frac{\partial \bar{u}_j}{\partial x_i} \right) \quad (1.9)$$

where, μ_t is the eddy viscosity having the same dimensions as the dynamic viscosity.

Santos (2000) pointed out that there are two main ways to solve turbulence modelling problems based on the Reynolds decomposition: diffusion models (first-order closure, based on Boussinesq analogy) and Reynolds stress model (second-order closure, which does not use the eddy viscosity concept).

It is worth to note that, the numerical simulations to be performed in this thesis are a continuity of some investigations carried out by Turpin (2010) [70] concerning the turbulent fluid flow around wall-mounted obstacles and the aeolian transport of erodible and non-erodible particles. Turpin (2010) [70] evaluated the use of the first order two-equations models K- ϵ and K- ω and found out that K- ϵ was better employed in numerical simulations of an entire industrial site (macro-scale) and the K- ω model gave better results when employed to model the fluid flow surrounding stockpiles and roughness elements (micro-scale). Also, Turpin (2010) [70] indicated that the Large Eddy Simulation (LES) seemed a good choice to enhance the accuracy of the results for simulations involving non-erodible particles.

The $K-\epsilon$ turbulence model is a RANS model which uses the Boussinesq analogy. The eddy viscosity is determined based on the values of turbulent kinetic energy (K) and dissipation rate of K (ϵ). The turbulent kinetic energy is given by Equation 1.10.

$$K = 1/2(\overline{u'^2} + \overline{v'^2} + \overline{w'^2}) \quad (1.10)$$

The dissipation rate (ϵ) of the turbulent kinetic energy is caused by the work of the smallest eddies against the viscous stresses in the fluid flow. The dissipation is the main destruction term in the turbulent kinetic energy equation, with similar order of magnitude as the production term and never negligible. Thus, the eddy viscosity is calculated as shown in Equation 1.11:

$$\mu_t = C_\mu \rho \frac{K^2}{\epsilon} \quad (1.11)$$

where:

C_μ is a constant given by Table 1.1.

As a consequence, two differential equations concerning the transport of turbulent kinetic energy (K) and the dissipation (ϵ) are written (Equation 1.12 and Equation 1.13).

$$\frac{\partial}{\partial t}(\rho K) + \frac{\partial}{\partial x_i}(\rho K \overline{u_j}) = \frac{\partial}{\partial x_i} \left[\left(\mu + \frac{\mu_t}{\sigma_K} \right) \frac{\partial K}{\partial x_i} \right] + G_K - \rho \epsilon \quad (1.12)$$

$$\frac{\partial}{\partial t}(\rho \epsilon) + \frac{\partial}{\partial x_j}(\rho \epsilon \overline{u_j}) = \frac{\partial}{\partial x_i} \left[\left(\mu + \frac{\mu_t}{\sigma_\epsilon} \right) \frac{\partial \epsilon}{\partial x_i} \right] + C_{1\epsilon} \frac{\epsilon}{K} G_K - C_{2\epsilon} \rho \frac{\epsilon^2}{K} \quad (1.13)$$

where:

$C_{1\epsilon}$, $C_{2\epsilon}$, σ_K et σ_ϵ are constants which values are presented in Table 1.1 and G_K represents the production of turbulent kinetic energy given by the following expression:

$$G_K = \mu_t \left(\sqrt{2S_{ij}S_{ij}} \right)^2 \quad \text{with} \quad S_{ij} = \frac{1}{2} \left(\frac{\partial \overline{u_i}}{\partial x_j} + \frac{\partial \overline{u_j}}{\partial x_i} \right) \quad (1.14)$$

Table 1.1: $K - \epsilon$ standard model constants [42]

$C_{1\epsilon}$	$C_{2\epsilon}$	C_μ	σ_K	σ_ϵ
1,44	1,92	0,09	1,0	1,3

The $K - \epsilon$ model allows the description of turbulence for very high Reynolds numbers. The model presents a good performance in a variety of industrial applications and demands reasonable computational effort. However, its main limitations concern complex fluid flows: recirculation, strong anisotropy, negative production (some unconfined or rotating flows) and overestimation of K in impinging flows [11].

An improved version of the standard $K - \epsilon$ was carried out by Shabbir (1998) [65], called the Realizable $K - \epsilon$ model. The Realizable $K - \epsilon$ contains modifications in the transport equation of dissipation and an important evolution of C_μ , written as a function of mean flow properties and turbulent kinetic energy, rather than assumed to be a constant as in the standard model. These modifications are written in terms of the averaged deformation and rotation tensors (Equations 1.15 to 1.17).

$$\frac{\partial}{\partial t}(\rho \epsilon) + \frac{\partial}{\partial x_j}(\rho \epsilon \overline{u_j}) = \frac{\partial}{\partial x_i} \left[\left(\mu + \frac{\mu_t}{\sigma_\epsilon} \right) \frac{\partial \epsilon}{\partial x_i} \right] + \rho C_1 S \epsilon - \rho C_2 \frac{\epsilon^2}{K + \sqrt{\nu \epsilon}} \quad (1.15)$$

$$S = \sqrt{2S_{ij}S_{ij}} \quad \text{and} \quad C_2 = 1,9 \quad (1.16)$$

$$C_1 = \max \left[0, 43; \frac{\eta}{\eta + 5} \right] \quad \text{with} \quad \eta = S \frac{K}{\epsilon} \quad (1.17)$$

Thus, this is a model more adapted to different classes of fluid flow including low values of Reynolds number (as in the near wall region) and also is set to avoid the overestimation of K production. This model was validated for a variety of turbulent flows: rotating, high pressure gradients, separations and recirculation. Shabbir (1998) [65] enunciates that this model has been obtained better results than the standard model.

In addition to the standard and realizable $K - \epsilon$ models, the literature reports the $K - \omega$ model [49] in which eddy viscosity is calculated as a function of K and the specific dissipation rate ω as presented in Equation 1.18:

$$\mu_t = \alpha^* \rho \frac{K}{\omega} \quad (1.18)$$

where:

α^* is calculated in function of the Reynolds number. For a high Reynolds number $\alpha^* = 1$.

This model is based on the relation between K , ω and a characteristic integral length (l), initially highlighted by Kolmogorov [76]:

$$\omega = \frac{CK^{\frac{1}{2}}}{l} \quad (1.19)$$

where:

C is a constant.

One of the advantages of the $K - \omega$ formulation is the near wall treatment. The $K - \omega$ model does not involve the complex non-linear damping functions required for the $K - \epsilon$ model and it is therefore more accurate. Equations 1.20 and 1.21 represent the formulation of the transport equations of the $K - \omega$ model.

$$\frac{\partial}{\partial t}(\rho K) + \frac{\partial}{\partial x_i}(\rho K \bar{u}_i) = \frac{\partial}{\partial x_j} \left[\Gamma_K \frac{\partial K}{\partial x_j} \right] + G_K - Y_K \quad (1.20)$$

$$\frac{\partial}{\partial t}(\rho \omega) + \frac{\partial}{\partial x_i}(\rho \omega \bar{u}_i) = \frac{\partial}{\partial x_j} \left[\Gamma_\omega \frac{\partial \omega}{\partial x_j} \right] + G_\omega + Y_\omega \quad (1.21)$$

where:

G_K and G_ω represent the production of K and ω , Γ_K and Γ_ω represent the effective diffusion of K and ω and Y_K and Y_ω represent the dissipation of K and ω .

Menter (1994) [49] reported that the $K - \omega$ gives more accurate results inside the logarithmic zone than the $K - \epsilon$ model for compressible flows and flow with adverse pressure gradients (the case of fluid flow surrounding stockpiles is an example). The model is better adapted to complex flows and in the near wall region has given more accurate results. This model is strongly dependent on the mesh refinement near the wall characterized by the chosen value of y^+ .

A variant of the $K - \omega$ model is the $K - \omega$ Shear Stress Transport (SST) model, developed by Menter (1994) [49]. The $K - \omega$ SST model was designed to give a highly accurate prediction of the flow separation under adverse pressure gradients by including the transport effects into the formulation of the eddy-viscosity. The $K - \omega$ SST model includes two main modifications: (i) the turbulent viscosity is modified (Equation 1.22) to better represent the effects of shear stress transport which allows solving a wider range of problems than those solved by the $K - \epsilon$ model and (ii) nother modification is the addition of a diffusion term in the ω equation and a specific function that allows the validity of the equations in the near and far wall zones (Equation 1.24). These two $K - \omega$ models are used for low and high Reynolds numbers.

$$\mu_t = \frac{\rho K}{\omega} \frac{1}{\max \left[\frac{1}{\alpha^*}, \frac{\Omega F_2}{a_1 \omega} \right]} \quad (1.22)$$

with

$$\Omega = \sqrt{2\Omega_{ij}\Omega_{ij}} \quad (1.23)$$

where:

Ω_{ij} is the average rotation tensor and F_2 is a function of ω .

$$\frac{\partial}{\partial t}(\rho\omega) + \frac{\partial}{\partial x_i}(\rho\omega u_i) = \frac{\partial}{\partial x_j} \left[\Gamma_\omega \frac{\partial \omega}{\partial x_j} \right] + G_\omega + Y_\omega + D_\omega \quad (1.24)$$

The four models presented previously are first-order Reynolds Averaged models.

Turpin (2010) [70] proposed that the LES allows a more precisely study of turbulent properties and flow structures downstream an obstacle as well the evolution of turbulence production. Ferziger (2002) [29] and Blasek (2001) [6] pointed out that LES is based on the observation that small turbulent structures are more universal in character than the large eddies. In general, LES is the preferred method for flows in which the Reynolds number is too high or the geometry is too large to allow application of DNS. In comparison to turbulence modelling based on the RANS equations, LES requires higher grid resolution. It is worth to note that the LES, succinctly introduced in this paragraph, is not explicitly performed in this thesis. Only very initial results are presented in the section devoted to present the perspectives

1.3 Turbulent wall flow properties

1.3.1 Velocity profile

The effect of walls on fluid flows is related to turbulence damping and there are many practical problems in which an accurate calculation of the flow field involving a solid surface is of great importance, such as: the quantification of dust emission of erodible and non-erodible particles from stockpiles (isolated, successive or placed in an industrial site surrounded by arrays of buildings) requires accurate results of the flow field calculated over the near wall region. It is important to point out that the local approach of the non-erodible particles over a surface characterizes this surface as a rough wall instead of a smooth wall.

Ludwig and Tillmann (1950) [47] found that near a smooth wall, the mean velocity points fall on the well known universal curve of y^+ (Equation 1.25) versus u^+ (Equation 1.26), even if a pressure gradient is presented.

$$y^+ = \frac{y \cdot u^*}{\nu} \quad (1.25)$$

$$u^+ = \frac{\bar{u}}{u^*} \quad (1.26)$$

where, u^* is the friction velocity given by Equation 1.27:

$$u^* = \sqrt{\frac{\tau_w}{\rho}} \quad (1.27)$$

where, finally, τ_w is the wall shear stress.

Figure 1.4, initially presented by Ludwig and Tillmann (1950) [47] and also published in the work of Clauser (1954) [17] presents the chart correlating the wall variable u^+ and y^+ . Other authors have also carried out this class of experimental work to determine this relation [40, 64].

As y^+ increases, the u^+ profile presents three typical regions (as seen in Figure 1.4 adapted from Chassaing (2000) [14]). The first region in the chart is the viscous sub-layer extending to $y^+ \approx 7$. In the viscous sub-layer the effects of the viscosity are considerably stronger than the turbulence effects. Furthermore, the relation between u^+ and y^+ has a form of a linear law $u^+ = y^+$.

After that, inside an intermediary zone (y^+ approximately between 7 and 30), it is the transition between the linear to the logarithmic profile. For values of y^+ from 30 to approximately 400 the velocity profile as presented in Figure 1.4 is represented by a logarithmic profile. The logarithmic

profile is more discussed hereunder as it is influenced by the presence of roughness over the wall. This logarithmic profile is presented by Equation 1.28. Finally, after the recovering region (log profile), the fluid flow enters inside a wake region. The velocity profile for a completely smooth surface is:

$$u^+ = \frac{1}{\kappa} \ln(y^+) + C \quad (1.28)$$

where, κ is the Von Kármán constant (≈ 0.4) and $C = 5.45$.

1.3.2 Roughness effects

The presence of roughness impacts significantly the fluid flow turbulent properties [68]. For rough walls, the most important effect found out over the fluid flow properties is the augmentation of shear stress (friction). The work of Nikuradse (1932) [55] was pioneer in describe the effects of a rough wall on the fluid flow. The main important effect of the roughness is the augmentation of the turbulence near the wall as well the diminution of the mean velocities in the exterior zone of the turbulent boundary layer.

A significant characteristic established was a change in the logarithmic profile (see Figure 1.5). This modification in the profile has been presented in several works [14, 17, 58, 71] which have given a relation between the logarithm profile and a new parameter called roughness height (h_s). The shift between the logarithm profile and the actual profile is represented by Δu^+ (Equation 1.29).

$$\Delta u^+(h_s^+) = \frac{1}{\kappa} \ln(h_s^+) - B \quad (1.29)$$

with,

$$h_s^+ = \frac{h_s \cdot u^*}{\nu} \quad (1.30)$$

where, $B = 2.98$, u^* is the friction velocity over the underlying surface and roughness elements and h_s is the mean height of the roughness elements.

The velocity profile of the logarithmic zone for a fluid flow over a rough wall may then be described as a parameter of the roughness height (Equation 1.31) based on Equation 1.28 and Equation 1.29:

$$u^+ = \frac{1}{\kappa} \ln(y/h_s) + C + B \quad (1.31)$$

where, B for a rough wall is then dependent on the flow regime and roughness height.

The concepts related to the presence of roughness elements on a smooth wall are not presented in this section of the bibliographic review due to correlated investigations which are presented in a section devoted to the local analysis of non-erodible particles.

1.3.3 Fluid flow around wall-mounted obstacles

The wind flow is strongly disturbed by complex wall-mounted obstacles. The presence of an obstacle creates features such as: three-dimensional vortices, impingement, upwash and downwash. The solid surfaces (ground floor and obstacles surface) generate more shear stress affecting the turbulent wind flow.

The generalities of a fluid flow around a wall-mounted obstacle have been largely investigated by different authors [7, 32, 44, 59, 61, 67]. These works represent several applications of the investigation of wall-mounted obstacle: contaminant dispersion, turbulence models validation and wind-tunnel studies comparison and description of atmospheric boundary layer.

As reported by Santos (2000) [60], the fluid flow around an isolated building is very complex, with highly unsteady and three-dimensional turbulent structures produced by the shear stress of the flow disturbed by the building. Under neutral atmospheric conditions, buoyancy forces do not affect the fluid flow and contaminant dispersion. Figure 1.6 shows a cubic obstacle and the usual flow structures for a wind flow perpendicular to one of the obstacle faces. Although, the final flow pattern depends on obstacles shape and dimensions and upstream flow characteristics, fluid flow

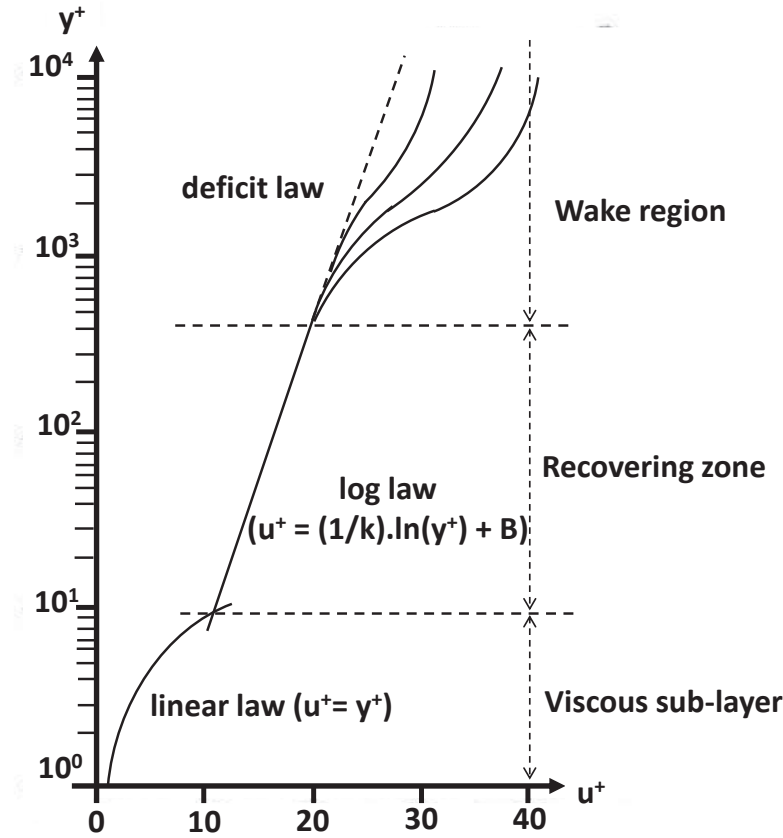


Figure 1.4: Chart correlating the wall variables u^+ and y^+ . Adapted from Chassaing (2000) [14]

around obstacles, generally, presents typical flow structures which are highlighted and numbered in Figure 1.6. These structures were shown as characteristics by several experimental and numerical reference works [20, 36, 50, 60, 67]. Thus, the five recognized flow structures around an obstacle are: (i) incident flow region (structure 1), (ii) horseshoe vortex (structure 2), (iii) separation regions (structure 3), (iv) near wake (structure 4) and (v) far wake (structure 5).

The incident flow region (structure 1) in Figure 1.6 presents the stagnation zone on the windward wall where the maximum values of pressure are noticed. Moreover, wind and friction velocity are smaller near the wall in the incident zone than in the other zones. Therefore, the fluid flows toward the ground from the stagnation zone and just before touching the ground, it returns to the main flow in the opposite direction (reverse flow), characterizing the first recirculation zone in this region. The second structure (horseshoe vortex) is generated by the interaction between the flow stream and the reverse incident flow. A combination of vorticity and pressure distribution in windward wall results in flow disturbances generating streamlines towards the ground and consequently its spanwise deviation forming the so-called horseshoe vortex due to its shape which is easily perceived in Figure 1.6 by the helical vortices formed on the incident zone and further downwind. The main horseshoe vortex induces the formation of other smaller similar vortices.

Fluid flow accelerates as the incident flow impinges on the windward wall, deviating (due to the acceleration) towards the roof and lateral sides of the obstacle. Hence, the separation regions are formed (see structure 3 in Figure 1.6) on the edges of the windward wall. The fluid flow momentum is higher (high velocity values after the flow acceleration) which causes flow detachment instead of smooth fluid movement around the obstacle. Downstream the wall-mounted obstacle, there exist the near and far wake regions (structure 4 and 5 in Figure 1.6, respectively). The near wake region is characterized by the recirculating region downstream the building. This region has intense circulatory motion, low flow velocities and high turbulence intensity. As reported by Santos (2000) [60], the turbulence causes mixing of adjacent layers inside and outside the separation regions. Large eddies will

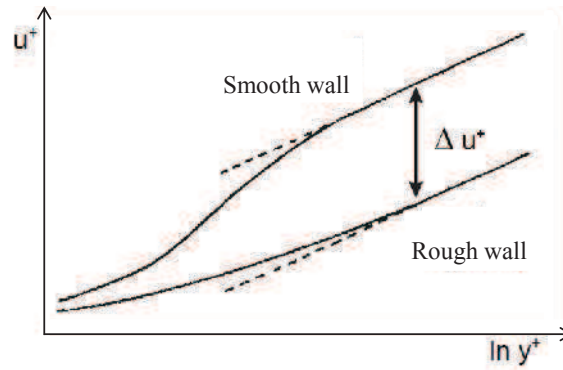


Figure 1.5: Shift in the logarithmic profile zone. Adapted from Cousteix (1989) [19]

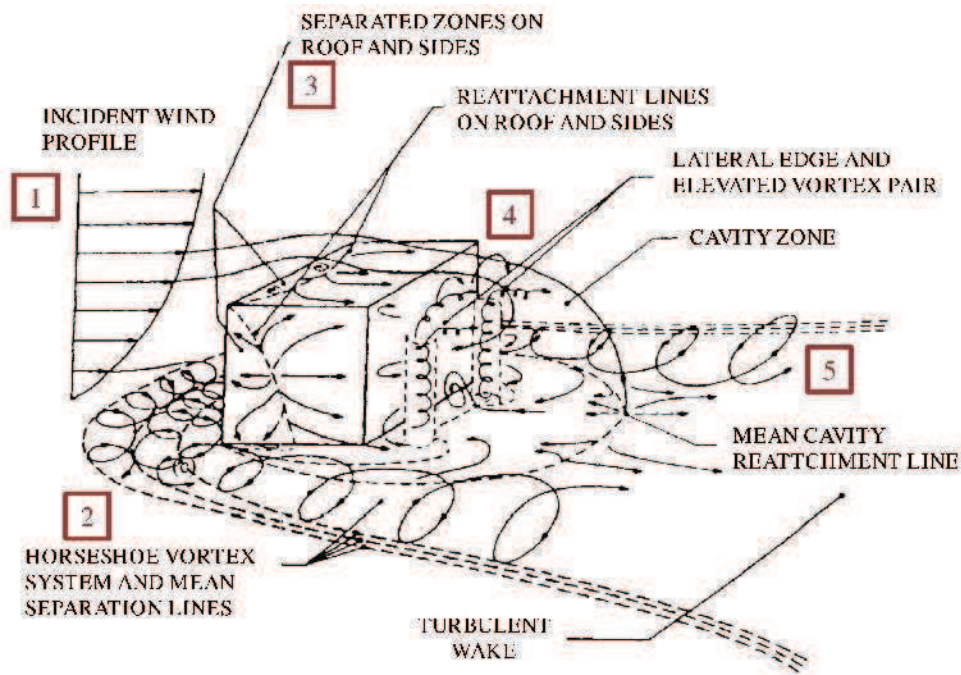


Figure 1.6: Main flow features observed around an isolated cubical obstacle. Adapted from Hosker (1980) [36]

occasionally penetrate both ways through this shear layer. The far wake region is located downwind the reattachment zone and remains till the fluid flow is no longer disturbed by the obstacle. In the far wake region, the turbulence intensity is still higher than in the regions of undisturbed flow, velocity is lower and there is air movement towards the ground.

In addition of studies about typical features around cubical obstacles as shown above, Badr (2007) [1], Toraño et al. (2009) [69] and Turpin (2010) [70] are examples of works that carried out studies about wind flow impinging stockpiles. Figures 1.7a and 1.7b present the results of numerical simulations of a scaled-up stockpile model oriented 90° to the wind flow direction. Turpin (2010) [70] also performed PIV measurements in a wind-tunnel in order to validate the numerical results.

Figure 1.7a shows contours of static pressure at the solid surfaces (ground and stockpile). Three main regions can be noticed: the incident flow region (structure A) where high levels of pressure (stagnation zone) are noticed; recirculation zones (structure B, also called near wake) downstream the stockpile where low pressure levels are perceived; further downwind is for turbulent wake (structure C). The transition between regions B and C is marked by the reattachment line.

Figure 1.7b shows a lateral view of the stockpile, presenting four typical flow features similar to those observed around the isolated cubical obstacle: flow impinging region (structure 1) where the

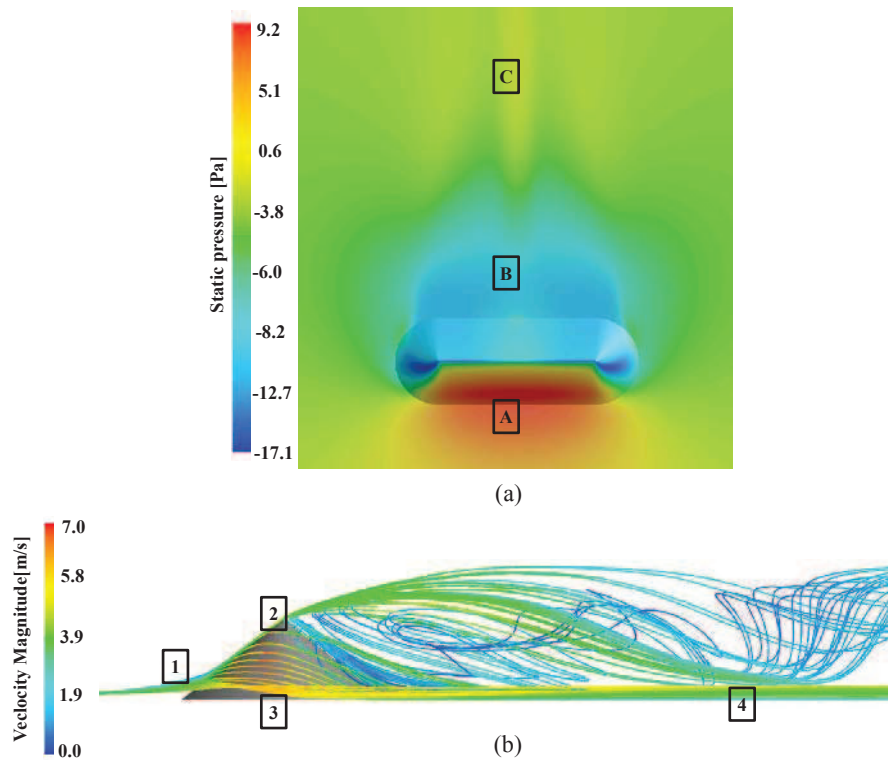


Figure 1.7: Numerical simulation of fluid flow around a stockpile perpendicular to the main wind flow direction: (a) Contours of thermodynamic pressure at the wall over and around the stockpile and (b) Coloured pathlines of fluid particles released from a line on the ground upstream the obstacle. Adapted from Turpin (2010) [70]

fluid flows towards the stockpile top and lateral walls (structures 2 and 3) characterizing separate zones and finally the reattachment (structure 4).

The literature review presented above showed various works concerning numerical simulations which were validated by different experimental techniques. It also presented some theoretical aspects of fluid flow structures around obstacles. Despite of the well established knowledge about this subject and the good agreement between numerical simulations results and experimental data presented by different authors, still there are many physical information to acquire, some numerical simulation problems to be sorted out and experimental techniques to evaluate and test.

1.4 Dust emission quantification and physics

This section of the bibliographic review describes the physics of the dust emissions phenomena. It describes the most widely used methodology for dust emission quantification of diffuse sources and works concerning the effects of non-erodible particles.

1.4.1 USEPA model for dust emission quantification from diffuse sources

Important quantities of dust can be emitted from mechanical disturbances or even natural aeolian erosion events on storage piles of granular materials. Much effort has been put to quantify and analyse the efficiency of atmospheric pollution control techniques in open storage yards of steelworks sites. As reported by Badr (2007) [1], fugitive dust emissions from stockpiles in open storage yards of industrial sites and its atmospheric dispersion have brought many environmental and economical problems.

The most widely used methodology to estimate dust emissions from diffuse sources is the model proposed by USEPA (2006) [75]. This model is based on emission factors. As explained in the

general USEPA guide about emission quantification (1985) [74], emission factors are representative values that attempts to relate the quantity of a pollutant released to the atmosphere with an activity associated with the release of that pollutant. These factors are usually expressed as the weight (mass) of pollutant divided by sources conditions (weight, volume or dimensions) or duration of the activity that causes the emission. Such factors facilitate emissions estimation of various sources of air pollution. Equation 1.32 shows the general equation for emissions estimation using emission factors:

$$E = A.EF.(1 - ER/100) \quad (1.32)$$

where E = emissions; A = activity rate; EF = emission factor and ER = overall emission reduction efficiency.

The USEPA general report (1985) [74] indicates that each emission factor is rated according to its robustness. The robustness is related to the amount of data used to statistically produce the emission factor, the quality of the data (how measurements were carried out) and the insufficiency of parameters such as temperature and reactant concentrations to describe the physical and chemical phenomena involved in the emission process. Thus, some emission factors yields to more realistic estimations than others.

The methodology of dust emission quantification from stockpiles of granular materials is part of a specific report of USEPA (2006) [75]. The model applies emission factors considering three main input data:

- a size parameter for the emitted particles, through a multiplier related to the aerodynamic particle size,
- a number of disturbances noticed over the pile during the period when the estimation of emission rate is performed and
- an erosion potential associated to the velocity distribution at 25 cm above the stockpile wall (perpendicular to the stockpile surface).

The emission factor (EF) for particle matter emissions due to wind erosion from mixtures of erodible and non-erodible surfaces material calculated as expressed in the Equation 1.33, in g/m^2 :

$$EF = k \sum_{i=1}^N P_i \quad (1.33)$$

where k is the particle size multiplier, N is the number of disturbances per year and P_i is the erosion potential corresponding to the observed fastest mile of wind for the i^{th} period between disturbances, given in g/m^2 .

The first factor presented in this equation is the particle size multiplier (k) which varies with the aerodynamic particle size as is presented in Table 1.2:

Table 1.2: Particle size multiplier (k) for several aerodynamic particle sizes

$> 30\mu m$	$15\mu m$	$10\mu m$	$2.5\mu m$
1.0	0.6	0.5	0.075

According to Table 1.2, for instance, emissions of PM_{10} are calculated by using $k = 0.5$.

The frequency of disturbances in each pile is taken into account by the variable N . USEPA model defines a disturbance as an action that results in the exposure of fresh surface material. On a storage pile, this would occur whenever aggregate material is added or removed from the pile surface. Hence, for a surface disturbed in daily basis, N would be equal 365, and, on the other hand, for a surface disturbed only each 4 months, N would equal 3 for an annual estimation.

The erosion potential (P) defines the value of dust mass emitted per unit of area of the stockpile (Equation 1.34).

$$\begin{cases} P = 58 (u^* - u_t^*)^2 + 25 (u^* - u_t^*) \\ P = 0 & \text{for } u^* \leq u_t^* \end{cases} \quad (1.34)$$

where u^* is the friction velocity (m/s) and u_t^* is the threshold friction velocity (m/s).

Therefore, the formulation of the erosion potential presents two concepts of velocity: friction velocity and threshold friction velocity. Threshold friction velocity is the friction velocity at which the wind erosion is initiated. The value of threshold friction velocity is dependent on some characteristics: surface material and free stream wind velocity in the region of the experiments. USEPA reports values of threshold friction velocity determined by field measurements with a portable wind-tunnel. Table 1.3 presents typical values of u_t^* for various materials linked to the roughness height and threshold wind velocity at 10 m.

Table 1.3: Threshold friction velocity for several material and conditions as reported by the USEPA (2006) [75]

Material	Threshold Friction Velocity (m/s)
Overburden	1.02
Scoria (roadbed material)	1.33
Ground coal (surrounding coal pile)	0.55
Uncrusted coal pile	1.22
Scraper tracks on coal pile	0.62
Fine coal dust on concrete pad	0.54

The friction velocity (u^*) used in this emission factor formulation is based on logarithm wind profile. This equation can then be rewritten as a linear function of the fastest mile of wind measured by an anemometer of reference for a period between disturbances (Equation 1.35). This fastest mile represents the magnitude of wind gusts with a typical duration of 2 min. However, the USEPA model recommends that the friction velocity equation based on the logarithmic profile (Equation 1.35) should not be applied because this equation was developed to describe a non disturbed wind velocity profile, i. e., does not have influence from any obstacle as the stockpile model.

The incoming flow is largely disturbed by the presence of an obstacle such as a storage pile. This perturbation is understood as significant variations of friction velocity on the surface relative to its reference value without perturbation. The method implemented by USEPA consider each zone of friction velocity of the same magnitude as a separate source. The friction velocity is then given by Equation 1.36, derived from an undisturbed logarithmic velocity profile (Equation 1.35), but which depends on the velocity u_s measured (or computed by CFD simulations) near the surface.

$$u^* = 0.053 u_{10}^+ \quad (1.35)$$

$$u^* = 0.10 \left(\frac{u_s}{u_r} \right) u_{10}^+ \quad (1.36)$$

where u^* is the friction velocity to take into account in Equation 1.34, u_s is the velocity measured (computed, as example, by CFD simulations) at the surface corresponding to a height of 25 cm from the ground, u_r is the approaching wind speed (far from the stockpile) and u_{10}^+ is the fastest mile of a reference anemometer for a period between disturbances.

USEPA proposes the exposure factor distributions shown in Figure 1.8, derived from wind tunnel measurement on isolated stockpiles. These subareas represent different levels of wind erosion exposure. Figure 1.8 illustrates examples of different piles shape and configuration subdivided in regions having the same values of the ratio u_s/u_r .

Finally, Equation 1.37 gives the global dust emission for a stockpile. M represents the number of different surfaces regarded as having the same value of the ratio u_s/u_r . The dust emission E is given in g .

$$E = k \sum_{i=1}^N \sum_{j=1}^M P_{ij} S_{ij} \quad (1.37)$$

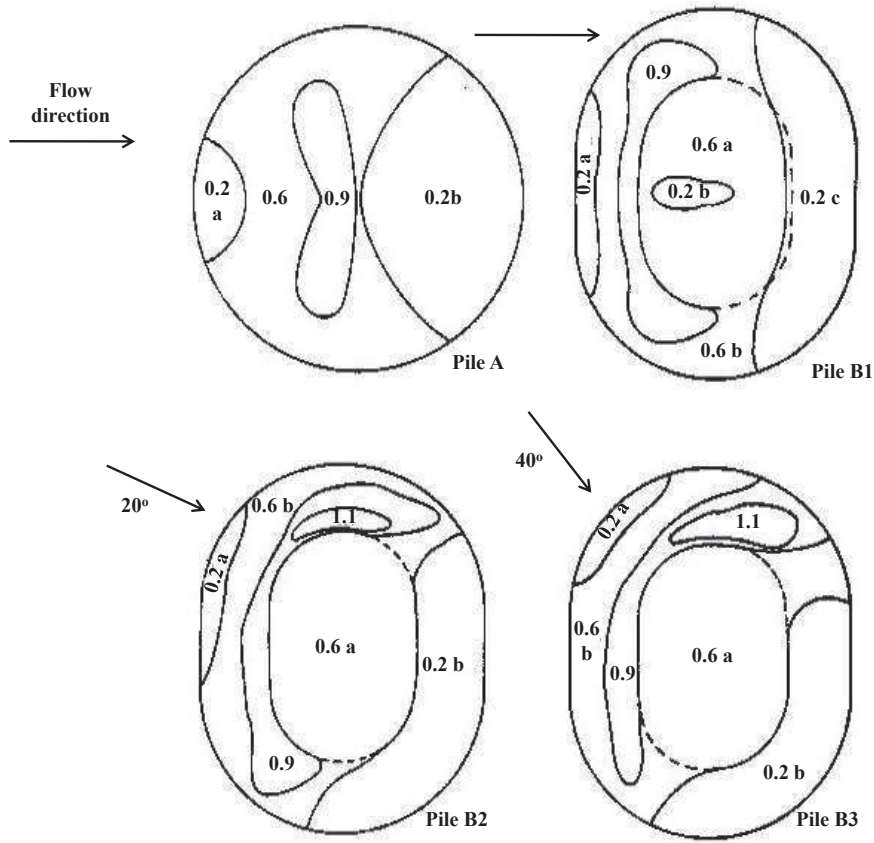


Figure 1.8: Contours of normalized surface windspeeds, u_s/u_r [75]

For each perturbation i , the stockpile dry exposed surface area is divided in different subareas (S_{ij}) (Figure 1.8) according to the friction velocity distribution over the piles. The overall value of P_{ij} is the summation of the values for each subarea (S_{ij}). Each surface (S_{ij}) calculated is then considered as a different source. The fastest mile of the wind velocity at 10 m height (u_{10}^+) is one of the input data as well as k (the particle size multiplier) and N (the number of perturbations), thus, must be determined prior running the model. The friction velocity u^* can be calculated using Equation 1.36. For each ratio u_s/u_r , a value of u^* is calculated. The threshold friction velocity, which is the friction velocity at which the wind erosion is initiated, is determined experimentally and basically depends on the material and its granulometry used, thus it is also an input data to the model. The erosion potential P_{ij} is estimated using Equation 1.34 for each surface (subarea, j) in which the stockpile was divided. The values of friction velocity and threshold friction velocity are needed. It is important to note that emissions depend on exposure levels, especially by the different values of u_s/u_r , but also surface distributions associated with different values of u_s/u_r .

1.4.2 Non-erodible particles and their influence on dust emission quantification

A surface of a granular material agglomeration is frequently a mixing of erodible and non-erodible particles. The particles with relatively large diameters are not transported by the wind and remain over the eroded surface. The discussion about the general effects of non-erodible particles on wind erosion can be found in the literature [9,12,13,33,37,46,54,58,71]. The threshold friction velocity of a surface covered by a large number of roughness elements (represented by non-erodible particles) assumes a large value which indicates that the take-off of erodible particles is rather more difficult. The erodible particles are sheltered by the non-erodible particles which reduces soil erodibility. Brown et al. (2008) [9] stated that roughness elements attenuate wind erosion by physically covering a portion of the surface and by extracting a portion of the wind momentum. Some of the literature works about non-erodible particles effects on erodible surfaces above mentioned are described hereafter.

Raupach et al. (1993) [58] investigated the effects of roughness elements by proposing a param-

eter that relates the threshold friction velocity for rough and smooth walls. These authors stated that soil erosion is strongly attenuated by the presence of non-erodible particles. There are several types or classes of non-erodible particles related to different diameters of the roughness elements. The work of Raupach et al. (1993) [58] was based on two main simplifications: it has considered the roughness density parameter (λ) without taking into account the shape of roughness elements and it has disregarded the near wall turbulence. The roughness density (λ) is presented in Equation 1.38:

$$\lambda = \frac{N_p b(h_{NEP})}{S_{NEP}} \quad (1.38)$$

where N_p is the number of roughness elements and b and h_{NEP} are width and height [mm], respectively. S_{NEP} is the total area of the domain where the elements are distributed [mm^2]. As in the formulation proposed by Raupach et al. (1993) [58] (Equation 1.38), the shape of the non-erodible particle is not taken into account, a cylinder with b equals to h_{NEP} and a hemisphere leads to the same parameter λ (N_p and S_{NEP} are the same in both situations). The shape of the non-erodible particle is taken into account by a more recent study that may be seen later.

In the work of Neuman and Nickling (1995) [54], wind-tunnel simulations were carried out to study the decay of particles mass flux due to the presence of non-erodible particles on an erodible bed. These authors investigated the influence of non-erodible particles on shear stress distribution over the surface and measured the threshold friction velocity. It was shown that the velocity profile is an important parameter to the physical understanding of the mass flux decay. Friction velocity and surface geometric roughness were also shown to be very important parameters. These results confirm previous hypothesis that particle transport is reduced due to the presence of the non-erodible particles over a large range of roughness density.

Brown et al. (2008) [9] also stated that surface roughness decreases the effects of wind erosion on granular materials by means of wind-tunnel examination. This work performed experimental measurements of the wall shear stress. As mentioned earlier, the amount of non-erodible particles may shelter the erodible particles and avoid wind erosion. However, it is important to state that a small quantity of non-erodible particles may result in an opposite effect, i.e., a stronger shear stress on the erodible surface which can be explained by the presence of turbulent eddies around isolated roughness particles.

Turpin et al. (2010) [71] performed three-dimensional numerical simulations, characterizing the fluid flow over a bed simulating erodible particles covered by roughness elements (non-erodible particles). The authors implemented two different geometries (spherical and cylindrical) with a mono-dispersed distribution of the non-erodible particles. Mono-dispersion distribution means that all elements have the same heights and diameters.

Two parameters are used to describe the influence of non-erodible particles on wind erosion of granular materials: geometry of the roughness elements and the friction velocity ratio (R_{fric}). R_{fric} , shown in Equation 1.39, is the ratio between u_s^* , the mean friction velocity over a smooth wall, and u_r^* the mean friction velocity over the underlying surface around the roughness elements.

$$R_{fric} = u_s^*/u_r^* \quad (1.39)$$

The roughness elements are represented by spherical and cylindrical elements in numerical simulations, whilst natural beds are usually constituted of irregular roughness elements. Figure 1.9a shows a cylindrical element used in the numerical simulations and its typical dimensions: h_{NEP} (height) and b (diameter). Spherical and cylindrical elements differ in relation to their influence on the original flow modification. Spherical elements slightly perturb the flow field and cylindrical elements tend to create flow detachment, recirculating zone downstream the element and zones of low friction velocity linked to the development of large vortices on the lee sides. Turpin et al. (2010) [71] explain that a natural roughness element is closer, in changes flow generated, to a cylindrical configuration than a spherical one.

Numerical simulations results have shown that a low velocity region is created downstream of the roughness element; this region constitutes an area of low shear stress on the wall and thereby forms a

protection area for the underlying erodible particles. If roughness height increases, detachment of the flow appears and forms larger wakes zone downstream. If height and breadth of the roughness element increase, the flow patterns are significantly modified. At higher Reynolds number the recirculation area downstream the element is well developed. Another noteworthy phenomenon is that as the height and elements number increase, the wake zones are enlarged and as a consequence, the surrounding roughness elements interact with each other leading to friction velocity decrease on the surface.

The parameter R_{fric} is, initially, related to the cover rate TDC and h_{NEP}/b as shown in Equation 1.40. TDC is the cover rate which indicates the ratio between the sum of the projected surfaces of roughness elements ($\sum S_{floor}$) and the total erodible surface area (S_{NEP}). Numerical simulations carried out by Turpin et al. (2010) [71] allowed to determine the values of R_{fric} for cylindrical and spherical roughness elements and the least square method allowed to calculate the constants a_p , m_p and n_p corresponding to the following formulation:

$$1 - R_{fric} = a_p \cdot TDC^{m_p} (h_{NEP}/b)^{n_p} \quad (1.40)$$

However, the geometrical parameter (h_{NEP}/b) was tested by numerical simulations of flow around an isolated roughness element for different configurations. For each configuration, the drag coefficient (C_d), shown in Equation 1.41, was calculated. It was plotted against two dimensionless geometrical parameters (h_{NEP}/b and $S_{frontal}/S_{floor}$) as shown in Figure 1.9b and Figure 1.9c, respectively. These figures show that the relation between C_d and $S_{frontal}/S_{floor}$ does not depend on the shape of the roughness element whereas different relationships between C_d and h_{NEP}/b are obtained for different shapes of the roughness element (spherical or cylindrical). Therefore, the use of $S_{frontal}/S_{floor}$ allows a more general equation to quantify R_{fric} .

$$C_d = \frac{F_d}{(1/2)\rho S_{frontal} u_s^{*2}} \quad (1.41)$$

where F_d is the drag force, ρ is the air density, $S_{frontal}$ is the frontal surface of the roughness element and u_s^* is the friction velocity on the smooth surface.

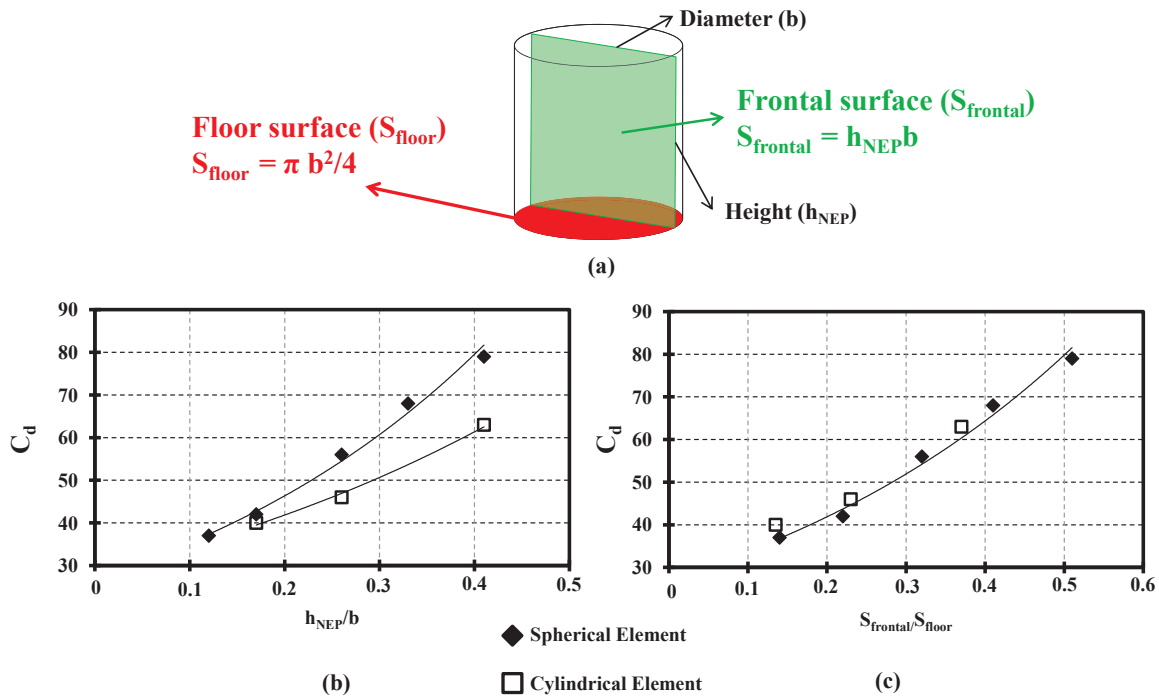


Figure 1.9: (c) Cylindrical roughness element. Evolution of the drag coefficient C_d for isolated cylindrical and spherical roughness elements as a function of: (b) h_{NEP}/b and (c) $S_{frontal}/S_{floor}$ [70]

A further investigation performed by Turpin et al. (2010) [71] enabled an adjustment of Equation 1.40 considering the range of new variables $S_{frontal}/S_{floor}$ and TDC .

- for $S_{frontal}/S_{floor} \cdot TDC \leq 2$:

$$1 - R_{fric} = a_{p1} \cdot TDC^{m_{p1}} \left(\frac{S_{frontal}}{S_{floor}} \right)^{n_{p1}} \quad (1.42)$$

- for $S_{frontal}/S_{floor} \cdot TDC > 2$:

$$1 - R_{fric} = a_{p2} \cdot TDC^{m_{p2}} \left(\frac{S_{frontal}}{S_{floor}} \right)^{n_{p2}} \quad (1.43)$$

Finally, Figure 1.10 shows the evolution of the parameter R_{fric} in function of the geometrical parameter $S_{frontal}/S_{floor} \cdot TDC$. The use of two sets of coefficients in Equations 1.42 and 1.43 is justified by the slope break around 2.

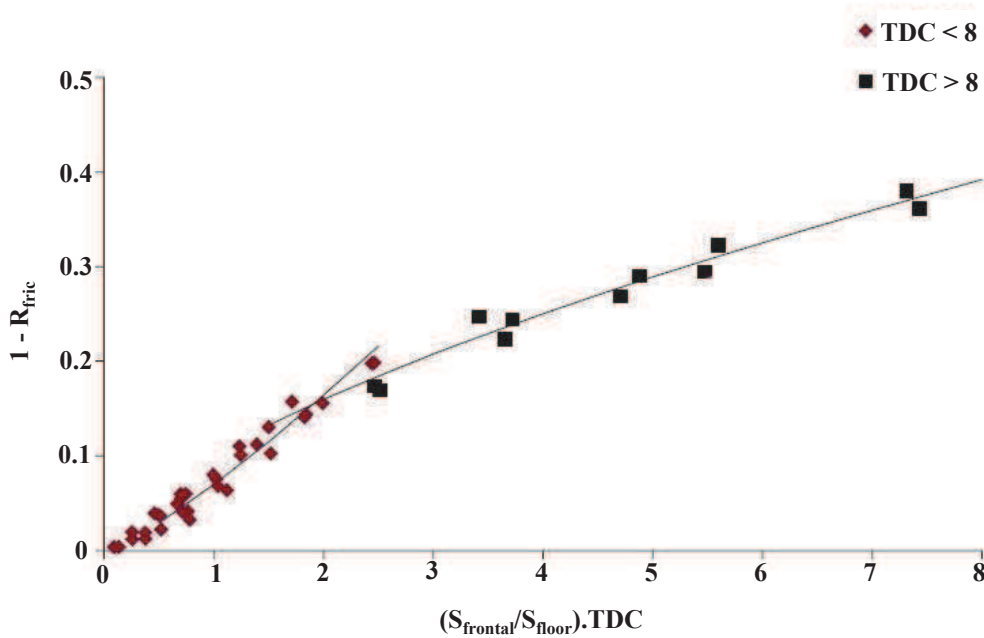


Figure 1.10: Evolution of $1 - R_{fric}$ in function of the value of $S_{frontal}/S_{floor} \cdot TDC$ [71]

Turpin et al. (2010) [71] investigated mono-dispersed bed (the elements have all the same height and breadth) of non-erodible particles; however, in nature, particles have a variety of dimensions and formats. Poly-dispersed beds of non-erodible particles are still an open subject in the literature.

The works described above presented the local analysis of non-erodible particles in order to investigate its influence on the total emitted mass flux of particles. Those authors developed wind-tunnel techniques to measure shear stress distribution on the solid surfaces as well as numerical simulations. Next paragraphs present also experimental and numerical works that focused on another impact of non-erodible particles: temporal decreasing of the emitted mass flux.

Descamps (2004) [21] has investigated the time decay of particles mass flux emitted from a bed of granular materials exposed to a turbulent flow. The developed model is based on the interaction between two phenomena: particles take-off and near wall turbulence structures. The near wall turbulent structures are closely correlated to the take-off of a particle towards the free stream flow. Thus, the particle is transported outside the surface layer. Once this particle is in the fully turbulent boundary layer (away from the near wall region), there are two possible fates: atmospheric dispersion or deposition, depending on its diameter, shape and density.

The next paragraphs expose the numerical model proposed by Descamps (2004) [21] to quantify the mass flux decay of a bed of particles. The emission model is divided in three main parts (cf. Descamps (2004) [21] for more details about the model algorithm):

- the aerodynamic entrainment of particles,
- the definition of take-off criterion and
- the pavement modelling

The aerodynamic entrainment is based on the strong link between particles take-off and turbulent structures above the surface. These turbulent structures are supposed to be independent of the presence of particles over the surface and have a well known statistical spatial periodicity. The spatial periodicity of appearance of turbulent vortex structures has been studied and calculated as a non-dimensional value by numerical simulations (as those carried out by Jimenez and Moin (2000) [38]). The spatial periodicity (λ_p) is non-dimensional and related to kinematic viscosity ν [m^2/s] and friction velocity u^* [m/s] (Equation 1.44):

$$\lambda_p^+ = \frac{\lambda_p u^*}{\nu} \quad (1.44)$$

Therefore, λ_p is a useful parameter to calculate the number of possible occurrences of take-off along spanwise (λ_{p-y}) and streamwise (λ_{p-x}) directions. Figure 1.11 shows an schematic configuration of bed surface divided in boxes in which an ejection (of a turbulent eddy), and consequently a take-off of a particle is possible. In Figure 1.11, l and L represents the bed width and length, respectively. Thus, by supposing a strong correlation between wall structures and particles take-off, the numbers of possibilities of taking-off along the spanwise and streamwise directions can be estimated by l/λ_{p-y} and L/λ_{p-x} , respectively.

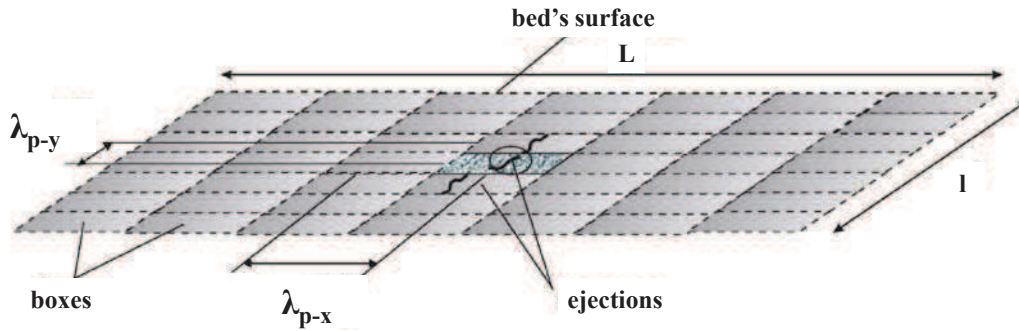


Figure 1.11: Number of taking-off possibilities at the bed surface. Adapted from Descamps (2004) [21]

Finally, the time step of the model is given by T_b which is the average periodicity of occurrence of wall structures [5].

$$T_B^+ = \frac{T_B u_\tau^2}{\nu} \approx 250 \quad (1.45)$$

After defining the number of take-off possibilities and the time step, it is necessary to determine a take-off criterion which can be established considering the balance of forces exerted on a particle lying at a flat horizontal surface. The balance of forces described in Equation 1.46 involves the lift forces (upward), the adhesive forces and the particle weight (downward). The aerodynamic or lift force and adhesive force are determined by the probability density functions as given by Mollinger and Nieuwstadt (2000) [52] and Zimom (1982) [83]. Thus, given a representative diameter D_p

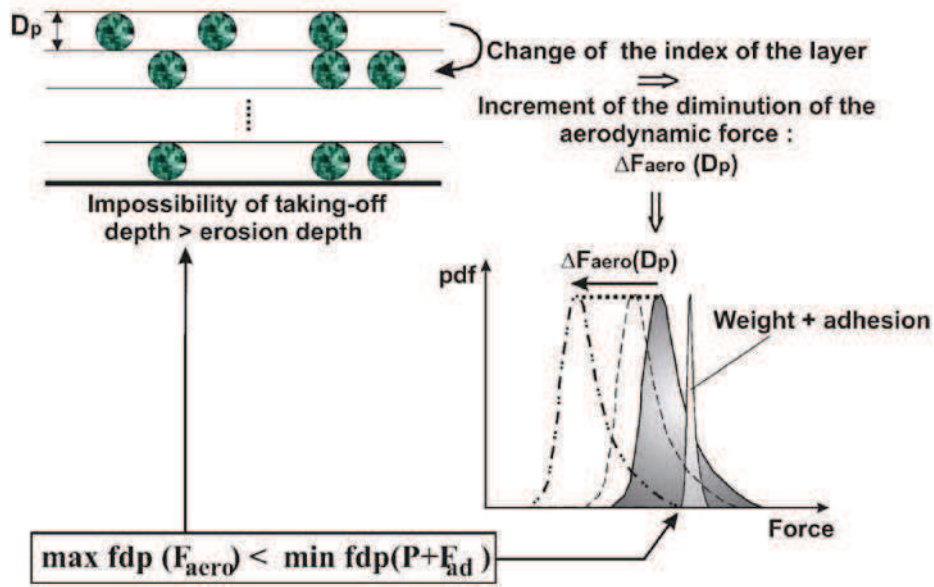


Figure 1.12: Balance of forces exerted on a particle and the effect of pavement on particle take-off [22]

(representative of a range of diameters), Equation 1.46 presents the take-off criterion which gives the decision if a particle either takes-off or stays over the surface.

$$\bar{F}_{aero} + F'_{aero} \geq \bar{F}_{ad} + F'_{ad} + F_g \quad \Rightarrow \quad \text{Particle take-off} \quad (1.46)$$

The phenomenon of pavement, previously discussed, leads to a temporal emission rate decay. Based on the work carried out by Descamps (2004) [21], the erosion depth is a suitable parameter to indicate if particles take-off is still physically possible. The erosion depth is a certain depth where the overall bed surface is completely overlaid by non-erodible particles. Figure 1.12 shows the concepts involved in erosion depth. The lift force incrementally decreases for particles having a deeper position in the bed.

Figure 1.13 shows schematically the modelling of the bed pavement. Some approaches presented herein are also explained in Figure 1.12. The most important characteristic viewed in these two figures is the decrease of the aerodynamic force when the erosion depth increases. When the maximum value of the probability density function of lift force is lower than the minimum value of the sum of the probability density function of adhesion and weight forces, the take-off is no longer possible.

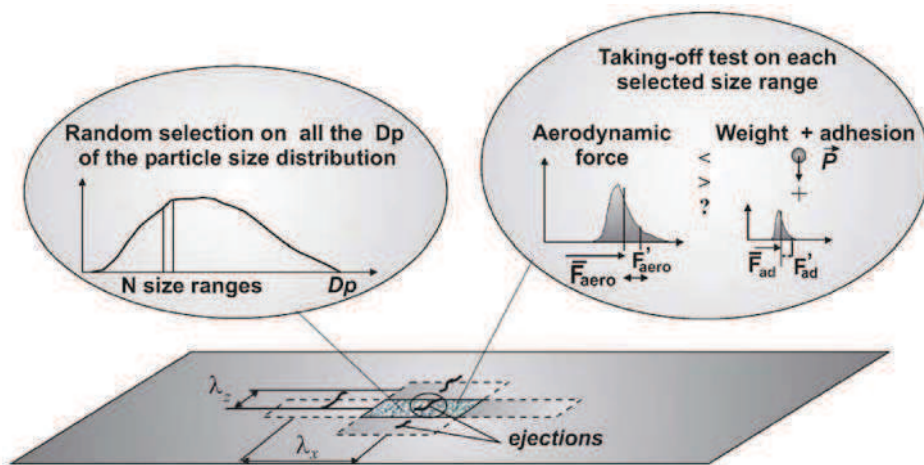


Figure 1.13: Principle of the emitted mass flux simulation [22]

The results obtained by the model are the time evolution of the emitted mass rate of particles as

well as the diameter distribution of eroded particles. Figure 1.14 shows the results obtained by the model in terms of temporal mass flux evolution for a wind velocity equals to 10 m/s and for several values of cover rates (TDC) (0, 5, 10 and 20%).

The model input variables are:

- exposition time to the turbulent flow (t_{expo} [s]),
- flow velocity (U_{∞} [m/s]),
- particle density (ρ [kg/m³]) and size distribution,
- non-dimensional values of streamwise, spanwise and temporal appearing periodicities (λ_{p-x}^+ , λ_{p-y}^+ and T_b^+),
- sizes of the bed (L and l [m]),
- kinematic viscosity (ν [m²/s]) and
- density of the flow (ρ_{fluid} [kg/m³]).

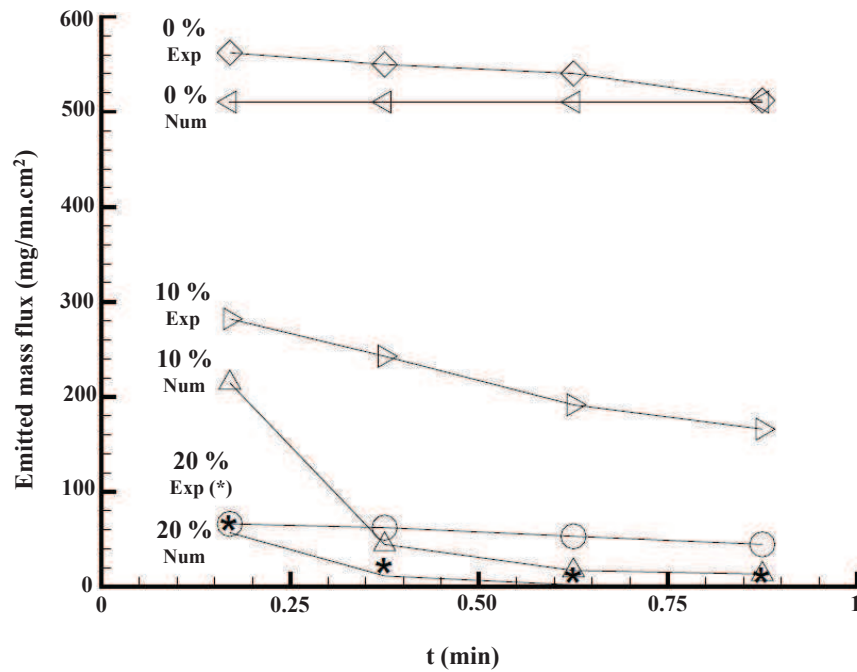


Figure 1.14: Results obtained by the model of a wide size distribution for several values of cover rate, by numerical and experimental approaches [22]

The work of Descamps et al. (2005) [22] has concluded that the rate of this decrease depends on the flow velocity and the characteristics of the particles. In order to improve the accuracy of the estimation of fugitive particle emissions with a wide size distribution, it is necessary to take into account this temporal decrease. The most important drawback of the model developed by Descamps (2004) [21] is related to the definition of the erosion depth.

1.5 Conclusions of the literature review

The literature review presented numerical and experimental works dealing with the analysis of storage piles of granular materials which due to wind erosion acts as a diffuse source of pollutants on industrial sites. The main objectives of those works were related to the development of theoretical support to enhance the accuracy of dust emission quantification.

The first part of the review showed general concepts about the wind erosion of diffuse sources. The particle entrainment mechanisms indicated the way the particles are transported after a wind erosion event which can be: saltation, suspension or reptation. Several studies presented discussions about the erodibility of particles by a turbulent flow.

Other studies have focused on the effects of a turbulent wind flow impinging diffuse sources. The impact of the presence of wind barriers and the analysis of fluid under a variety of dimensions, shapes and quantity of sources are examples of studies found in literature. The investigation of the fluid flow surrounding wall-mounted obstacles showed the lack of information regarding the fluid flow structure on and around oblong stockpiles. The basic features (initially noticed for a cubical obstacle) were identified around oblong stockpiles. Finally, the influence of a successive stockpile was not found in literature.

The review of dust emission quantification methodologies of diffuse sources has been focused on the most widely used model proposed by USEPA [75]. The argument not found in literature concerning the methodologies is the quantification of re-emission that may be noticed on the ground region surrounding stockpiles. Precedent investigations have not been interested in these surrounding regions which are, in fact, often strongly charged with silt particles on industrial sites.

The final part of the review exhibited the influence of non-erodible particles on aeolian erosion of diffuse sources. A lack of information was identified after this review concerning the effects of different erodible rates in the mixing of the agglomerated particles. Several conclusions were drawn from studies considering only the analysis of turbulent flow over a flat bed of material. However, the following sections of the literature review showed that the wall-mounted obstacle shape is highly important in modifying the structure of the flow.

A numerical and an experimental work about this influence were presented. The first one, an experimental investigation, showed the temporal decrease of the emitted mass flux of a bed of erodible and non-erodible particles. Also, the same authors proposed a numerical model to calculate the temporal decrease of emitted mass flux. A lack of information was identified regarding the shape of the eroded pile. Precedent studies were only focused on flat bed of particles. The second work investigated, numerically, the local fluid flow around the non-erodible particles. A formulation was defined to link the evolution of the mean friction velocity (shear of the erodible wall) and the geometrical parameters of the non-erodible particles which were taken as roughness elements in the numerical simulations. The lack of information noticed concerns the range of validity of the formulation: all configurations represented equal diameters and emerging heights for the elements. Since several analysis showed in the thesis are numerical, a review was also done about the most used turbulence models.

Chapter 2

Experimental details

The experimental techniques performed in the present work used the wind-tunnel facilities installed in the Industrial Energy Department (*Département Energétique Industrielle*) at *Ecole des Mines de Douai*. The wind-tunnel was arranged in two configurations, each one with specificities for the respective technique. The configurations required for the techniques carried out in the present work are quite different compared to the original test section used in a previous work [70] studying Particle Image Velocimetry (PIV). The first configuration enables surface flow visualization while the second one is devoted to emitted mass flux measurements. The oil-film visualization investigates the fluid flow pattern formed over a plane surface around a wall-mounted obstacle. The second experimental technique aims the quantification of the emitted mass flux of a granular material stockpile model formed by a mixing of erodible and non-erodible particles of sand.

2.1 Wind-tunnel description

The basic configuration of the wind-tunnel used for both experimental techniques is schematically presented in Figure 2.1a. The wind-tunnel has the following main dimensions: $H_s = 0.80$ m of height, $W_s = 1.50$ m of width and $L_s = 8.12$ m of length.

In its original configuration, the wind-tunnel presented these components:

- a circular plate of $0.95m$ diameter, used to modify the stockpile model orientation inside the test section (the incoming flow orientation has strong influence on the final flow pattern),
- plexiglass walls (transparent) at test sections boundaries,
- honeycombs and very fine grid were placed upstream and downstream the test section, close to inlet and outlet regions presenting, respectively, an important function to break-up the great flow features coming from inlet region and to prevent ventilator perturbations at outlet region and
- small obstacles are set upstream of the test section, near the entrance of the wind-tunnel, to ensure the formation of a turbulent boundary layer.

Different tests were carried out to define quantity, dimensions and disposition of the small obstacles allowing the formation of a fully developed turbulent boundary layer, $\delta = 0.160m$, larger than the stockpile model height. A detailed part of the Figure 2.1a presents the small obstacles and the entrance of the wind-tunnel. Furthermore, the photograph in Figure 2.1b presents the test section which can be observed the camera location (above the test section and plexiglass walls), the black painted obstacle model and illumination arrangement previously used for PIV measurements.

The experimental scaled-down model is placed at the test section located 6.20 m downstream the entrance of the wind-tunnel enabling the development of a turbulent boundary layer. The velocity profile upstream the test section was investigated and validated by means of Laser Doppler Anemometry (LDA) measurements. Figure 2.2a and Figure 2.2b (adapted from Turpin (2010) [70]) present two plots: (a) vertical profile of the longitudinal velocity in wall units comparing to reference

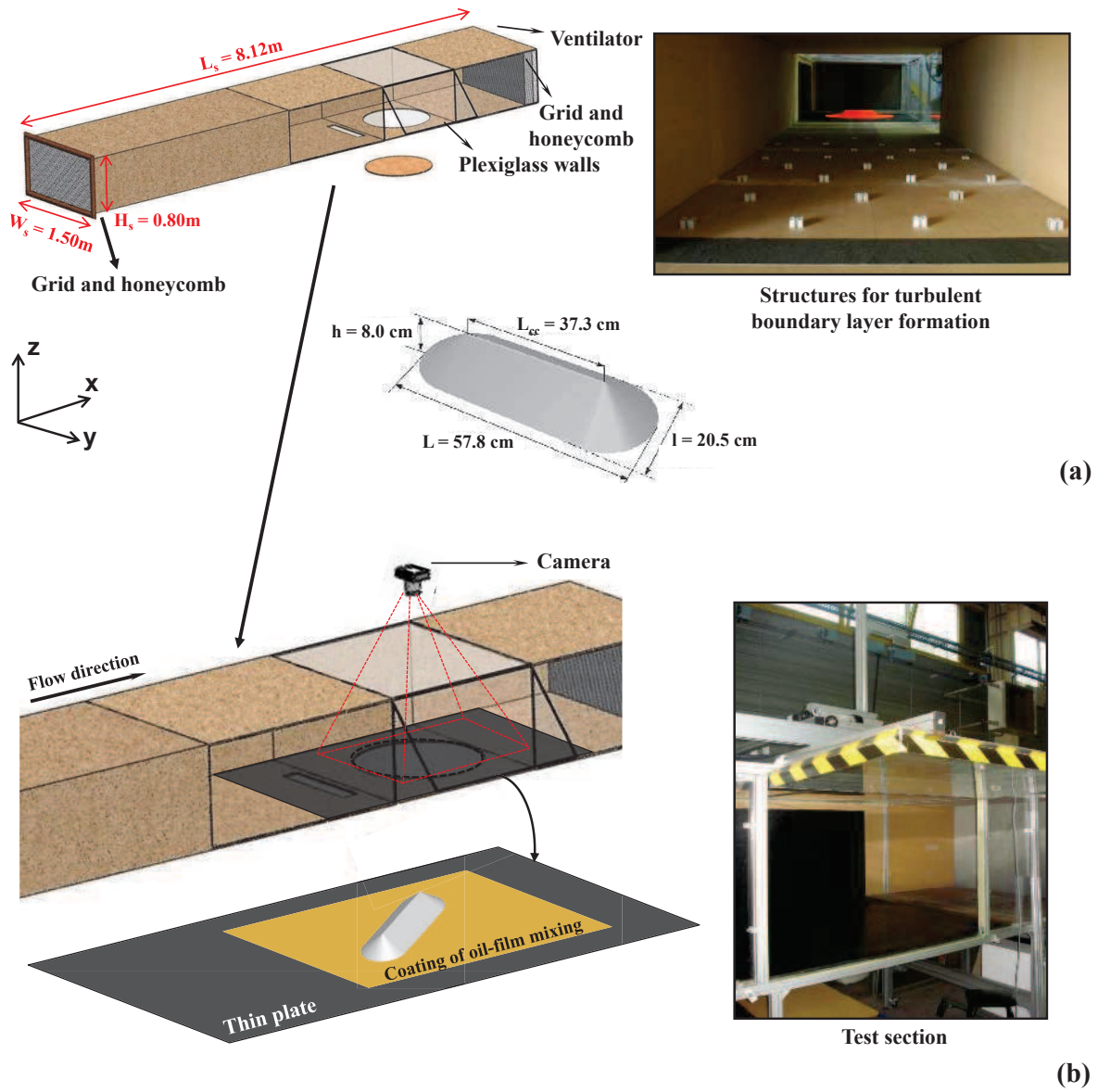


Figure 2.1: Wind-tunnel facilities: (a) original wind-tunnel and main dimensions and (b) configuration for oil-film surface flow visualization

values [63] and (b) turbulence intensity at the entrance of the test section also compared to reference values. The plot exhibited in Figure 2.2a shows the classical pattern, i. e., the velocity profile is firstly linear and far from the wall it assumes a logarithmic profile. LDA measurements were compared with reference data [63] and the overall values have shown good agreement. Details concerning the velocity profile at the test section inlet can be found out in the work of Turpin (2010) [70]. The vertical profile of longitudinal velocity was also measured at other spanwise locations. The results have indicated small disparities between the transversal profiles of about 4% which can be neglected. It is worth to note that, the wind-tunnel is exactly the same that used for previous experimental works except for the test section. It means that all information given in this section is valid for the present investigations.

2.2 Surface flow visualization: oil-film technique

This section is focused on the presentation of the surface flow visualization. This technique aims to investigate the fluid flow pattern over a given wall surface. There is a wide range of surface flow visualization methods as can be seen in several reference works about this subject [34, 43, 53]. These

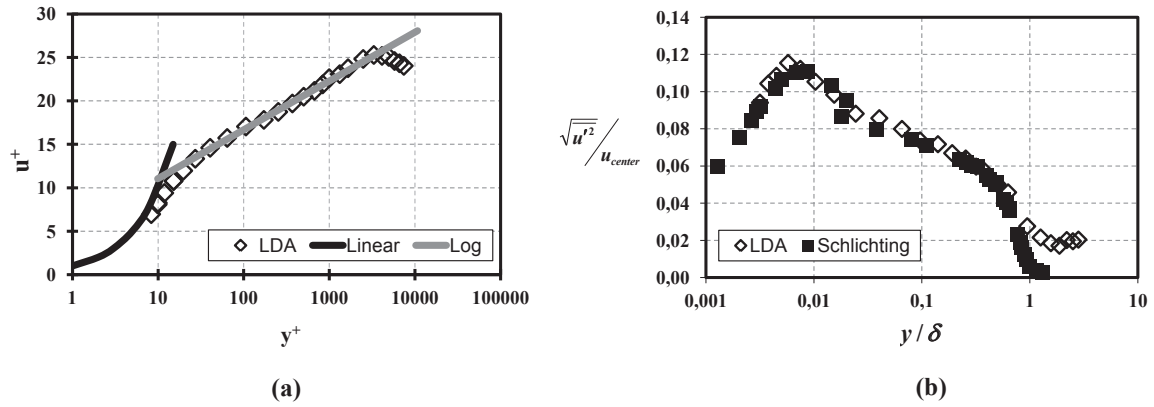


Figure 2.2: Validation of the incoming wind profile at the entrance of the test section by literature data [63]: (a) linear and log laws of the velocity profile and (b) turbulence intensity. Adapted from Turpin (2010) [70]

works were applied to solve engineering problems in aero-, thermo- and hydrodynamics areas. Guiming (1994) [34] has studied a flow visualization technique employing surface oil flow and liquid crystal thermography suitable for use in impulse wind-tunnels (short test time and very low static pressure compared to conventional wind-tunnels). The photographs of oil flow pattern were very useful revealing detailed features of three-dimensional separated flow. Leeuw et al. (1995) [43] developed a visual comparison between experimental oil-film visualization and numerical flow simulation applied in a simplified configuration of an air-intake of a hypersonic transport vehicle. Also, the comparisons presented good agreement and the experimental technique was very useful to feature the fluid flow on the wall. Furthermore, Mosharov et al. (2009) [53] in a Patent Application Publication, has shown an invention of an aero- and hydrodynamics experiment particularly applied to optical methods of studying a structure of a gas or liquid stream on object surfaces. The surface studied was coated with a viscous liquid layer having insoluble and visible particles. The study showed that particles subjected to an outer stream move together with the viscous liquid.

The experimental technique of surface flow visualization chosen to be performed in the present study is the oil-film method. The experimental photographs show the wall flow topology on the surface of interest which in the present study is the ground region surrounding a wall-mounted obstacle. The wall-mounted obstacle is a stockpile model representative of those ones found out on industrial sites (cf. Figure 2.1a which presents the numerical model; Figure 2.5 presents a top view of the experimental model). The technique is quite easily implemented in any wind-tunnel: it does not require expensive financing (as laser techniques need) and gives photographs with good spatial resolution and good accuracy.

The method consists in coating an oil mixture over a given wall exposed to flow friction. A thin layer of the mixture is coated over a plane surface around an object around which the wall flow pattern is analysed. Wind flow overpass the test section with oil-film mixture layer and creates some changes on its initial pattern (homogeneous). Due to friction forces the wall flow features are then revealed. Indeed, variation of color are directly linked to wall shear stress distribution on the coated surface.

The oil-film mixture has three components: (i) oil, (ii) small particles which are the solid part (coloured powder) and (iii) a chemical agent which allows the mixing between the others two components. As proposed by Desreumaux and Bourez (1989) [23], the paraffin oil was initially used as the oil part and the oleic acid as the mixing component. Figure 2.3 shows the three components presented hereupon and some laboratory equipments used to make the oil-film mixture.

In the report of Desreumaux and Bourez (1989) [23], the use of titan oxide as the solid part and coloured powder was proposed. This component and its initial proportion was imposed with interesting results for velocities near 20.0 m/s, which is very higher than the maximum velocity in the present tests. For all tested configurations in the present work the velocity value of 6.5 m/s was



Figure 2.3: Three compounds used in the oil-film mixture: (a) paraffin oil, (b) yellow powder and (c) oleic acid

set as the free stream velocity. Firstly, new proportions were defined for the free stream velocity equal to 6.5 m/s after a direct linear proportion from reference values. It is worth to note that, in this thesis, several tests have been also done with titan oxide as the coloured powder (solid part). It was found that, the stabilization time of the wall featuring is too long (more than four hours). Moreover, the contrast of the final image is not good enough. The tests using titan oxide has been given up and the coloured powder has been changed to a yellow powder used usually as a colorant for coating walls and others decorations works (Figure 2.3b). After some tests carried out in this thesis, the most suitable proportion was defined to perform the technique in a wind-tunnel with a free stream velocity equal to 6.5 m/s. The most suitable proportion results in the visible typical flow structures on the wall after a viable duration time (for instance, the oil-film may still be modified by the friction, i.e., it is not dried up). Each different experience is specific and the quantity of the components must be analysed before the real tests.

The choice of oil and powder and their proportion is mainly based on experience and preliminary tests for each experimental conditions or configuration [34]. Furthermore, the characteristics of the technique depend on some factors: free stream wind velocity, material of the wind-tunnel wall, wall-mounted obstacle dimensions and shape, surface roughness and inclination. For the free stream wind velocity, high values of the velocity enable the possibility to use more quantity of powder: the wall friction is strong enough to modify the initial oil-film pattern. The cases with low velocity values (the case shown in the present study) must have an oil-film mixture more liquid: the lower levels of wall friction require a less viscous oil-film. Often, some obstacles with small dimensions need a mixture more liquid than that used for large dimensions explained by the higher shear stress presented around the last ones. Surface roughness and inclination also influence the proportion to be applied. Rough walls present high wall shear stress levels and consequently the oil-film mixture can be more pasty. Inclined walls are the most difficult situations to apply the technique seen that it is necessary to choose a proportion that is enough to be changed to the friction and to maintain over the inclined surface without flowing downwards.

An ideal proportion was found suitable for the all tested configurations (different orientations and number of stockpiles) to be applied around the obstacle at the bottom wall. The values of each component to be applied are the following: 128.6 g/m^2 of paraffin oil, 5.3 g/m^2 of coloured powder and 23 drops/m^2 of oleic acid. The region chosen to be coated in the wind-tunnel is that enough to visualize all the wall flow structures around the pile, for example, for the perpendicular stockpile: 5.0 cm (approximately $0.25l$) upstream to the visualization of the windward wall, stagnation zone and flow acceleration, 83.0 cm (approximately $4.1l$) downstream due to the necessity to visualize the wake zone and reattachment point and 20.0 cm (approximately $1l$) on each side of the stockpile to visualize the formation of the main vortices and the flow acceleration effects on the laterals. l is the stockpile length represented in Figure 2.4.

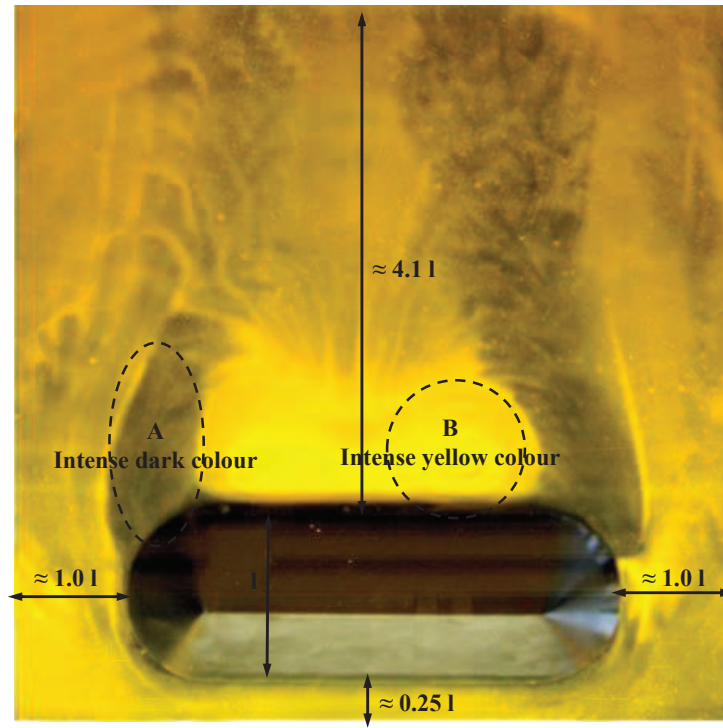


Figure 2.4: Typical photograph of oil-film surface flow visualization

During the experimentation, photographs were successively taken each 30 minutes. Figure 2.5 represents all the photographs of an oil-film experience. The time evolution of the method can be seen in these images. This is a four hours experience. After 90 minutes (the third photograph) of experience, the most important modifications in the original oil-film mixture pattern are noticed. Later, until the last photograph, vortices are well formed, as well as, separation and wake zones. If the experiment is left running more than the necessary, accumulation zones may lose the most suitable pattern due to the sedimentation of tracers (coloured particles) and oil drying.

Qualitative and quantitative analysis were carried out considering the photograph for which no more significant changes are noticed in the wall flow pattern. The qualitative analysis were basically made with the comparison between the experimental photographs and wall shear stress contours from numerical simulations. As already explained hereupon, the physical mechanism involved in this method is the wind shear stress acting at the wall where is coated the oil-film mixture. Thus, in the regions where high values of numerical shear stress are noticed, the experimental photograph indicates zones of a thin layer of oil-film mixture leading to a decrease of the yellow colour intensity (region A in Figure 2.4). On the other hand, regions of smaller values of wall shear stress, if visualizing experimental photographs, result in no changes of the oil-film mixture or even an accumulation zone (mixture coming from those regions with a large motion) with a thick layer of mixture having an intense yellow colour (region B in Figure 2.4).

2.3 Dust emission investigation in wind-tunnel

The wind-tunnel previously described was reasonably modified for the conception and set-up of an original experimental technique. The new experiment on view in this section was performed intending the direct assessment of particles taking-off in wind-tunnel. The present section exposes the modifications imposed on the wind-tunnel described earlier to carry out the experimental measurements.

The alterations needed in the wind-tunnel for the accomplishment of this original technique were mainly appended in the test section, upstream the ventilator as highlighted in Figure 2.6. The entire zone upstream the test section and the ventilator are the same as the previously mentioned configuration. Briefly, the technique consists in two ways of measuring the emitted dust mass from a stockpile model made of real granular particles of sand: continuously mass measurements and

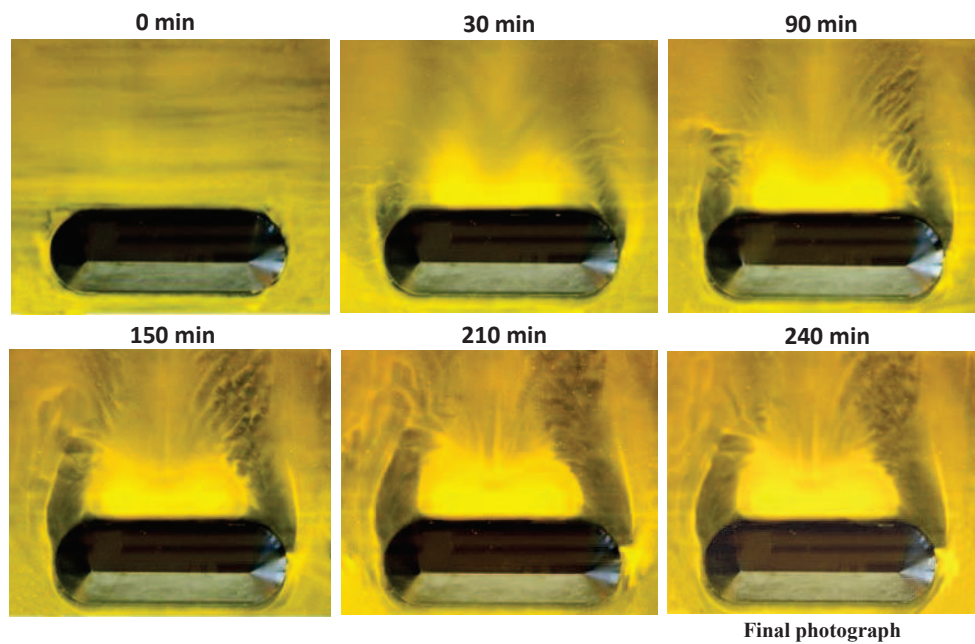


Figure 2.5: Temporal evolution of oil-film mixture at wall in wind-tunnel around the stockpile oriented 90° to the wind flow direction

mass balance. The mass balance is executed outside the wind-tunnel in which does not take into account the evolution of the emitted mass, but only the initial and final stockpile weight. On the other hand, the continuous measurement system focus on the temporal evolution of the emitted mass flux. Moreover, to achieve the continuous measurements some modifications were necessary in the original test section. The next paragraphs are concentrated on the explanations about the continuous measurement system and the experimental data processing.

Firstly, a totally airtight box was installed under the original circular plate which is located in the test section. In addition, the above mentioned box contains the continue mass measurement system associated to the circular plate where the oblong stockpile model is positioned. Essential structures of this experimental configuration are listed hereafter and are associated to the reference numbers highlighted in Figure 2.6: (i) supports, (ii) airtight box, (iii) circular plate, (iv) the weighing balance, (v) the sand stockpile model, (vi) high quality photograph system and (vii) a filter.

The experimental device (Figure 2.6) presents structures that the operator must have a special attention. The supports of the weighing device, as well as the supports of the airtight box (not shown in Figure 2.6), must be horizontally leveled and parallel to the circular plate. These supports are easily handled by the operator before the experiments. In addition, the supports are always in number of three. This condition enables easily the equilibrium of the piece over that. The airtight box was cautiously designed to avoid the creation of a fluid flow by-pass. The fact of having a by-pass inside the box, where is installed the weighing device, may perturb the measurements by creating zones of high pressure over the weighing device. Furthermore, the experimental data are acquired with a frequency of 5 Hz being extremely sensible to, for instance, flow by-pass over the weighing device.

The location of the sand stockpile model on the circular plate was determined based on the expected static pressure distribution over the plate. The static pressure may be associated to the distribution of force at the wall. Numerical results for a similar oblong stockpile and incoming wind flow shown the static pressure distribution in Figure 2.7. The chosen position takes into consideration the smallest differences of static pressure around the pile near the contact with the wind-tunnel ground wall. The black dashed lines represent the circular plate and the experimental oblong stockpile is represented by the numerical model. The circular plate is completely free of contact with the wind-tunnel ground wall. The weighing system used in our experiments is an electronic BEL Engineering Mark K30.1 with 0.1 g of precision connected to a PC to effectuate mass measurements. For the construction of the sand stockpile it was designed a system acting as a hopper found out on industrial

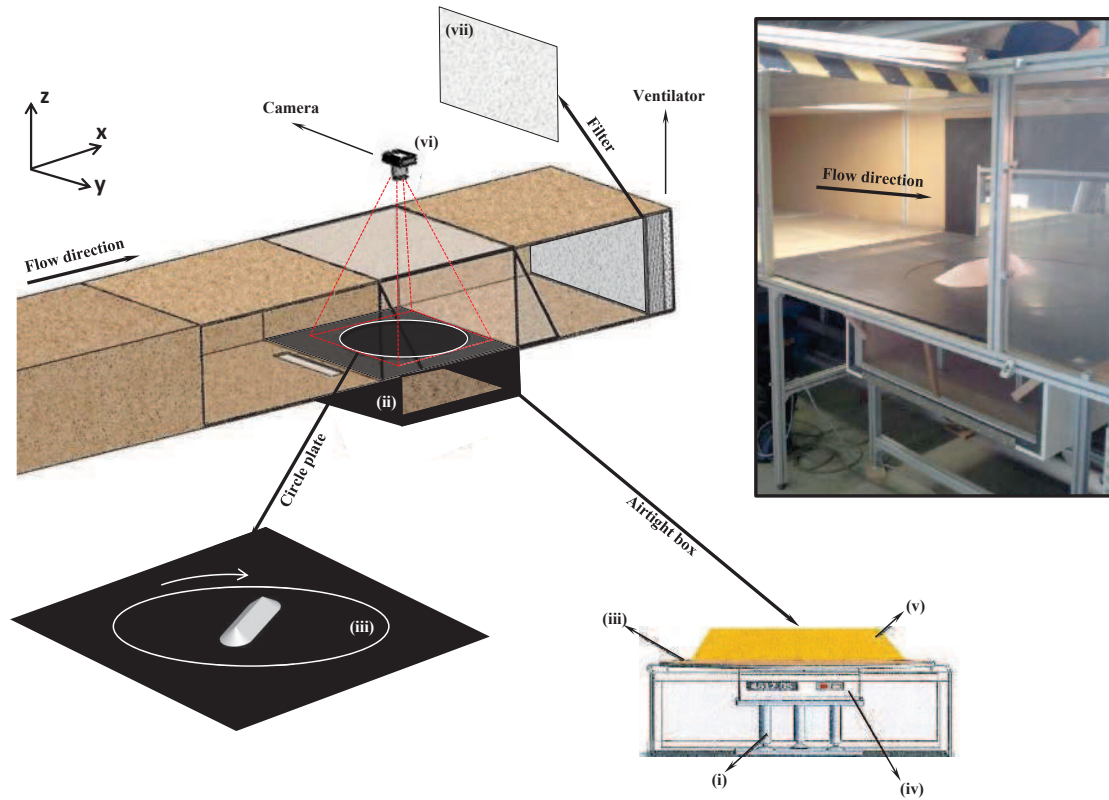


Figure 2.6: Wind-tunnel configurations: dust emission quantification

sites. The mold over the hopper where the sand is discharged has the same volume and surface of the original wood made stockpile model (see Figure 2.8 for more details).

A high quality camera was then installed over the wind-tunnel top wall (transparent one). The resolution of the photographs is 3648x2650 pixels. The area visualized by the camera is more concentrated on the stockpile. This system is capable of visualizing extremely detailed distribution of particles over the sand stockpile model surface. Photographs were taken each 30 seconds until the final covering of the stockpile surface. This device also permits the temporal evolution of specific zones of wind erosion on the pile. As we test silt sand particles the installation of a filter was obligatory to protect the ventilator downstream the wind-tunnel.

The sand stockpile model is assembled on the circular plate by the means of the structure containing stockpile mold and hopper shown in Figure 2.8. The mixture of sand is discharged in the mold. The two sizes of particles of the tested sand (erodible and non-erodible) are very mixed before discharging in the mold. A temporary support holds the amount of sand. Thus, the operator has to pull this support to make fall the amount sand similarly as in industrial hoppers. Before the wind-tunnel experiments, a preliminary analysis was carried out to verify the repeatability of shape and dimensions of the oblong stockpile obtained. Figure 2.9 shows the mean dimensions of the sand stockpile in a top and side view. The results have shown a maximum coefficient of variation (normalized measure of the dispersion of a distribution and calculated as the ratio of standard deviation to the mean value) equal to 5.2 %. Values of the coefficient of variation close to 5 % represent a good agreement.

The weighing system is reset before having the sand stockpile model over the circular plate. The free stream velocity is set on the wind-tunnel frequency controller and the wind-tunnel is started. The connection to a PC performs (frequency of 5 Hz) the data storage from the weighing device in a text file which is plotted versus time to the evaluation of the temporal evolution of emitted mass.

Further analysis of the experimental data are carried out. The methodology used to perform the processing of the weighing data are presented in section 3.1.1 concerning the investigation of a perpendicular stockpile. The experimental data present a strong signal-to-noise ratio caused by some

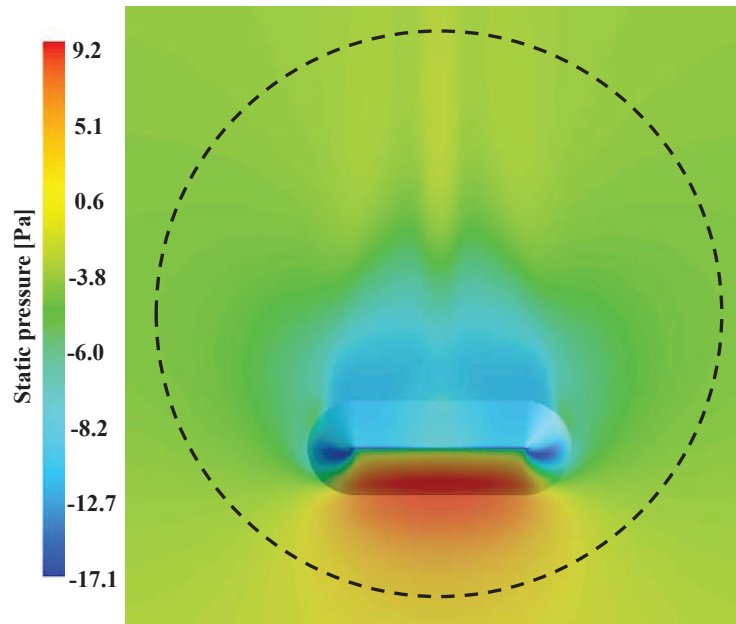


Figure 2.7: Numerical contours of static pressure and the delimitation of the wind-tunnel circular plate

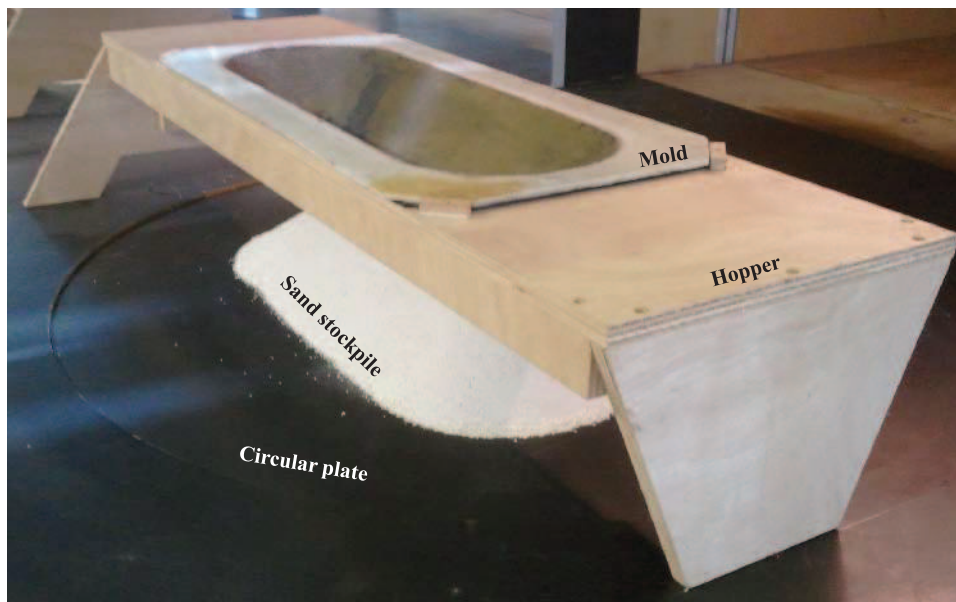


Figure 2.8: Hopper and mold used for the construction of the sand stockpile model

inconveniences during the measurements: vibrations of the circular plate, instabilities of the balance support system and the inherent turbulence of this genre of fluid flow. Hence, the raw experimental data require a processing step to result the temporal evolution of the emitted mass flux. As the methodology was very detailed in a previous section it was decided to not repeat the steps herein.

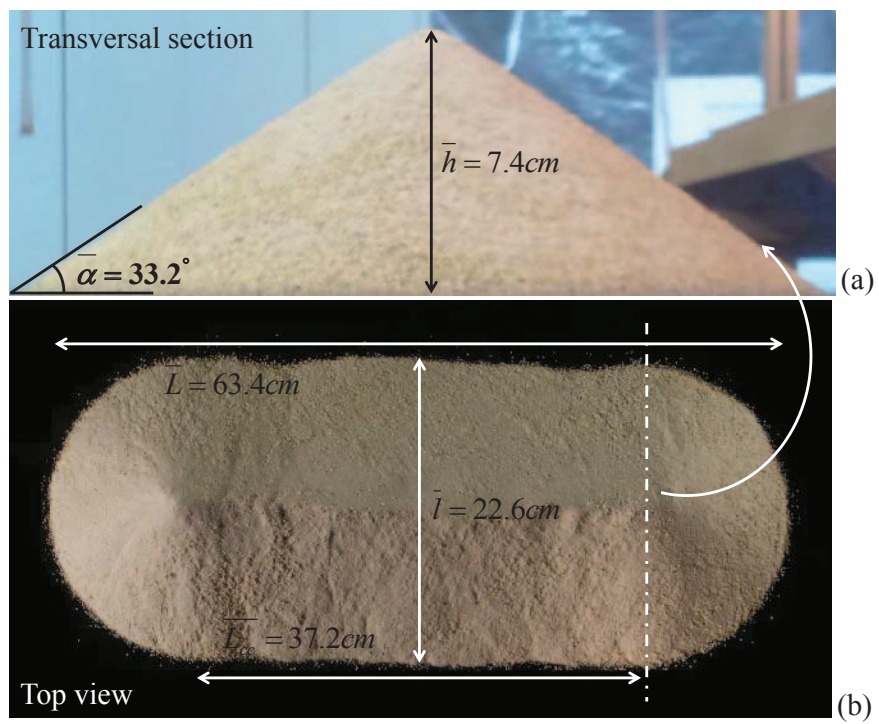


Figure 2.9: Oblong stockpile made with sand: shape and dimensions. (a) top view and (b) side view

Chapter 3

Influence of non-erodible particles on dust emissions

The main objective of this thesis is to improve the knowledge of physical phenomena involved in dust emission from stockpiles due to wind erosion. As explained in section 1.4.2, the surface of a stockpile of granular material is constituted of erodible and non-erodible particles. The latter are characterized by strong inertia that plays an important role on erodibility and, as a consequence, on dust emission. Furthermore, the non-erodible particles are usually very large and act as a shelter to the erodible smaller particles. These phenomena are not directly taken into account by the USEPA emission model; although numerous works using several approaches (see section 1.4.2) have proven that accounting for the non-erodible particles as part of the initial mixing of particles in the piles greatly modifies the total amount of emitted dust and its temporal variation. This chapter presents these discussion using two approaches:

- a wind tunnel experimental work to quantify dust emission using a scaled stockpile sand (section 3.1.1) and
- a numerical simulation of the fluid flow around the erodible and non-erodible particles to investigate their behaviour as roughness elements (section 3.2).

3.1 Investigation of non-erodible particles effects by wind-tunnel simulations

3.1.1 Effects of non-erodible particles on aeolian erosion: wind-tunnel simulations of a sand oblong storage pile

This section is presented as an article entitled **"Effects of non-erodible particles on aeolian erosion: wind-tunnel simulations of a sand oblong storage pile"**. The novelty of this article is related to the oblong shape of the pile. The pile shape is based on the pile models used in the experiments using PIV carried out by Turpin (2010) [70]; however, in the present work, sand is used to simulate the mixing of erodible and non-erodible particle which gives a rounded crest and characteristic dimensions (width, length, height and angle of response) to the stockpile. In the experiments, a bimodal granulometry (125 μm and 875 μm) of sand was used to simulated erodible and non-erodible particles and two surface cover rate of non-erodible particles (10% and 20%) and three free stream velocity values (6, 7 and 8 m/s) were investigated. This article is to be submitted to the **"Atmospheric Environment"** journal.

Effects of non-erodible particles on aeolian erosion: wind-tunnel simulations of a sand oblong storage pile

B. Furieri^{a,b}, S. Russeil^{a,b}, J. M. Santos^c, J. L. Harion^{a,b}

^a*Univ Lille Nord de France, F-59500 Lille, France*

^b*EMDouai, EI, F-59500 Douai, France*

^c*Universidade Federal do Espírito Santo, DEA, 29060-970 Vitória, ES, Brazil*

Abstract

Non-erodible particles have strong influence on the aeolian erosion phenomena. An oblong stockpile model of sand (bimodal granulometry) was implemented to perform wind-tunnel experiments as similar literature works have only carried out experimental investigations on a flat bed of particles. Thus, the influence of the fluid flow structures around the complex obstacle will be analysed. The tested configurations consisted of two different values of non-erodible particles cover rate (10% and 20%), and three free stream velocities (6, 7 and 8 m/s). Good repeatability was found. The results showed that the largest amount of particles emitted was for the highest wind velocity and the smallest cover rate. The temporal decreasing of emitted mass flux was found steeper for larger amount of non-erodible particles and higher velocity. The mass flux of particles decreases very strongly in the first four minutes of measurements and the cover rate influences this downward sloping. The same analysis applies for the effects of the free stream velocity. The qualitative analysis (high quality photographic system) of the stockpile surface gradual change has shown that non-erodible particles agglomeration induces a pavement effect on some areas of the pile. This analysis indicated typical wind erosion zones: high wall friction on the crest line and lateral sides; low wall friction on the windward wall near the ground and on the recirculation downstream the leeward wall. The results and discussions presented here allows for the understanding of the impact of non-erodible particle on dust emissions.

Keywords:

Aeolian erosion, Stockpiles, Diffuse dust emission, Non-erodible particles, Wind-tunnel

1. Introduction

The phenomenon of dust emission from piles of granular material exposed to wind erosion has been studied by many researchers using different tools such as computational fluid dynamics, field and wind-tunnel experimental analysis. The studies of Cong et al. (2011), Neuman et al. (2009) and Roney and White (2006) are examples of aeolian erosion investigation of diffuse sources found in literature. Cong et al. (2011) carried out a CFD study (validated by precedent field and experimental measurements) to verify the role of porous fences in reducing dust emissions which was confirmed. Neuman et al. (2009) have evaluated some environmental control techniques of diffuse dust emissions from mine tailings by wind-tunnel simulations. Roney and White (2006) estimated dust emission by means of wind-tunnel experiments in which near surface steady-state concentration profiles and velocity profiles are obtained in order to use a control volume approach to estimate emission rates. The estimated emission rates are comparable to those obtained from field studies and lend to the validity of the wind-tunnel method for determining fugitive dust emission rates.

The granular material subjected to wind erosion is constituted by particles that are classified based on their inertia, as erodible or non-erodible. Discussions concerning non-erodible particles and the erodibility of surfaces were carried out in various studies (Gillette and Stockton, 1989; Roney and White, 2006, 2010; Benkhaldoun et al., 2011; Webb and Strong, 2011). In general, the authors have concluded that the amount of particles emitted due to wind erosion is strongly attenuated by the presence of non-erodible particles.

The studies of Neuman and Nickling (1995), Li and Martz (1995) and Descamps et al. (2005) performed, over flat beds of particles, numerical simulations and experimental wind-tunnel tests. The emitted mass flux was found to decrease with time due to the presence of non-erodible particles causing a phenomena called "pavement effect" which represents the influence of non-erodible particles on the taking-off of erodible particles. The "pavement effect" is the erodible surface covering by the non-erodible particles, i.e., erodible particles are impeded to take-off.

Other studies have carried out numerical and theoretical investigations about the local impact of non-erodible particles, i.e., at the scale of one par-

ticle (Raupach et al., 1993; Gillies et al., 2007; Turpin et al., 2010). These studies analysed the micro-scale features of the fluid flow, using numerical simulations around a given number of non-erodible particles. Raupach et al. (1993) have developed a theory to describe the dependence upon roughness density of a ratio of threshold friction velocities (between a surface without and a surface with roughness elements). Gillies et al. (2007) have evaluated the shear stress behavior on complex rough surfaces. A drag plate was constructed to measure the surface shearing stress on representative surface samples in a wind-tunnel boundary layer. In Turpin et al. (2010), the numerical domain is a narrow area surrounding one particle or an array of well defined particles. The numerical simulations results indicated that the mean friction velocity decreases as the number of non-erodible particles increases and the amount of dust emitted depends on the friction velocity. Thus, the emitted mass flux tends to decay as non-erodible particles cover the stockpile surface.

Summing up the literature, numerous works have already performed wind-tunnel simulations of flat beds, sinusoidal or conic piles to investigate the influence of non-erodible particles on dust emission. However, none of them examined oblong piles. Thus, experimental wind tunnel tests on oblong piles (for instance, those found in industrial sites of steel production) are firstly carried out in the present study. The shape and dimensions of the pile were similar to those tested in the studies of Turpin and Harion (2009) and Furieri et al. (2012) in which the air flow pattern on and around the oblong shaped stockpile is discussed. In the present work, the wind-tunnel tests are carried out for two proportions of non-erodible particles (mass of non-erodible particles divided by the total mass of particles in the stockpile) and three free stream velocity values using a bimodal distribution of sand (two main mean particles diameters, $125\mu\text{m}$ and $850\mu\text{m}$). The expected results aims to give a better comprehension of the local fluid flow mechanisms surrounding the non-erodible particles as well as the global quantification of the influence of velocity and cover rate on the emissions.

2. Experimental set-up

2.1. Wind-tunnel and measurements procedures

The experimental investigation was conducted in a wind-tunnel. During the experimental measurements weighing of the stockpile model was per-

formed and high quality photographs were taken using a system installed perpendicularly above the wind-tunnel test section.

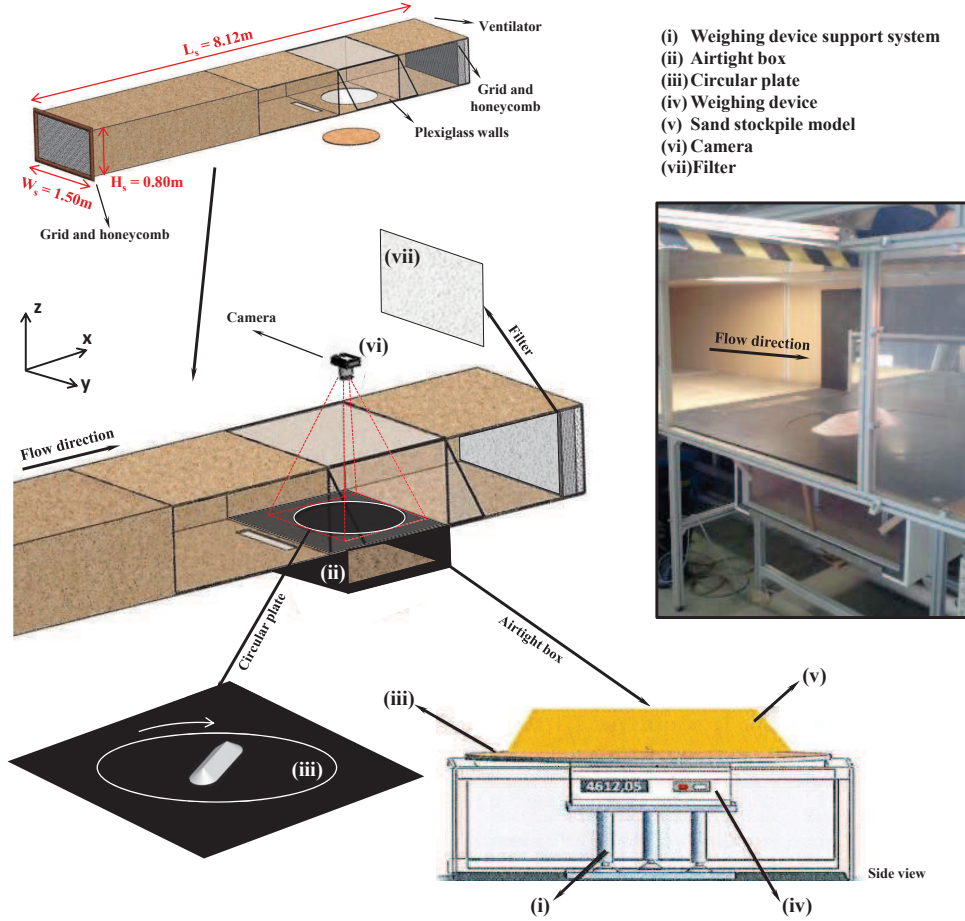


Figure 1: Wind-tunnel set-up

The wind-tunnel presented in Fig. 1 has the same fundamental characteristics of that described by Furieri et al. (2012) in which a surface flow visualization technique was performed. At the inlet of the test section, a turbulent boundary layer was created by means of several obstacles placed upstream the zone of measurements. The test section was modified in order to allow continuous weighing of the sand stockpile mass. Fig. 1 presents the weighing system placed inside an airtight box underneath the circular plate (test section). The airtightness is necessary to avoid flow disturbances. The

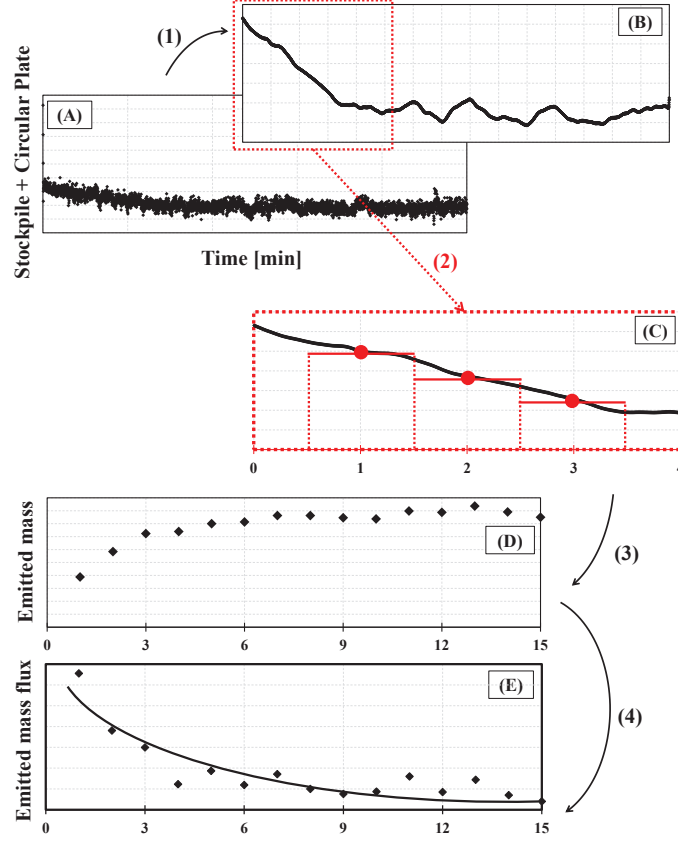


Figure 2: Post-treatment of temporal weighing data recording

weighing device is the electronic balance BEL Engineering Mark K30.1 which has a resolution of 0.1 g . Records measurements at a frequency of 5 Hz are controlled by a program developed within Labview software. Typical records present high signal-to-noise ratio caused by:

- turbulence inherent to the fluid flow,
- vibrations of the circular plate ((iii) in Fig. 1) and
- instabilities of the balance support system ((i) in Fig. 1).

The plot (A) in Fig. 2 shows the time series of raw data and its post-treatment. The procedure to obtain the final curve that represents the temporal variation of emitted mass flux (emitted mass per units of time and

surface of the eroded pile) is presented in the plots (B)-(E) in Fig. 2. In order to process the raw data, four steps were followed:

- (1) Calculation of the moving average (period of 60 seconds) to reduce the data fluctuations seen in (A) in Fig. 2. The graphic (B) in Fig. 2 represents the result of this averaging procedure;
- (2) Discretization of the mass evaluated each minute. For instance, the mass of time instant equal to 1 minute is the average of the data measured between 0'30" and 1'30". (3) in Fig. 2 shows the calculation of the discretized emitted mass;

$$m_{emitted}(t_i) = m_{initial} - m(t_i) \quad (1)$$

where, $m_{emitted}(t_i)$ is the calculated emitted mass, $m_{initial}$ is mass at the beginning of the experience and $m(t_i)$ is the mass at the time instant i . i varies from 0 (beginning of experience) to N (end of experience).

- (4) Calculation of the emitted mass flux (Equation 2). The emitted mass flux is the amount of mass emitted to the free stream flow per unit of area and time. (E) in Fig. 2 shows the time series of emitted mass flux;

$$Q_{t_i} = \frac{m_{emitted}(t_i) - m_{emitted}(t_{i-1})}{(t_i - t_{i-1}) \cdot S} \quad (2)$$

where, Q is the emitted mass flux in $g/min.m^2$, t is the time in minutes, m is the mass in g and S is the area of the stockpile model surface in m^2 .

- Fitting with an exponential curve (Equation 3) as seen in (E). Values of the coefficients A and b are determined by means of the least square method.

$$Q_{(i)} = A \cdot e^{-bt_i} \quad (3)$$

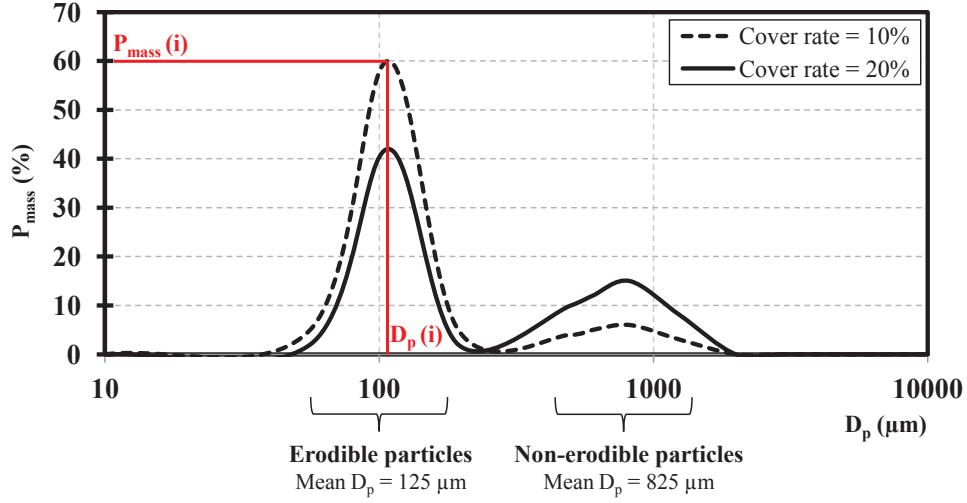


Figure 3: Distribution of sand granulometry for the two tested cover rates

2.2. Granulometry description and oblong stockpile formation

The sand particles used in the wind tunnel experiments present a bimodal distribution of granulometry (Fig. 3) in order to allow for the investigation of the influence of non-erodible particles on dust emissions from a pile constituted of erodible and non-erodible particles. The fine particles present a mean diameter of $125 \mu\text{m}$ and the coarse particles, $850 \mu\text{m}$. The cover rates of non-erodible particles (the mass of non-erodible particles divided by the total mass of sand) was determined using a sequence of sieves in which the particles were sifted and weighted to give the mass percentage of each particles diameter range (Fig. 3). Two cover rate values are considered in the present study: 10 and 20%.

Fig. 4 presents the take-off criterion obtained from the experimental studies of Iversen and White (1982), White (1982) and Foucaut and Stanislas (1996). This criterion is based on the friction velocity (U^*) and particle diameter (\tilde{D}_p): from Foucaut and Stanislas (1996) Equations 4 and 5 and from White (1982) Equation 6. The criterion is used to determine, for given flow and particle characteristics, the erodibility conditions of the particle, i. e., if the particle is erodible or non-erodible.

$$\tilde{D}_p = D_p/D_{pref} \rightarrow D_{pref} = \left(\frac{\nu^2}{\gamma_p} \right)^{1/3} \quad (4)$$

$$\tilde{U}^* = U^*/U_{ref}^* \rightarrow U_{ref}^* = (\gamma_p \nu)^{1/3} \quad (5)$$

where, ν is the kinematic viscosity of air, $\gamma_p = (\rho_p g / \rho_{air})$ the apparent gravity, ρ_p is the particle density, ρ_{air} is the air density and g is gravity.

$$\tilde{U}_t^* = 22.71 \tilde{D}_p^{0.043} + 10.23 \tilde{D}_p^{-0.118} - 32.5 \quad (6)$$

where, U_t^* is the threshold friction velocity. The threshold friction velocity is the friction velocity in which wind erosion is initiated. This velocity is affected by surface and soil properties and herein is a function of the particle size (Equation 6).

Three free stream velocities (6, 7 and 8 m/s) were tested in the wind tunnel. The friction velocity is estimated by Equation 7 determined by Kurose and Komori (2001). Fig. 4 shows the calculated values of dimensionless friction velocity.

$$U^* = U_s^* (1 + 0.00431 h_s^+) \quad (7)$$

where, U_s^* is the friction velocity for the smooth wall and h_s^+ is taken as the dimensionless mean diameter of the non-erodible particles. The friction velocities for smooth walls were experimentally measured for sand particles in a reference work (Descamps, 2004).

The two ranges of sand particles diameters (erodible and non-erodible) used in this work are shown as shaded areas in Fig. 4. The erodible and non-erodible ranges of particles are, respectively, 56.0 - 194.2 and 500.0 - 1250.0 μm . The intersections between the plots of dimensionless friction velocity (horizontal dashed lines) and the take-off criterion curve (black filled line) define the critical diameters (D_A and D_B) for each velocity. The critical diameters indicate the dimensionless diameter range of erodible particles ($D_A < \tilde{D}_p < D_B$). Particles with dimensionless diameter lower than D_A are non-erodible due to adhesion forces. On the other hand, particles with dimensionless diameter greater than D_B are non-erodible due to their inertia.

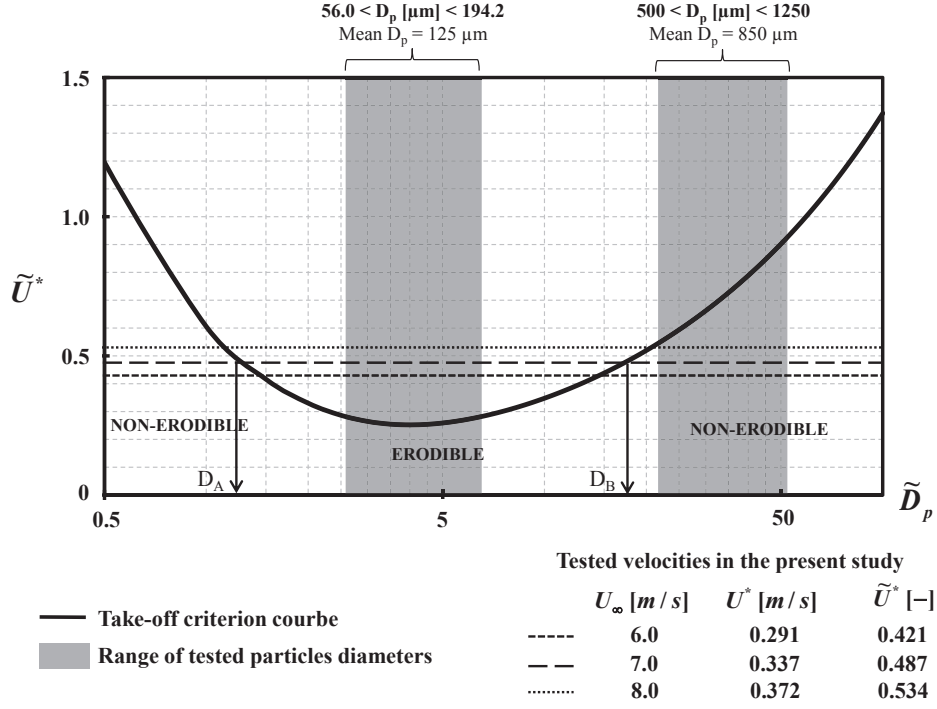


Figure 4: Take-off criterion: particles diameters and velocities tested

The oblong stockpile tested has the following dimensions: 0.074 m (height), 0.226 m (length) and 0.635 m (width), and 33.2° of angle of repose (characteristic of an agglomeration of sand (Ferreira and Lambert, 2011)). The sand stockpile models were built inside the wind-tunnel using a device manufactured at Mines Douai similar to an industrial hopper (see Fig. 5). Several tests were performed to ensure the repeatability of the pile shape and dimensions given by this device.

3. Results and discussions

3.1. Repeatability of mass balance and continuous weighing

Preliminary tests were performed to verify the experimental measurements repeatability. The typical configuration chosen for the repeatability tests consisted of cover rate equal to 20% and free stream velocity equal to 7 m/s. Fig. 6 presents the temporal evolution of the emitted mass flux and the

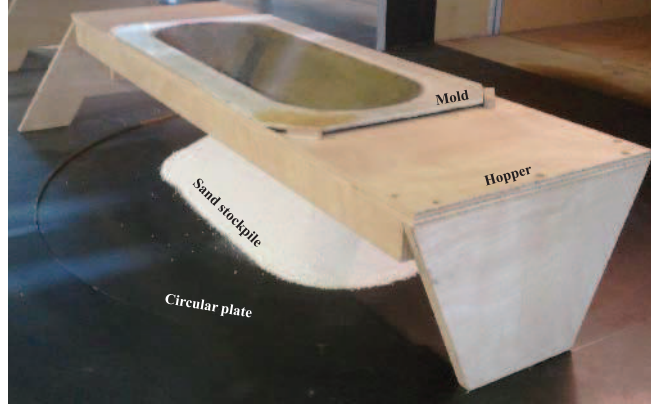


Figure 5: Wind-tunnel experimental hopper

emitted mass (calculated as the difference between the measured initial and final total mass of the stockpile) for several tests. The temporal evolution of the flux was calculated as described in section 2.1. Fig. 6 shows similar tendency and values among the repeatability tests. The emitted mass flux presents a generally good agreement concerning the temporal decreasing. Emitted mass presents standard deviation equal to 15.3 and coefficient of variation (defined as the ratio of the standard deviation to the mean) equal to 6.5%.

3.2. Typical case: general description of wind erosion

This section presents an overall description of the wind erosion over a granular material stockpile. The typical case considered here has cover rate equal to 10% and free stream velocity of 7 m/s. Fig. 7 presents a top view of the stockpile exposed to a perpendicular incoming flow in which distinctive zones can be highlighted and numerical results of wall shear stress distribution on almost identical stockpile to illustrate details about the fluid flow on this obstacle (cf. Turpin and Harion (2009) for details about the numerical simulation).

It is worth to note that, there is a slight difference between the geometry (stockpile dimensions and crest shape) of the stockpile models used in the numerical and experimental simulations. The numerical simulation used a stockpile of coal particles in which the angle of repose is 38° (Turpin and Harion, 2009). On the other hand, the experimental work used a stockpile of

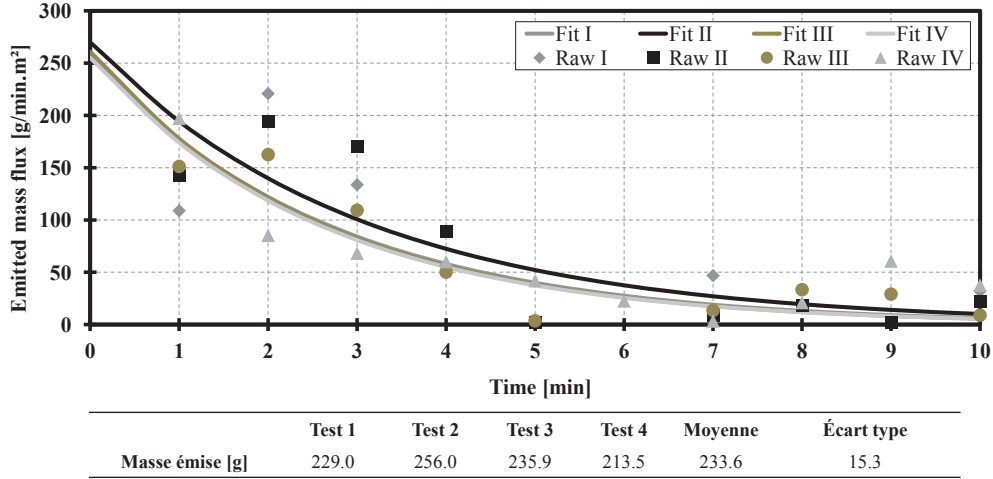


Figure 6: Repeatability tests of emitted mass flux and mass balance (cover rate = 20% and free stream velocity = 7 m/s)

sand in which the angle of repose is 33.2° . However, a qualitative comparison is possible. The following significant fluid flow features are indeed noticed in both pictures:

- flow separation zones where high friction on crest line and lateral sides occur
- stagnation zone on windward wall where low levels of wall shear stress take place
- recirculation zone on leeward wall

Fig. 7 presents six typical regions of wind erosion: two zones of high levels of wall shear stress and erodible particles take-off (2 and 4), two zones of particles agglomeration and low wall shear stress (1^b and 5), one zone showing no modifications on the original mixing of particles and low levels of wall shear stress (3), a zone on the ground surrounding the pile in the recirculation region (6) and finally, a zone on the pile surface where high wall shear stress and agglomeration are observed (1^a).

The wall shear stress on the stockpile surface causes the take-off of fine particles which reveals the presence of the largest particles on the pile surface and their displacement towards the stockpile bottom induced by gravity

effects (from region 2 to 1^a and 1^b as shown in Fig. 7(a)). After the pavement effect, when no more emission is noticed, regions 1^a and 1^b exhibit the non-erodible particles as seen in Fig. 7. The most important change in the original stockpile shape occurs in region 2 due to the high levels of shear stress. The highest levels of wall shear stress occur on both lateral sides of the pile facing the wind flow (regions 1^a and 2) as shown by the numerical simulation. Region 1^a is the first erodible region on the pile to be totally covered by the non-erodible particles.

A gradual variation of the wall shear stress is noticed on the windward wall from the bottom to the top (expressed herein by regions 3 and 4 in Fig. 7) and the corresponding distribution of non-erodible particles is found in the photographs. Non-erodible particles are more concentrated on the windward wall near the crest line. This can be explained by the fact that the fluid flow detaches from the crest line (region 4) where there are high velocity gradient values and thus, high shear stress levels. These particles near the crest line are not moved due to gravity forces as they remain horizontally (or in a small inclination) at the top of the stockpile and thus, protect this region against wind erosion. In the impingement zone (region 3), the flow is deviated towards the lateral walls and the crest and the initial sand distribution remains.

Fig. 7(b) shows low levels of wall friction in region 5 and Fig. 7(a) presents an agglomeration of non-erodible particles due two phenomena: rolling of particles emerged on the crest line and recirculating zone on the leeward wall. Finally, in region 6 (delimited by dashed white lines), the fluid flow structures on the ground, illustrated in Fig. 7 by the arrows, (cf. Furieri et al. (2012) for more details concerning the fluid flow pattern on the ground region surrounding stockpiles) causes the particles of sand to accumulate. It is worth to note that, in region 6, some non-erodible particles have effectuated reptation movements which were clearly visualized during the experiments.

Fig. 8 shows the temporal variation of the emitted mass flux and the corresponding experimental photographs. The white lines shown in the photographs in Fig. 8 bounds the agglomeration of non-erodible particles which is caused, as mentioned before, by the particles that have rolled from the top to the bottom (from region 2 to region 1^a and 1^b in Fig. 7) or have emerged due to wind erosion. The region bounded by the white lines does not present any significant modifications after 10'30" (the last photography presented in this image) which is in agreement with the emitted mass flux that decreases tending to a very small value. The curve shown in Fig. 8 indicates a fairly

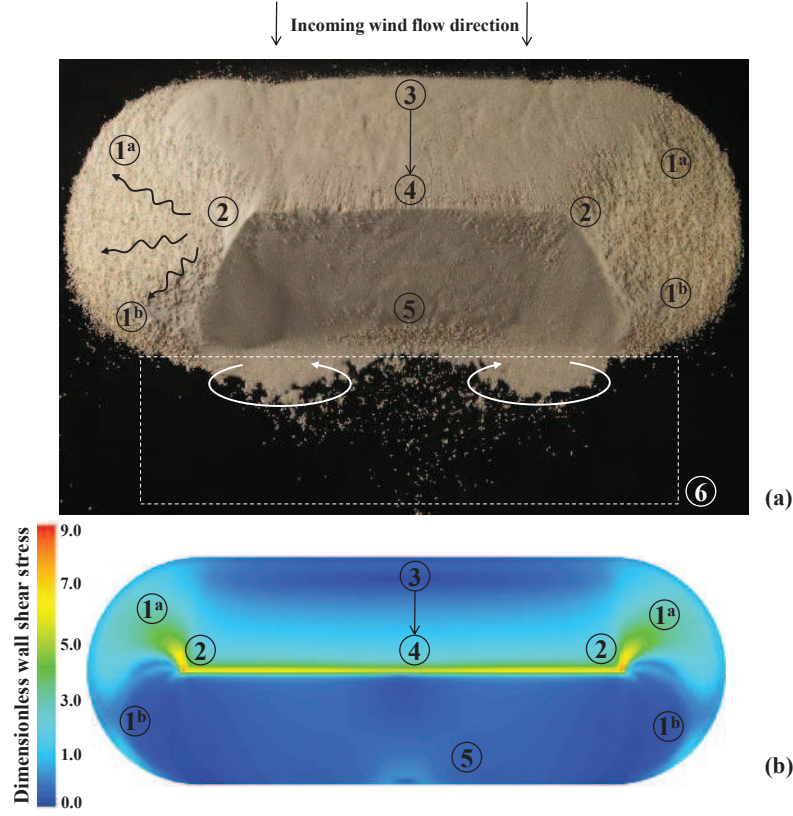


Figure 7: (a) Top view of eroded sand stockpile (cover rate = 10% and free stream velocity = 7m/s) and (b) Numerical results of wall shear stress distribution on the pile surface (for the two approaches, wind flow from top to bottom). The numerical data of wall shear stress is presented as a non-dimensional value, divided by the value calculated on the non-disturbed zone far from the pile.

rapid decrease of the emitted mass flux which may be associated to the surface covering observed in the photographs. These analysis of Fig. 8 leads to the conclusion that the decreasing of the emitted mass flux is directly correlated to the covering of erodible surface by non-erodible particles.

3.3. Cover rate influence on particles emission

Two pile configurations with different cover rates were tested: 10 and 20%. Fig. 9 and Fig. 10 summarize the influence of cover rate on dust emissions for a given free stream air flow velocity equal to 8 m/s.

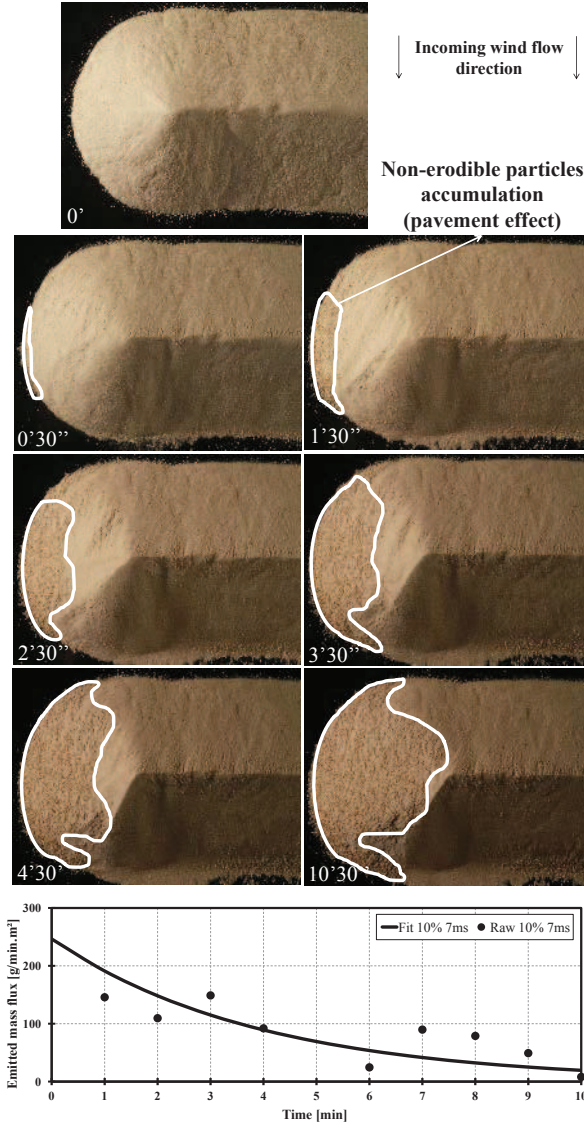


Figure 8: Typical evolution of experimental wind-tunnel photographs from beginning and temporal evolution of the mass flux (cover rate = 10% and free stream velocity = 7 m/s)

Fig. 9(a) shows the temporal variation of the emitted mass flux. Fig. 9(b) presents the photographs of the pile. These photographs were chosen to enable the analysis of the effect of the non-erodible particles on dust emission

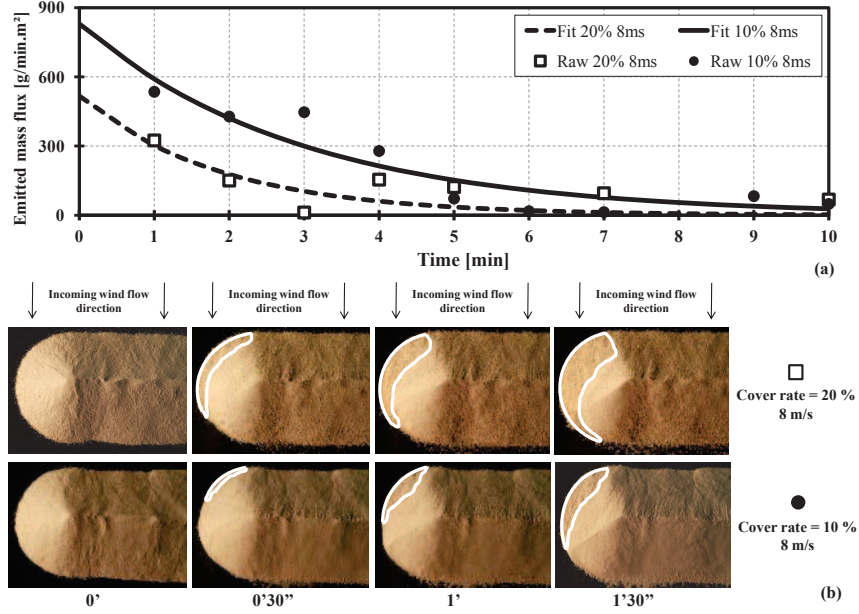


Figure 9: Cover rate influence on time evolution of the emitted mass flux for airflow = 8 m/s: (a) plot of emitted mass flux and (b) experimental wind-tunnel photographs

from the lateral walls of the stockpile that represents the most eroded region. It is clearly noticeable that the white lines bounding the eroded areas evolve differently for different cover rates (Fig. 9(b)) and the emitted mass flux present different time decaying trends for different cover rates (Fig. 9(a)). The emitted mass flux decays faster in the case of 20% cover rate due to the larger amount of non-erodible particles in the pile. As previously discussed, the emitted mass flux is directly related to the mass of erodible particles taken-off from the stockpile lateral walls which exhibit the highest levels of wall shear stress. It can be confirmed by a more detailed observation of particles distribution on the pile sides (regions A and B in Fig. 10).

Fig. 10 shows the region on the pile surface where the largest values of wall shear stress occur (red dashed line). This region is determined by the numerical simulations results as presented in Fig. 7(b). The same figure also shows the regions where the pavement effect has occurred which are bounded by white filled lines and it can be noticed that these two regions are different for different cover rates, being smaller for smaller cover rate. In Fig. 10(a) (cover rate 20%), more than half of the region bounded by the red dashed

line is covered by non-erodible particles. In Fig. 10(b) (cover rate 10%), a smaller region covered by non-erodible particles is noticed. The mass flux temporal evolution for cover rate 20% indicates an intense decreasing from one to four minutes. On the other hand, the emitted mass flux for cover rate 10% results is weaker for the same time interval. It means that the amount of fine particles decreases faster for larger values of the cover rate.

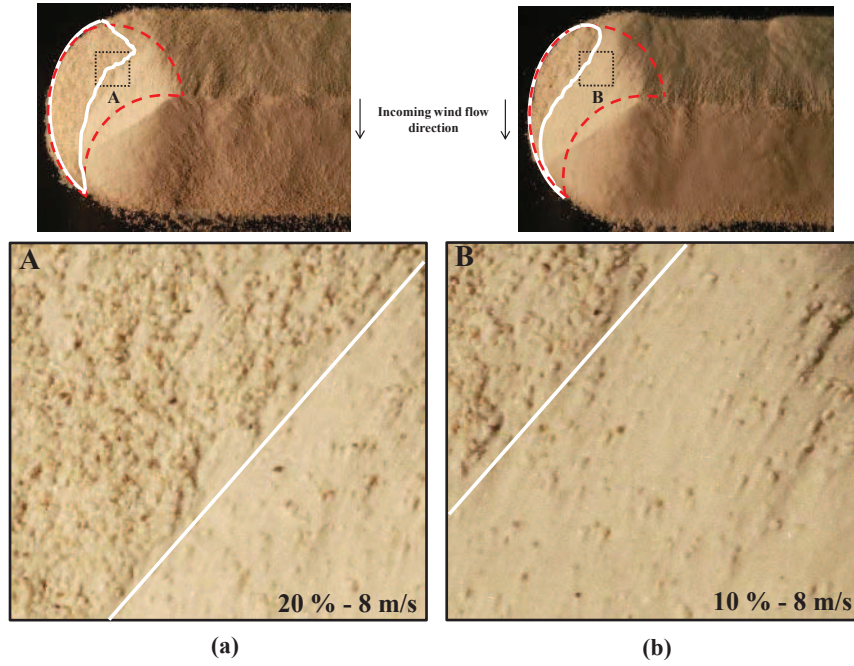


Figure 10: Detailed analysis of the pavement of the regions A and B at 1'30'': (a) cover rate = 20% and free stream velocity = 8 m/s and (b) cover rate = 10% and free stream velocity = 8 m/s

3.4. Free stream velocity influence on particles emission

Fig. 11(a) presents the temporal variation of mass flux for the cover rate 10% and two of the tested free stream velocities (7 and 8 m/s). Fig. 11(b) shows photographs at the instant $t = 6'30''$ (chosen arbitrary) for each free stream velocity presented in the plot. The influence of free stream velocity on the erodible surface covering is associated with the correlation between friction velocity and free stream velocity.

Fig. 11(b) presents the regions of non-erodible particles agglomeration at the chosen time instant for all tested velocities: region A on the stockpile lateral walls, region B on the crest and windward wall and region C near the ground on the leeward wall. Region A is larger for 8 m/s than for 7 m/s. Regions B and C are totally covered by non-erodible particles for 8 m/s at $t = 6'30''$. On the other hand, these regions are not paved for 7 m/s at the same selected time.

As seen in Fig. 11(a), the emitted mass flux decreases more rapidly for 8 m/s. It is explained by the higher friction over the wall (when compared to the free stream velocity 7 m/s) that causes non-erodible particles rapidly emerge and agglomerate on the surface and thus accelerates the pavement occurrence. The plots also shown that the free stream velocity has a smaller influence on the decrease than the cover rate. The tendency for the very small values of the emitted mass flux is very similar for the two tested velocities. Indeed, the higher friction observed for 8 m/s is counterbalanced by the faster covering of the erodible surface.

3.5. Comparison of emitted mass for all tested configurations

The emitted mass dependence on free stream velocity is presented in Fig. 12 for all tested cover rates. Fig. 12(a) shows the results for all six configurations tested in the wind tunnel and Fig. 12(b) presents the results obtained by fitting second order polynomial curves these experimental data.

The influence of cover rate on the amount of emitted mass for the free stream velocity of 6 m/s is very weak while it is very significant for 7 m/s and 8 m/s. The emitted mass doubles as the cover rate decreases from 20% to 10% for 7 m/s and 8 m/s. It is worth to note a more rapid increasing of emitted mass with free stream velocity as cover rates decreases.

The curves presented in Fig. 12(b) seem to be analogous to the formulation proposed by the USEPA (2006). This model is the most widely used in the world for the estimation of dust emission from diffuse sources. The erosion potential parameter in the USEPA model, which is the parameter directly used to quantify the amount of dust emitted, is proportional to the square of velocity as also shown in the curves presented in Fig. 12(b).

In summary, there is a strong dependence of the emitted mass on the percentage of non-erodible particles. For the same value of free stream velocity, the amount of non-erodible particles strongly impact dust emission.

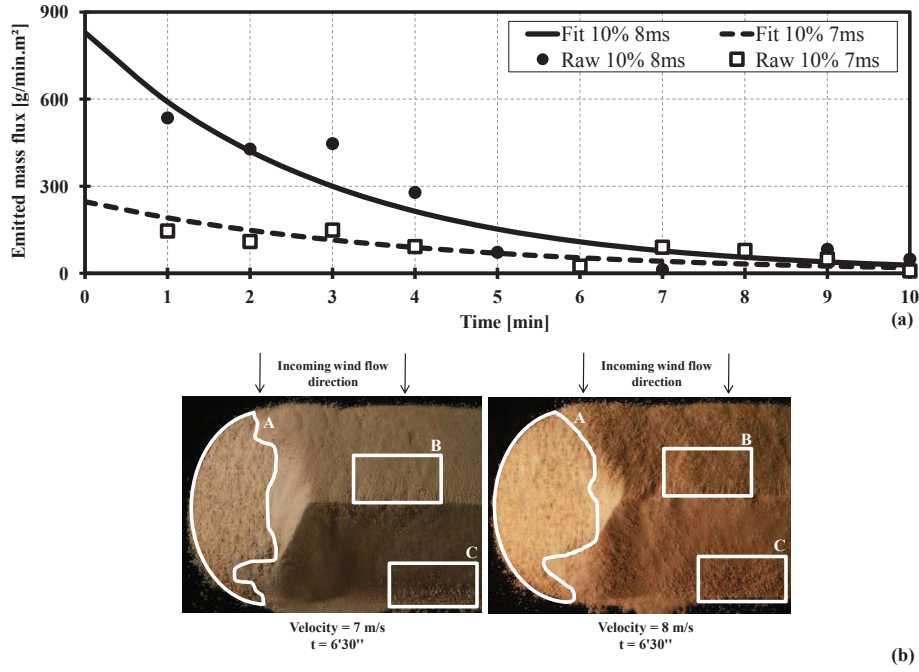


Figure 11: Influence of the incident free stream velocity: (a) plot of emitted mass flux and (b) experimental wind-tunnel photographs

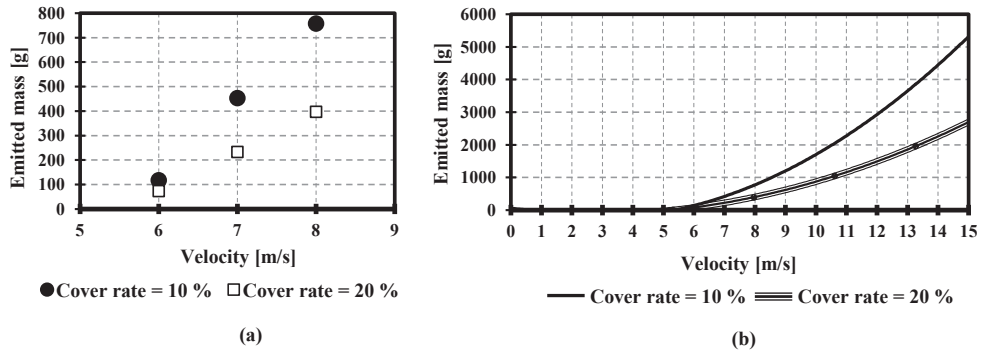


Figure 12: Emitted mass for all tests carried out: (a) mass balance - wind-tunnel experiments and (b) fitting with a power law function of dust emission for lower and higher velocity values than the tested ones

4. Conclusions

Wind tunnel experimental work was carried out to investigate the influence of non-erodible particles on the aeolian erosion of a sand pile model. Six experimental configurations were tested: two cover rates (10% and 20%) and three free stream velocities (6, 7 and 8 m/s). The granular material used in the experiments was sand with bimodal granulometry: an erodible ($125\ \mu\text{m}$) and a non-erodible portion ($850\ \mu\text{m}$). A weighing system was installed under the test section in order to measure continuously the sand stockpile mass.

The general conclusions obtained in this study were:

- the analysis of temporal emitted mass flux indicates that its decay rates depend on the amount of non-erodible particles present in the granular material: it decreases faster for a larger amount of non-erodible particles,
- non-erodible particles accumulation on the pile surface causes a decrease in the amount of particles taken-off towards the free stream flow,
- numerical simulations results of wall shear stress distribution agree with erodible and non-erodible particles agglomeration on the pile surface noticed from photographs,
- the photographs presented in this work indicate the impact of the turbulent flow structures around the stockpiles on particles take-off: zones of high shear stress on the crest line and lateral sides and zones of low shear stress on the leeward wall (recirculation). The photographs also show the gradual change of pavement on the pile lateral sides which are the zones where the potential of particles take-off is most significant. In these zones, non-erodible particles emerge and, due to gravity effects and wind friction, roll down towards the ground, accumulating in the bottom of the stockpile,
- the free stream velocity (for the same cover rate) influences the initial decay rate of the emitted mass flux, as velocity increases, the decay rate of emitted mass flux also decreases,
- mass balance (before and after the wind exposure) indicates that highest emission occurs for the highest velocity (8 m/s) and the lowest cover rate (10%) tested,

The results and discussions obtained herein are essential as a first step to understand the impact of non-erodible particles on dust emissions of oblong stockpiles. The experimental simulations of different pile orientation in relation to the wind direction and different cover rates values are the main perspectives for future studies. The analysis of the temporal decreasing of emitted mass flux should be included in the mathematical methodologies used for dust emission quantification.

5. Acknowledgements

This work was carried out with the financial support of EDF R&D.

References

- Badr T., Harion J-L., 2007. Effect of aggregate storage piles configuration on dust emissions. *Atmospheric Environment* 41, 360-368.
- Benkhaldoun F., Sari S., Seaid M., 2011. A flux-limiter method for dam-break flows over erodible sediment beds. *Applied Mathematical Modelling*. Article in Press.
- Cong X., Cao S., Chen Z., Peng S., Yang S., 2011. Impact of the installation scenario of porous fences on wind-blown particle emission in open coal yards. *Atmospheric Environment* 45, 5247-5253.
- Descamps I., *Erosion éolienne d'un lit de particules à large spectre granulométrique*. Ph.D Thesis, University of Valenciennes, France, 2004.
- Descamps I., Harion J-L., Baudoin B., 2005. Taking-off model of particles with a wide size distribution. *Chemical Engineering and Processing* 44, 159-166.
- Diego I., Pelegry A., Torno S., Toraño J., Menendez M., 2009. Simultaneous CFD evaluation of wind flow and dust emission in open storage piles. *Applied Mathematical Model* 33, 3197-3207.
- Ferreira A., Lambert R., 2011. Numerical and wind tunnel modeling on the windbreak effectiveness to control the aeolian erosion of conical stockpiles. *Environmental Fluid Mechanics*. DOI 10.1007/s10652-010-9176-x.

- Ferreira A., Oliveira R., 2009. Wind erosion of sand placed inside a rectangular box. *Journal of Wind Engineering and Industrial Aerodynamics* 97, 1-10.
- Ferreira A., Farimani A., Sousa A., 2010. Numerical and experimental analysis of wind erosion on a sinusoidal pile. *Environmental Fluid Mechanics*. DOI 10.1007/s10652-010-9168-x
- Foucaut J-M., Stanislas M., 1996. Take-off threshold velocity of solid particles lying under a turbulent boundary layer. *Experiments in Fluids* 20, 377-382.
- Furieri, B., Russeil S., Harion J-L., Santos J., Turpin C., 2012. Experimental surface flow visualization and numerical investigation of flow structure around an oblong stockpile. *Environmental Fluid Mechanics* 12(5).
- Gillette D., Stockton P., 1989. The effect of nonerodible particles on wind erosion of erodible surfaces. *J. of Geophysical Res.* 94, 12885-12893.
- Gillies D., Nickling W., King K., 2007. Shear stress partitioning in large patches of roughness in the atmospheric inertial sublayer. *Boundary Layer Meteorology* 122, 367-396.
- Iversen J., White B., 1982. Saltation threshold on Earth, Mars and Venus. *Sedimentology* 29,111-119.
- Kurose R., Komori S., 2001. Turbulence structure over a particle roughness. *International Journal of Multiphase Flow* 27,673-683.
- Li L., Martz L., 1995. Aerodynamic dislodgement of multiple size grains over time, *Sedimentology* 42, 683-694.
- Liu X., Dong Z., Wang X., 2006. Wind tunnel modeling and measurements of the flux of wind-blown sand. *Journal of Arid Environments* 66, 657-672.
- Neuman C., Nickling W., 1995. Aeolian sediment flux decay: non-linear behaviour on developing deflation lag surfaces. *Earth Surface Processes and Landforms* 20, 423-435.
- Neuman C., Boulton J., Sanderson S., 2009. Wind tunnel simulation of environmental controls on fugitive dust emissions from mine tailings. *Atmospheric Environment* 43, 520-529.

- Raupach M., Gillette D., Leys J., 1993. The effect of roughness elements on wind erosion threshold. *Journal of Geophysical Research* 98, 3023-3029.
- Roney J., White B., 2006. Estimating fugitive dust emission rates using an environmental boundary layer wind tunnel. *Atmospheric Environment* 40, 7668-7685.
- Roney J., White B., 2010. Comparison of a two-dimensional numerical dust transport model with experimental dust emissions from soil surfaces in a wind tunnel. *Atmospheric Environment* 44, 512-522.
- Toraño J., Torno S., Diego I., Menendez M., Gent M., 2009. Dust emissions calculations in open storage piles protected by means of barriers, CFD and experimental tests. *Environmental Fluid Mechanics* 9, 493-507.
- Turpin C., Badr T., Harion J-L., 2010. Numerical modeling of aeolian erosion over rough surfaces. *Earth Surface Processes and Landforms* 35, 1418-1429.
- Turpin C., Harion J-L., 2009. Numerical modeling of flow structures over various flat-topped stockpiles height: Implications on dust emissions. *Atmospheric Environment* 43, 5579-5587.
- USEPA, 2006. Miscellaneous Sources, Industrial Wind Erosion, AP-42, 5th edn, vol I, Chap 13.2.5, November 2006. <http://www.epa.gov/ttn/chief/ap42/ch13/final/c13/final/c13s0205.pdf>
- Webb N., Strong C., 2011. Soil erodibility dynamics and its representation for wind erosion and dust emission models. *Aeolian Research* 3, 165-179.
- White B., 1982. Two-phase measurements of saltation turbulent boundary layer. *Intl. J. of Multiphase Flow* 8, 459-473.

3.1.2 Influence of stockpile orientation on the non-erodible particles effects on dust emission

Last section has presented wind-tunnel experimental results of a sand made stockpile exclusively for a perpendicular incoming wind flow. As a matter of fact, earlier studies (cf. section 1.4.2) have shown that the incoming wind flow orientation has strong influence on the near wall flow pattern and consequently on dust emissions. For that main reason, the present section aims to extend the analysis shown in the last section for oblique piles. This influence has already been numerically studied in literature and in the present study. The near wall fluid flow pattern is extremely different than for a perpendicular oriented stockpile with more complex structures of the near wall fluid flow pattern.

Results are divided into three parts. Firstly, the distribution of non-erodible particles agglomerated over the surface is analysed together with numerical contours of the near wall flow velocity ratio (u_s/u_r). Secondly, several plots of temporal decrease of emitted mass flux are presented. They are similar to those shown in the previous section. The cover rate and the free stream velocity are the parameters used in the comparisons. Finally, the amount of emitted mass for all angles of incidence of the incoming wind flow, cover rates and velocity magnitude are summarized to enable the comparison of dust emissions.

3.1.2.1 Comparison of non-erodible particles distribution pattern with CFD contours

The non-erodible particles agglomeration over the stockpile surface may be correlated with the contours of near wall velocity distribution. It is worth to note that, the piles compared do not have exactly the same dimensions. But, the distribution of wall friction is analogous.

Figure 3.1 shows the comparison between experimental and numerical approaches of wind erosion prediction over an isolated stockpile oriented 30° to the incoming air flow. Figure 3.1a shows the photographs of the experimental work in wind-tunnel. The photograph characterizes the stockpile after the whole duration of the experimental test, i.e., no more erodible particle take-off is noticed. Over the experimental photograph, dashed lines highlight zones of interest. The zones are selected in terms of the pattern of non-erodible particles agglomeration. Indeed, they may indicate the situations shown hereafter:

- highly eroded zones: erodible particles (fine ones) take-off while non-erodible particles emerge, agglomerate and finally cover the surface,
- very weakly eroded zones, mainly near the bottom of the pile, where non-erodible particles agglomerate after falling down from region near the crest due to gravity effects,

Figure 3.1b displays the results of numerical simulations: contours of near wall velocity distribution (values of u_s/u_r). The near wall velocity distribution is taken in this section to represent wall friction.

For the numerical and experimental stockpile models oriented 30° , four regions were highlighted. Region A which is the zone of incoming wind flow impingement is divided into two subregions, namely A-1 and A-2. Subregion A-1 presents the smallest values of u_s/u_r as predicted by previously validated CFD calculations (Turpin and Harion (2009) [72], Furieri et al (2012) [31] and section 4.1.2). Here, very small modifications are noticed on the original pattern of sand arrangement existing before the experiments begin. On the other hand, in subregion A-2, the non-erodible particles emerge as the wall friction becomes higher and promotes the taking-off of erodible particles.

Region B exhibits the highest levels of wall friction which are seen over the pile's crest. This region presents three subregions, namely B-1, B-2 and B-3. Subregion B-1 corresponds to the highest levels of u_s/u_r (which reaches 1.40, the maximum value). Observing the experimental stockpile, a very large erosion is noticed. The stockpile shape at the end of the experimental work is not strictly the same as at the beginning of the tests. A high agglomeration of non-erodible particles is also observed, emerged after the erodible particles have taken-off. Subregions B-2 and B-3 indicate zones of low erosion levels. The pattern is then different to that shown in subregion B-1. It can be observed well delimited zones where the erodible surfaces are still covering the surface. In Region C the highlighted surface is entirely covered by non-erodible particles. Two situations occur: high wall

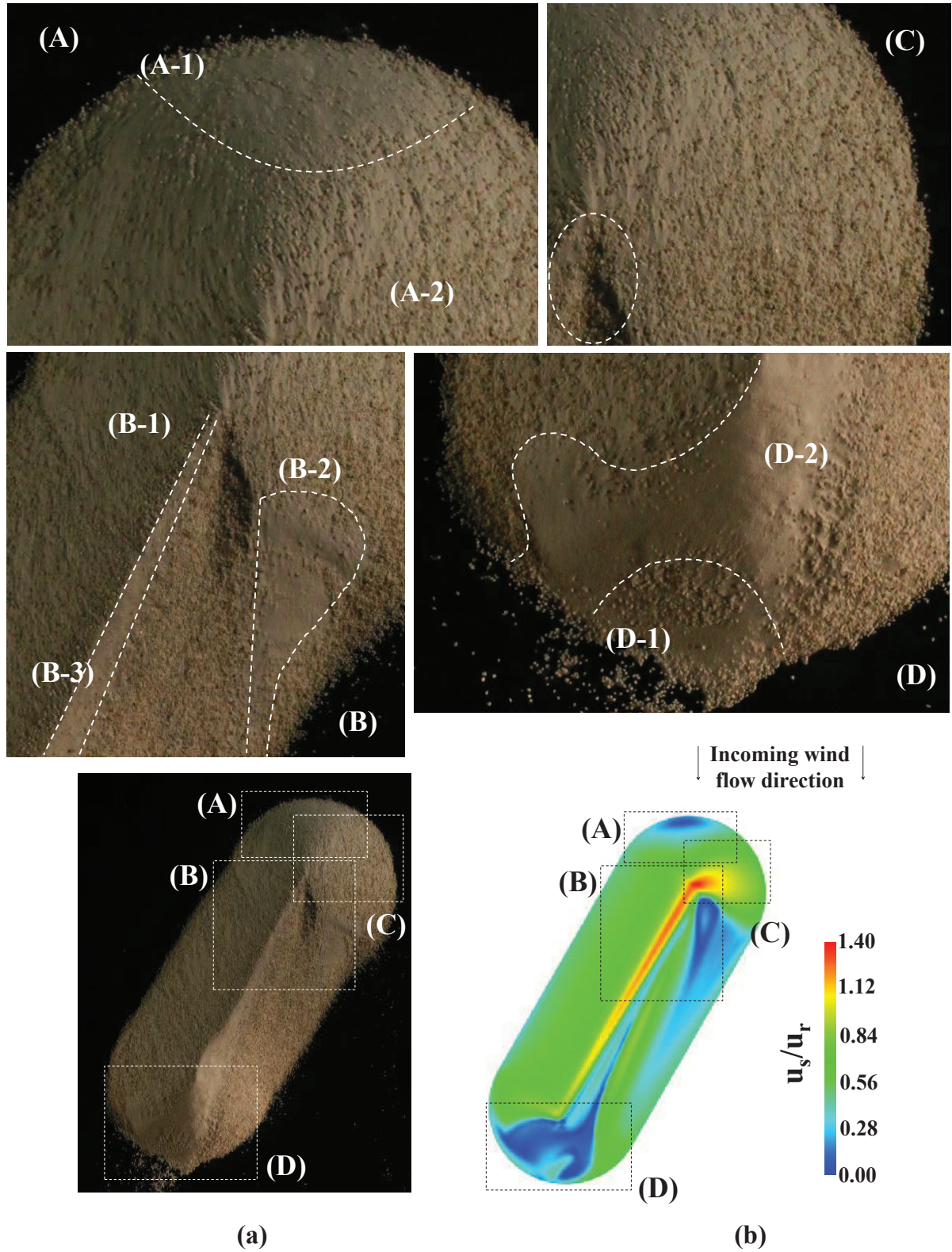


Figure 3.1: Qualitative comparison of erosion for an oblong stockpile oriented 30°: (a) experimental photographs representing a top view of the pile and some highlighted zones and (b) contours of u_s/u_r values from CFD calculations

friction with emerging non-erodible particles and the effects of gravity that causes the agglomeration near the ground in where the friction is much less important.

On Region D, the zones of different levels of erosion are easily noticed on the experimental photograph. The most upstream zone over the pile presents a local elevation of u_s/u_r values (sub-

region D-1). Accordingly, non-erodible particles accumulate over this sub-region. Over the subregion D-2 the original pattern remains unchanged with erodible particles covering the surface. Moreover, in the right of Region D, a significant agglomeration of coarse particles are observed. This region, on the most downstream part of the leeward wall, presents high levels of wind erosion.

Figures 3.1.2.1a and 3.1.2.1b are, respectively, experimental photographs and numerical contours of near wall wind velocity for the stockpile oriented 60° . For this orientation, four regions were also highlighted. Region E, in the right of the impingement zone on the windward wall, is divided in two subregions: E-1 and E-2. In Figure 3.1.2.1b, the numerical contours show two categories of wall friction. That corresponding to subregion E-1 presents low levels of wall friction (maximum u_s/u_r values equal to about 0.35) and in the photograph a distribution in which erodible particles cover the surface with a very low quantity of non-erodible particles is shown. The other side of region E (subregion E-2), presents a gradual evolution of the erosion levels over the stockpile surface. On the experimental photograph, the agglomeration of non-erodible particles is the pattern seen over subregion E-2.

Region F shows two very interesting subregions of this comparison. On subregion F-1, attention was paid to the crest line. The original shape of the stockpile model rounded crest is completely changed in which a great quantity of particles takes-off. The erosion stops after the covering by the non-erodible particles. The erosion levels shown by numerical simulations are around 1.80, the highest. On subregion F-2, a particular situation is noticed. Numerical results indicate low levels of u_s/u_r and a distribution of erodible particle is expected but not happens. As previously explained, the agglomeration of non-erodible particles seen in subregion F-2 may be uniquely caused by the emerged ones eroded on the crest rolling towards the bottom due to gravity effects.

The numerical distribution of near wall velocity shown in Region G (leeward wall of the stockpile oriented 60°) presents also a good agreement with the experimental photographs. At this point of the crest the wall friction is still important and coarse particles are noticed covering the surface. Also, subregion G-1 does not present the emerging of non-erodible particles and the pattern observed is a uniform distribution of fine particles. Near the ground level, the effects of the main vortex (formed on oblique oriented stockpiles and presented by Turpin and Harion (2009) [72] and Furieri et al (2012) [31]) are clearly seen in both representations of subregion G-2. Finally, region H, divided in subregions H-1 and H-2, shows the repartition of low and high friction (predicted in numerical simulations) in the distribution of non-erodible particles over the surface. The zone between subregions H-1 and H-2 should present a surface covered by fine particles due to the low levels of friction seen in the numerical contours. However, it presents an agglomeration of non-erodible ones. These particles are accumulated in this region caused by gravity effects.

The main conclusions obtained in this section fulfil the first aim of this section. A qualitative comparison was performed and a good agreement was noticed for the two tested orientations. The complex structures of the fluid flow over the surface of an oblique stockpile initially only predicted by numerical simulations [3, 31, 72], were partial qualitatively validated. The qualitative analysis concerned an oblong stockpile of a mixing of erodible and non-erodible particles. Herein, the qualitative investigation of the final distribution of non-erodible particles over the eroded pile's surface permitted the observation of different zones of wind erosion that exist over an oblong stockpile surface. For both wind flow directions, the numerical simulations predicted a crest highly eroded and an experimental pile's crest completely modified. The two possible patterns of non-erodible particles agglomeration over the stockpile surface were also attested in both orientations. Moreover, the effects of the main vortex on the leeward wall, as well as, the ineffective erosion regions over the pile are clearly noticed on the experimental photographs.

3.1.2.2 Influence of cover rate and wind flow velocity on the temporal evolution of emitted mass flux of sand

The present section analyses the temporal evolution of the emitted mass flux obtained by continuous measurements in wind-tunnel. Previously, section 3.1.1, with focus on the perpendicular orientation, has carried out an equivalent analysis that will be presented herein for 30° and 60° . Indeed, the present discussions concern the possible modifications that may occur on the influence of non-

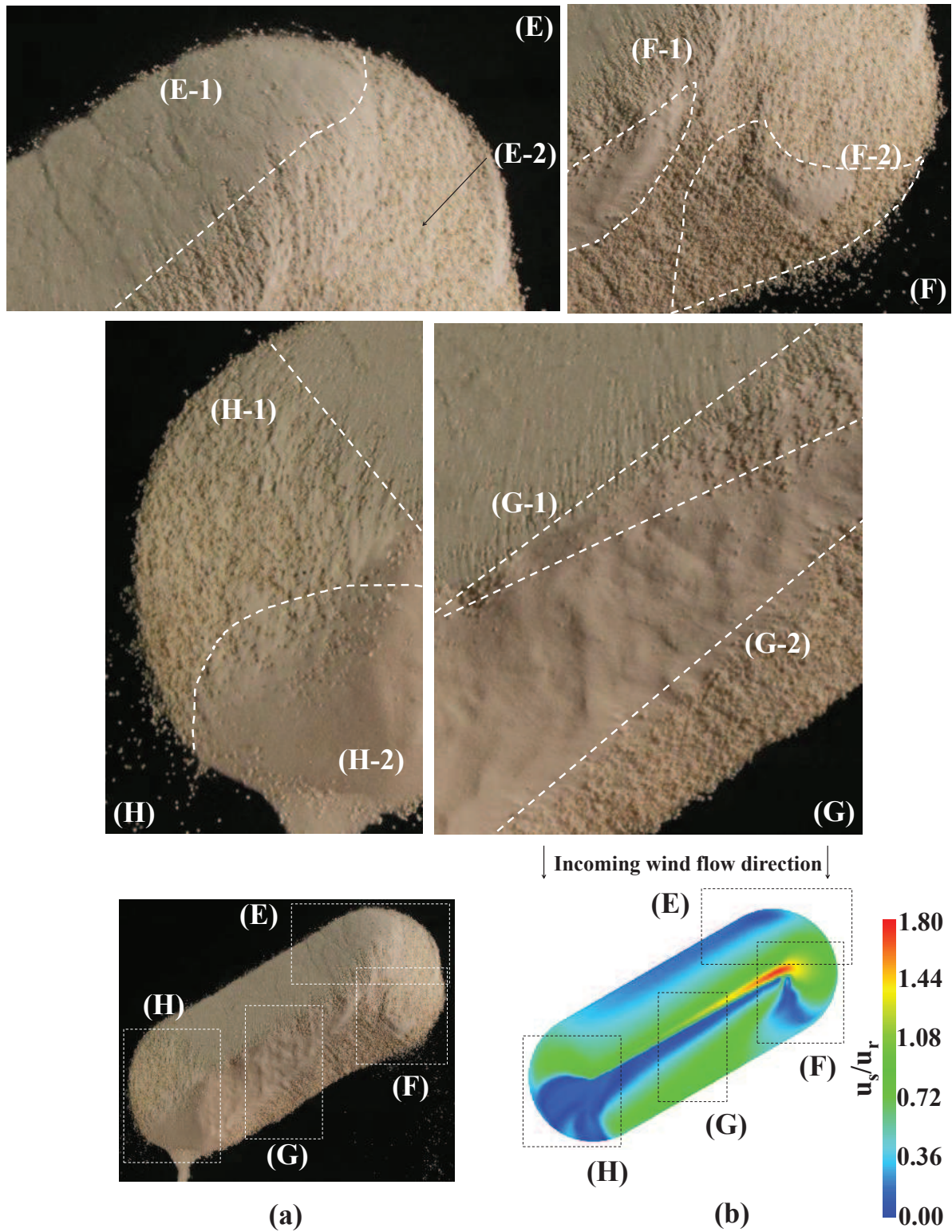
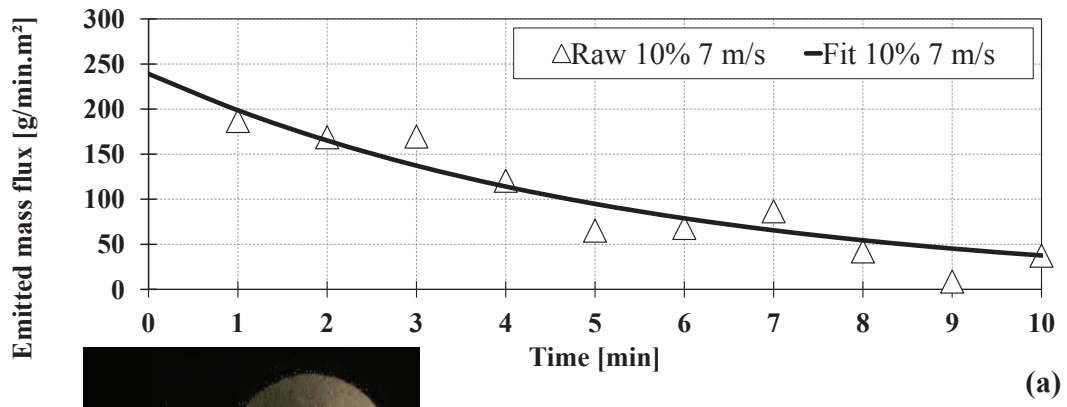


Figure 3.2: Qualitative comparison of erosion near the surface of an oblong stockpile oriented 60°: (a) experimental photographs representing a top view of the pile and some highlighted zones and (b) contours of u_s/u_r values from CFD calculations

erodible particles on the temporal evolution of emitted mass flux for oblique stockpiles. In addition, the influence of cover rate and incoming wind velocity magnitude on the plots of emitted mass flux are likewise subject of interest. The results are divided into three parts for each tested wind flow orientation:

- evolution of non-erodible particles agglomeration over the surface (known as covering of the



Orientation: 30°
Cover Rate: 10%
Wind velocity: 7m/s

↓ Incoming wind
flow direction ↓

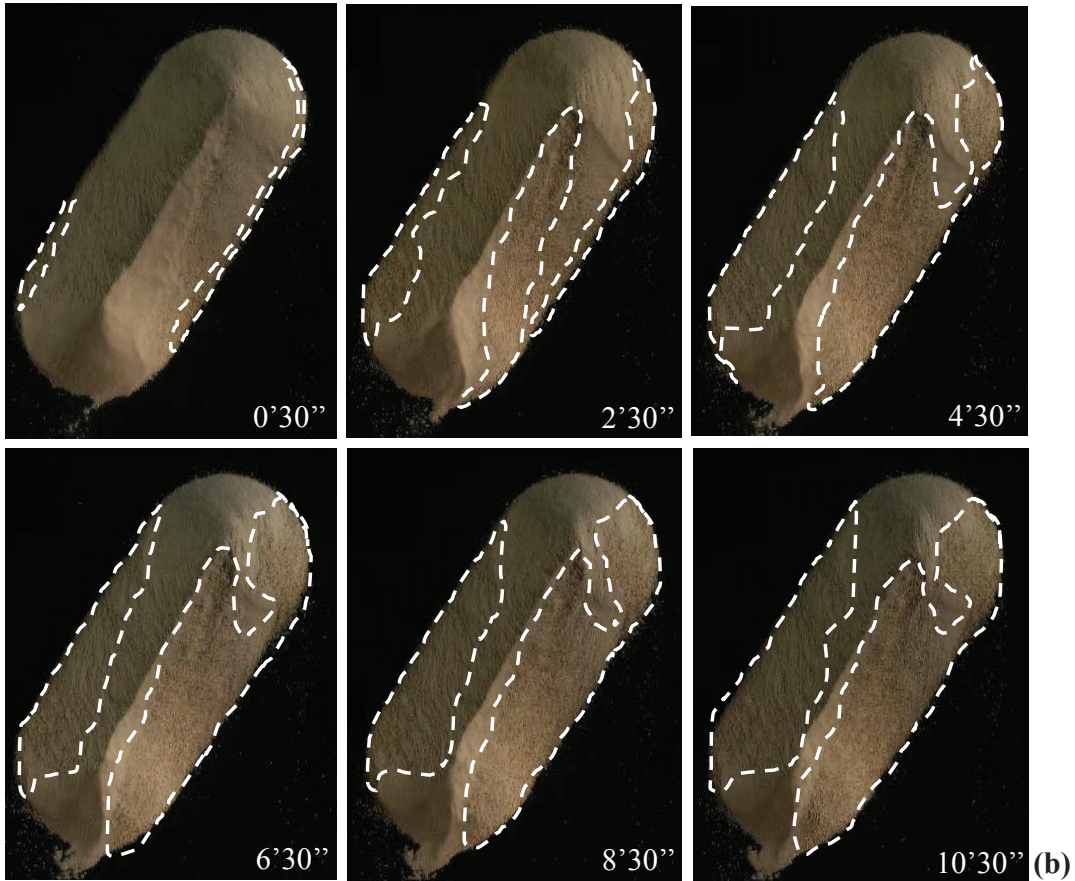


Figure 3.3: Temporal evolution of surface covering in wind-tunnel experiments of a stockpile oriented 30°, cover rate 10% and wind velocity 7 m/s: (a) plot of emitted mass flux and (b) experimental photographs of sand stockpile top view in which dashed lines show the evolution of non-erodible particles agglomeration

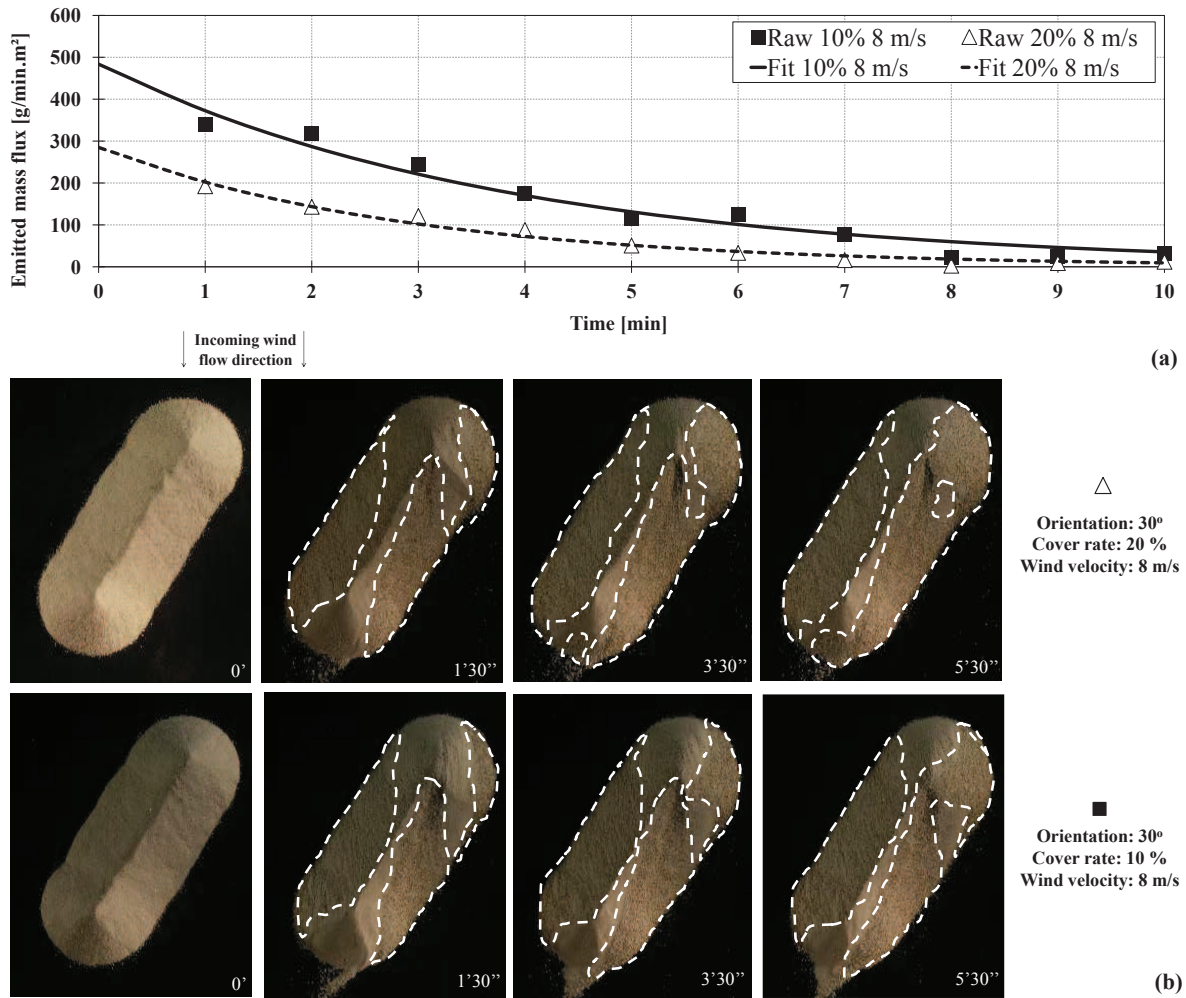


Figure 3.4: Influence of the cover rate on the temporal decrease of the emitted mass flux of a stockpile oriented 30° and wind velocity equal to 8 m/s: (a) plot of emitted mass flux and (b) experimental photographs of sand stockpile top view in which dashed lines show the evolution of non-erodible particles agglomeration

erodible surface) together with the decrease of the emitted mass flux for a given configuration: correlation between the zero mass flux reached in the plot and the last pattern observed by the surface covering,

- analysis of the plot of temporal evolution of emitted mass flux and the non-erodible particles distribution over the sand pile for a same incoming wind velocity and different cover rate values and
- identical analysis of the precedent item, but for three wind velocity magnitudes and one cover rate.

Figure 3.3 exhibits the temporal evolution of the emitted mass flux for an isolated stockpile submitted to a turbulent flow in wind-tunnel. Additionally, a sequence of photographs, which are top views of the stockpile during the experience, is presented.

The decrease of the emitted mass flux, noticed in the plot of Figure 3.3a, may be explained through the growing surface for non-erodible particles which covers more and more the pile surface. The emitted mass flux presents a rapid decrease during the first four minutes. The photographs in Figure 3.3b show the begin of the covering over the crest line, the most eroded zone over the pile, at 2'30''. The photographs after 2'30'' show the evolution of the pavement over the highly eroded regions, namely, the leeward wall (effects of the main vortex) and some zones over the windward wall. The pattern shown at 10'30'' remains unchanged if the air still flows over the pile. At this

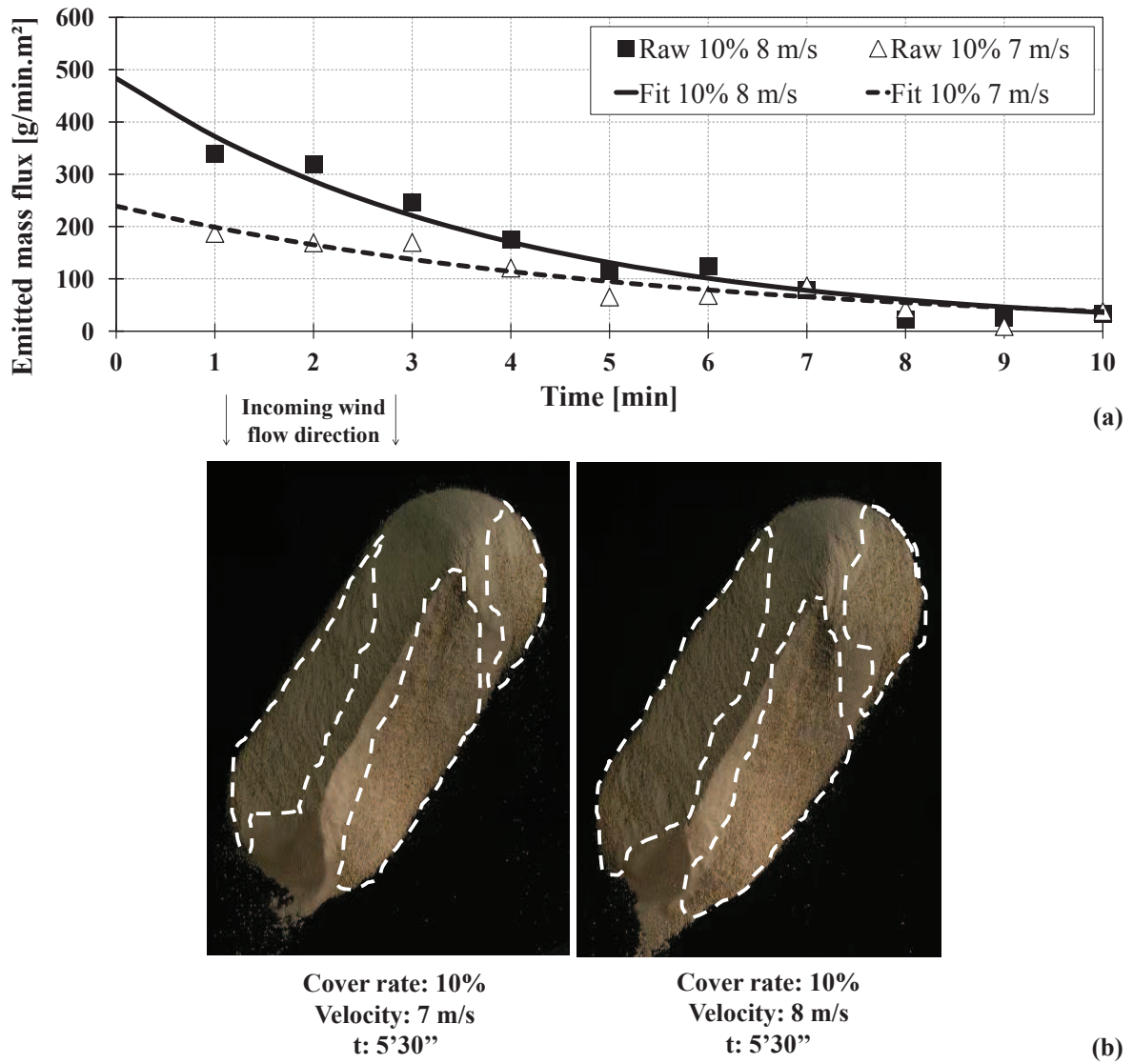


Figure 3.5: Influence of the wind velocity on the temporal decrease of the emitted mass flux of a stockpile oriented 30° and cover rate equal to 10%: (a) plot of emitted mass flux and (b) experimental photographs of sand stockpile top view in which dashed lines show the evolution of non-erodible particles agglomeration

time, the emitted mass flux is undoubtedly zero as shows the plot. Finally, it should be said that the temporal decrease of the emitted mass flux varies accordingly with the pavement of the surface by the non-erodible particles.

The influence of the amount of non-erodible particles, i.e., the cover rate, for the same orientation, is analysed in Figures 3.4a and 3.4b which present, respectively, the plot of temporal decrease of emitted mass flux and the evolution of the agglomeration of non-erodible particles over the stockpile surface for 10 and 20% and a high wind velocity of 8 m/s.

The temporal decrease seems to be slightly faster for the cover rate 20%. The erosion at the level of the stockpile crest is very strong for this orientation (30°). There are more erodible particles in the cover rate 10%. Thus, those erodible particles are rapidly eroded from the crest and enable the the agglomeration of the emerging non-erodible particles. The pavement occurs faster on the crest zone for this cover rate. The zero seems to be reached slightly faster for 20% as the mass flux is smaller since the beginning and the higher amount of non-erodible particles develops this condition. The cover rate has lower influence on the different evolution patterns of emitted mass flux decrease than it was observed for the perpendicular orientation.

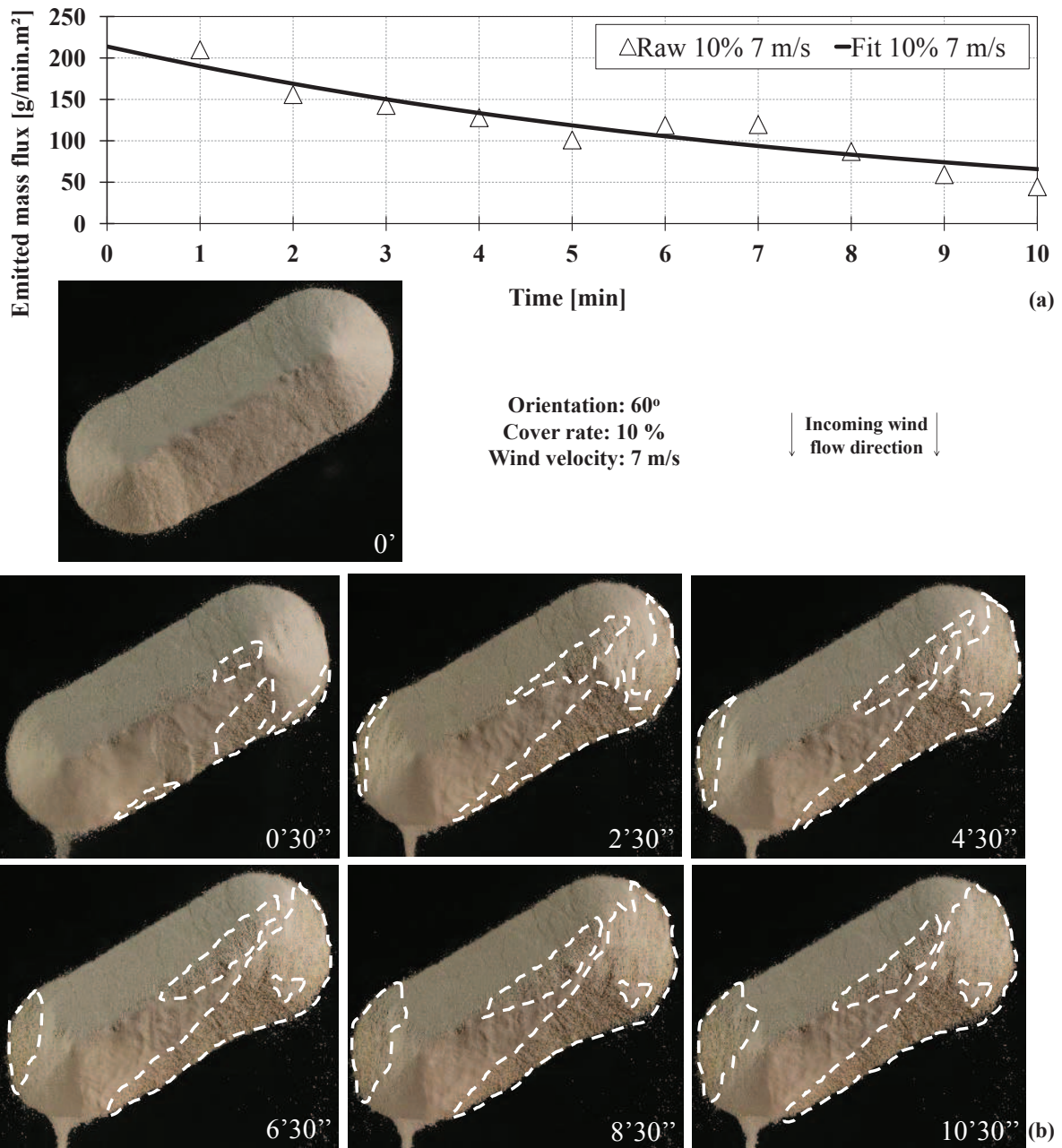


Figure 3.6: Temporal evolution of surface covering in wind-tunnel experiments of a stockpile oriented 60°, cover rate 10% and wind velocity 7 m/s: (a) plot of emitted mass flux and (b) experimental photographs of sand stockpile top view in which dashed lines show the evolution of non-erodible particles agglomeration

Figure 3.5 shows the temporal evolution and photographs for the two tested velocities and a same cover rate (10%). The photographs taken at the same time instant, indicate a higher covering for 8 m/s. The initial values (first four minutes, approximately) of emitted mass flux are also highly different among the tested velocities: almost two times the value for 8 m/s compared with 7 m/s. The plot for 8 m/s shows a rapid decrease. As a result of that the zero seems to be reached at the same time for the two configurations.

Identical analysis, as those carried out for the stockpiles oriented 30° are shown in Figure 3.6, 3.7 and 3.8 for another oblique configuration: 60°. The zones of erosion over the pile (see Figure 3.1.2.1 for more details about the distribution of wall erosion) shows that the main eroded zones are entirely covered at the instant 8'30'' and 10'30''. It is worth to note that, the instant of surface covering happens later for this orientation than for 30°. This is in-line with previous CFD calculations and

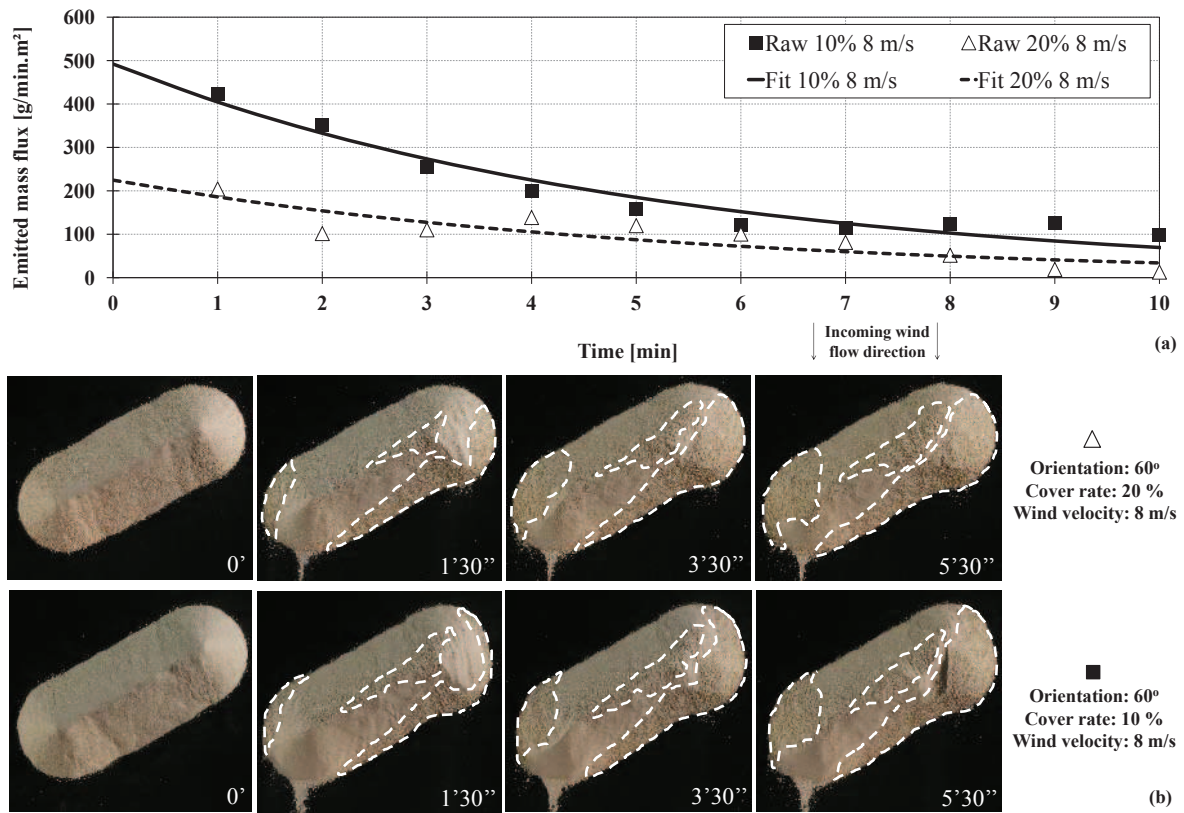


Figure 3.7: Influence of the cover rate on the temporal decrease of the emitted mass flux of a stockpile oriented 60° and wind velocity equal to 8 m/s: (a) plot of emitted mass flux and (b) experimental photographs of sand stockpile top view in which dashed lines show the evolution of non-erodible particles agglomeration

mathematical quantification of dust emission (Turpin and Harion (2009) [72] and Furieri et al. (2012) [31]) have already predicted that the oblique orientation 30° is the more eroded among the tested configurations.

Furthermore, Figures 3.7 and 3.8, showing respectively the influence of cover rate and wind velocity. The analysis of the influence of cover rate is quite different for 60° . The temporal evolution presents a slower decrease for the tested case presenting more non-erodible particles. The photographs in Figure 3.7 qualitatively check this statement. The evolution of the covering is very similar between the two cover rate values. The very strong erosion in these oblique configurations cause a high movement of the coarse particles over the surface. Thus, for a longer time the erodible surface is free for erosion. The wind velocity promotes equally evolution in time for each tested velocity.

The last part of this section concerns the summary of mass balance (weighing of the sand model stockpile before and after the wind-tunnel experiments) for the three incoming flow orientations tested in this work. Thus, Table 3.1 shows the values of emitted mass. These values are shown in grammes. For each value, an interval is presented, which is the result of the uncertainty calculated by means of repeatability tests carried out for at least one configuration of all tested orientations (those tests are detailed, for the perpendicular configuration, in section 3.1.1). The uncertainty considered for the values of emitted mass flux is the standard deviation of the repeatability tests which is about 100 g/min.m^2 . The values of emitted mass shown in Table 3.1 reveal a pattern similar to that predicted in the numerical quantification (cf. section 4.1.2 for more details about the dust emissions estimation). There is a generally good agreement between the present experimental mass balance and numerical prediction.

The values of emitted mass for the orientation 30° are slightly higher (mean values) or even may present the same values of other orientations depending on the uncertainty. For all tested cases, the dust emission is considerably lower for the highest cover rate value (20%). Also, for all orientations

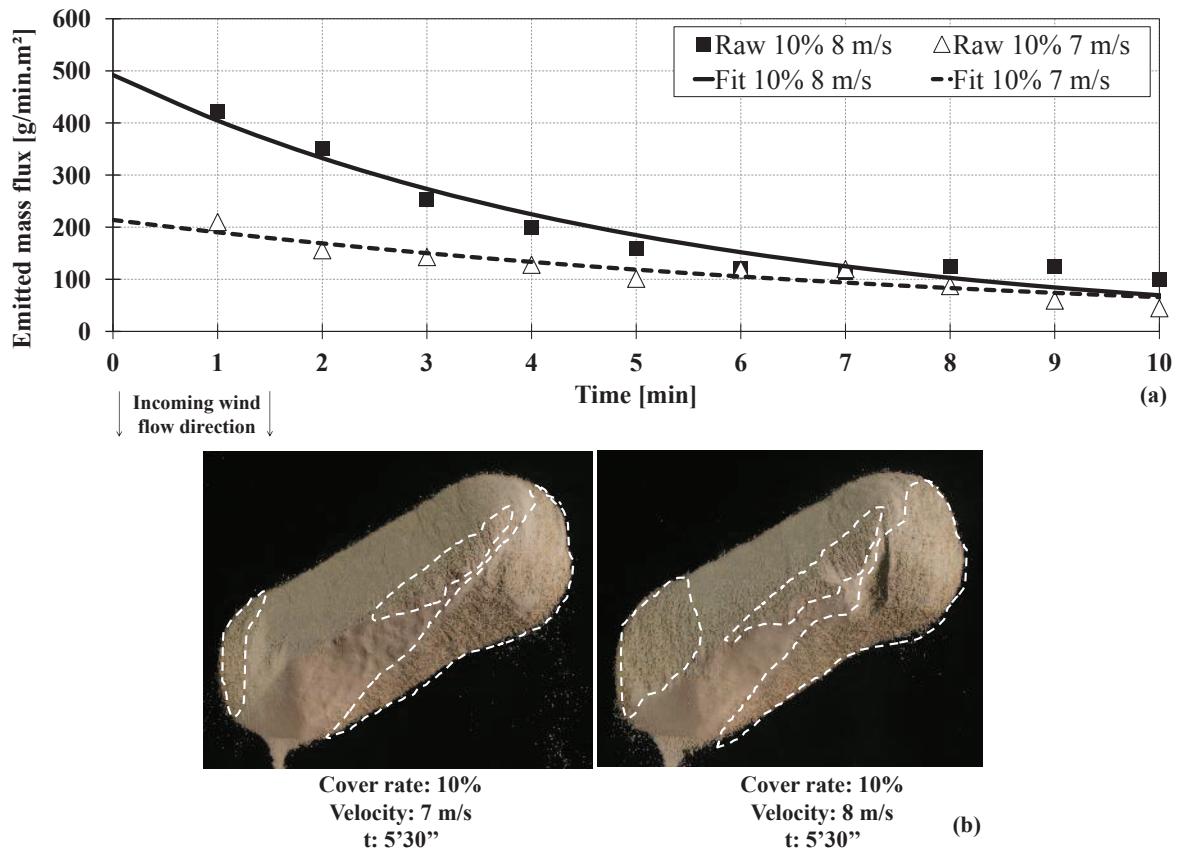


Figure 3.8: Influence of the wind velocity on the temporal decrease of the emitted mass flux of a stockpile oriented 60° and cover rate equal to 10%: (a) plot of emitted mass flux and (b) experimental photographs of sand stockpile top view in which dashed lines show the evolution of non-erodible particles agglomeration

and cover rate values tested, the dust emission increases with the increase of wind velocity.

3.1.2.3 Conclusions

Wind-tunnel experiments were carried out for oblique oblong stockpiles, additionally to the results previously presented for the perpendicular orientation. The overall results have shown a good agreement between numerical distribution of wall friction, and qualitative visualization of the agglomeration of non-erodible particles on the stockpile surface. The zones of strong wind erosion, namely the crest and the effects of the main vortex on the leeward wall, are easily identified in the experimental photographs. Furthermore, during the experiments the non-erodible particles cover the erodible surface of the piles. The pavement condition is noticed in the plots of emitted mass flux in which a temporal decrease exists for all tested configurations. Cover rate and wind velocity magnitude have shown influence on the temporal decrease but with lower importance. Briefly, higher cover rates cause the faster covering of the surface.

These last two sections are primarily important in the definition of the characteristics of the turbulent wind flow over oblong stockpile models composed by real particles. It is worth to note that, this genre of analysis of the wind flow on the wall of a storage pile has never been yet carried out. Previously works in the open literature have only been focused on flat bed of particles. This statement reinforces the fact that these investigations are recent and largely assists the understanding of the diffuse sources erosion behaviour in the presence of non-erodible particles and various meteorological conditions (for instance, incoming wind flow orientation and magnitude). The main practical application of this study is the summary of the overall information acquired for the three tested wind flow orientations to achieve a proposition of substantial modifications in the mathematical model of dust emission quantification widely used (USEPA (2006) [75]). Finally, the results have checked, for

Table 3.1: Summary of emitted mass balance [g]

Orientation	Velocity [m/s]	Cover rate: 10%		Cover rate: 20%	
		$M_{min} - M_{max}$	\bar{M}	$M_{min} - M_{max}$	\bar{M}
30°	6	183.9 - 204.5	194.2	91.0 - 101.2	96.1
	7	441.0 - 490.4	465.7	232.2 - 258.2	245.2
	8	758.9 - 843.9	801.4	396.5 - 440.9	418.7
60°	6	165.9 - 184.5	175.2	90.3 - 100.5	95.4
	7	436.0 - 484.8	460.4	222.5 - 247.5	235.0
	8	756.5 - 841.1	798.8	380.8 - 423.4	402.1
90°	6	126.9 - 141.1	134.0	80.9 - 89.9	85.4
	7	429.0 - 477.0	453.0	221.2 - 246.0	233.6
	8	717.4 - 797.8	757.6	376.1 - 418.3	397.2

the several tested conditions, the presumption that non-erodible particles have a strong influence on the dust emission pattern.

3.2 Local analysis of the influence of non-erodible particles on dust emissions by means of numerical simulation approach

Previous sections have been focused on experimental measurements to analyse the influence of non-erodible particles on the aeolian erosion of granular material agglomerations. The present section, on the contrary, focuses on numerical simulations. Two numerical works were performed about the non-erodible particles which are taken herein as roughness elements. The first analysis is about steady simulations applying a RANS turbulence models in which the domain contains a poly-dispersed distribution of roughness elements. The main objective is the validation of a formulation presented in literature that associates the evolution of mean friction of an erodible surface with geometrical parameters of the roughness elements. The second part, initially presented in the perspectives of the study, deals with a LES investigation of roughness elements. The objectives include the understanding of the turbulence on a bed of roughness elements and particularities given by an unsteady simulation.

3.2.1 Numerical modelling of aeolian erosion over a surface with poly-dispersed roughness elements

Numerical simulations were carried with an open-source CFD code to obtain the fluid flow description over a bed of poly-dispersed roughness elements. The results are presented as an article, to be submitted to the **"Earth Surface Processes and Landforms"** journal, entitled **"Numerical modelling of aeolian erosion over a surface with poly-dispersed roughness elements"**. The investigation is interested in the evolution of the shear stress over the underlying surfaces surrounding non-erodible particles. The domain containing an erodible surface in the presence of non-erodible particles impinged by a turbulent boundary layer represents a typical surface of granular materials agglomeration. The reference work performed by Turpin et al. (2010) [71] proposed a formulation to describe the evolution of the mean friction velocity over the surface in the presence of roughness elements which represent the non-erodible particles. The mean friction velocity (shear at the wall) is a function of geometrical parameters of the domain. The formulation permits the understanding and quantitative analysis of how the presence of non-erodible particles attenuates the aeolian erosion. In fact, the purpose of the paper is check the validity of the formulation for a larger range of cases. The original formulation is based on numerical simulations of mono-dispersed distributions of roughness elements. The present numerical simulations are all based on a poly-dispersed distribution.

Numerical modelling of aeolian erosion over a surface with poly-dispersed roughness elements

B. Furieri^{a,b}, J. L. Harion^{a,b}, M. Milliez^c, S. Russeil^{a,b}, J. M. Santos^d

^a*Univ Lille Nord de France, F-59000 Lille, France*

^b*Mines Douai, EI, F-59500 Douai, France*

^c*CEREA, EDF R&D, Ecole des Ponts ParisTech, Université Paris Est, F-78401
Chatou, France*

^d*Universidade Federal do Espírito Santo, DEA, 29060-970 Vitória, ES, Brazil*

Abstract

The present study is focused on the analysis of the mean wall friction velocity on a surface including roughness elements exposed to a turbulent boundary layer. These roughness elements represent non-erodible particles over an erodible surface of an agglomeration of granular material on industrial sites. A first study (Turpin et al., 2010) has proposed a formulation that describes the evolution of the friction velocity as a function of geometrical parameters and cover rate with different mono-dispersed roughness distributions. The present simulations deal with poly-dispersed distribution of particles with a random sampling of diameter, height, position and arrangement. The evolution (relative to geometrical parameters of the roughness elements) of the friction velocity for several poly-dispersed distributions of roughness elements was analysed by the equation proposed in the literature and compared to the results obtained with the numerical simulations. This comparison showed a very good agreement. Thus, the formulation developed for mono-dispersed particles was found to be also valid for a larger spectra of particles noticed on industrial sites. The present work aims also to investigate in details the fluid mechanics over several roughness particles.

Keywords:

wind erosion, non-erodible particles, roughness elements, CFD, open-source simulations, wall shear stress assessment

Table 1: Definition of symbols used in this paper

Symbol	Units (SI)	Definition
$a_{p1}, m_{p1}, n_{p1},$ a_{p2}, m_{p2}, n_{p2}		Coefficients of Equation 2
b	[mm]	Roughness element diameter
C_R		Roughness element drag coefficient
C_S		Surface drag coefficient
h	[mm]	Roughness element height
h_S	[mm]	Mean roughness elements height
m		Surface shear stress inhomogeneity parameter
N_p		Number of roughness elements
P_{fric}		Roughness element geometrical parameter ($TDC \cdot S_{floor}/S_{frontal}$)
R_{fric}		Friction velocity ratio
R_t		Threshold friction velocity ratio
R		Correlation coefficient
S_{floor}	[mm ²]	Roughness element basal surface
$S_{frontal}$	[mm ²]	Roughness element frontal surface
S	[mm ²]	Computational domain basal surface
TDC		Cover rate ($TDC = (\sum S_{floor})/S$)
u_R^*	[ms ⁻¹]	Friction velocity for an erodible surface protected by roughness elements
u_S^*	[ms ⁻¹]	Friction velocity for a smooth erodible surface
u_t^*	[ms ⁻¹]	Threshold friction velocity
u_{t-R}^*	[ms ⁻¹]	Threshold friction velocity for an erodible surface protected by roughness elements
u_{t-S}^*	[ms ⁻¹]	Threshold friction velocity for a smooth erodible surface
x, y and z	[m]	Computational coordinates
x^+, y^+, z^+, u^+ and h_S^+		Coordinates, streamwise wind velocity and mean roughness height in wall units
β		Ratio of roughness element to surface drag coefficients
λ		Roughness density
ν	[m ² s ⁻¹]	Kinematic viscosity
ρ	[kgm ⁻³]	Air density
σ		Ratio of roughness element basal to frontal area ($S_{floor}/S_{frontal}$)
τ	[Pa]	Total shear stress
τ_R	[Pa]	Roughness element shear stress
τ_S	[Pa]	Surface shear stress
τ_{ref}	[Pa]	Reference shear stress computed over an erodible surface without roughness elements

1. Introduction

This work is within the framework of environmental effects caused by the aeolian erosion of granular materials (for example, coal or iron) commonly encountered on industrial sites. Diffuse sources generated by aeolian erosion events have motivated several studies (Zobeck et al. (2003); Castel (2006); Roney and White (2006); Badr and Harion (2007); Guingo and Minier (2008); Neuman et al. (2009); Roney and White (2010); Ferreira and Lambert (2011); Furieri et al. (2012)). Another kind of investigations is concerned with the quantitative analysis of atmospheric pollution. For that aim, mathematical

models are often employed. The models commonly encountered for the quantification of dust emission from diffuse sources present a lack of information regarding: the effects of coarse particles on the decrease of the emitted mass flux, the interactions between nearby sources and all kind of buildings that surround the sources, the atmosphere stability, and others.

Thus, the present study focuses on the local analysis of an erodible surface exposed to wind erosion in the presence of coarse particles found on granular material agglomerations. These particles are treated in our study as roughness elements over a smooth surface. For a given wind velocity, an agglomeration of granular material with a large size distribution, is a mixing of erodible and non-erodible particles (Gillette and Stockton (1989); Neuman and Nickling (1995); Neuman (1998); Al-Awadi and Willetts (1999); Gimenez et al. (2006); Lopez et al. (2007); Jiang et al. (2008); Benkhaldoun et al. (2011); Webb and Strong (2011)). By definition, the erodibility of particles submitted to aeolian erosion depends on the incoming wind flow velocity and their diameter. The non-erodible particles do not take-off from the surface because of their inertia.

The analysis of an erodible surface in the presence of non-erodible particles exposed to a turbulent wind flow is usually carried out by means of the wall shear stress repartition over the erodible surface. This approach was introduced, for roughness studies, by Schlichting (1968). The total stress (τ) is split into τ_R , the stress on roughness elements (non-erodible particles) and τ_S , the stress on the underlying surface.

Earlier investigations have shown that the soil wind erosion is strongly attenuated by the presence of non-erodible particles. The near fluid flow over erodible surfaces in the presence of non-erodible particles (roughness elements) can be summarized by the following points Raupach et al. (1993); Neuman and Nickling (1995); King et al. (2005); Shao and Yang (2005); Gillies and Nickling (2007); Turpin et al. (2010):

- increase of the threshold friction velocity,
- decrease of the mean friction velocity and consequently of the soil erodibility and
- temporal decrease of the emitted mass flux

In fact, a phenomena commonly called pavement effect happens as the non-erodible particles emerge on the erodible surface and finally cover the

whole surface. Thus, the erodible particles can not be exposed to wind flow. The protection is characterized by the decrease of the mean shear stress on the underlying surface.

The purpose of this work is to continue the original research initiated by Turpin et al. (2010) for mono-dispersed particles. Numerical simulations were performed from which a mathematical formulation was proposed to associate the geometrical characteristics of the non-erodible particles and the mean friction velocity of the erodible surface. Shortly, the above mentioned formulation proposes an evolution of the value of the friction velocity on the underlying surface (i.e., applied to erodible particles) as a function of roughness elements parameters.

The formulation developed by Turpin et al. (2010) is presented by Equations 1 and 2.

$$R_{fric} = \frac{u_R^*}{u_S^*} \quad (1)$$

$$1 - R_{fric} = a_p \cdot (TDC)^{m_p} \cdot (S_{frontal}/S_{floor})^{n_p} \quad (2)$$

where:

in Equation 1, u_R^* and u_S^* are the friction velocities for, respectively, rough and smooth walls. In Equation 2, TDC is the cover rate, $S_{frontal} = bh_{NEP}$ and $S_{floor} = \pi b^2/4$ are respectively the frontal and the basal area of a roughness element represented by a cylindrical non-erodible particle (b and h_{NEP} are the particle diameter and height, respectively), a_p , m_p and n_p are empirical coefficients determined by the mono-dispersed numerical simulations carried out in the previous study. The coefficients depend on the range of the particle parameters.

The formulation proposed by Turpin et al. (2010) was achieved after several similar numerical simulations. It was found that the parameter $1 - R_{fric}$ increases with the increase of $P_{fric} = TDC \cdot (S_{frontal}/S_{floor})$ in two different ways: higher slope when P_{fric} is between 0 and 2 and a smaller slope when P_{fric} is between 2 and 8. This behaviour is linked to the modification of the flow regime due to a modification of the roughness elements distribution. This modification observed in the flow behaviour was also previously found out by Lee and Soliman (1977). Therefore the coefficients in Equation 2 depend on the range of P_{fric} .

In the present paper, the range of cases to be simulated was based on the same limits imposed by Turpin et al. (2010) for their formulation: the

parameter P_{fric} is equal to a maximum of 8 which covers a large range of particles in nature.

Despite the contribution of the formulation to improve the understanding of the impacts of the non-erodible particles and the manner in which the friction velocity is accounted for, the formulation still presents a restriction. The numerical simulations carried out by Turpin et al. (2010) suppose that all the roughness elements show the same emerging level and have the same diameter. Nevertheless, on industrial sites, the mono-dispersed condition is very rarely accomplished. It has arisen the interest in checking the robustness of the formulation proposed by Turpin et al. (2010) (Equation 2), with the same parameters and coefficients for a poly-dispersed roughness elements distribution, or perhaps, determining some modification to be considered in the model coefficients.

For each simulation in the present study, particles diameters and heights are randomly chosen from a defined range of values. Therefore, numerical simulations were carried out with the open source Computational Fluid Mechanics (CFD) code *Code_Saturne* (Archambeau et al. (2004)). Moreover, the present work will exclusively investigate cylindrical particles, as they are more representative than spherical particles of the fully random pattern observed on industrial sites. In addition, a particular attention is paid to the fluid mechanics analysis over a surface presenting roughness elements. The effects of roughness particles are important on the turbulent pattern of the wind flow (Lee and Soliman (1977); Li and Martz (1995); Kurose and Kumori (2001); Carney et al. (2005); Orlandi and Leonardi (2008); Sutton and Neuman (2008)). This investigation aims to improve the manner in which some models take into account the evolution of the amount of non-erodible particles.

2. Numerical simulations

2.1. Geometry, meshing and boundary conditions

All the results presented in this study were obtained by means of numerical simulations. The three dimensional (3D) equations of mass and momentum governing the phenomena were computed with the open-source code *Code_Saturne* (Archambeau et al. (2004)) which is based on a finite volume approach for co-located variables on an unstructured grid. It can handle complex geometries and physics. In our numerical simulations, we used a steady Reynolds Average Navier Stokes (RANS) approach and turbulence

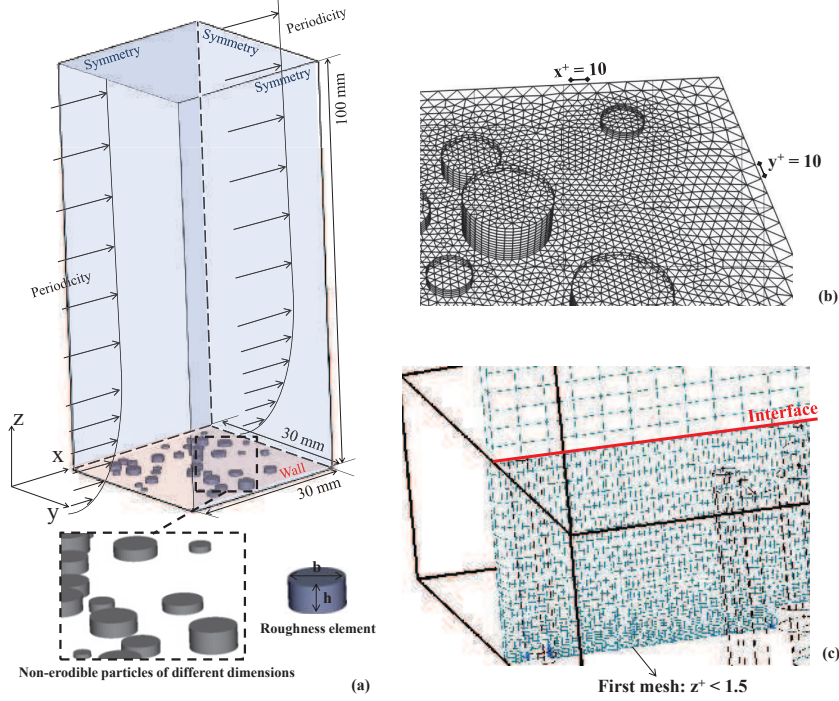


Figure 1: Computational domain: (a) dimensions and boundary conditions, (b) mesh on the wall of the erodible surface and roughness elements and (c) vertical mesh distribution

143 effects were accounted for by using the $k-\omega$ Shear Stress Transport (SST)
 144 model without wall functions for the turbulence damping near walls.

145 Figure 1(a) shows the computational domain and the boundary condi-
 146 tions. The poly-dispersed pattern of the numerical simulations can be no-
 147 ticed in Figure 1. For all tested configurations, the domain is a rectangular
 148 box. The base is a square of 30 mm and the height is 100 mm. The dimen-
 149 sions of the base of the computational domain were chosen to be statistically
 150 representative of the repetition pattern of the particles: flow pattern and
 151 turbulent characteristics. Badr (2007) has validated these dimensions for a
 152 mono-dispersed configuration with non-erodible elements with diameters of
 153 1.0 to 3.0 mm and cover rates up to 20%. Later in the present work, a com-
 154 parison for different spatial distributions of particles, for a same tested case,
 155 is presented to validate the domain dimensions for poly-dispersed configura-
 156 tions.

157 A periodic boundary condition is applied in the streamwise flow direction,

158 since the pattern of the flow solution is expected to be periodic (Turpin et
 159 al., 2010). In this way, the mass flow is fixed for a corresponding mean
 160 longitudinal velocity value equal to 8 m/s. For the upper boundary condition
 161 and laterals, symmetry is imposed to reduce computational efforts. Smooth
 162 walls with no-slip conditions are set at roughness elements and ground walls.

163 Meshing and turbulence modelling choices were based on previous similar
 164 numerical calculations carried out by Turpin et al. (2010). Figures 1(b) and
 165 (c) present the meshing details. The mesh is produced by an extrusion from
 166 triangular cells defined on the erodible surface and roughness elements walls
 167 (see Figure 1(b)) towards the interface boundary of the computational do-
 168 main. Indeed, the calculation domain was divided into two parts with an in-
 169 terface at a height equal to three times the largest diameter (see Figure 1(c)).
 170 The use of an interface allows to mesh the upper part with quadrilateral ele-
 171 ments for a better computational efficiency. Near the particles and the walls
 172 the mesh was constructed with hexahedral and pentahedral elements for a
 173 good refinement in the spanwise and streamwise directions. As required by
 174 the closure of the turbulence model there is a mesh refinement near the wall
 175 surface where $z^+ \leq 1.5$ (to ensure no use of wall functions) based on the
 176 friction velocity for the smooth case.

177 It is worth to note that, the numerical simulations performed by Turpin
 178 et al. (2010) were validated with previous numerical and experimental stud-
 179 ies concerning roughness elements. The same comparison and validation is
 180 performed in the present study (Figure 2). The comparison plots the ratio
 181 of threshold friction velocity $R_t = u_{t-r}^*/u_{t-s}^*$ versus the roughness density
 182 $\lambda = N_p b h_{NEP} / S_{NEP}$ in logarithmic representation.

183 The roughness density λ was defined by Marshall (1971) which stated
 184 that the shear stress partition depends primarily on the roughness density
 185 parameter λ and on lesser extend on roughness shape and distribution. With
 186 our numerical results the same mean behaviour was found out.

$$R_t = \frac{u_{t-r}^*}{u_{t-s}^*} = \left[\frac{1}{(1 - m\sigma\lambda)(1 + m\beta\lambda)} \right]^{1/2} \quad (3)$$

187 where, β is the ratio of the drag coefficient C_R of an isolated roughness
 188 element on the surface to the drag coefficient C_S of the substrate surface
 189 itself. Values for C_R are approximately 0.25 for cylinders (Taylor, 1988)
 190 and values for C_S have been reported to be approximately 0.0025 (Crawley
 191 and Nickling, 2003). σ is the basal-to-frontal area ratio of the roughness

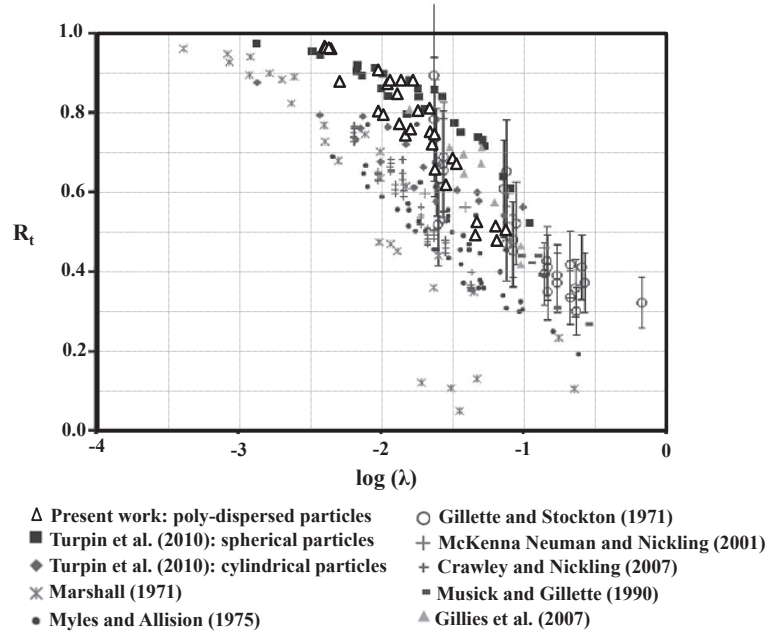


Figure 2: Comparison of the friction velocity ratio R_t from various sources (Marshall (1971), Lyles and Allison (1975), Gillette and Stockton (1989), Musick and Gillette (1990), McKenna Neuman and Nickling (1995), Crawley and Nickling (2003), Gillies et al. (2007), Turpin et al. (2010)) with those from the numerical simulations presented in this paper. Error bars 20% represent the accuracy of the Gillette and Stockton (1989) data.

elements, and $m < 1$ is a parameter accounting for differences between the average substrate surface stress and the maximum stress on the surface at any point (see Turpin et al. (2010) for more details).

A comparison was performed between the numerical data of Turpin et al. (2010) and those presently obtained with the above mentioned numerical model *Code_Saturne* for the same mono-dispersed configurations. These extra simulations make sure that the code and numerical model used in the present work give the same results as previously taken into consideration to construct the formulation. Table 2 presents the three mono-dispersed configurations simulated with *Code_Saturne* and previously with Fluent in Turpin et al. (2010). A good agreement was found out for the values of $1 - R_{fric}$ calculated with the two codes. The three cases were chosen to represent very different particles distributions. These results are plotted in Figure 3(a) by three extra couple of points, green and red.

Two additional simulations were performed (beyond the tests presented in Table 3) to validate the representativeness of the computational domain: for the same values of TDC and $(S_{frontal}/S_{floor})$, the geometry parameters were changed (particle heights, diameters and distribution). The values of $1 - R_{fric}$ computed with the numerical results show a maximum difference of 5.2% between the tested cases. This low difference validates the domain dimensions and we may consider that it is well representative of the repeatability found in nature.

Table 2: Comparison of mono-dispersed configurations: present numerical simulations with *Code_Saturne* vs (Turpin et al., 2010) numerical simulations with Fluent

Test	N_p	b [mm]	h [mm]	TDC	$1 - R_{fric}$ <i>Code_Saturne</i>	$1 - R_{fric}$ Fluent
A	14	1.830	0.600	4.06	0.163	0.160
B	42	1.960	0.800	13.98	0.379	0.374
C	14	0.870	0.100	0.89	0.002	0.000

2.2. Tested configurations

Several configurations of poly-dispersed particles were carried out and they are listed in Table 3. The parameters that define each test are:

- range of particle diameters (b),
- mean diameter (\bar{b}),
- range of particle heights (h_{NEP} as a percentage of \bar{b}),
- mean height ($\overline{h_{NEP}}$),
- number of particles (N_p),
- cover rate $TDC = (\sum S_{floor})/S$,
- $P_{fric} = TDC \cdot (S_{frontal}/S_{floor})$,
- $1 - R_{fric}$ directly assessed from numerical computations of the mean friction velocity on the erodible surface (u_r^*),
- $1 - R_{fric}$ calculated with the formulation proposed by Turpin et al. (2010) (Equation 2).

Table 3: Tested configurations

Test	b [mm]	\bar{b} [mm]	h [% (\bar{b})]	\bar{h} [mm]	N_p	TDC	P_{fric}^*	$u_r^*[m/s]$	$1 - R_{fric}^{**}$	$1 - R_{fric}^{***}$
1	0.5-1.0	0.75	20 - 50	0.263	20	0.97	0.396	0.3415	0.049	0.032
2	0.5-1.5	1.00	10 - 30	0.200	18	2.01	0.536	0.3419	0.048	0.039
3	0.5-1.0	0.75	20 - 50	0.263	23	1.38	0.636	0.3379	0.059	0.053
4	0.5-1.0	0.75	20 - 50	0.263	43	2.05	0.927	0.3302	0.081	0.079
5	1.5-2.0	1.75	10 - 30	0.350	15	3.88	1.149	0.3237	0.099	0.090
6	0.7-1.7	1.20	10 - 40	0.300	34	4.13	1.206	0.3266	0.091	0.093
7	0.5-1.0	0.75	20 - 50	0.263	52	2.58	1.226	0.3239	0.098	0.100
8	1.0-1.5	1.25	10 - 30	0.250	42	5.87	1.426	0.3183	0.114	0.109
9	2.5-3.5	3.00	10 - 20	0.450	11	8.44	1.611	0.3099	0.137	0.118
10	0.5-1.5	1.00	20 - 50	0.350	46	4.16	1.942	0.3026	0.157	0.168
11	1.0-3.0	2.00	20 - 45	0.650	11	4.64	2.088	0.2984	0.169	0.169
12	0.7-1.7	1.20	10 - 40	0.300	54	6.57	2.111	0.3419	0.154	0.160
13	1.0-1.5	1.25	10 - 45	0.333	51	6.67	2.163	0.3012	0.161	0.165
14	1.0-2.0	1.50	40 - 50	0.675	20	4.32	2.492	0.2916	0.188	0.196
15	1.0-3.0	2.00	25 - 45	0.700	14	5.98	2.542	0.2909	0.190	0.190
16	1.5-2.0	1.75	05 - 50	0.481	25	8.51	2.793	0.2910	0.190	0.193
17	0.7-1.7	1.20	20 - 50	0.420	56	7.28	3.279	0.2809	0.218	0.222
18	1.0-3.0	2.00	20 - 40	0.600	25	8.14	3.379	0.2822	0.214	0.225
19	2.0-2.5	2.25	40 - 50	0.750	15	6.50	3.678	0.2724	0.242	0.250
20	1.0-3.0	2.00	10 - 50	0.600	34	11.67	3.945	0.2776	0.227	0.239
21	1.0-3.0	2.00	45 - 50	0.950	22	7.28	4.404	0.2534	0.294	0.282
22	0.9-2.9	1.90	20 - 50	0.665	34	11.72	5.114	0.2567	0.285	0.295
23	0.5-2.5	1.50	45 - 50	0.713	54	11.03	6.706	0.2394	0.333	0.365
24	1.3-1.8	1.50	45 - 50	0.713	53	10.16	6.116	0.2336	0.350	0.345
25	1.8-2.0	1.88	45 - 50	0.891	40	12.45	7.532	0.2285	0.364	0.392

* $P_{fric} = S_{frontal}/S_{floor} \cdot TDC$

** = Present numerical simulations

*** = Turpin et al. (2010)

Smooth friction velocity - $u_s^* = 0.3591$ m/s

228 To define a test case, a random sampling of diameters (among the pos-
229 sible values established in the range) and height values of each particle is
230 done. A cover rate for the test is also specified. A routine developed for the
231 construction of numerical cases stops the sampling of particles as the defined
232 cover rate value is reached.

233 Since the particles do not present the same diameter and height we must
234 choose a mean value of $S_{frontal}/S_{floor}$ to be representative of this distribution
235 and to be replaced in the formulation of Turpin et al. (2010) (Equation 2).
236 The mean value of the parameter $S_{frontal}/S_{floor}$ may be calculated in two
237 ways: $\overline{S_{frontal}/S_{floor}}$ or $S_{frontal}/S_{floor}$. A maximum difference of 5% was
238 found out among the overall tested cases. Finally, the second approach was
239 chosen: $\overline{S_{frontal}/S_{floor}}$. Table 4 details the sampling for a given configuration
240 (test 11). The accumulation of cover rate after each random sample, the
241 dimensions and the computed values of $S_{frontal}$ and S_{floor} are presented.

Table 4: Summary of particles of Test 11 with $\bar{b}=2.00, \bar{h}_{NPE}=0.650$ and $P_{fric} = 2.088$

Element	b [mm]	h [mm]	$S_{frontal}$	S_{floor}	$S_{frontal}/S_{floor}$	Accumulated TDC
1	1.14	0.39	0.45	1.02	0.44	0.11
2	1.86	0.83	1.54	2.72	0.57	0.42
3	2.39	0.91	2.18	4.47	0.49	0.91
4	2.71	0.66	1.78	5.75	0.31	1.55
5	2.74	1.05	2.88	5.90	0.49	2.21
6	1.17	0.42	0.49	1.08	0.46	2.33
7	2.68	1.16	3.12	5.65	0.55	2.96
8	2.43	0.98	2.38	4.65	0.51	3.47
9	2.56	0.76	1.93	5.13	0.38	4.04
10	2.04	0.65	1.33	3.28	0.41	4.41
11	1.65	0.44	0.73	2.15	0.34	4.64

$$\overline{S_{frontal}/S_{floor}} = 0.45$$

$$\text{TDC} = 4.64 \%$$

$$1 - R_{fric} = A \cdot (\text{TDC})^M \cdot (S_{frontal}/S_{floor})^N = 0.123(4.64^{0.613})(0.45^{0.77}) = 0.169$$

242 3. Results and discussions

243 The results section is divided in two parts. Firstly, the discussions concern
244 the comparisons between numerical results of previous (Turpin et al., 2010)
245 and present works to test the relevance of Equation 2 using poly-dispersed
246 particles. The second part analyses the flow characteristics over the flat
247 bed of poly-dispersed particles: distribution of wall shear stress, fluid flow
248 patterns surrounding the various particles and roughness wind velocity profile
249 for smooth and rough simulations.

250 3.1. Analysis of the validity of mono-dispersed formulation for poly-dispersed 251 configurations

252 The main purpose of this section is the evaluation of the mathematical for-
253 mulation initially proposed for mono-dispersed particles (Equation 2). The
254 evaluation will be carried out by a comparison between the values calculated
255 with Equation 2 and the results of numerical simulations of poly-dispersed
256 configurations done for this work (cf. Table 3). The aim is to check whether
257 the same representation in the poly-dispersed cases can be used.

258 Figure 3 presents two plots: Figure 3(a) shows the evolution of $1 - R_{fric}$
259 versus the parameter $P_{fric} = \text{TDC} \cdot (S_{frontal}/S_{floor})$ computed by the two ap-
260 proaches mentioned above and Figure 3(b) shows the correlation between
261 these values of $1 - R_{fric}$.

262 The formulation is, as shows the plot, well-founded enough to represent
263 a wide range of particle diameters and heights distribution. Figure 3 shows
264 a good agreement between the formulation and the numerical results when

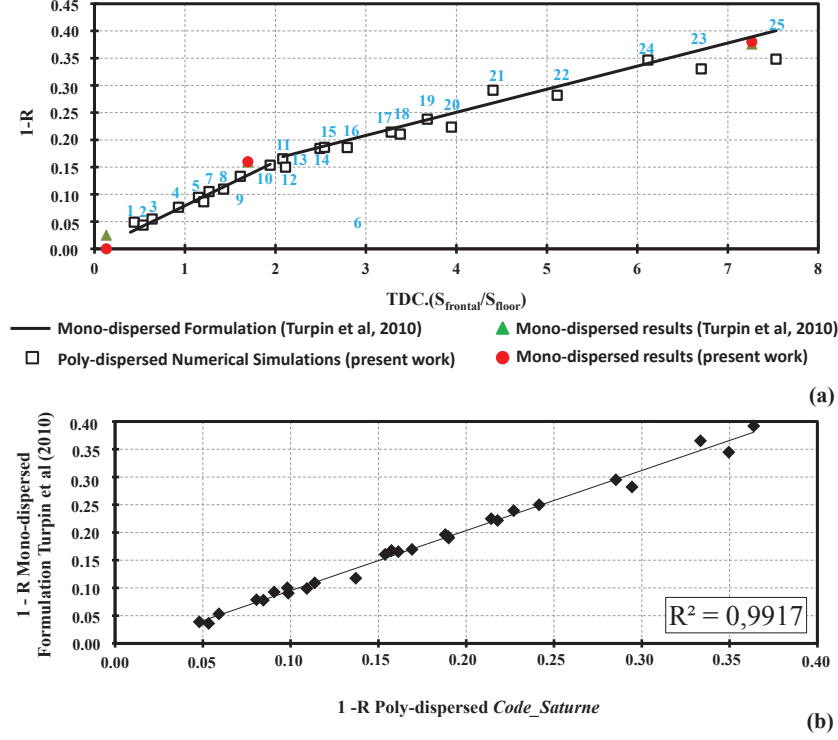


Figure 3: Parameter $1-R_{fric}$: (a) $1-R_{fric}$ calculated by the present numerical simulations and $1-R_{fric}$ calculated with the formulation proposed by Turpin et al. (2010) and (b) correlation between $1-R_{fric}$ compared with the formulation of Turpin et al. (2010) and with the results of the numerical simulations R is the value of the correlation coefficient

applied to poly-dispersed particles, Figure 3(a), with a high correlation $R^2 = 0.9917$ (Figure 3(b)). The break in the slope is observed in the same way for the poly-dispersed numerical simulation results (Figure 3(a)).

3.2. Analysis of fluid flow over roughness elements

The second part of this section presents a focus on the fluid flow characteristics for various cases. Top and three-dimensional visualizations illustrate the distribution of wall shear stress over the erodible surface surrounding the roughness elements. Also, the effects of the roughness elements on the mean velocity profile are analysed comparing the velocity profile for various roughness configurations with the one over a smooth wall. The discussions

275 carried out in this section concern the fluid flow features observed around
276 the different emerging forms of the non-erodible particles.

277 3.2.1. Top visualization of the shear stress partitioning over the erodible sur- 278 face

279 Figure 4 presents for four tested configurations a top view of the wall
280 shear stress distribution. The cases were represented with the same scale of
281 values. The values of wall shear stress are normalized by the value computed
282 in the smooth case ($\tau_{ref} = 0.158Pa$).

283 Figure 4(a) presents the configuration with the smallest mean diameter
284 (Test 13 - $\bar{b}_{13}=1.25$ mm) among the tests shown in Figure 4. The range
285 of diameters is also small (between 1.0 and 1.5 mm) which means a test
286 close to the mono-dispersed distribution. The number of particles ($N_b=51$)
287 is among the most elevated of the overall tested configurations and the cover
288 rate reaches almost 7%. The range of particle heights is important (between
289 10 and 45% of \bar{b}). However, as the mean diameter is small, this configuration
290 does not present any high emerging particles. The most part of the surface
291 presents a normalized wall shear stress values (τ/τ_{ref}) of about 0.800. The
292 highest wall friction values are found on the detachment points of the most
293 emerged particles. Test 13 presents only very small zones with the normalized
294 wall shear stress around 1.700. Moreover, the arrangement of the roughness
295 elements in this configuration is characterized by: small diameters, large
296 number and magnitude of gaps between the elements and free zones on the
297 erodible surface. Accordingly, the known effects of wakes on the erodible
298 surface (diminution of the overall erosion) are reduced for this configuration.

299 Figure 4(b) represents Test 15. This configuration has been chosen to be
300 compared with both Tests 13 (Figure 4(a)) and 16 (Figure 4(c)). Firstly, it
301 can be noticed that Tests 13 and 15 present about same cover rate values
302 (6.67% and 5.98%, cf. Table 3). However, the parameter P_{fric} is higher for
303 Test 15 which induces an augmentation in the value of $1 - R_{fric}$ (from 0.161
304 for the Test 13 to 0.190 for the Test 15). Also, it shows a slight diminution
305 of the mean rough friction velocity (from 0.3012 to 0.2909).

306 In Test 15, although observing larger wake zones downstream particles of
307 greater diameters (vs. Test 13), higher maximum values of the normalized
308 wall shear stress are reached. The wakes of the larger particles (high diameter
309 values) have normally the main impact on the reduction of the overall erosion.
310 However in this case, some of these larger particles are located in the wake of
311 upstream particles (in the lower left of Figure 4(b)) and have therefore weaker

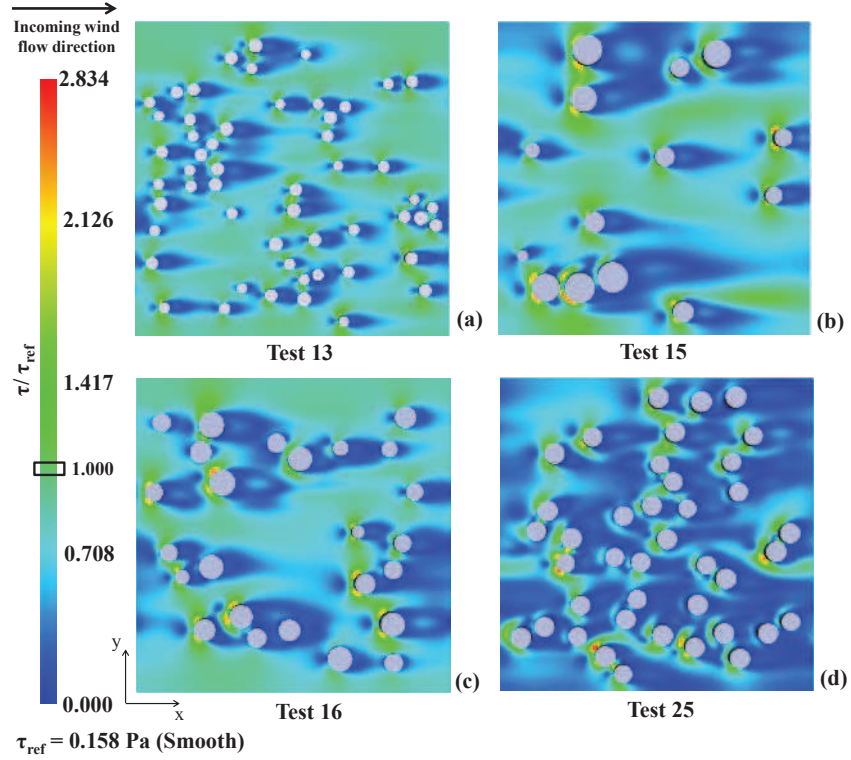


Figure 4: Distribution of non-dimensional wall shear stress over the erodible surface surrounding the roughness elements: (a) Test 13, (b) Test 15, (c) Test 16 and (d) Test 25

reducing impacts. On the other hand, particles positioned transversely to the flow direction (upper left of Figure 4(b)) produce a very large area of protection inducing a reduced wall friction.

Test 16 in Figure 4(c) presents a mean rough friction velocity very close to Test 15 (0.2910 and 0.2909, respectively). But, the ranges of diameter and height as well as the cover rate are quite different. This comparison is then interesting to show the influence of each parameter on the modifications of the friction velocity on the erodible surface. Test 16 has a higher cover rate, normally resulting in a reduction of the mean friction velocity. On the other hand, Test 16 presents more elevated emerging particles which lead to higher zones with normalized wall shear stress close to the maximum. In addition, Test 15 with a smaller cover rate, presents larger particles than Test 16 which possibly increases wake zones and reduces the mean friction velocity.

325 Finally, Figure 4(d) shows a high agglomeration of non-erodible particles
 326 (Test 25). The most part of the erodible surface shows a normalized shear
 327 stress lower than 0.250. The cover rate is the highest (12.45 %) among the
 328 overall tested configurations. Furthermore, due to the presence of high parti-
 329 cles, the agglomeration of wakes has more influence on the overall distribution
 330 of wall shear stress.

331 Lee and Soliman (1977) have classified the flow over roughness elements
 332 with the values of the cover rate. Two regimes have been identified: isolated
 333 roughness flow ($TDC < 8$) and wake interference flow ($8 < TDC < 44$).
 334 Based on these definitions, Tests 13 and 15, previously presented in Figure 4,
 335 represent two cases of isolated roughness flow. Tests 16 and 25 belong to the
 336 wake interference flow regime. But our work show that we cannot conclude
 337 of a direct link between the flow regime and the erosion potential of a bed of
 338 particles.

339 Indeed, it has been shown previously, for mono-dispersed configurations
 340 (Turpin et al., 2010), that the increase of roughness proportion, i.e., the in-
 341 crease of the parameter P_{fric} causes the decrease of the mean friction velocity.
 342 Our study confirmed that statement for poly-dispersed configurations. Nev-
 343 ertheless, this conclusion is not true for the cover rate (TDC) itself as other
 344 geometry parameters also influence the final value of the mean friction ve-
 345 locity. For instance, Test 15 which cover rate is 5.98%, lower than the one
 346 of Test 13, presents a slightly lower mean friction velocity. However, Test 15
 347 presents a mean particle diameter of about twice as large as the one of Test
 348 13 which causes the augmentation of the protection zones and consequently
 349 the reduction of the mean friction velocity.

350 3.2.2. *Three-dimensional visualization of fluid flow over roughness elements*

351 Three-dimensional visualizations are presented in Figure 5. The differ-
 352 ences observed in the roughness element dimensions may explain the impor-
 353 tant differences in wall shear stress results. Figure 5(a), presenting Test 9,
 354 contains particles with very low heights, but with great diameters. It means,
 355 a low value of the parameter $(S_{frontal}/S_{floor}) = 0.190$ (cf. Table 3). The
 356 highlighted region a-1 shows the detail of the wall shear stress distribution
 357 surrounding a particle. The normalized shear stress around this particle is
 358 not greater than 2.000. Even the particles which are not placed in the wake of
 359 other elements do not present high levels of wall shear stress. Despite the low
 360 level of shear stress computed around each single particle, it can be noticed
 361 that for a significant extended area of the underlying erodible surface the

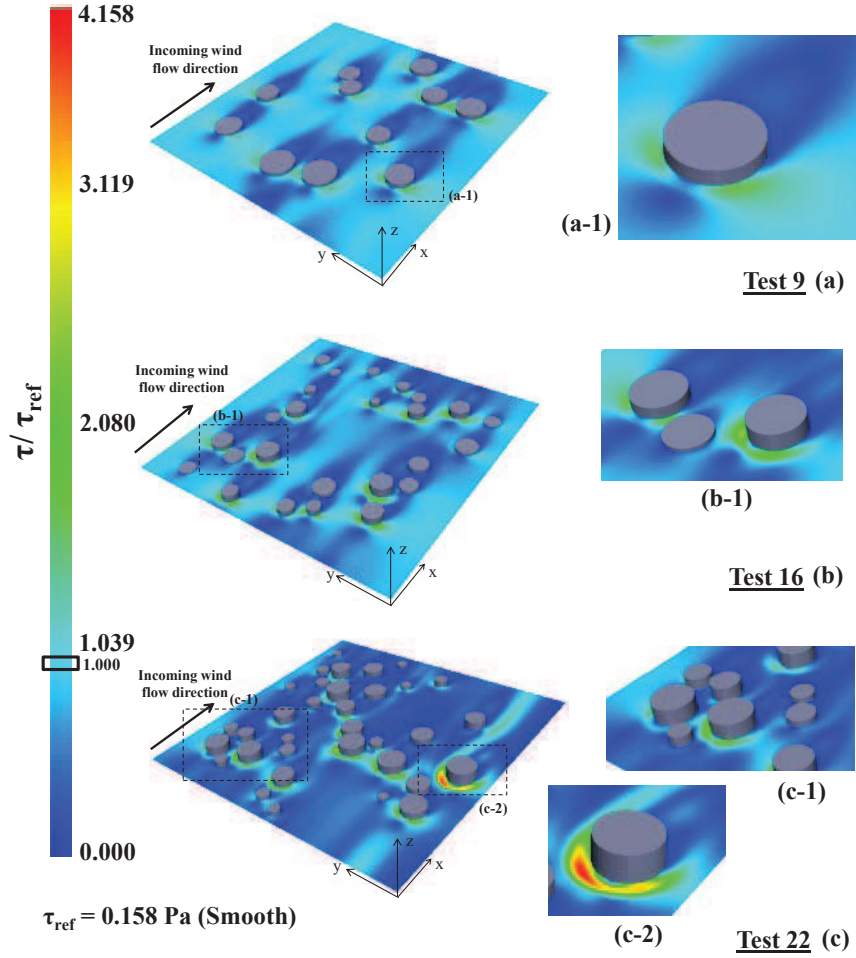


Figure 5: Three-dimensional view for three tested cases - distribution of non-dimensional wall shear stress with focus on specific roughness elements: (a) Test 9, (b) Test 16 and (c) Test 22

mean normalized wall shear stress is greater than 1.000 which means erosion levels higher than the smooth case.

Test 16 in Figure 5(b) shows larger wake zones compared to Test 9 for some particles. Assisted by the highlighted region b-1 one can identify the variability of the influence on the shear stress caused by the roughness height. These three particles have almost the same diameter. The level of the normalized shear stress on the wall surrounding each particle increases with the

369 increase in height.

370 The distribution of Test 16 has an overall mean height much higher than
371 Test 9. This causes an increase of the parameter ($S_{frontal}/S_{floor}$). By apply-
372 ing Equation 2 it leads to a higher value of $1 - R_{fric}$ for a same cover rate,
373 which is verified in the simulations. Concerning the shear stress distribution,
374 particles with larger diameters exhibit an expanded region over them with
375 an increase in shear stress. Therefore, one can observe higher mean friction
376 velocities for Test 16.

377 For Test 22 (Figure 5(c)), the wake zones are the largest. Furthermore,
378 two highlighted regions are noticed. Region c-1, shows an agglomeration of
379 roughness elements and the formation of a high wake with the lowest levels of
380 the normalized wall shear stress. Region c-2, exhibits the pattern found out
381 over a highly emerged particle. The effects of a main vortex formed around
382 the highlighted particle is noticed over the entire represented domain.

383 Figures 6(a), 6(b) and 6(c), focused on Tests 9 and 22, present, respec-
384 tively, streamlines at a XZ plane, streamwise component of the wall shear
385 stress (τ_{xz}) and plot of the evolution of streamwise wall shear stress. In Test
386 9 a smaller roughness element shows low friction levels surrounding; there
387 are no complex structures that could affect the ground surface (see the small
388 peak upstream the element in Figure 6(c)). On the other hand, in Test 22
389 the high area of the windward wall of the emerged particle promotes the
390 formation of vortices (notably towards the left) that impact the ground re-
391 gion (Region B) and increase the velocity gradient and consequently the wall
392 shear stress. Moreover, Figure 6(b) displays the distribution of the longitudi-
393 nal component of the wall shear stress on the underlying surface surrounding
394 the roughness elements. The values were normalized by the value computed
395 for the smooth case (τ_{ref}). Near the windward wall of the highest particle
396 (Region B) peaks of negative longitudinal wall shear stress values are ob-
397 served ($\tau_{xz}/\tau_{ref} = -3.35$ in Figure 6(c)). Region B is indeed associated to
398 negative values of X-velocity in Figure 6(a). The roughness element high-
399 lighted in Test 9 shows a maximum negative value of $\tau_{xz}/\tau_{ref} = -0.50$, in
400 Region A, which is very smaller than the value noticed in Region B.

401 The three-dimensional visualization allowed more local analysis of the
402 turbulent fluid flow surrounding a roughness element with variability in their
403 aspect ratios. The analysis have shown that the fluid flow pass over the
404 low emerged particles without main influence on the ground wall while high
405 emerged particles present strong shear stress levels on the windward wall with
406 the creation of a main vortex which causes elevated friction on the ground

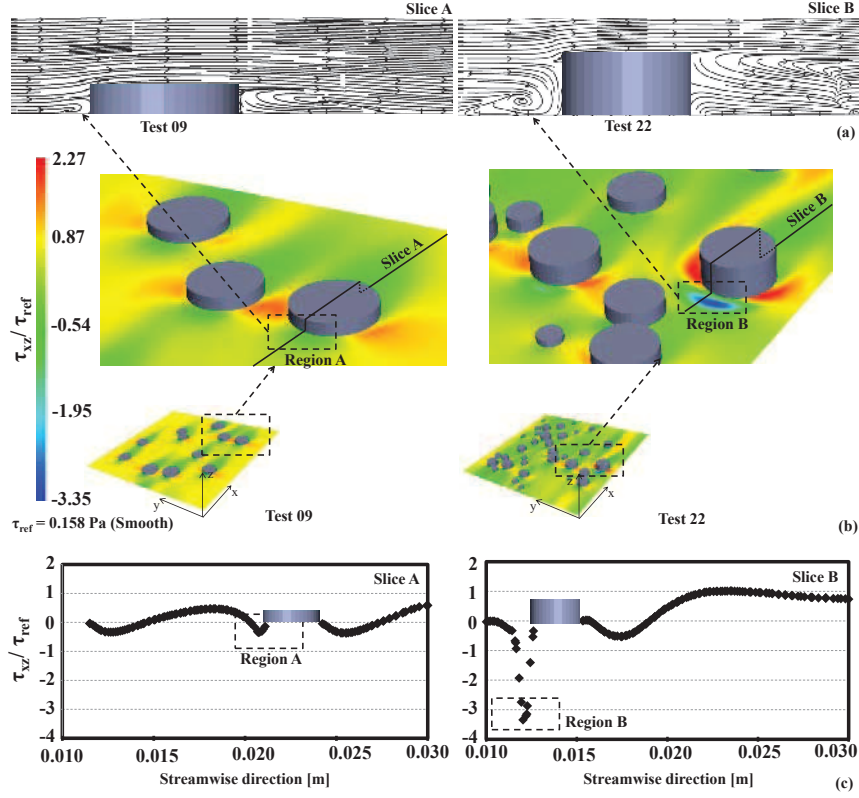


Figure 6: Local fluid flow modified due to the roughness elements for Test 9 and Test 22: (a) streamlines plotted on a XZ plane, (b) contours of the streamwise component of the wall shear stress and (c) evolution of the streamwise component of the wall shear stress

407 wall. This analysis is useful to check the discussions of Figure 4 mainly
 408 concerning the influence of the emerging height.

409 3.2.3. Analysis of the vertical velocity profile for roughness elements im- 410 mersed in a turbulent boundary layer

411 The numerical simulations of poly-dispersed non-erodible particles deal
 412 with the study of a turbulent boundary layer in the presence of roughness
 413 elements. Figure 7 plots mean velocity profiles (spanwise averaged) for Tests
 414 5, 15 and 22 (see Table 3) illustrating different cover rates and roughness
 415 proportions. The profiles of $u^+ = u/u^*$ and $z^+ = z.u^*/\nu$ (respectively, lon-
 416 gitudinal velocity and vertical coordinate both calculated in wall units) are
 417 plotted. u^* is the mean shear velocity over the erodible and roughness ele-

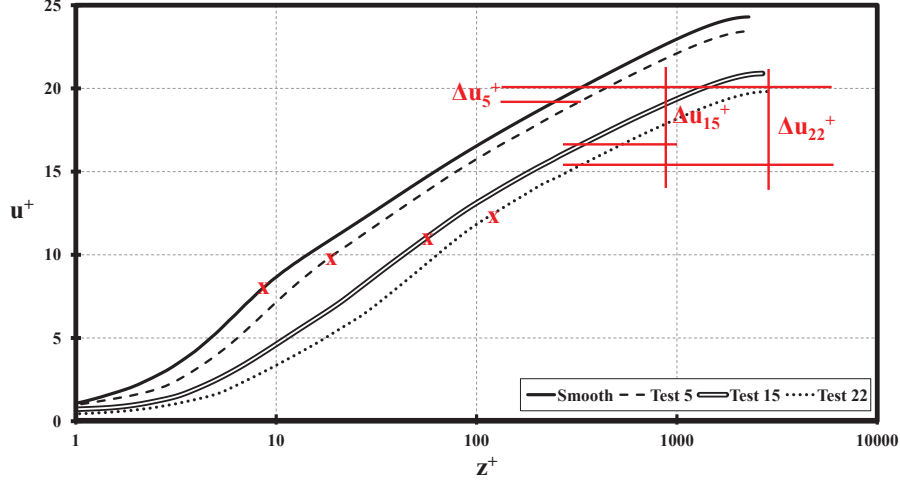


Figure 7: Vertical velocity profiles in wall units: comparison between the smooth configuration and different configurations of roughness elements

ments surfaces for each test. The profiles are extracted at a same streamwise coordinate ($x = 0.0299m$) close to the periodic boundary ($x = 0.03m$).

The roughness height in wall units is defined by: $h_S^+ = h_S u^* / \nu$. For the smallest value of the cover rate (3.88 %, Test 5) and mean roughness height equal to 0.350 mm ($h_S^+ = 8.29$), the profile is the most similar to that over a smooth surface. Test 15 and 22 present respectively a cover rate of 5.98% and 11.72% and mean roughness height of approximately 0.700 mm ($h_S^+ = 19.2$) and 0.665 mm ($h_S^+ = 18.97$).

For those configurations, the profiles are gradually distant ($\Delta u_5^+ < \Delta u_{15}^+ < \Delta u_{22}^+$). The red marks in Figure 7 are a visual approach to point out the beginning of the logarithmic zone of the velocity profile built. These marks also indicate the height of the turbulent boundary layer over an array of roughness elements. Thus, Figure 7 illustrates that in comparisons to the smooth pattern the effect of the roughness elements change is to the vertical profile (slope changes close to the wall) and also the height of the viscous layer.

These numerical simulations results agree with the experimental work carried out by Clauser (1954). This reference work has defined the turbulent boundary layer in which roughness elements are immersed in the logarithmic zone of the velocity profile, the profiles must approach straight lines of

438 slope close to 5.6 (Clauser, 1954) which can be noticed in our tested cases.
 439 Moreover, it can be seen that, as the cover rate or roughness elements height
 440 increases there is a different transition between the logarithmic and the linear
 441 profile. As it was also remarked by Turpin et al. (2010) for their simulations,
 442 a distinct break in slope is observed close to the wall ($z^+ < 5$).

443 4. Conclusions

444 The main objective of this paper was the analysis of a mathematical for-
 445 mulation previously proposed in the open literature for the quantification of
 446 the mean friction velocity evolution of a domain partially covered by rough-
 447 ness elements. These roughness elements represent non-erodible particles
 448 over an erodible surface. The above mentioned formulation (detailed in the
 449 work of Turpin et al. (2010)) has been defined after some results of numeri-
 450 cal simulations validated with experimental works. However, the formulation
 451 was only representative of a bed of particles with equal diameters and heights,
 452 i.e., mono-dispersed distribution. On industrial sites, this condition is very
 453 rarely encountered.

454 Thus, several numerical simulations were carried out (with an open-source
 455 CFD code) to check the application of this formulation to poly-dispersed
 456 roughness elements (i. e., with different diameters and heights). The com-
 457 parison has shown a very good agreement. Some validations were addition-
 458 ally performed: three mono-dispersed configurations to compare the current
 459 simulations and those previously carried out, results of friction velocity ratio
 460 compared with various experimental and field simulations and modifications
 461 of the particle distribution to validate the domain dimensions. All compar-
 462 isons and validations have presented good agreement.

463 A finer analysis of the numerical simulations results has shown that:

- 464 • the cover rate and the surface ratio ($S_{frontal}/S_{floor}$) are still (for a poly-
 465 dispersed distribution) the main parameters defining the evolution of
 466 the mean friction velocity over the erodible surface. The increase of
 467 their product (i.e., the parameter P_{fric}) leads to the diminution of the
 468 mean friction velocity,
- 469 • the mean particle diameter presents a high influence on the erosion
 470 of the ground surface due to the formation of more extended wake
 471 zones downstream the roughness elements inducing the reduction of
 472 the erosion,

- the mean particle height presents a high influence on the erosion of the ground surface due to the vortices potentially highly eroding the region around the roughness elements and

Finally, the present results state that the original formulation given by Turpin et al. (2010) is useful, without any modification in its form and coefficients, for a wide range of particles, with a random distribution and a large spectra of dimensions. The application on fugitive dust emissions is then more refined due to the poly-dispersed numerical simulations carried out.

5. Acknowledgements

This work was carried out with the financial support of EDF R&D.

References

- Al-Awadhi JM, Willetts BB. 1999. Sand transport and deposition within arrays of non-erodible cylindrical elements. *Earth Surface Processes and Landforms* 24: 423-435.
- Archambeau F, Mchitoua N, Sakiz M. 2004. Code_Saturne: a nite volume code for the computation of turbulent incompressible flows industrial applications. *International Journal of Finite Volumes*, 1(1).
- Badr T. 2007. Quantification des émissions atmosphériques diffuses produites par érosion éolienne. Thèse de Doctorat, Université de Valenciennes et du Hainaut Cambrésis, Département Énergétique Industrielle, Ecole de Mines de Douai.
- Badr T, Harion J-L. 2007. Effect of aggregate storage piles configuration on dust emissions. *Atmospheric Environment* 41: 360-368.
- Benkhaldoun F, Sari S, Seaid M. 2012. A flux-limiter method for dam-break flows over erodible sediment beds. *Applied Mathematical Modelling* 36: 4847-4861.
- Carney SK, Bledsoe BP, Gessler D. 2005. Representing the bed roughness of coarse-grained streams in computational fluid dynamics. *Earth Surface Processes and Landforms* 31: 736-749.

- 502 Castel IY. 2006. A simulation model of wind erosion and sedimentation as
503 a basis for management of a drift sand area in The Netherlands. *Earth*
504 *Surface Processes and Landforms* 32: 602-611.
- 505 Clauser FH. 1954. The turbulent boundary layer. Johns Hopkins University,
506 Baltimore. Maryland.
- 507 Crawley DM, Nickling WG. 2003. Drag partition for regularly arrayed rough
508 surfaces. *Boundary-Layer Meteorology* 107: 445-468.
- 509 Descamps I, Harion J-L, Baudoin B. 2005. Taking-off model of particles with
510 a wide size distribution. *Chemical Engineering and Processing* 44: 159-166.
- 511 Ferreira A., Lambert R., 2011. Numerical and wind tunnel modeling on the
512 windbreak effectiveness to control the aeolian erosion of conical stockpiles.
513 *Environmental Fluid Mechanics* 11: 61-76.
- 514 Foucaut J-M, Stanislas M. 1996. Take-off threshold velocity of solid particles
515 lying under a turbulent boundary layer. *Experiments in Fluids* 20: 377-382.
- 516 Furieri, B, Russeil S, Harion J-L, Turpin C, Santos J. 2012. Experimental sur-
517 face flow visualization and numerical investigation of flow structure around
518 an oblong stockpile. *Environmental Fluid Mechanics* 12 (5).
- 519 Guingo M, Minier J-P. 2008. A new model for the simulation of particle
520 resuspension by turbulent flows based on a stochastic description of wall
521 roughness and adhesion forces. *Journal of Aerosol Science* 39: 957-973.
- 522 Gillette D, Stockton P. 1989. The effect of nonerodible particles on wind
523 erosion of erodible surfaces. *J. of Geophysical Res.* 94: 12885-12893.
- 524 Gillies D, Nickling W, King K. 2007. Shear stress partitioning in large patches
525 of roughness in the atmospheric inertial sublayer. *Boundary Layer Meteoro-*
526 *logy* 122: 367-396.
- 527 Gimenez R, Leonard J, Duval Y, Richard G, Govers G. 2006. Effect of bed to-
528 pography on soil aggregates transport by rill flow. *Earth Surface Processes*
529 *and Landforms* 32: 602-611.
- 530 Jiang Y, Matsusaka S, Masuda H, Qian Y. 2008. Characterizing the effect
531 of substrate surface roughness on particle-wall interaction with the airflow
532 method. *Powder Technology* 186: 199-205.

- 533 King J, Nickling WG, Gillies JA. 2005. Representation of vegetation and
534 other nonerodible elements in aeolian shear stress partitioning models for
535 predicting transport threshold. *J. Geophys. Res.* 110, F04015.
- 536 Kurose R, Komori S. 2001. Turbulence structure over a particle roughness.
537 *International Journal of Multiphase Flow* 27: 673-683.
- 538 Lee BE, Soliman BF. 1977. An investigation of the forces on three dimen-
539 sional bluff bodies in rough wall turbulent boundary layers. *Journal of*
540 *Fluids Engineering* 23: 503-510.
- 541 Li L, Martz L, 1995. Aerodynamic dislodgement of multiple size grains over
542 time, *Sedimentology* 42: 683-694.
- 543 Lopez MV, Herrero JMD, Hevia GG, Gracia R, Buschiazzi DE. 2007. De-
544 termination of the wind-erodible fraction of soils using different method-
545 ologies. *Geoderma* 137: 407-411.
- 546 Marshall JK. 1971. Drag measurements in roughness arrays of varying density
547 and distribution. *Agricultural Meteorology* 8: 269-292.
- 548 Neuman C, Nickling W. 1995. Aeolian sediment flux decay: non-linear be-
549 haviour on developing deflation lag surfaces. *Earth Surface Processes and*
550 *Landforms* 20: 423-435.
- 551 Neuman C. 1998. Particle transport and adjustments of the boundary layer
552 over rough surfaces with an unrestricted, upwind supply of sediment. *Ge-*
553 *omorphology* 25: 1-17.
- 554 Neuman C, Boulton J, Sanderson S. 2009. Wind tunnel simulation of environ-
555 mental controls on fugitive dust emissions from mine tailings. *Atmospheric*
556 *Environment* 43: 520-529.
- 557 Orlandi P, Leonardi S. 2008. Direct numerical simulation of three-dimensional
558 turbulent rough channels: Parametrization and flow physics. *Journal of*
559 *Fluid Mechanics* 606: 399-415.
- 560 Raupach M, Gillette D, Leys J. 1993. The effect of roughness elements on
561 wind erosion threshold. *Journal of Geophysical Research* 98: 3023-3029.

- 562 Roney J, White B. 2006. Estimating fugitive dust emission rates using an
563 environmental boundary layer wind tunnel. *Atmospheric Environment* 40:
564 7668-7685.
- 565 Roney J, White B. 2010. Comparison of a two-dimensional numerical dust
566 transport model with experimental dust emissions from soil surfaces in a
567 wind tunnel. *Atmospheric Environment* 44: 512-522.
- 568 Schlichting H. 1968. *Boundary-Layer Theory*. (Seventh ed.) McGraw-Hill:
569 New York.
- 570 Shao Y, Yang Y. 2005. A scheme for drag partition over rough surfaces.
571 *Atmospheric Environment* 39: 7351-7361.
- 572 Sutton SLF, Neuman CM. 2008. Sediment entrainment to the lee of roughness
573 elements: Effects of vortical structures. *Journal of Geophysical Research*
574 113: F02S09.
- 575 Taylor PA. 1988. Turbulent wakes in atmospheric boundary layer. In *Flow
576 and Transport in the Natural Environment: Advances and Applications*.
577 Steffen WL, Denmead OT (eds.) Springer: Berlin. 270292.
- 578 Turpin C, Badr T, Harion J-L. 2010. Numerical modelling of aeolian erosion
579 over rough surfaces. *Earth Surface Processes and Landforms* 35: 1418-1429.
- 580 Turpin C, Harion J-L. 2010. Effect of the topography of an industrial site on
581 dust emissions from open storage yards. *Environmental Fluid Mechanics*
582 10: 677-690.
- 583 US EPA, 2006. *Miscellaneous Sources, Industrial Wind Ero-*
584 *sion, AP-42, 5th edn, vol I, Chap 13.2.5, November 2006.*
585 <http://www.epa.gov/ttn/chief/ap42/ch13/final/c13/final/c13s0205.pdf>
- 586 Webb N, Strong C. 2011. Soil erodibility dynamics and its representation for
587 wind erosion and dust emission models. *Aeolian Research* 3: 165-179.
- 588 Zobeck T, Sterk G. 2003. Measurement and data analysis methods for field-
589 scale wind erosion studies and model validation. *Earth Surface Processes
590 and Landforms* 28: 1163-1188.

3.3 Non-erodible particles effects on the methodology of dust emission quantification

Previous sections aimed the description of the influence of non-erodible particles on the aeolian erosion of storage piles of granular materials. For that objective, numerical and, mainly experimental works were performed. The results have given relevant conclusions about the wind erosion on the wall of an oblong stockpile containing erodible and non-erodible particles:

- reduction of the mean wall friction velocity on the erodible partition of a given surface in the presence of non-erodible particles,
- temporal decrease of the emitted mass flux,
- increase of the total emitted mass as it is reduced the amount of non-erodible particle in the mixing.

In such manner, the present investigation aims to use the experimental data presented in earlier sections to propose modifications in the USEPA mathematical methodology of dust emission quantification [75] (see section 1.4.1 for more details about references and utilization of the take-off velocity).

This model, as seen in section 1.4.1, is based on the definition of emission factors. The main relation is the definition of the erosion potential (P shown in Equation 3.1) recalled here:

$$P = 58(u^* - u_t^*)^2 + 25(u^* - u_t^*) \quad (3.1)$$

where,

$$u^* = 0.10u_{10}^+(u_s/u_r) \quad (3.2)$$

The original methodology, as suggests USEPA (2006) [75], specifies the time evolution of the emitted mass flux:

"Field testing of coal piles and other exposed materials using a portable wind tunnel has shown that particulate emission rates tend to decay rapidly (half-life of a few minutes) during an erosion event. In other words, these aggregate material surfaces are characterized by finite availability of erodible material (mass/area) referred to as the erosion potential. Any natural crusting of the surface binds the erodible material, thereby reducing the erosion potential."

The variable number of perturbations N (see section 1.4.1) is directly related to this observation. However, the erosion potential recalled in Equation 3.1 does not take into account this phenomena and the particle size distribution is not taken into account as a parameter of the model.

In this section, we will examine the results of measurements by analysing the emitted mass weighing for different configurations tested. The same experimental set-up presented in section 3.1.1 was used. Indeed, the mass balance (emitted mass of sand weighed before and after the experiments) has been performed for four mass percentages of non-erodible particles (%EP): 50%, 65%, 80% and 90%, i. e., total mass of non-erodible particles divided by the stockpile mass. Three values of free stream velocities were tested: 6, 7 and 8 m/s. All tested configurations were carried out for an isolated and perpendicular oriented stockpile. These data will be useful to plot the emitted mass versus the percentage of non-erodible particles. Additionally to the experimental data, the value of 100% of non-erodible data was also considered. For a stockpile presenting only non-erodible particles, the emitted mass is zero. It is worth to note that, the experimental data used in the propositions are based on a bimodal granulometry of sand.

At first, wind-tunnel experimental tests resulted in the values presented in Table 3.2. Figure 3.9 shows the results obtained by the wind-tunnel measurements for one wind velocity, 8 m/s. The emitted mass ($M_{balance}$ [g]) is represented as a function of the percentage of erodible particles (%EP = 1 - %NEP). Two additional informations have been added on this figure. On the one hand, the point %EP = 0 (%NEP = 100 - only non-erodible particles constitute the granular pile) correspond to an emitted mass equals to zero. On the other hand, the dashed line presents the value

of emission defined with the USEPA model for the same configuration. The wind exposure (u_s/u_r ratio) was produced by a numerical simulation corresponding in terms of geometry to an oblong, isolated and perpendicular oriented stockpile. The threshold friction velocity is a constant value dependent only of the material investigated. It is worth to note that, the threshold friction velocity value for sand was determined after wind-tunnel experiments [35] which is equal to 0.25 m/s.

Table 3.2: Mass balance for a perpendicular oriented stockpile and various percentage values of non-erodible particles

%EP	Mass Balance [g]		
	6 m/s	7 m/s	8 m/s
0	0.0	0.0	0.0
50	4.3	36.2	57.2
65	28.7	115.8	195.2
80	85.4	254.2	397.2
90	134.0	453.0	757.6

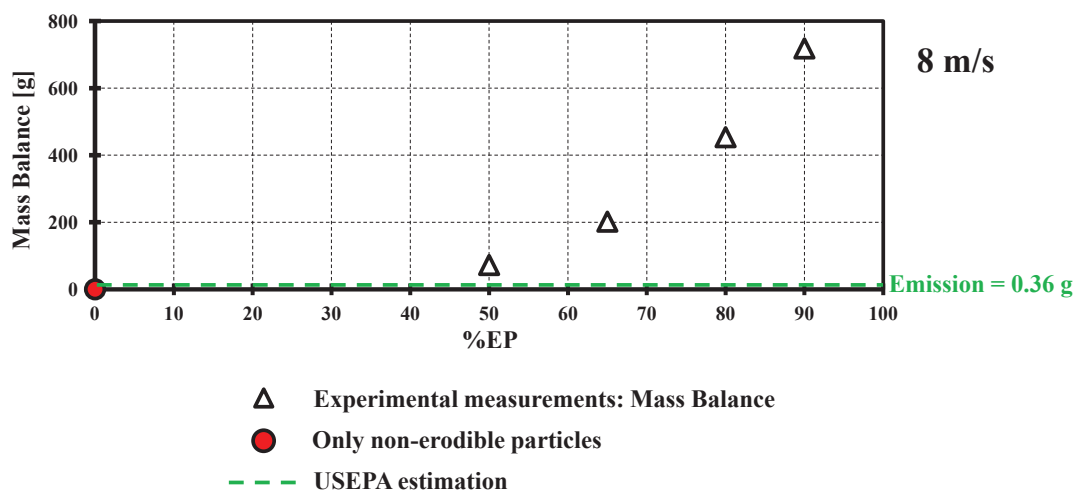


Figure 3.9: Results obtained by the wind-tunnel measurements for one wind velocity

The value obtained by the USEPA model is consistent with the measurements. It corresponds to relatively low value of %EP, corresponding to a proportion of non-erodible particles of the order of 85%, which is a commonly encountered configuration for coal or ore on industrial sites.

Figure 3.10 shows that the results can be fitted, as function of %EP, by a function like:

$$M_{balance} = a_1(\%EP)^{a_2} \quad (3.3)$$

In Equation 3.3, the emitted mass is presented as a function of the proportion of erodible particles. The two coefficients (a_1 and a_2) were defined by the least square method and the results are shown in Figure 3.11. The coefficient a_1 increases with the velocity and a_2 is the same for all tested velocities. Figure 3.10 shows plots of mass balance and percentage of non-erodible particles for the three tested velocities representing the data correlation shown in Equation 3.3. Equation 3.3 allows to predict the proportion of non-erodible particles for the emitted mass calculated by USEPA methodology. The estimated emitted mass of 0.36 g (shown in Figure 3.9) applied in Equation 3.3 using the coefficients presented in Figure 3.11 for 8 m/s and results in 88% of non-erodible particles, which agrees with the above mentioned proportion.

From these results, it seems possible to propose a modification of the erosion potential (Equation 3.1) by taking into account the influence of the parameter %EP. The proposition of modification presented in this thesis, is to substitute the two constants 58 and 25 by two functions such as that defined by Equation 3.4 :

$$P_{mod} = b_1(\%EP)^{b_2}(u^* - u_t^*)^2 + c_1(\%EP)^{c_2}(u^* - u_t^*) \quad (3.4)$$

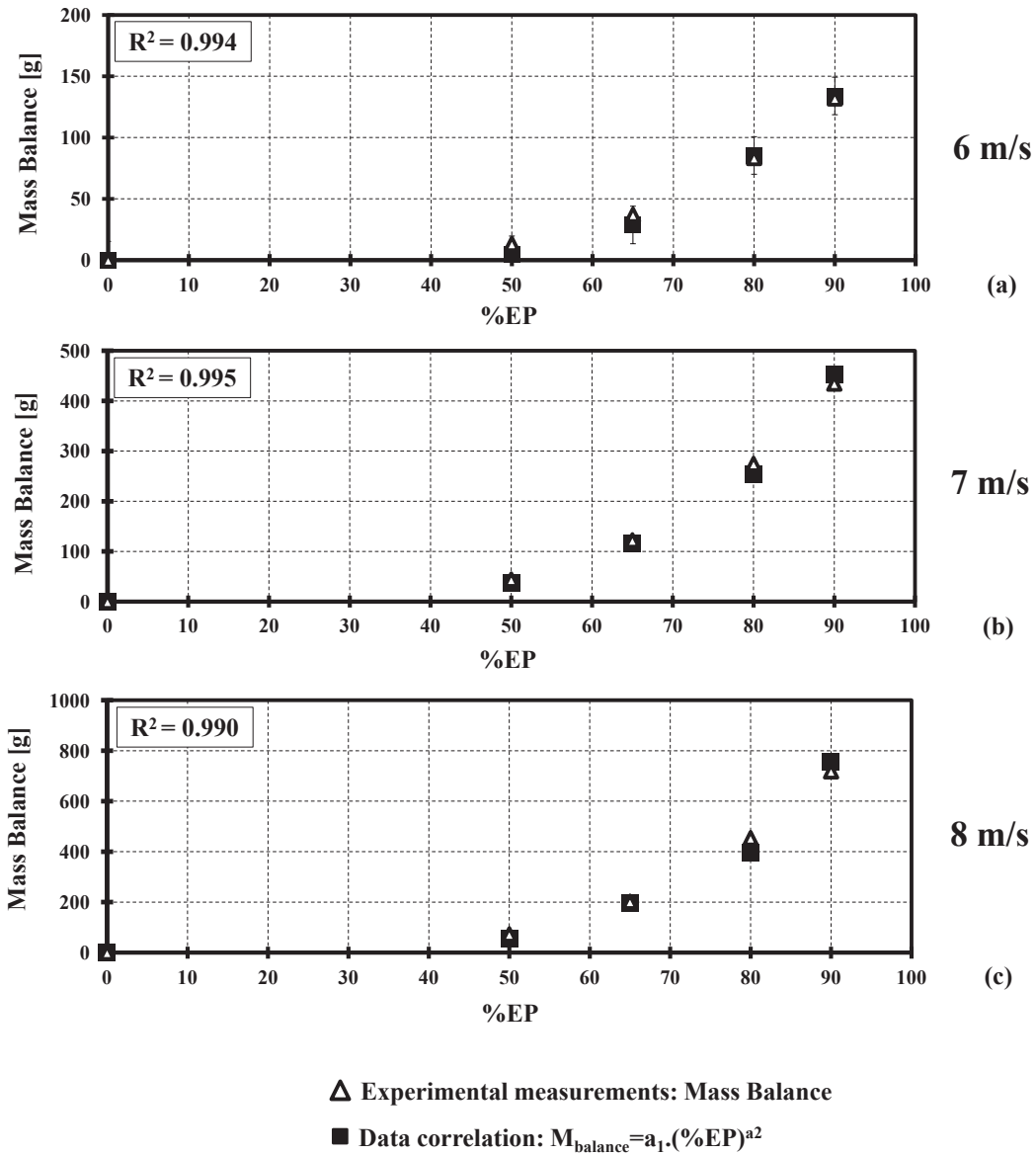


Figure 3.10: Plots of the correlation between emitted mass calculated in wind-tunnel and the values of $M_{balance}$ by the Equation 3.3

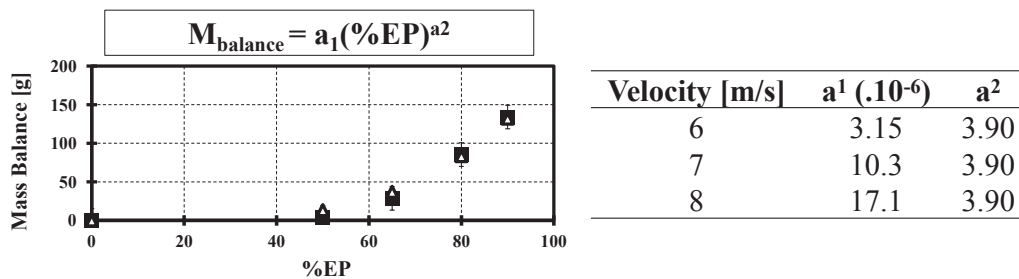


Figure 3.11: Steps of data management carried out to propose modifications in the USEPA methodology of diffuse dust quantification

The next aim is to find the best values of the coefficients b_1 , b_2 , c_1 and c_2 to correlate with the values of emitted mass quantified by Equation 3.3. Again, the least square method is applied to calculate these coefficients. The emitted mass is calculated, as previously for results presented on

Figure 3.10, by using the USEPA model, but with a erosion potential given by Equation 3.4.

The values found for the coefficients are: $b_1 = 0.0047$, $b_2 = 3.90$, $c_1 = -0.0007$ and $c_2 = 3.90$. These values are valid for the three tested velocities. Figures 3.12a, 3.12b and 3.12c shown the plots comparing the calculations. An overall good agreement was found between the data for all tested velocities with only a difference for elevated cover rates in the cases where the wind velocity is equal to 6 and 8 m/s.

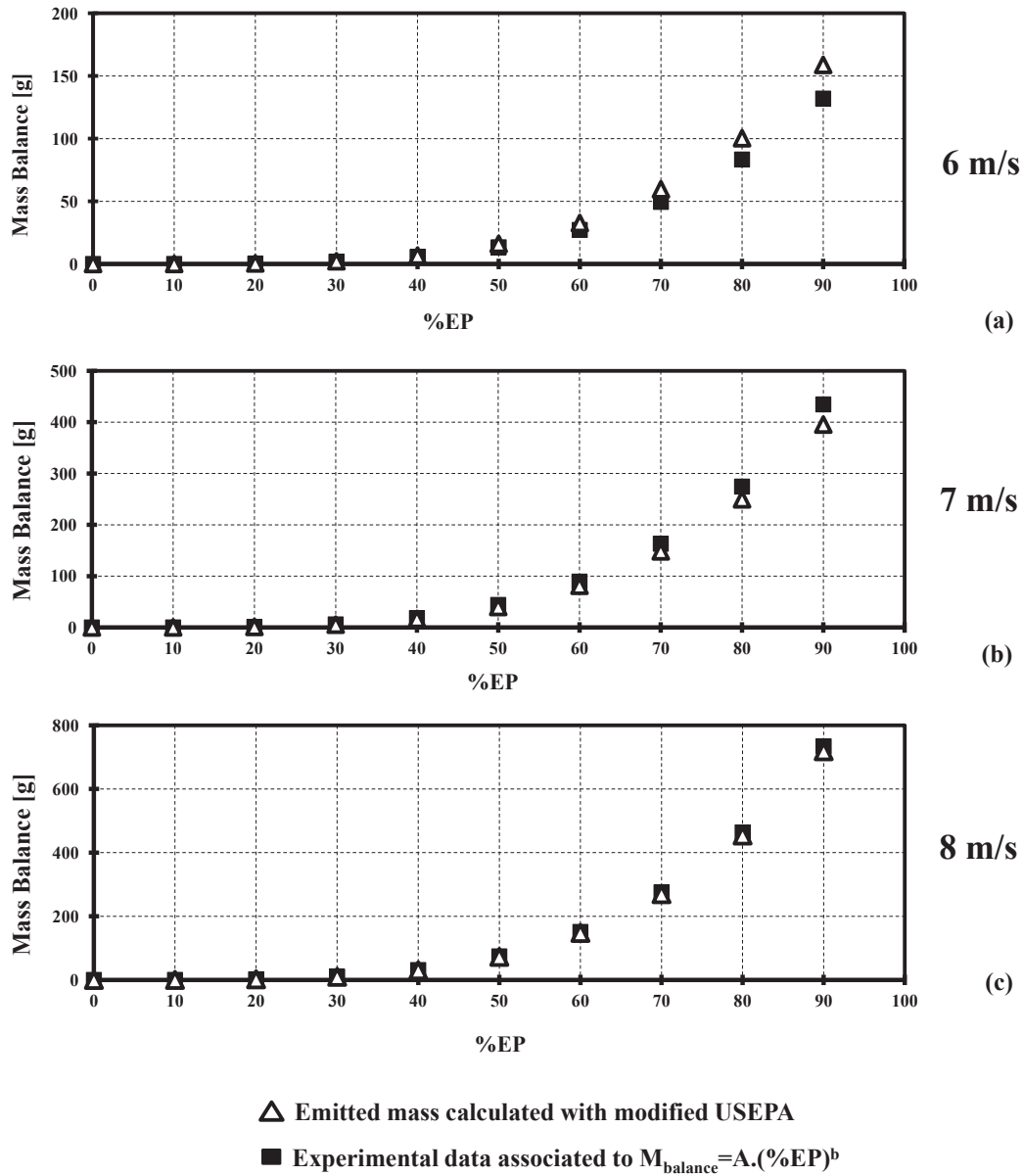


Figure 3.12: Plots of the correlation between emitted mass calculated in wind-tunnel and the values of $M_{balance}$ by the Equation 3.3

As extensively said, the values and equations proposed in this section are only a first step in the modifications needed in the USEPA methodology of dust quantification. In fact, the results were based on experimental works that may be improved to consider more conditions of granular materials stored in wind eroded open yards. The formulations proposed in this section presented results in good agreement with the experimental measurements. This attests that the propositions could be well representative of the reality found on industrial sites.

Chapter 4

Analysis of aeolian erosion over oblong stockpiles: experimental and numerical approaches for turbulent fluid flow featuring and dust emission quantification

The present chapter is devoted to numerical and experimental simulations for the prediction of fluid flow over several arrangements of oblong storage piles. Previous works carried out dust emission studies about open yards of storage piles. However, those literature works did not take into account the re-emission from the ground surface around the stockpiles. In industrial sites, the vicinity of a stockpile is significantly loaded with silt particles originated from: piles disturbances, pile erosion and transport of material in the surrounding regions. Moreover, from the literature review, a lack of information regarding the influence of a successive stockpile was identified. Finally, a new shape of storage pile crest was simulated to analyse its impact on emissions of particles.

This chapter is divided into two main sections, (i) investigation of an isolated stockpile and (ii) investigation of various arrangements of two successive stockpiles:

- (i) the first subsection studies the ground region surrounding an oblong stockpile by means of numerical and experimental simulations. For the experimental investigation the oil-film surface flow visualization is firstly applied. In this approach the potential zones of particle take-off are identified assisted by both experimental and numerical simulations. From numerical simulations the contours of near wall velocity distribution are analysed. The second subsection aims to quantify the amount of particles emitted from the stockpile and from the ground surface around the pile. The main result is the calculation of the contribution of re-emission in the global emissions of an open storage yard.
- (ii) the results of the second section are a continuation of the investigations presented in the first section. In fact, the numerical analysis in these subsections were all performed with the open-source code *Code_Saturne*. For analysis of a second successive stockpile, various arrangements are studied, including the impacts of wind orientation, the gap between the piles and wind speed are analysed.

4.1 Investigation of isolated oblong stockpiles

4.1.1 Experimental surface flow visualization and numerical investigation of flow structure around an oblong stockpile

This subsection presents the results as an article published in the "**Environmental Fluid Mechanics**" journal and entitled "**Experimental surface flow visualization and numerical investigation of**

flow structure around an oblong stockpile". It presents the main results and comparisons carried out about the surface flow visualization technique and numerical simulations of the fluid flow around three tested stockpiles configurations. This article discusses the wall and air flow surrounding the stockpile and its associated potential of dust emission due to wind erosion of the region around piles.

Experimental surface flow visualization and numerical investigation of flow structure around an oblong stockpile

B. Furieri · S. Russeil · J.-L. Harion · C. Turpin ·
J. M. Santos

Received: 9 January 2012 / Accepted: 23 July 2012
© Springer Science+Business Media B.V. 2012

Abstract Emission factors are largely used to quantify particle emissions from industrial open storage piles. These factors are based on the knowledge of velocity distribution and flow patterns over the stockpile surface which still requires further research. The aim of the present work is to investigate the airflow characteristics over a single typical oblong pile and in its near-ground surroundings for various wind flow directions. Wind tunnel experiments using an oil-film surface coating technique were carried out for near-wall flow visualization. Numerical simulation results, favorably compared to PIV measurements, were used to allow comparison analysis of flow features. For the stockpile oriented 90° to the wind main direction, typical topology of flow around wall-mounted obstacles were observed, notably a wake zone downstream the pile including two main counter-rotating vortices. Further analysis of numerical wall shear stress distribution and streamlines indicates that two complex three-dimensional vortical flow structures develop downstream the pile. For other incoming wind flow directions (30 and 60°), the flow characteristics over the storage pile greatly differ as a single helical main vortex develops from the pile's crest. Corresponding high values of wall shear stress are noticed downstream the storage pile. For each configuration studied, downwash and upwash zones are induced by the vortical structures developed. This near-wall flow topology combined with areas of high friction levels may be linked to potential dust emission from the ground surface surrounding industrial stockpiles.

Keywords Oil-film surface visualization · Wind tunnel experiments · Flow topology around stockpiles · Wall shear stress · Computational fluid dynamics · Particle image velocimetry

B. Furieri (✉) · S. Russeil · J.-L. Harion · C. Turpin
Mines Douai, 948, Rue Charles Bourseul, 59500 Douai, France
e-mail: bruno.furieri@mines-douai.fr

J. M. Santos
Departamento de Engenharia Ambiental, Universidade Federal do Espírito Santo (UFES),
Av. Fernando Ferrari 514, Goiabeiras, Vitoria, ES, 29.060-970 Brazil

1 Introduction

Dust emissions from diffuse sources are an important environmental problem nowadays in many urban and rural regions. Most of the pollutants emitted to the air are from diffuse sources including traffic, industries, households, energy sector and also agriculture. This work deals with the problem of dust sources found in industrial open storage yards such as steel plants. The major problem with diffuse sources is the complexity to measure actual emissions rates on real yards. Thus, an analytical method, which formulation was proposed by US EPA [26], is often applied for estimating these open sources emissions. This widely used model employs emission factors that require the knowledge of the pile wind exposure. This latter one is characterized by the ratio between the near wall velocity (u_s at 25 cm above the pile surface) and the free-stream velocity (u_r at 10 m). In the US EPA reference document, the wind exposure is given in terms of wall distribution of u_s/u_r for only two classical stockpiles shapes: conelike and oblong flat-topped piles. These data were obtained from specific experimental measurements carried in a wind tunnel. To extend this approach to stockpiles of various shapes and configurations, numerical simulation was considered a suitable tool to map the degree of wind exposure.

In a first paper of Badr and Harion [2], numerical simulations performed by means of a computational fluid dynamics software were proved to be efficient in predicting the wind flow over flat-topped and conelike stockpiles. Indeed comparisons between calculated and measured values of u_s/u_r for a hundred points over the pile surface have shown a good agreement. The authors have then studied the effect of various aggregate storage piles configurations on dust emissions, see [3]. Using the piles' wind exposure assessed from data of numerical simulations, they showed that the pile's dimensions (length vs width) govern the velocity distribution near the pile surface and strongly affect the emission rates.

In a following paper from Toraño et al. [21], computational fluid dynamics was also used to determine the degree of wind exposure for a semi-circular stockpile. It was found a strong influence of the main wind flow direction on the flow near the pile surface and on the corresponding emission rates. As various studies have shown that most of the aeolian erosion occurs in the vicinity of the stockpile crest, the influence of its shape was analysed by Turpin and Harion [23]. Considering flat-topped piles, various clipping heights were then examined to determine their impact on dust emission taking also into account the main flow direction. It was found that the stockpile crest flattening provides no reduction of the pollution. In the same field, windbreak effectiveness has been numerically studied for various configurations, see for example [21] or [7]. The barriers used for pile protection were shown to significantly reduce the emission, depending on their location upstream the pile base and on their relative height to the pile. The US EPA model has also been applied to real open storage yards which contain several piles, and not only isolated ones as in all above mentioned studies. Diego et al. [6] have implemented an algorithm based on the US EPA model in a commercial CFD software. This approach has enabled to simultaneously calculate diffuse emissions rates. Two parallel neighboring real yards of oblong shape were considered. These authors have found for the tested case that the upwind-exposed pile protect the downstream one. This led to a different contribution from each pile to the total emission. On the other hand, the experimental investigation performed by Ferreira and Fino [8] has shown that in some cases the above mentioned protection is not observed as the threshold friction velocity may be significantly affected by turbulence or vorticity, specially in the wake. A whole real industrial site was numerically investigated by Turpin and Harion [24]. Three stockpiles and seventeen surrounding buildings have been included in the computational domain. Multiple flow separation and wakes interaction were noticed in this complex industrial configuration.

Finally the strong influence of the surrounding buildings on the piles wind exposure was clearly highlighted.

It is worth to note that in all previously cited studies, the same approach is used: the US EPA method with the u_s/u_r distribution assessed by means of CFD simulation. Moreover these studies mainly focus on the velocity distribution only near the stockpile surface. As a consequence no detailed flow topology over the pile and in its vicinity is presented, neither the wall shear stress distribution which is also undoubtedly involved in particles take-off mechanisms. The knowledge of these near-wall flow structures is of major importance when dealing with possible emission of particles which have settled around the piles due to material handling and/or transportation operations. This is particularly relevant on real industrial sites where the areas around the stockpiles are loaded with particle matter, moreover with a large part of silt material content. It appears then worthy to thoroughly investigate the whole flow structures developing over and around the stockpile, having in mind their possible implication in dust emission.

As a first step, the present study is focused on a commonly encountered configuration which is composed of a single oblong stockpile. It may be considered as a wall-mounted obstacle disturbing the turbulent wind flow close to the ground. Many works have been reported for such configurations: cubic or rectangular isolated buildings, as well as arrays of buildings, see for example [10, 17–19]. But contrarily, very few works can be found concerning flow topology around stockpiles structures. And thus the airflow characteristics over an oblong stockpile are yet not well known.

In this study experimental and numerical methods are used to investigate the flow pattern over and in the vicinity of a storage pile model. Numerical computation of the airflow over the stockpile is validated by means of particle image velocimetry (PIV) measurements. Furthermore to analyse wall friction distribution and near-wall flow topology, surface flow visualization (with oil-film coating on the wall) was chosen as in previous work [14, 16]. Indeed, this approach offers the possibility of two-dimensional wall visualization with a good spatial resolution of the main physical parameter involved in wind erosion, i.e. the wall friction.

The present paper does not deal with the quantification of the mass flow rate of dust emission. This study should be considered as a preliminary step to understand the flow features that may lead to emission of particles that have settled in the vicinity of storage piles. The discussion of dust emission estimation is left for future work. Results presented are then limited to the analysis of airflow topology and surface flow characteristics for three different main wind flow directions.

2 Experimental details

This section presents the configurations tested, the experimental set-up and the flow analysis techniques. In this paper two different flow visualization techniques have been used: an oil-film technique for surface fluid flow visualization and the PIV technique. The PIV results were taken from a previous study of Turpin [22] to validate the CFD computations. The surface oil-film technique was carried out to complement the PIV investigations, specifically for the analysis of the wall flow topology in the surroundings of the stockpile.

2.1 Tested configuration and wind tunnel facility

Experimental investigations were performed in a wind tunnel in which a scaled-down stockpile model was set up. A single oblong stockpile was chosen with its shape and dimensions

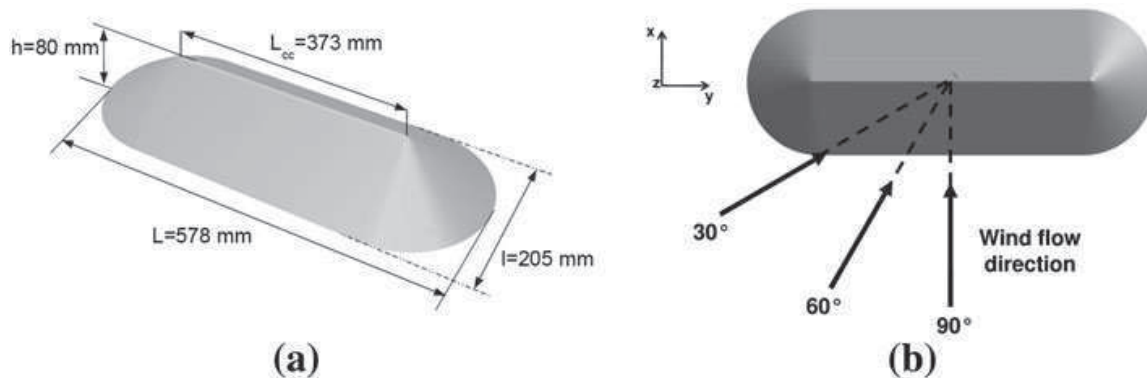


Fig. 1 Oblong shape pile configuration: **a** model dimensions, **b** wind angles of incidence

representative of typical coal storage piles with an angle of repose equal to 38° [25], see Fig. 1a. This model was made in wood to a scale ratio of 1:200. As the incoming wind flow direction is well known to highly influence the flow topology over the stockpile [23,24,26], three airflow angles of incidence have been investigated: 90, 60 and 30° (see Fig. 1b) for a single free-stream velocity equal to 6.5 m/s.

The wind tunnel is schematically presented in Fig. 2. It has the following dimensions: $H_s = 0.80$ m of height, $W_s = 1.50$ m of width and a length equal to $L_s = 8.12$ m. The blockage ratio (frontal area of the model divided by the wind-tunnel section) is 3.2 % which agrees with the value recommended in literature: <5.0 % [4,20]. The test section, where the measurements were taken, is located 6.20 m downstream from the wind tunnel entrance to allow the fully development of a turbulent boundary layer.

Details of wind tunnel characteristics can be seen in Fig. 2: (i) a rotating circular bottom plate which is used to change the stockpile model orientation inside the test section, (ii) Plexiglas walls on the sides of the test section that allow flow visualization, (iii) honeycombs and very fine grids placed upstream and downstream to respectively suppress large-scale vortices entering the wind tunnel and to prevent fan perturbations at the outlet, (iv) roughness elements set near the entrance of the wind tunnel to promote the development of the turbulent boundary layer upstream the test section. Different tests have been carried out to define quantity, dimensions and disposition of these obstacles allowing the formation of a turbulent boundary layer. This was checked by means of some LDA measurements of the streamwise velocity and its fluctuation, see Fig. 2. The turbulent boundary layer thickness, δ , is equal to 0.160 m which is significantly higher than the scaled down pile model [22]. During the experimentation the stockpile model is thus exposed similarly to conditions observed in real industrial sites.

2.2 Particle image velocimetry technique

To validate numerical simulations of airflow characteristics over stockpiles, some PIV measurements were carried out. Nowadays, this technique provides accurate results suitable for checking the validity of numerical models. The PIV technique is based on illuminating seeding particles in the airflow field to be investigated. The choice of these particles is one of the task to be carefully handled: they must be sufficiently small to be suspended in the airflow but also sufficiently large for their scattering to be detected by a CCD-camera when illuminated by a laser sheet. If so, the seeding particles are visible and it is possible to determine the air-flow velocity field by calculating the particle displacements over a well defined time step. The

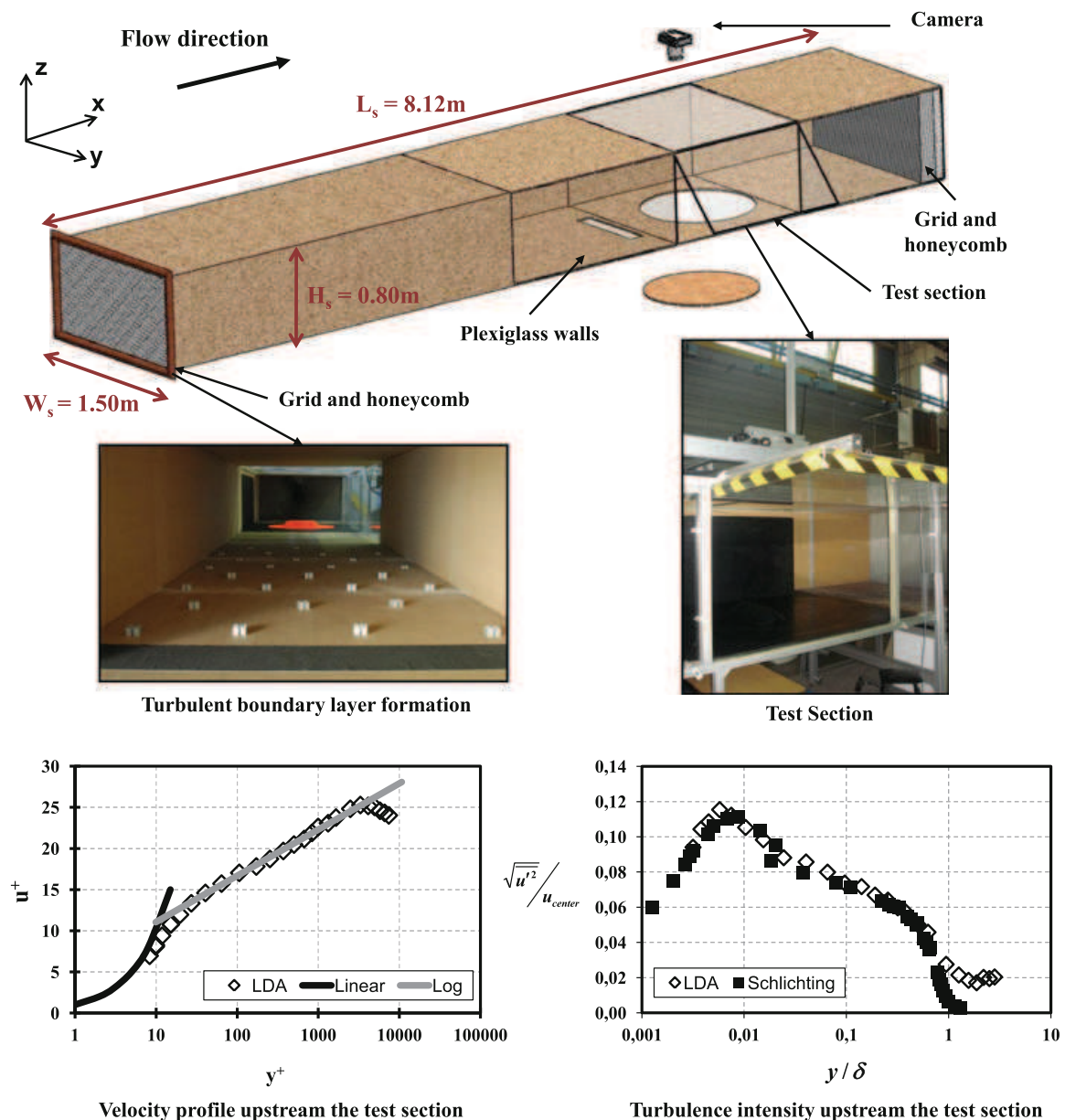


Fig. 2 The experimental wind tunnel set-up

particles seeding was achieved by means of a smoke generator. PIV-2D2C (two dimensions, two velocity components) experimentations have been carried out using the Dantec Dynamics system with a CCD Flowsense 2M camera (spatial resolution of $2,048 \times 2,048$ pixels) and a Continuum NdYag laser. The acquisition of couples of images, synchronized with the laser shots frequency, led to an acquisition rate equal to 4 Hz. The software Dynamic Studio was used for the images post-processing with the following parameters: time step between two images of $120 \mu\text{s}$, interrogation zones of $3.8 \times 3.8 \text{ mm}^2$ with 32×32 pixels and an overlapping of 25 %. Various previous tests have shown these parameters suitable for the measurements carried out. Special attention was also paid to the statistic convergence to determine the appropriate samples number. Main features of the PIV system are reported in this paper, for more details the reader should refer to [22]. Most of the velocity vertical profiles $U(z)$ presented in subsequent paragraphs have been extracted from PIV measurements that have been performed in a vertical plane (XZ plane) parallel to the main flow direction, for the three angles of incidence.

Even if the scaled-down stockpile model and the bottom wall of the wind tunnel were painted with a low-reflection coating (*Rhodamine* dye based), less spatial resolution is observed in the very near-wall region. This renders the very near-wall flow structures analysis difficult to address. Thus surface flow visualization techniques appear as a relevant method to complement PIV measurements.

2.3 Surface flow visualization technique

Surface flow visualization methods are characterized by the fact that they directly supply wall informations, see [1, 11–13, 15]. A surface flow visualization technique was then used with the aim to study the near-wall flow topology and wall shear stress distribution. The oil-film coating method applied is a mechanical one, i.e. based on changes in position of discrete quantities (tracers) in oil mixture covering the surfaces exposed to flow friction. The oil-film mixture is basically composed of three components: oil as the main element, a colored tracer and an agent which allows the mixing between the two others. As reported by Guiming [11], the choice of the components proportions is mainly based on experience and preliminary tests, as it depends on the wind velocity, the wind tunnel walls material, the obstacle shape, its dimensions and surface roughness. Initially, the compounds (paraffin oil, titanium oxide, oleic acid) proposed by Desreumaux and Bourez [5] for a airflow velocity of 20 m/s were used. Various tests were performed after having adjusted the proportions to the present free-stream velocity equal to 6.5 m/s. Unfortunately, the results obtained were not satisfactory due to the very long stabilization time needed to obtain interesting results and also to the deficient contrast observed in photographs. Finally, an oil mixture made with yellow colored powder was shown to be more efficient for the visualizations when using the following composition: 128 g/m² of paraffin oil, 5 g/m² of yellow dye and 23 drops/m² of oleic acid. Numerous tests were also made to try to visualize the surface flow topology on the stockpile walls which are inclined at 38° to the horizontal plane. But these were unfortunately unsuccessful. Indeed due to gravity effects, the surface inclination led the oil-film mixture to flow downhill.

The photographic camera was placed right above the scaled-down stockpile model with its optical axis vertical perpendicular to the bottom wall, see Fig. 2. The spatial resolution of 6 millions pixels was found enough to allow the visualization of detailed flow features, see Fig. 3. Furthermore the photographs have been geometrically calibrated to correct the camera optical system possible distortions. A calibration grid was used to determine the scale ratios to be applied to correct x and y coordinates taken from the pictures when dealing with vortices positions. Attention was also paid to contrast enhancement and elimination of optical reflection to ensure maximum picture quality. The examination of successive shots taken at given time intervals, typically 15 min, has enabled to determine the appropriate duration of each experiment. When the wall oil-film pattern presented no more significant modification between two consecutive photographs, the experience could be stopped. This stabilization time, which depends on the configuration considered, was found to last up to five hours. In following sections each visualization which is presented is the last one of a successive set of pictures that were recorded until visualization of vortices, separation lines and recirculating zone showed no noticeable changes. As an example, Fig. 3 shows the temporal evolution of successive photographs with varying color intensities: intense yellow indicates areas of low friction while the darkest regions (black) correspond to higher values of wall shear stress.

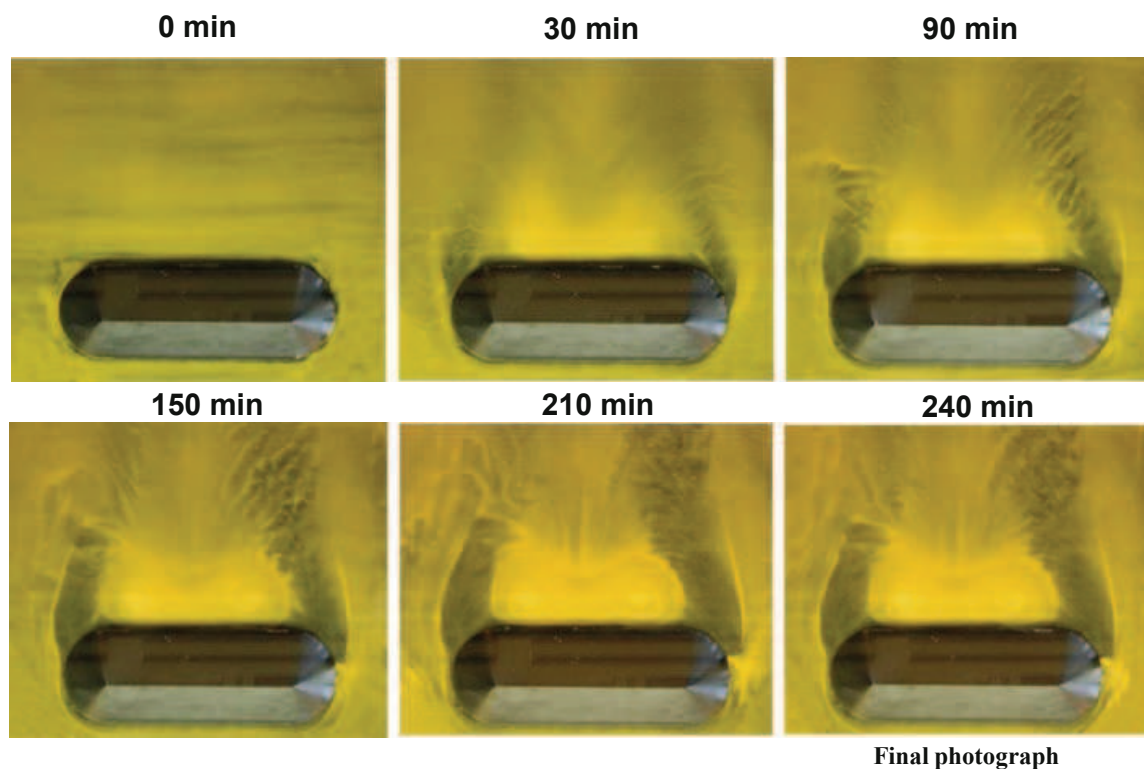


Fig. 3 Temporal evolution of oil-film mixture coating, for the stockpile oriented 90° to the main wind flow direction (*top view* along Z-axis)

3 Numerical simulation background

3.1 Presentation of numerical modelling

The three-dimensional Reynolds averaged Navier–Stokes equations governing the flow around the stockpile were solved using a finite volume based CFD code [9]. Figure 4 shows the computational domain with indications of dimensions and boundary conditions applied, using the stockpile oriented 90° to the main wind flow direction as an example. The axis origin is located at the intersection of the vertical axis of symmetry of the pile and the bottom

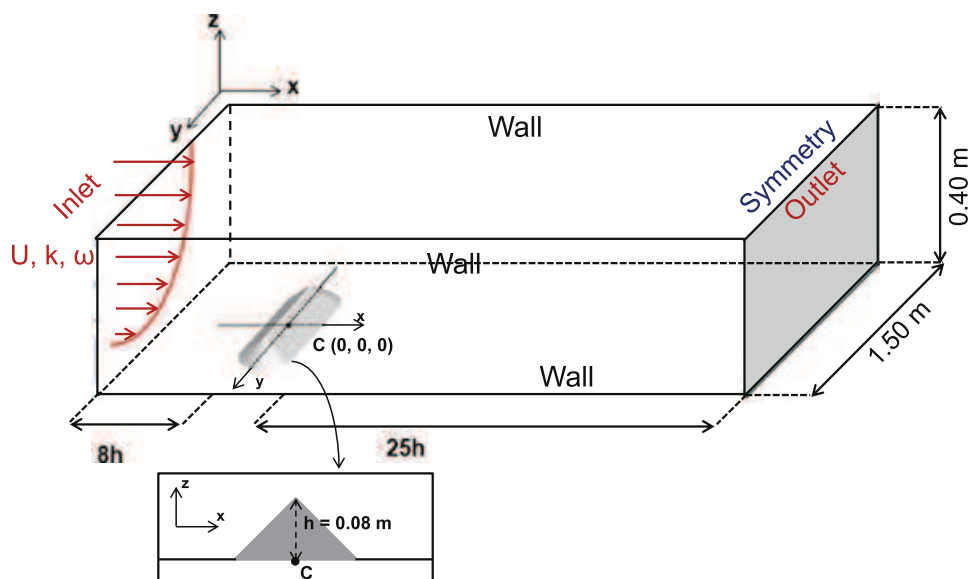


Fig. 4 Computational domain: dimensions and boundary conditions

surface, see “Point C” in Fig. 4. The domain is extended a sufficient distance upstream (8 h) and downstream (25 h) from the stockpile model to ensure that the results are not influenced by the domain size for the three tested configurations. Based on previous study [23], the $k - \omega$ shear stress transport turbulence model was chosen for the simulations with the transitional flow option which is suitable for such flows with adverse pressure gradient, flow separation and reattachment. For the turbulence near-wall modelling no wall functions were applied to ensure better accuracy. This required very fine mesh refinement near the ground surface and stockpile walls. Indeed the size of the first cell adjacent to the walls was chosen to be no more than $z^+ = 4$ which falls within the recommendations required by the use of this turbulence model without any wall functions ($z^+ \leq 5$). Mesh sensitivity tests have been previously carried out by Badr and Harion [2] for the same kind of configurations. The mesh size and distribution were then chosen in accordance with their findings. The mesh was produced by an extrusion of triangular cells defined on the pile and ground walls towards the upper wall of the computational domain. This led to a final mesh composed of ≈ 5.3 millions cells. The computations were carried out with an upwind second order spatial discretization scheme for momentum, turbulence kinetic energy and its specific dissipation. The SimpleC algorithm was used for the pressure-velocity coupling, see [9]. Inlet conditions were specified by applying two-dimensional vertical profiles of longitudinal velocity, turbulent kinetic energy and dissipation rate. These were obtained from previous simulation of a flow in a simple channel having the same height and width as the present computational domain. A boundary condition of fully developed flow type was set at the outlet of the computational domain. Symmetry conditions were applied for the upper side. Finally, smooth walls with no-slip conditions were set at lateral, bottom and stockpile walls. Others details of the numerical procedure can be found in reference [22].

In this paper numerical results are presented in dimensionless form. The coordinate variables are thus divided by the stockpile height (h) which is an usual characteristic length chosen for such problem. In the approach adopted in the US EPA model [26] the velocity measured at 10 m in real scale is chosen as the reference velocity. In our scaled-down model configuration, this corresponds to the velocity calculated at 0.05 m height which leads to $U_{ref} = 5.26$ m/s. Similarly wall shear stress values are herein divided by the value calculated over the undisturbed zone, i.e. in regions where the turbulent boundary layer flow pattern is out of influence of the stockpile. Observing the contours of shear stress over the whole ground surface, this reference value was chosen as $\tau_{ref} = 0.07$ Pa. Therefore, all regions where τ_{yz}/τ_{ref} values are different from unity are areas under the stockpile’s influence.

3.2 Validation of numerical results

In this section the validation of CFD simulations is ascertained by comparing numerical results to PIV data. For that purpose a few velocity profiles distributed throughout the computational domain around the stockpile model are analysed. This comparison is detailed hereunder for the configuration where the stockpile is perpendicular to the incoming airflow: four vertical velocity profiles and an horizontal profile perpendicular to the main wind flow direction are reported in Fig. 5. These vertical profiles present the mean longitudinal velocity u/U_{ref} versus the vertical coordinate z/h , while the horizontal profile is plotted over the transversal distance y/h . For the two other configurations, where the stockpile is oriented 30° and 60° to the main wind flow direction, two additional profiles are given in Fig. 6.

To assess the differences between computed and measured velocities, averaged relative errors were calculated for the whole data set, see Eq. 1. They are reported on each profile chart.

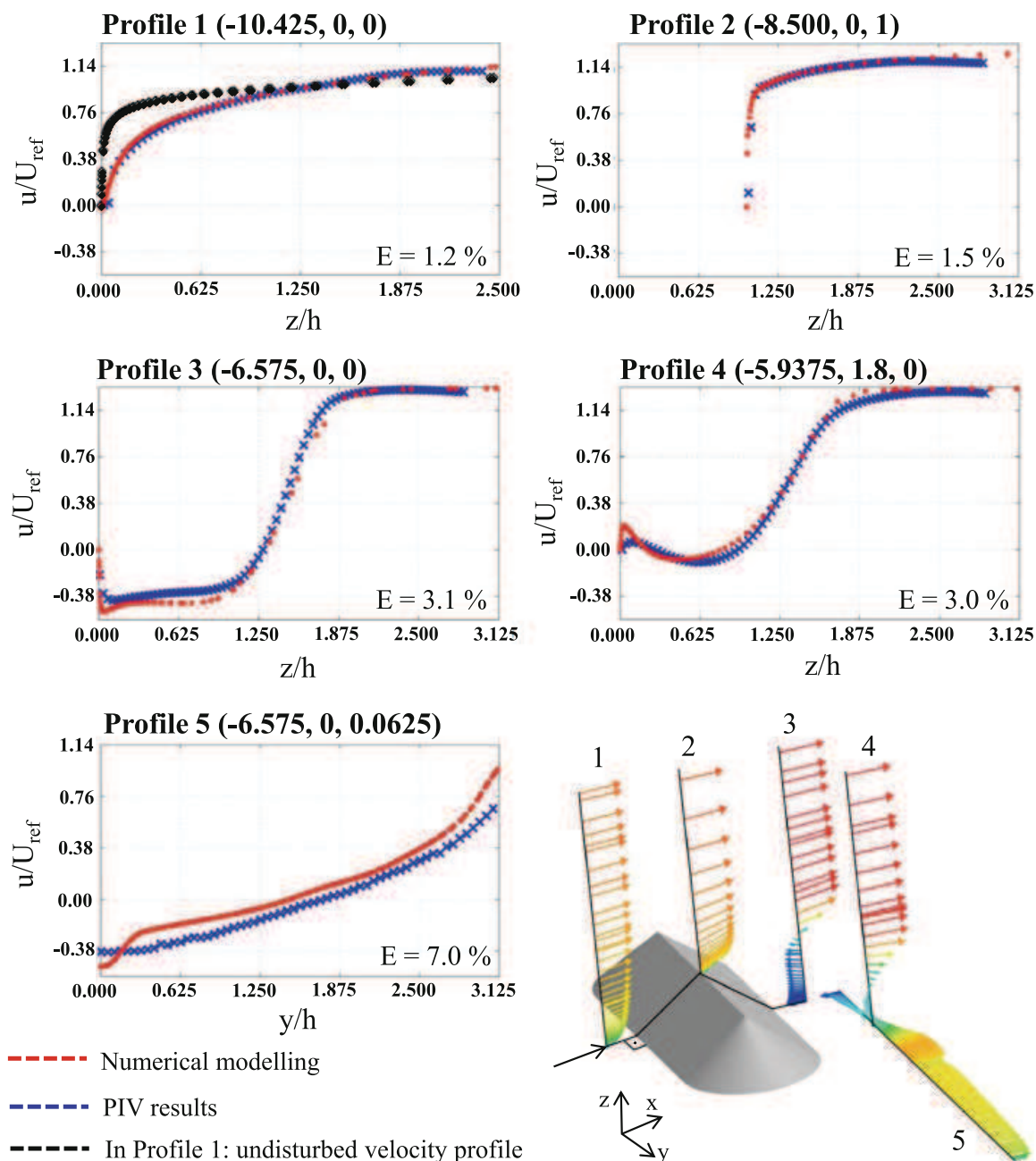


Fig. 5 Profiles of non-dimensional longitudinal velocity: numerical results and PIV measurements, for the stockpile perpendicular to the main wind flow direction

$$E = \frac{\sum_{i=1}^n |u_{exp} - u_{num}|}{n \cdot [\max(u) - \min(u)]} \quad (1)$$

In Fig. 5, it can be seen that the profiles 1 and 2, which are located in the upstream part and on top of the pile, present the smallest values of relative error. This indicates that the incoming flow and its upstream deceleration are well predicted by numerical calculations. In addition, the profile 1 in Fig. 5 also shows the undisturbed velocity profile at the same x coordinate. This comparison illustrates how much the stockpile modifies the incoming wind flow. The three other profiles, namely profiles 3, 4 and 5, are placed further downstream in the stockpile model's near wake. For the two vertical profiles the airflow recirculation leads to some negative values of the velocity that are observed on both numerical and experimental profiles. For these two profiles, errors are found to be roughly equal to 3 %. For the horizon-

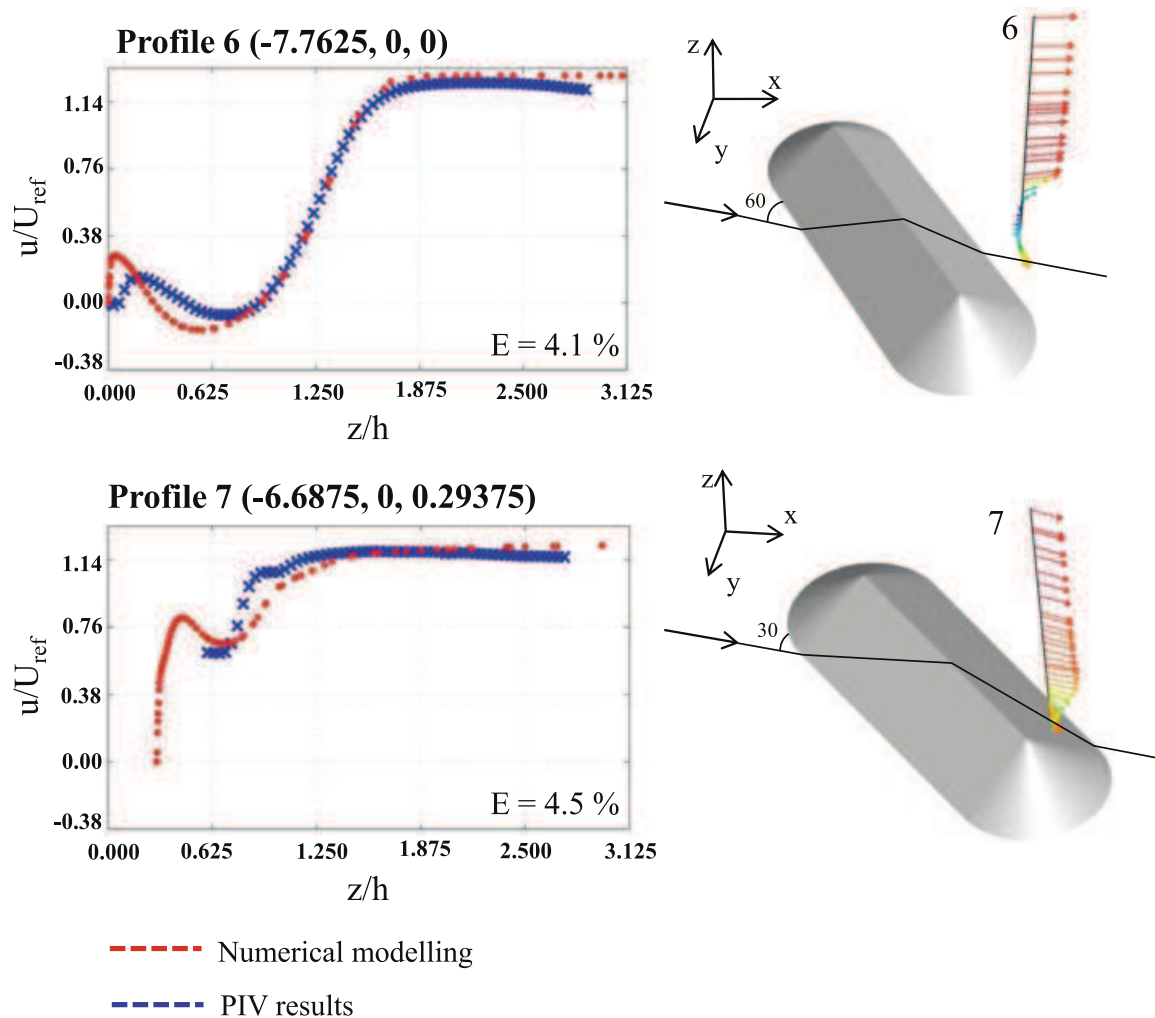


Fig. 6 Profiles of non-dimensional longitudinal velocity: numerical results and PIV measurements, for the stockpile oriented 30 and 60° to the main wind flow direction

tal profile located in the very near wall region the error increases probably due to less PIV resolution and accuracy near the wall, but reaches no more than 7 %. In Fig. 6, the profiles 6 and 7 represent respectively the configurations with angles of incidence equal to 30 and 60°. A generally good agreement is noticed between numerical and experimental data. Although the complexity of these three-dimensional flows, the numerical model presented hereupon proved its ability to correctly predict the airflow topology over the stockpile.

4 Results

In this section the wall flow topology is first analysed by means of both numerical simulation and surface flow visualization. Main wall flow features are discussed as well as the wall shear stress distribution around the pile model (in the dimensionless form in which the reference value of wall shear stress τ_{ref} is presented in Sect. 3.1). These experimental results additionally support the numerical model validation. In a second step an analysis of the three-dimensional airflow topology over the pile enables to highlight how vortical structures develop downstream.

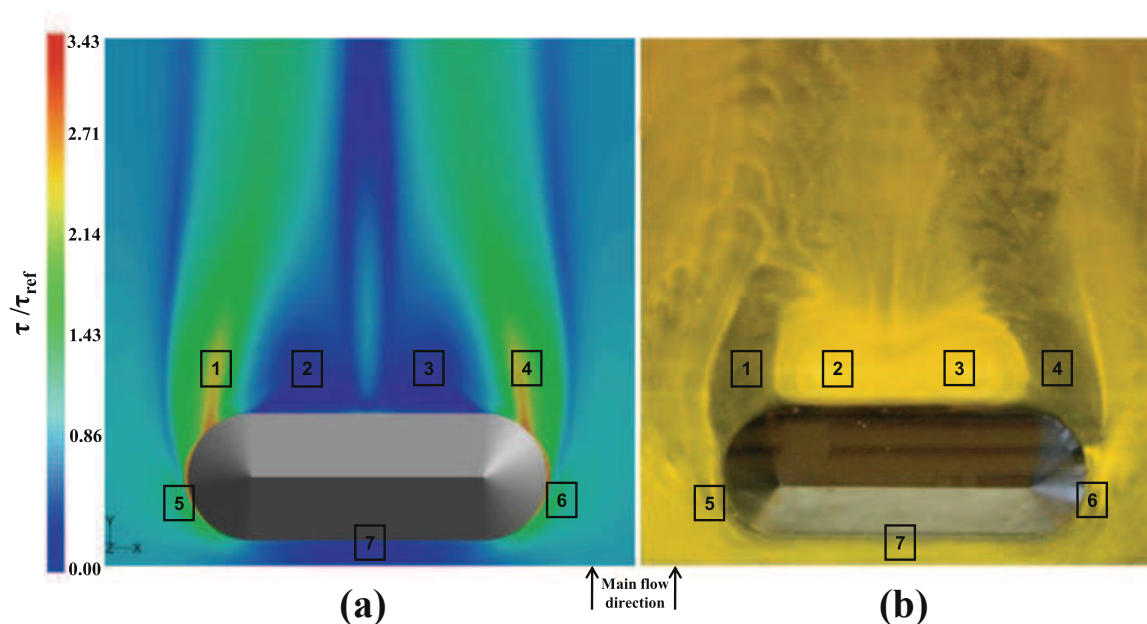


Fig. 7 Wall flow analysis for the stockpile oriented 90° to wind flow direction: **a** Numerical contours of non-dimensional wall shear stress, **b** surface flow visualization

4.1 Analysis of wall flow topology: experimental and numerical data comparison

4.1.1 Wind flow direction perpendicular to the stockpile

Figure 7 shows the wall shear stress distribution around the stockpile obtained by numerical simulation (Fig. 7a), and the corresponding experimental surface flow visualization (Fig. 7b). These numerical contours reveal the same surface flow structure. Indeed, the main incoming stream flow is greatly disturbed due to the wall-mounted obstacle. An overall qualitative analysis reveals four different flow features. Firstly, a wake zone is not surprisingly noticed downstream the pile. It is characterized by low wall friction values ($\tau \leq 0.5\tau_{ref}$) and a pair of symmetrical contra-rotative vortices identified as zones 2 and 3 in Fig. 7. The highest wall shear stress values ($\tau \approx 3.4\tau_{ref}$) are found on each side of the pile in the near-downstream region: see zones 1 and 4. These are due to the flow acceleration which initially occurs on zones 5 and 6 on each side of the pile and whose effect extends over several h downstream. Finally, the last feature noticeable in Fig. 7b is zone 7 upstream the stockpile where the incoming flow decelerates down to the stagnation area leading to low values of wall shear stress ($\tau \approx 0.2\tau_{ref}$).

A careful examination of Fig. 7b allows the observation that the two vortices are not strictly symmetrically arranged in the pile wake. A possible explanation lies in the fact that this kind of symmetrical flow configurations is strongly sensitive to the airflow angle of incidence. Thus even, a very small default in the model positioning in the wind tunnel may have led to such slight dissymmetry. Experimentally, it was actually difficult to measure the incidence angle of the stockpile model with an accuracy better than 1° and its position was potentially not strictly perpendicular to the incoming main flow direction.

A more quantitative comparison between numerical simulation and experimental visualizations was undertaken in parallel to support the numerical model ability to describe the flow over the stockpile and particularly in the vicinity of the surrounding wall. This comparison was carried out for this sole configuration (angle of incidence equal to 90°) because well identified flow structures can be analysed and measured. These are the centre position of

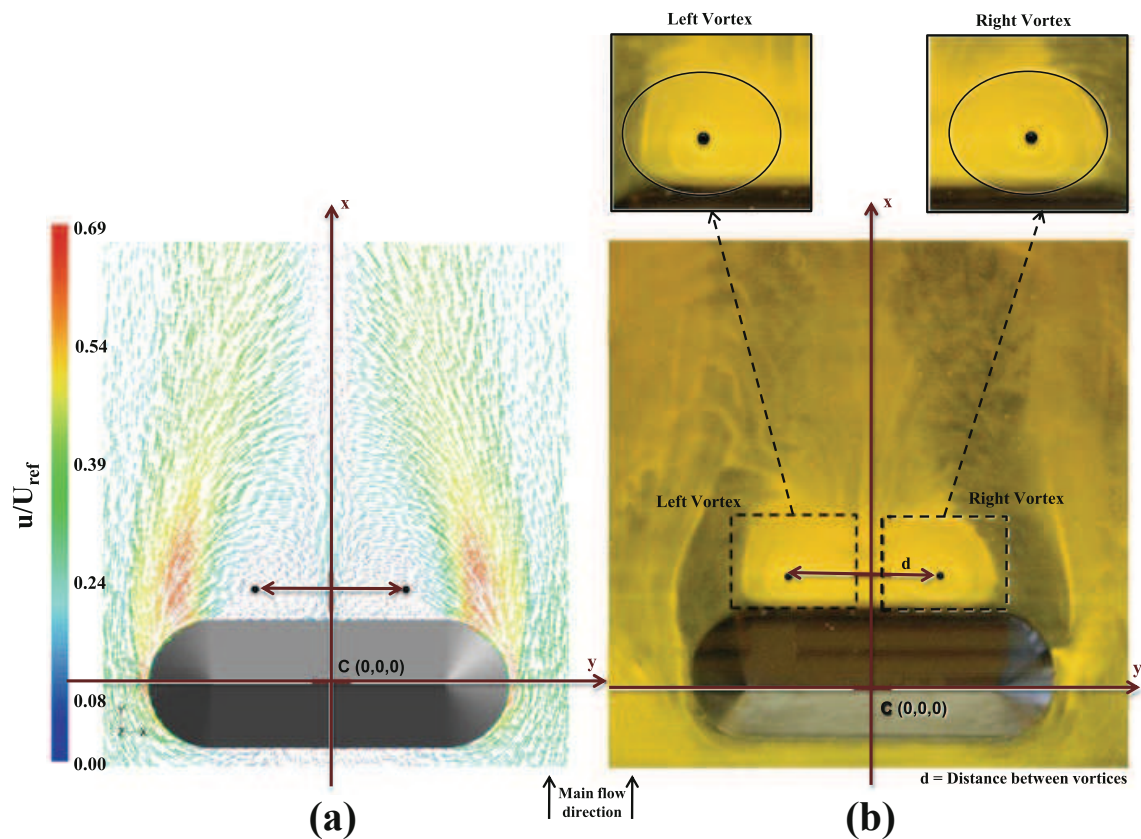


Fig. 8 Wall flow structures used in quantitative analysis: **a** numerical vector field (vectors colored by non-dimensional velocity magnitude), **b** surface flow visualization

Table 1 Results of quantitative comparison between numerical simulation and wind tunnel experiments for the stockpile perpendicular to the wind flow direction

	Numerical simulation		Experimental work		Difference (%)	
	x/h	y/h	x/h	y/h	x/h (%)	y/h (%)
Left vortex	1.785	-1.894	2.066	-1.724	13.6	9.9
Right vortex	1.785	1.894	2.147	1.466	20.2	29.1
	d/h		d/h		d/h (%)	
Distance between vortices (d)	3.788		3.156		16.7	

each vortex in the stockpile's wake and the distance between these two vortices. Figure 8 presents these typical features for both numerical simulation and oil-film experimental flow visualization. Comparisons are shown in Table 1. The difference of the distance between the vortices is found to be approximately equal to 17 %. For the vortices centre positions the differences vary from almost 10 to 29 %. This tends to demonstrate that the vortex positions are more strongly influenced by the probable stockpile misalignment mentioned above, but the wake and overall flow topology are found similar.

4.1.2 Wind flow direction oriented 30 and 60° to the stockpile

Figure 9 respectively presents numerical wall shear stress distribution (Fig. 9a) and the experimental surface flow visualization (Fig. 9b) in the vicinity of the stockpile model oriented

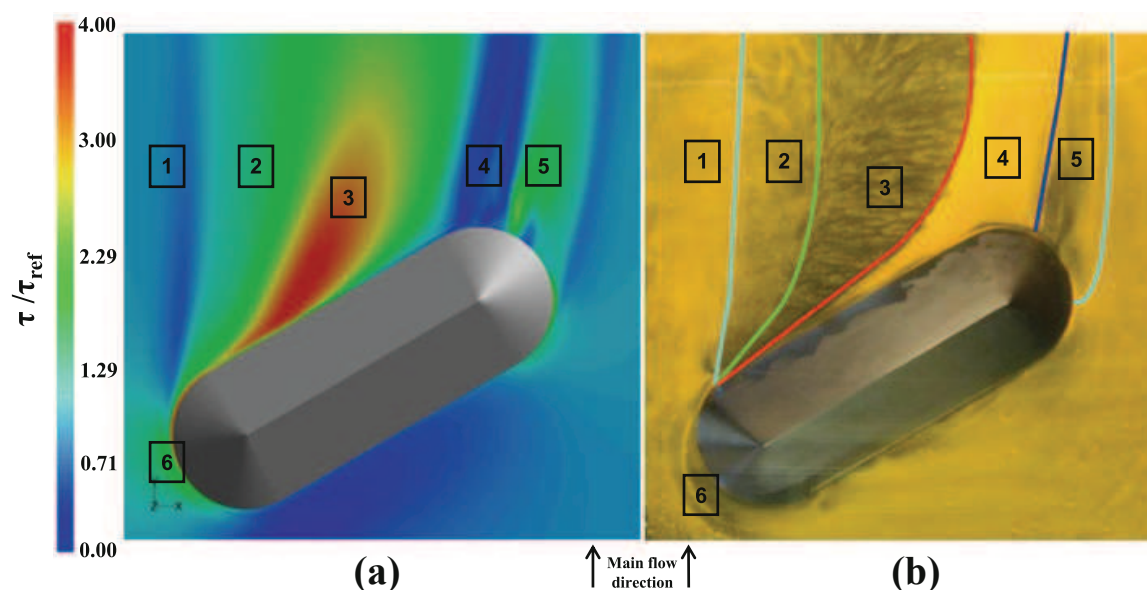


Fig. 9 Wall flow analysis for the stockpile oriented 60° to wind flow direction: **a** numerical contours of non-dimensional shear stress, **b** surface fluid flow visualization

60° to the incoming wind flow main direction. An overall examination of both figures shows that the main stream flow is strongly disturbed by the obstacle presence. For the two cases the same near-wall flow topology is revealed in the surroundings of the pile. Different zones can be identified, each corresponding to a specific flow feature. It can firstly be noticed that the flow accelerates on the left side of the obstacle. Corresponding high shear stress values can be seen near the stockpile, see zone 6 in Fig. 9. The highest wall shear stress values (up to $4\tau_{ref}$) are found downstream the pile: see zone 3 starting from the leeward side of the storage pile model and extending downstream the pile in the main flow direction. It is worth to note that this was not observed for the previous case with the stockpile perpendicular to the incoming flow where a wake zone with low values of walls shear stress was noticed. This clearly indicates a strong influence of the angle of incidence on the flow behavior over the stockpile and in its vicinity, as reported by [23] and in the following section. On the right side of the stockpile the fluid undergoes similar acceleration as on the left side (zone 5), but of smaller strength and extent. In remaining downstream zones, a gradual evolution of shear stress levels at wall is noticed from low values (zone 1 corresponding to no influence of the pile undisturbed) to higher values (zone 2 and then 3). Finally a region of oil-film mixture accumulation is found in zone 4 between two regions of high wall friction. It is characterized by the lowest levels of wall friction.

Results for the 30° configuration are shown in Fig. 10 which presents the wall shear stress distribution obtained by numerical simulation (Fig. 10a) and the oil-film flow visualization (Fig. 10b). Comparing both figures in this case is slightly more difficult than for the preceding cases due to the smaller changes in the shear stress distribution. As it can be seen from Fig. 10b, less gradients are observed in the color intensity levels which are more uniformly distributed. Nevertheless the results can be described roughly in the same manner as for the 60° configuration: the main stream flow is disturbed due to the wall-mounted obstacle leading to the same kind of behavior, i.e. a deviation of the incoming main flow which is more affected on the windward left side, accelerating region, creation of separation line and high values of wall friction downstream the pile. The zones corresponding to this description are highlighted by figures in Fig. 10b. They are found to be distributed around the stockpile model similarly as for the previous case where the angle of incidence was 60° .

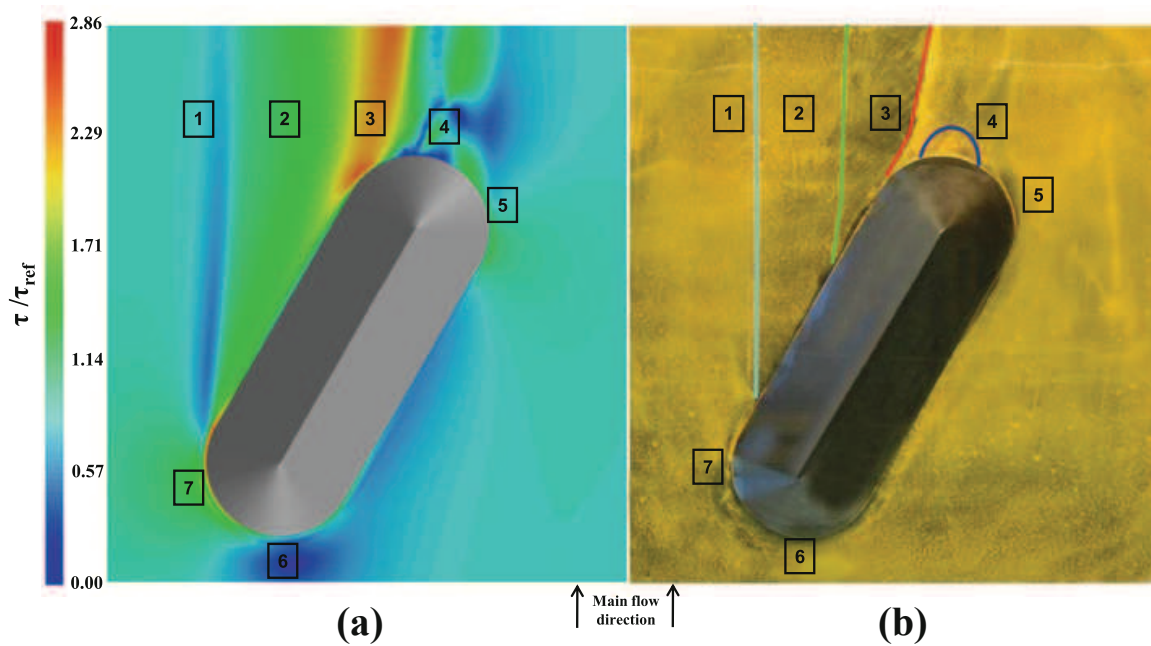


Fig. 10 Wall flow analysis for the stockpile oriented 30° to wind flow direction: **a** numerical contours of non-dimensional shear stress, **b** surface fluid flow visualization

4.2 Airflow features around stockpiles: a numerical investigation

As already mentioned, one of the objectives of this work is to investigate the airflow topology over the stockpile with the aim to discuss implication on possible emission of dust which has settled around the piles. Numerical results, which were obtained from the model previously introduced, are used for that purpose.

4.2.1 Wind flow direction oriented 90° to the stockpile

Figure 11a, b present a three-dimensional visualization of fluid flow features around the stockpile perpendicular to the wind flow main direction using pathlines colored by velocity magnitude. These pathlines were released from a horizontal line located upstream the pile at 0.125 h above the ground surface. In Fig. 11a distribution of the wall shear stress around the stockpile is also reported. It is obvious that the pile strongly disturbs the incoming flow. Flow deviation and acceleration occur on both lateral sides of the stockpile, as already depicted in previous section from wall shear stress analysis. On the contrary, the near wake zone is characterized by low values of wall shear stress as also already mentioned. The flow separation, which occurs from the pile's crest and lateral sides, leads to complex three-dimensional slow recirculating vortical structures downstream the stockpile. However two main contra-rotative vortices with their rotation axis perpendicular to the ground can be clearly noticed in the wake near the ground surface. Farther from the wall their axis of rotation is strongly curved by the main flow passing over the pile crest. For further physical insight Fig. 11b shows one main vortex (for more clarity) highlighted by means of three-dimensional pathlines released near the wall. This representation allows a general overview of the wake flow pattern: an overall spiral trajectory first upwards, perpendicular to the wall, which is then curved from vertical to horizontal towards the downstream part of the domain. A sketch of this rotation axis curvature is presented in Fig. 11c. From this recirculating flow outline, it is then obvious that

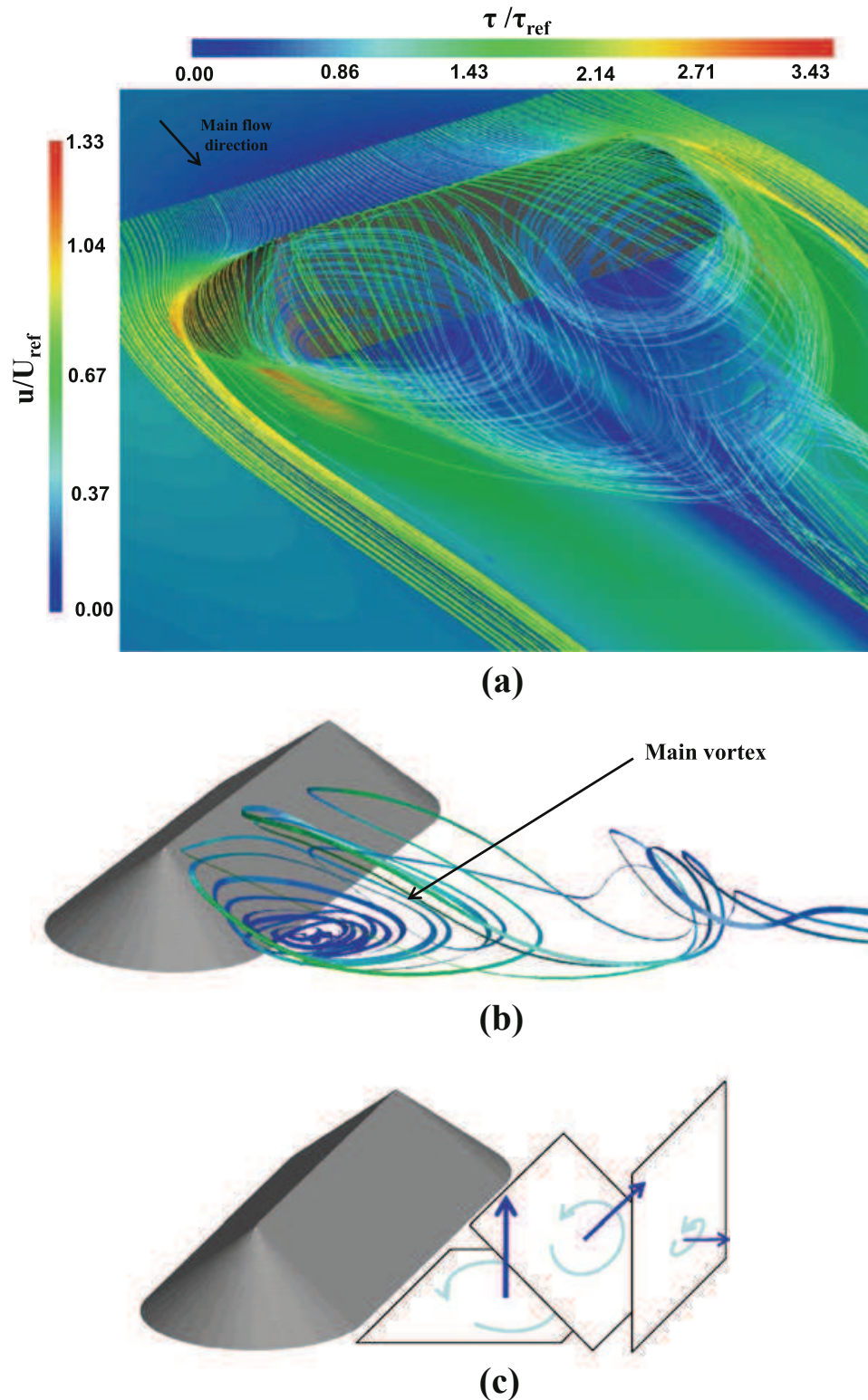


Fig. 11 Airflow topology over the stockpile oriented 90° to the wind flow direction: **a** three-dimensional pathlines colored by velocity magnitude and distribution of wall shear stress, **b** pathlines released from the ground, **c** schematic drawing of the rotation axis curvature

the near wall flow vortices revealed by the experimental visualization technique correspond to a vortex pair developing near the wall with a vorticity perpendicular to the ground.

Analysing a spanwise vertical plane (YZ plane) also appears worth of interest to understand the airflow topology and its link with the wall shear stress distribution in the wake zone.

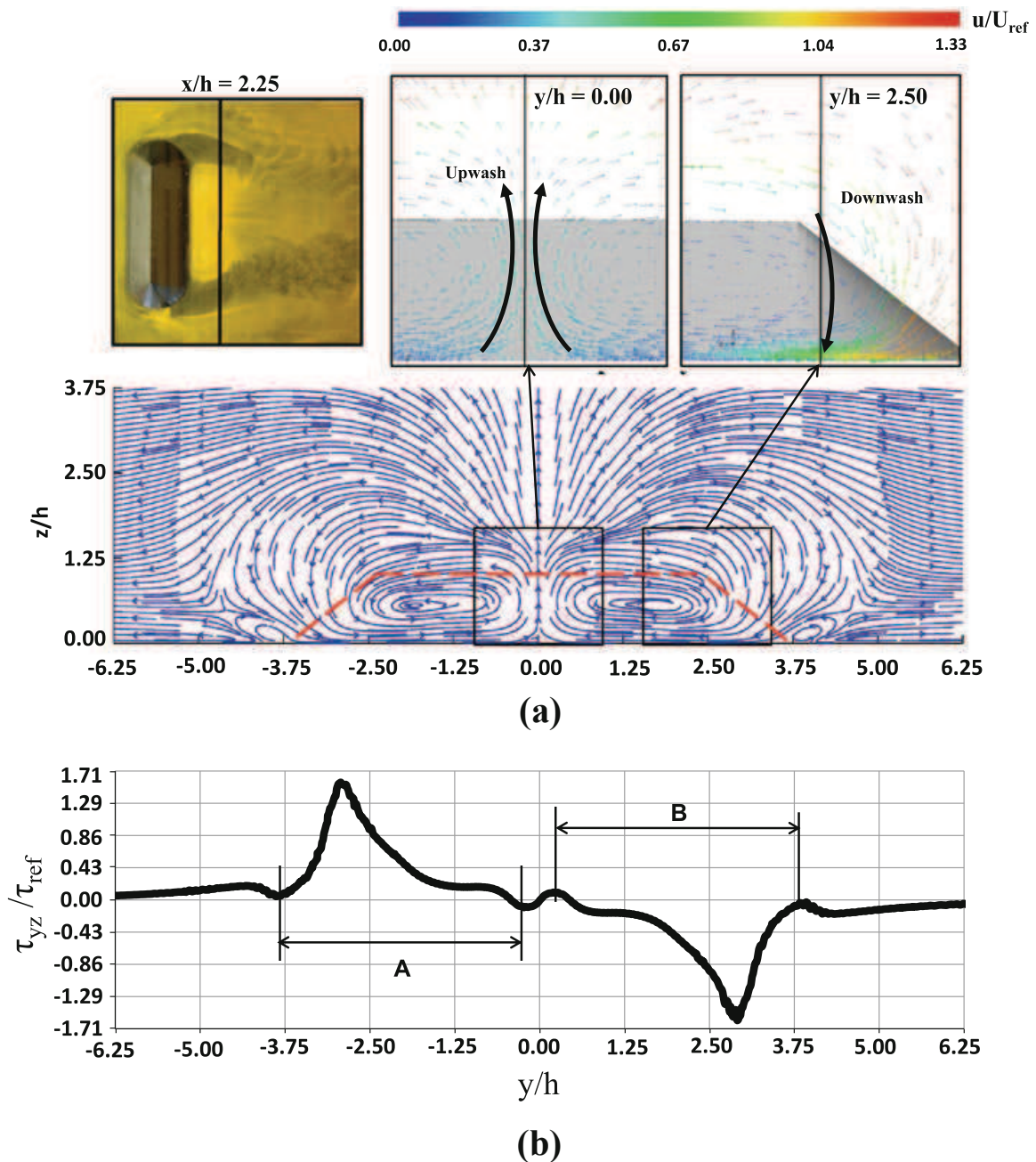


Fig. 12 Analysis in a transversal plane ($x/h = 2.25$) of the airflow topology for a stockpile oriented 90° to the wind flow direction: **a** streamlines calculated in the transversal plane, **b** plot of non-dimensional wall shear stress

Figure 12a presents streamlines in a YZ plane located downstream the pile, at $x/h = 2.25$, as well as two inserts where velocity vectors are plotted. In Fig. 12b the spanwise wall shear stress (τ_{yz}) profile is plotted at the same location. As expected two main contra-rotative vortices are highlighted by the streamlines in this transversal plane. To these two vortical cells correspond two distinct zones in the wall shear stress profile: zone A and B which are areas of high wall friction, see Fig. 12b. Due to the presence of opposite-signed vorticities, positive values are found in zone A ($-4.375 < y/h < -0.625$) while negative ones are encountered in zone B (symmetric of zone A, $0.625 < y/h < 4.375$). In-between, in the symmetry plane at $y/h = 0$, as the fluid leaves the wall upwards, the spanwise wall shear stress is null. This typical flow feature, commonly called an upwash zone, can also be clearly noticed from the

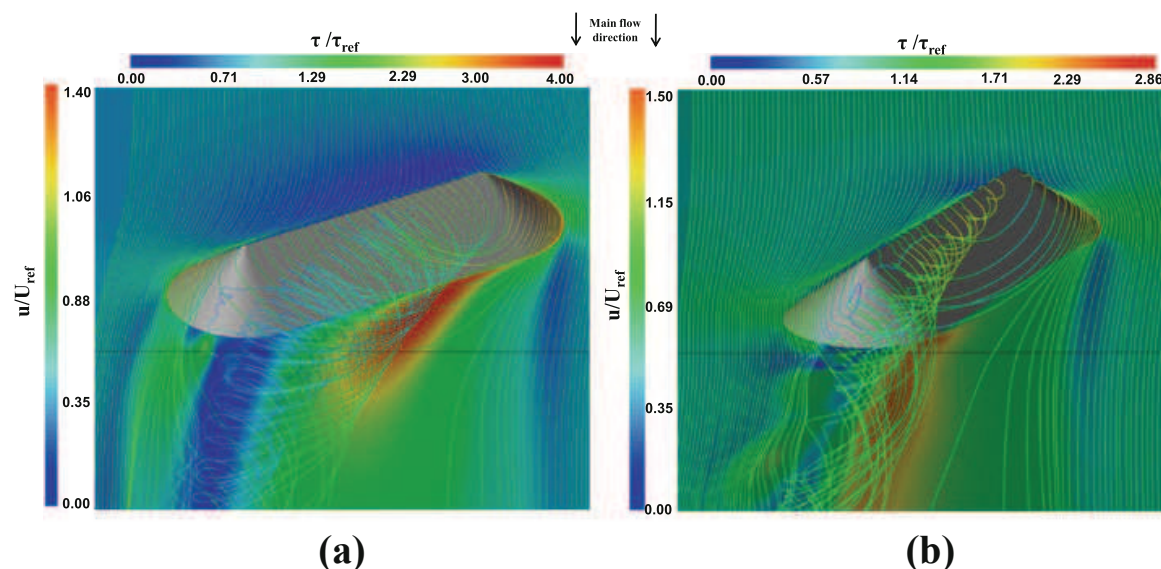


Fig. 13 Three-dimensional views of pathlines colored by non-dimensional velocity magnitude and wall shear stress distribution around the stockpile oriented: **a** 60° to the wind flow direction, **b** 30° to the wind flow direction

velocity field presented in the left insert in Fig. 12a. The highest levels of spanwise wall friction are noticed near both left and right lateral sides of the stockpile, for $y/h = \pm 3.125$. These two regions correspond to areas where the airflow moves downwards to the ground surface, see the right insert in Fig. 12a. These downwash zones which experienced the highest transverse velocity gradients have already been highlighted from previous two-dimensional contours of wall shear stress (zones 1 and 4 in Fig. 7a). Lastly, it can be noticed that more away from the pile ($y/h < -5.5$ and $y/h > 5.5$) the spanwise wall shear stress is null, which shows no more influence of the stockpile: the only shear stress contribution is oriented with the incoming airflow.

It is worth to note that on real industrial sites, flow acceleration which occurs on both lateral sides of the storage pile may correspond to potential emission zones if the dust threshold friction velocity is reached. Furthermore, the complex wake flow structure with upwash and downwash zones previously described may additionally contribute to transport these diffuse emissions towards downstream.

4.2.2 Wind flow direction oriented 60 and 30° to the stockpile

Figure 13a, b respectively show three-dimensional pathlines of the airflow over the storage pile where it is oriented 60 and 30° to the main flow direction. For each configuration the distribution of wall shear stress in the pile surroundings is also reported. Similar airflow patterns are noticed for both angles of incidence. Indeed, the incoming airflow separates near the stockpile crest and a sole main helical vortex is formed. Further downstream from the stockpile, it develops with its axis of rotation aligned with the main flow direction. This important longitudinal vortical structure leads to high levels of wall shear stress in a zone which extends far downstream the storage pile, as already noticed in Sect. 4.1.2.

For the pile oriented 60° to the main flow direction, Fig. 14a presents the streamlines plotted in a cross-sectional vertical YZ located at a distance $x/h = 2.875$ downstream the pile. In Fig. 14b the spanwise wall shear stress (τ_{yz}) profile is also plotted for this same x -coordinate. Negative and positive values of τ_{yz} reveal that two contra-rotative vortices are developing downstream the stockpile. High positive values of wall shear stress corresponding

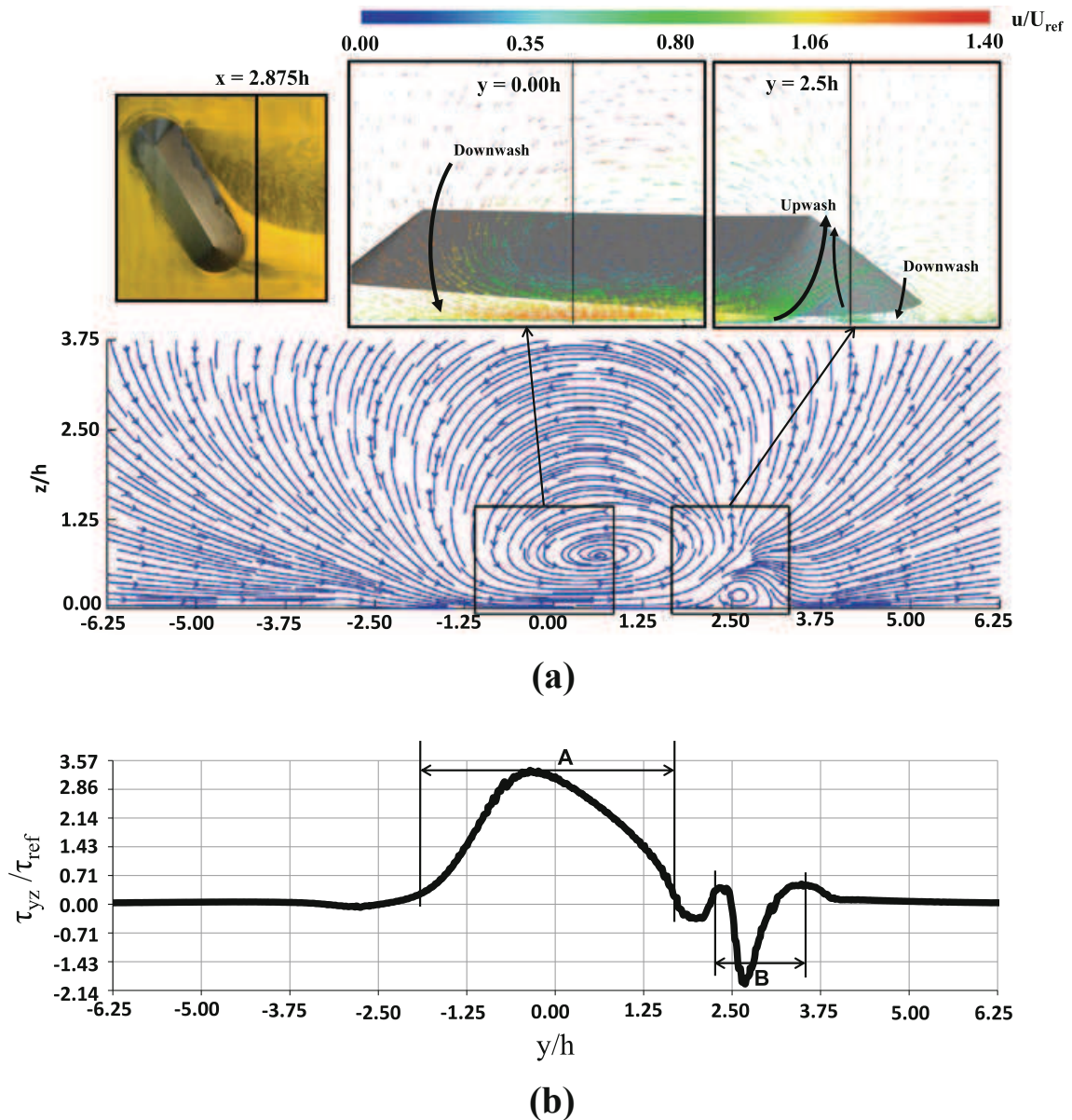


Fig. 14 Analysis in a transversal plane ($x/h = 2.875$) of the airflow topology for a stockpile oriented 60° to the wind flow direction: **a** streamlines calculated in the transversal plane, **b** plot of non-dimensional spanwise wall shear stress

to the main longitudinal vortex are indeed noticed, see zone A in Fig. 14b. Meanwhile, a smaller secondary contra-rotative vortex, induced by the primary one, is also found near the ground for $2.25 < y/h < 3.75$, see zone B in Fig. 14b. The main vortex is the more intense one with a maximum value of τ_{yz}/τ_{ref} nearly equal to 3.5 while the secondary vortex is less intense as $\tau_{yz}/\tau_{ref} \simeq 2.1$. Corresponding to this flow topology, a zone of downwash flow can be identified near the middle plane ($y/h = 0$) and a smaller one near $y/h = 3$, see inserts in Fig. 14a. In the vicinity of the lateral side of the stockpile model $y/h = 2.5$ an upwash zone is highlighted by the streamlines between the two contra-rotating vortices.

The same analysis applies for the configuration with the stockpile oriented 30° to the wind flow direction. Corresponding streamlines and wall shear stress distribution are reported in Fig. 15a and τ_{yz} is plotted on Fig. 15b. Similarly, a main primary vortex exists for $-1.875 < y/h < 1.25$ (zone A in Fig. 15b) and an induced contra-rotating secondary vortex is noticed,

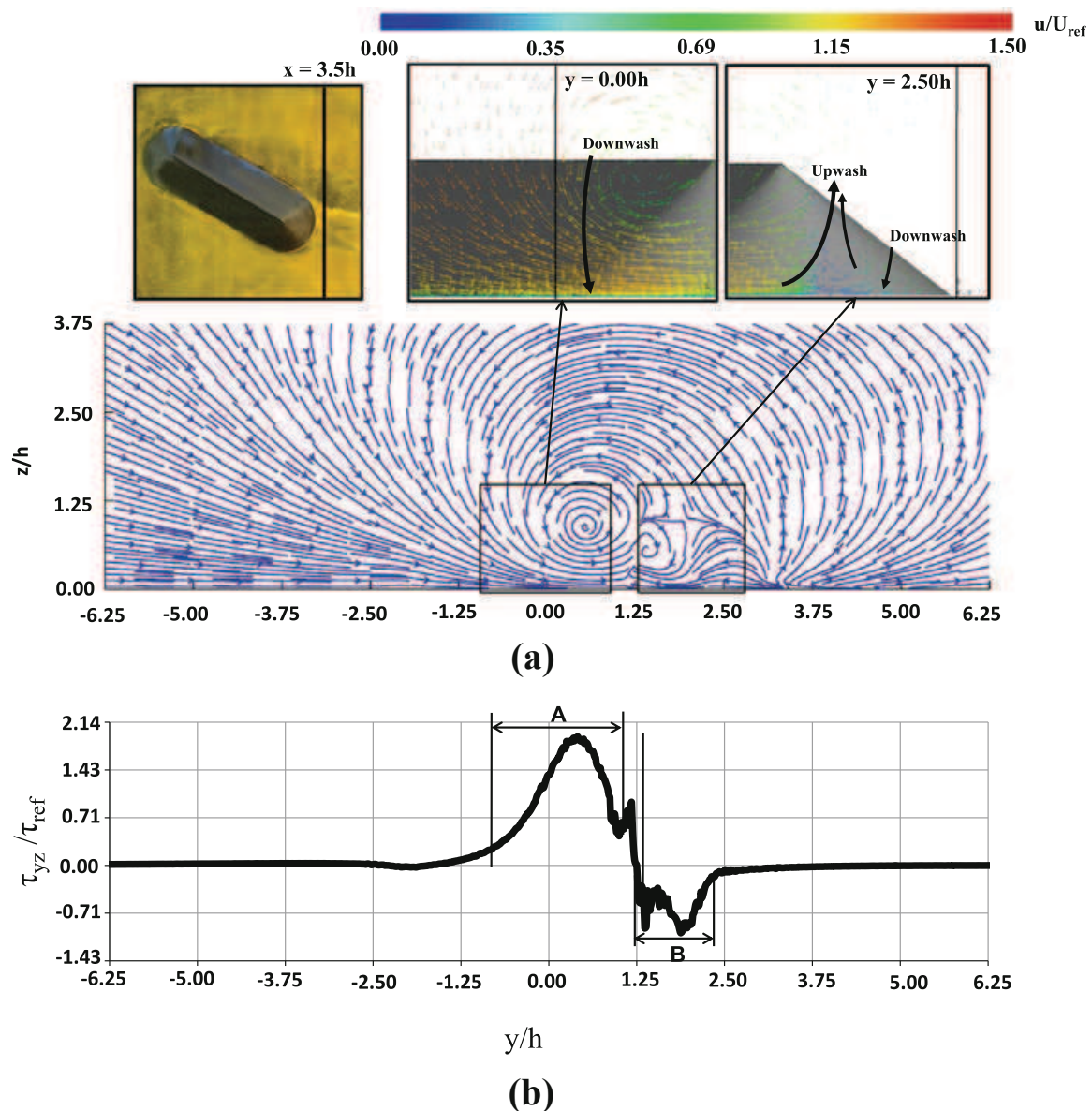


Fig. 15 Analysis in a transversal plane ($x/h = 3.5$) of the airflow topology for a stockpile oriented 30° to the wind flow direction: **a** streamlines calculated in the transversal plane, **b** plot of non-dimensional spanwise wall shear stress

see zone B in Fig. 15b). Finally, zones of downwash and upwash flows are also found, see inserts in Fig. 15a.

As in previous paragraph, the flow features depicted for these two configurations may be viewed as implied in possible fugitive emission from the surrounding ground of real industrial piles. Indeed the main longitudinal vortex and corresponding near flow downwash and upwash zones may transport dust emission from the near wake to far downstream.

5 Conclusions

Surface flow visualization around an oblong shape stockpile and corresponding airflow topology have been investigated. For a free-stream incoming airflow magnitude of 6.5 m/s, three angles of incidence have been analysed: 90° , 60° and 30° . An oil-film coating method and

numerical simulations validated by means of PIV measurements have been carried out to investigate wall shear distribution and airflow characteristics. Even if the airflow over the storage pile exhibits a complex three-dimensional topology, it was found that both numerical and experimental results were in good agreement allowing the possibility to analyse flow characteristics using both methods.

For the stockpile oriented 90° to the main flow, typical surface flow features of flow around wall-mounted obstacles were observed: stagnation zone upstream the pile, contra-rotating vortices in a low friction recirculation zone, and flow separation occurring on each lateral side and characterised by high friction levels. For the angles of incidence equal to 30° and 60° , high values of wall shear stress which are found in the near wake extend a certain distance (several h) downstream the stockpile.

The analysis of the airflow characteristics over the stockpile, made to complement the study of the near-wall flow, reveals important flow features. For the configuration where the storage pile model is perpendicular to the incoming flow, two main helical three-dimensional vortices are noticed. They are found to grow near the wall surface with an upward motion and then develop horizontally towards the downstream direction. For the two other configurations (angles of incidence equal to 30° and 60°), a single main longitudinal vortex is developing from the stockpile crest with its axis aligned with the main flow direction. Additionally a contra-rotative induced secondary vortex is noticed near the wall. In accordance with these flow topologies, downwash and upwash zones are identified.

Finally it is worth to note that both airflow turbulent structures and areas of high friction levels may be linked to potential dust emission from the ground surface surrounding industrial stockpiles. This quantification analysis is left for future work.

Acknowledgements This work was carried out with the financial support of EDF R&D.

References

1. AbuOmar MM, Martinuzzi RJ (2008) Vortical structures around a surface-mounted pyramid in a thin boundary layer. *J Wind Eng Ind Aerodyn* 96:769–778
2. Badr T, Harion J-L (2005) Numerical modelling of flow over stockpiles: implications on dust emissions. *Atmos Environ* 39:5576–5584
3. Badr T, Harion J-L (2007) Effect of aggregate storage piles configuration on dust emissions. *Atmos Environ* 41:360–368
4. Chen T, Liou L (2011) Blockage corrections in wind tunnel tests of small horizontal-axis wind turbines. *Exp Therm Fluid Sci* 35:565–569
5. Desreumaux O, Bourez JP (1989) Préparation de bouillies pour visualisation pariétales sur maquette de sous-marin à CEPRA 19. Rapport de l'Institut de Mécanique des Fluides de Lille (IMFL), numéro 89/19
6. Diego I, Pelegry A, Torno S, Toraño J, Menendez M (2009) Simultaneous CFD evaluation of wind flow and dust emission in open storage piles. *Appl Math Model* 33:3197–3207
7. Ferreira AD, Lambert RJ (2011) Numerical and wind tunnel modeling on the windbreak effectiveness to control the aeolian erosion of conical stockpiles. *Environ Fluid Mech* 11:61–76
8. Ferreira A, Fino M (2012) A wind tunnel study of wind erosion and profile reshaping of transverse sand piles in tandem. *Geomorphology* 139(140):230–241
9. FLUENT User's guide V6.3. <http://www.ansys.com/Products/Simulation+Technology/Fluid+Dynamics/ANSYS+Fluent>
10. Gowardhan A, Pardyjak E, Senocak I, Brown M (2011) A CFD-based wind solver for an urban fast response transport and dispersion model. *Environmental Fluid Mechanics*. doi:10.1007/s10652-011-9211-6
11. Guiming T (1994) Surface oil flow technique and liquid crystal thermography for flow visualization in impulse wind tunnels. *Acta Mech Sin* 10:220–226
12. Havel B, Hangan H, Martinuzzi R (2001) Buffeting for 2D and 3D sharp-edged bluff bodies. *J Wind Eng Ind Aerodyn* 89:1369–1381

13. Lee H-W, Park JJ, Lee JS (2002) Flow visualization and film cooling effectiveness measurements around shaped holes with compound angle orientations. *J Heat Mass Transf* 45:145–156
14. Leeuw WC, Pagendarm H-G, Post FH, Walter B (1995) Visual simulation of experimental oil-flow visualization by spot noise images from numerical flow simulation. In: Sixth Eurographics workshop on visualization in scientific computing, vol 50. Springer, Wien, pp 150–165
15. Mosharov VY, Radchenko N (2009) Method of gas or liquid flow visualization on an object surface. <http://www.patentstorm.us/applications/20090038407/fulltext.html>
16. Pagendarm HG, Post H (1995) Comparative visualization—approaches and examples. *Vis Sci Comput* 15:95–108
17. Sada K, Sato A (2002) Numerical calculation of flow and stack-gas concentration fluctuation around a cubical building. *Atmos Environ* 36:5527–5534
18. Santos JM, Reis NC, Goulart EV, Mavroidis I (2009) Numerical simulation of flow and dispersion around an isolated cubical building: the effect of the atmospheric stratification. *Atmos Environ* 43:5484–5492
19. Shi RF, Cui GX, Wang ZS, Xu CX, Zhang ZS (2008) Large eddy simulation of wind field and plume dispersion in building array. *Atmos Environ* 42:1083–1097
20. Takeda K, Kato M (1992) Wind tunnel blockage effects on drag coefficient and wind-induced vibration. *J Wind Eng Ind Aerodyn* 42:897–908
21. Toraño J, Torno S, Diego I, Menendez M, Gent M (2009) Dust emissions calculations in open storage piles protected by means of barriers, CFD and experimental tests. *Environ Fluid Mech* 9:493–507
22. Turpin C (2010) Amélioration des modèles de quantification des émissions particulaires diffuses liées à l'érosion éolienne de tas de stockage de matières granulaires sur sites industriels. PhD Thesis, University of Valenciennes, Industrial Energy Department, Ecole de Mines de Douai, France
23. Turpin C, Harion J-L (2009) Numerical modelling of flow structures over various flat-topped stockpiles height: implications on dust emissions. *Atmos Environ* 43:5579–5587
24. Turpin C, Harion J-L (2010) Effect of the topography of an industrial site on dust emissions from open storage yards. *Environ Fluid Mech* 10:677–690
25. US EPA (1985) Windbreak effectiveness for storage-pile fugitive-dust control. A wind Tunnel Study. Department of Marine, Earth and Atmospheric Sciences, North Carolina State University, EPA, NC 27695-8208
26. US EPA (2006) Miscellaneous sources, industrial wind erosion, AP-42, 5th edn, vol I, Chap 13.2.5, November 2006. <http://www.epa.gov/ttn/chief/ap42/ch13/final/c13/final/c13s0205.pdf>

4.1.2 Aeolian erosion of storage piles yards: contribution of the surrounding areas

Previous section has shown, numerically and experimentally, on the ground region surrounding oblong stockpiles, potential zones of particles take-off. As it was depicted, this subject is of great significance as a good part of the industrial sites presents the ground region strongly charged with silt particles. Thus, the objective is to present a quantification of these particles take-off which we can call re-emission. It presents the emission quantification of the dust re-emission from the ground region surrounding the stockpile and the comparison to the emissions calculated on the stockpile surface. The USEPA (2006) [75] is used with that aim. Input parameters of the model, for instance, surface and threshold friction velocity, are taken otherwise to fit the new conditions established for the quantification of emissions from the ground region. Thus, this subsection presents the results as an article entitled **"Aeolian erosion of storage piles yards: contribution of the surrounding areas"** submitted to the **"Environmental Fluid Mechanics"** journal. The status is currently under review.

Aeolian erosion of storage piles yards: contribution of the surrounding areas

Furieri, B · Santos, J M · Russeil, S ·
Harion, J-L

Received: ? / Accepted: ?

Abstract Dust emissions from stockpiles surfaces are often estimated applying mathematical models such as the widely used model proposed by the USEPA. It employs specific emission factors, which are based on the fluid flow patterns over the near surface. But, some of the emitted dust particles settle downstream the pile and can usually be re-emitted which creates a secondary source. The emission from the ground surface around a pile was not yet an interest for previous works that used the USEPA model for dust emission quantification. Nevertheless, two input parameters can be chosen judiciously to fit the specific conditions of this secondary source: threshold friction velocity and the dimensions of the area region where the re-emission may occur. This work aims to quantify the contribution of dust re-emission from the areas surrounding the piles in the total emission of an open storage yard. Three angles of incidence of the incoming wind flow are investigated (30° , 60° and 90°). Results of friction velocity from numerical modelling of fluid dynamics were used in the USEPA model to determine dust emission. It was found that as the wind velocity increases, the contribution of particles re-emission from the ground area around the pile in the total emission also increases. The dust emission from the pile surface is higher for piles oriented 30° to the wind direction. On the other hand, considering the ground area around the pile, the 60° configuration is responsible for higher emission rates (up to 43%). The global emissions assumed a minimum value for the piles oriented perpendicular to the wind direction for all wind velocity investigated.

Keywords Re-emission of settled dust · Dust emission quantification · USEPA model · CFD

Furieri, B
Mines Douai
948, Rue Charles Bourseul
59500 - Douai - France
Tel.: +33 3 27 71 23 86
Fax: +33 3 27 71 29 15
E-mail: bruno.furieri@mines-douai.fr

1 Introduction

Diffuse sources such as open storage yards are commonly found at industrial sites. Aeolian erosion of granular material may cause release of large quantities of dust to the atmosphere. The estimation of dust emission from stockpiles is often carry out by two approaches: field measurements or mathematical models. The most widely used mathematical model to estimate dust emissions from stockpiles is that proposed by the United States Environmental Protection Agency (USEPA) [13]. This is an empirical model based on several experimental measurements that defines an emission factor which relates the average emission rate to an independent variable (for example, source mass or dimensions, production rate or number of sources). The emission factor used to estimate dust emission rates from stockpiles depends on the erosion potential which is a function of the friction velocity on the stockpile surface and the threshold friction velocity u_t^* (defined as the friction velocity above which particles take off). The USEPA model proposes a subdivision of the whole pile surface area into isosurfaces of the friction velocity. Each of these areas is treated as a distinctive source and the total dust emission is afterall calculated as a summation of the emissions from each area.

A literature review shows several works using the USEPA model to quantify dust emission rates from storage piles [1–3, 7, 8, 10, 11]. Badr and Harion [1] investigated the influence of wind flow conditions and pile dimensions (height and width) on dust emission rates of an aggregate storage pile using the USEPA model. Numerical simulations were carried out to obtain the needed local wind properties near the pile. The authors concluded that changing pile configuration can reduce dust emissions. It was also found that an intermediate pile height shape leads to lower dust emissions, reaching 24% of reduction from their maximum values. Toraño et al [7] also carried out a similar study on various shapes of piles. These authors found a strong influence of the wind flow on the typical fluid flow structures around a pile and consequently on the dust emission rates calculated by using the USEPA model. Toraño et al [7] also stated that a semicircular stockpile shape corresponds to lower emission rate when compared to conic and flat-topped stockpile shapes. Diego et al [2] carried out an implementation of the USEPA model in a commercial CFD package to calculate emission rates. They investigated a configuration of parallel stockpiles and found out that one pile works as a protection to the other pile. Toraño et al [8] studied the influence of wind barriers on dust emissions from storage piles using numerical simulation and the USEPA model and compared their results with literature data and industrial measurements. Their study has shown a reduction of about 66% on dust emission due to the existence of barriers. Turpin and Harion [10] based their work on the analysis of the great influence of the stockpile crest on the overall dust emission. Several clipping heights of flat-topped piles were examined to determine their impact on dust emission. The main conclusion was that the flattening of stockpile's crest does not reduce the pollution. Turpin and Harion [11] employed the USEPA model to investigate the influence of nearby buildings on dust emissions from stockpiles of real industrial sites. The complex configuration of these sites was simulated: three stockpiles and several rectangular and cylindrical buildings. The remarkable influence of the obstacles on the total stockpile dust emissions was highlighted by these results. Ferreira et al [3] performed numerical and experimental simulations of fluid flow around a conical pile under atmospheric flow conditions influenced by wind barriers. Although these authors have not quantified dust emissions, they compared the u_s/u_r distribution to experimental results of pile erosion and a consistent correlation was observed.

The studies described above used different techniques to investigate the influence of various parameters on the emission rate. However, it is worth to note that, these works did not take into account the emissions from the ground surface around the stockpiles. In industrial sites, the vicinity of a stockpile is significantly loaded with small granular particles originated from: piles perturbations, pile erosion or transport of material in the surrounding regions. Furieri et al [5] have previously studied the near wall flow features (by the oil-film flow visualization technique) and three-dimensional air flow structure around piles (using numerical simulations validated by PIV measurements). The presence of regions of potential particles take-off from the ground was highlighted by the authors.

The present work aims to quantify the amount of particles emitted from the stockpile and from the ground surface around the pile. The friction velocity distribution on the pile surface and on the ground around the pile is calculated by using CFD. The USEPA model, usually employed to quantify the amount of particles from the stockpile, is used here to quantify emissions from the surrounding ground region. The contribution of particles re-emission from the ground around a pile in the overall dust emission from an open storage yard is discussed considering three different stockpiles orientations and its dependence on wind velocity magnitude.

2 Numerical simulation background

Numerical simulations were performed to solve the three-dimensional Reynolds Averaged Navier-Stokes equations governing the flow around the stockpile using a finite volume based CFD code [4]. Fig. 1 shows the computational domain and the boundary conditions. The dimensions of the real stockpile were scaled-down by a factor of 1:200 for numerical simulations: 0.578 m (width), 0.205 m (length) and 0.08 m (height). The model tested was an oblong stockpiles with an angle of repose equal to 38° [12] representative of coal piles commonly found in real industrial sites. Spanwise and vertical dimensions correspond to the wind-tunnel dimensions where PIV experiments were carried out to validate the results of numerical simulations, see Turpin [9]. Dimensions of upstream and downstream zones were chosen to ensure that the results are not influenced by the size of the domain. In fact, the vertical dimension of the computation domain was set as half of the wind-tunnel height. Turbulence effects were accounted for by using the $k-\omega$ Shear Stress Transport (SST) model with the option Transitional Flow (available on the FLUENT package [4]). This option yields the enhancement of certain modelling conditions: adverse pressure gradient, flow separation and reattachment [10,9]. Mesh size was chosen based on sensitivity tests previously carried out by Badr and Harion [1] for the same configurations. The size of the first cell at the wall was taken as $z^+ = 4$ ($z^+ = \rho u^* z / \mu$), as required for the use of this turbulent model ($z^+ \leq 5$) to ensure that no wall functions are used (for better accuracy) to account for the turbulence damping near walls. The mesh is produced by an extrusion from triangular cells defined on the ground surface and pile walls (see Fig. 2(a)) towards the top boundary of the computational domain (see Fig. 2(b)).

The inlet boundary conditions for velocity (u , v and w), turbulent kinetic energy (k) and specific dissipation rate (ω) were obtained from previous numerical simulations of a flow in a channel with the same dimensions (height and width) of the computational domain used in the present work. In these previous simulations, a periodic streamwise flow was set to produce a fully developed channel flow and the converged flow field is

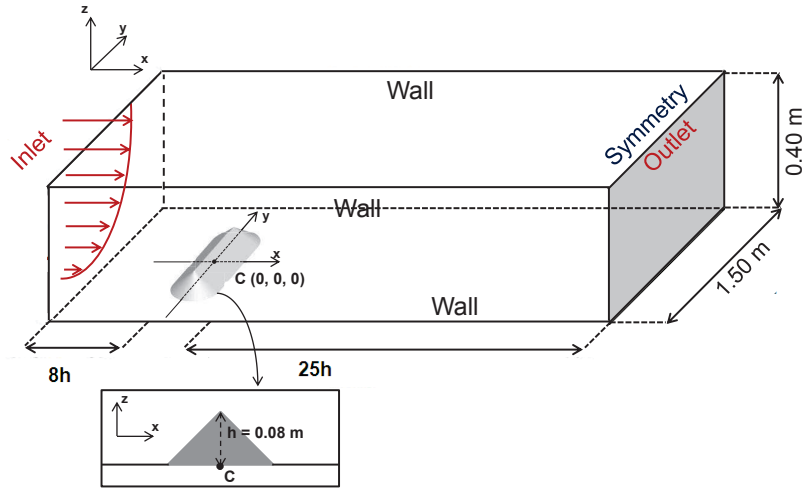


Fig. 1 Schematic configuration of the computational domain and boundary conditions.

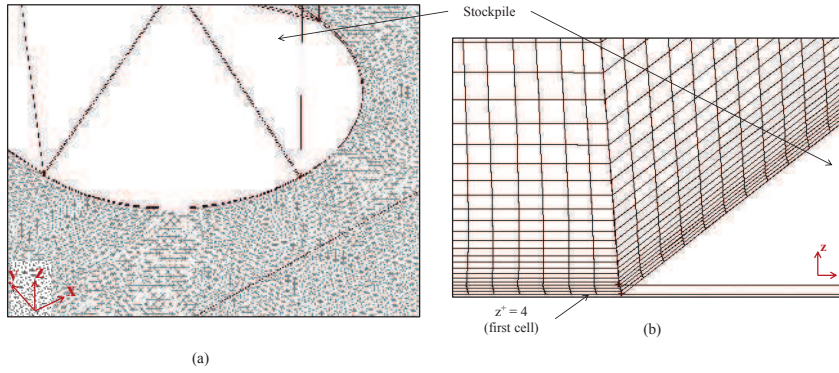


Fig. 2 Mesh (a) on the ground surface ($z=0$) around the pile and (b) above the stockpile surface on the symmetry plane ($y=0$).

considered to be the inlet condition for the present simulation. For the outlet boundary conditions, it is assumed that the flow is fully developed and for the upper boundary condition, symmetry was imposed. Finally, smooth walls with no-slip conditions are set at domain lateral walls, as well, at stockpile and ground walls. Further details of the numerical procedure can be found in Turpin [9].

3 USEPA model to estimate aeolian dust emission

This section presents two distinctive parts. At first, the USEPA mathematical model is described in details by an algorithm. Each parameter is also presented with the expla-

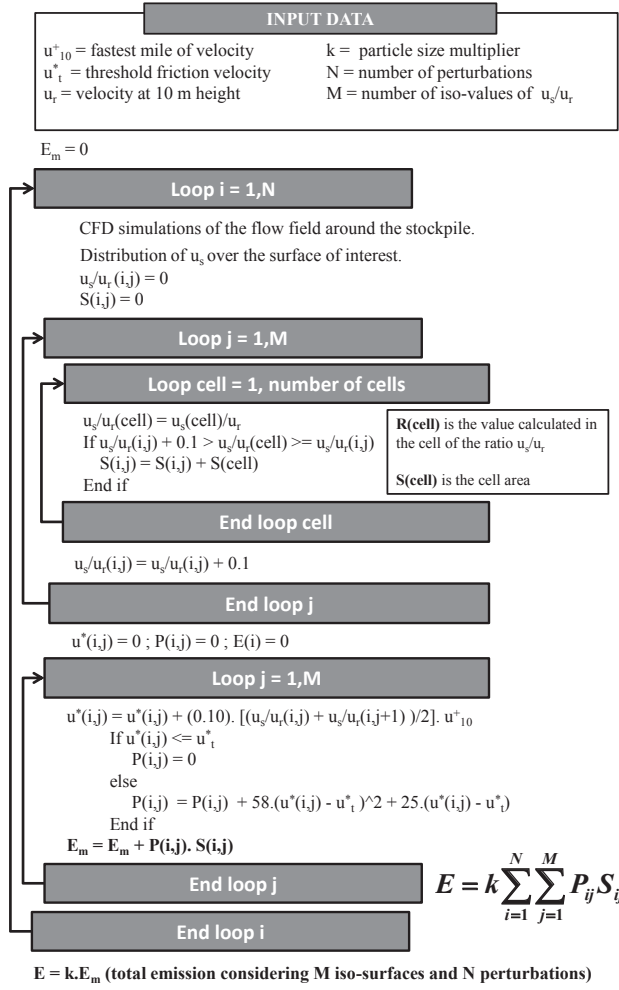


Fig. 3 USEPA model algorithm.

131 nation of the chosen value in our study. The second part deals with the discretisation
 132 levels that are obtained when CFD simulations are used.

133 3.1 Mathematical model set-up

134 The model used for the assessment of dust emission [13] is presented herein under
 135 an algorithm chart in Fig. 3. Several input data are required: particle size multiplier
 136 (taken for the average particles size) (k), wind erosion threshold friction velocity (u_t^*),
 137 distribution of u_s/u_r on the surface of interest (u_r is the reference velocity at 10 m
 138 height from the ground and u_s is the velocity at 25 cm from the surface, both for
 139 real scale), number of perturbations (N), number of isosurfaces of u_s/u_r (M) and the

highest velocity value (fastest mile wind speed) measured by an anemometer at a reference height for a period between perturbations (u_{10}^+).

A perturbation is defined in the USEPA guide [13] as an intervention done on a storage pile yard for maintenance and transport of material. The first loop concerns the number of perturbation per year (operations on pile's surfaces). For the sake of simplification, the results of dust emission in the present work are presented in kg per perturbation. The number of perturbations should be defined for a practical application of emission quantification on a real industrial site.

It is worth to note that, the u_s/u_r ratios which are obtained by CFD calculations are strongly influenced by the wind flow direction, which changes during a day in industrial sites. The threshold friction velocity value is subjected to particle matter characteristics, such as granulometry, density, moisture and, if existent, surface treatment. The friction velocity is calculated based on the ratio between near wall velocity u_s and free stream velocity u_r .

The USEPA model is based on emission factors, see Equation 1. The methodology consists in implementing Equation 1 to calculate the emission rate (E). The whole pile surface is divided in different subareas each representing a given level of wind erosion exposure, i. e., a value of the ratio u_s/u_r . Each subarea is then considered as a single source (this explains the summation in Equation 1).

$$E = k \sum_{i=1}^N \sum_{j=1}^M P_{ij} S_{ij} \quad (1)$$

where P_{ij} is the erosion potential (g/m^2) and S_{ij} (m^2) is the fraction of the surface area (subarea) corresponding to a constant value of u_s/u_r . In this equation, the erosion potential is calculated based on the difference between the friction velocity (u^*) for the fastest mile of the wind and the wind erosion threshold friction velocity (u_t^*) as shown in Equation 2.

$$\begin{cases} P = 58 (u^* - u_t^*)^2 + 25 (u^* - u_t^*) & \text{for } u^* > u_t^* \\ P = 0 & \text{for } u^* \leq u_t^* \end{cases} \quad (2)$$

The friction velocity is then calculated as presented in Equation 3 which is based on the logarithmic velocity profile of the undisturbed surface boundary layer. However, for the fluid flow disturbed by a stockpile the USEPA model proposes Equation 4 to determine friction velocity.

$$u^* = 0.053 u_{10}^+ \quad (3)$$

$$u^* = 0.10 \left(\frac{u_s}{u_r} \right) u_{10}^+ \quad (4)$$

Fig. 4a shows an example of typical contours of u_s/u_r calculated by numerical simulations. From the calculation of the friction velocity we can define erodible and non-erodible zones over the surfaces of interest. Zones with friction velocity greater than the erosion threshold value are denominated erodible. On the other hand, for $u^* < u_t^*$, zones are called non-erodible. Larger values of u_s/u_r are found downstream the stockpile. Wall shear stress and friction velocity values are also large. On the other hand, in the stagnation zone, upstream the pile, the lowest levels of u_s/u_r are noticed.

Table 1 Chosen values of u_s/u_r to be replaced in the equations of the USEPA methodology of dust quantification: in left of the table those originally proposed by the model and in right those taken from numerical simulations.

USEPA model [13]		Reference works	
u_s/u_r range	Chosen Value	u_s/u_r range	Chosen Value
$0.0 \leq u_s/u_r < 0.4$	0.20	$0.0 \leq u_s/u_r < 0.1$	0.05
		$0.1 \leq u_s/u_r < 0.2$	0.15
		$0.2 \leq u_s/u_r < 0.3$	0.25
		$0.3 \leq u_s/u_r < 0.4$	0.35
$0.4 \leq u_s/u_r < 0.8$	0.60	$0.4 \leq u_s/u_r < 0.5$	0.45
		$0.5 \leq u_s/u_r < 0.6$	0.55
		$0.6 \leq u_s/u_r < 0.7$	0.65
		$0.7 \leq u_s/u_r < 0.8$	0.75
$0.8 \leq u_s/u_r < 1.0$	0.90	$0.8 \leq u_s/u_r < 0.9$	0.85
		$0.9 \leq u_s/u_r < 1.0$	0.95
$u_s/u_r \geq 1.0$	1.10	$1.0 \leq u_s/u_r < 1.1$	1.05
		$1.1 \leq u_s/u_r < 1.2$	1.15
		$1.2 \leq u_s/u_r < 1.3$	1.25
		$1.3 \leq u_s/u_r < 1.4$	1.35
		$1.4 \leq u_s/u_r < 1.5$	1.45
		$1.5 \leq u_s/u_r < 1.6$	1.55
		$1.6 \leq u_s/u_r < 1.7$	1.65

Reference works = Badr and Harion (2007) [1] and Turpin and Harion (2009) [10]

Finally, the dashed ellipses presented in Fig. 4a are examples of areas over the ground surface in which the surface boundary layer is not disturbed by the stockpile. It can be checked by the values of u_s/u_r on these regions. Indeed, from the logarithmic law governing an undisturbed wind velocity profile [6] for a roughness height equal to 0.03 m (open flat terrain) [14] the value of u_s/u_r over an undisturbed region is approximately 0.366 (see Fig. 6). This value is identical to that found in the numerical simulation (highlighted in the colormap of u_s/u_r values in Fig. 4a).

In order to calculate the re-emission of silt particles settled on the ground surface around the stockpile, two input parameters of the formulations presented above (Equations 1 to 4) have different values to that usually used to assess the emissions from the stockpile surface.

Firstly, a delimited surface S must be defined around the pile to represent the region in which the amount of settled dust has to be assessed. The choice of the dimensions of this area should be driven by the quantity of material emitted by the stockpile surface and on how far it accumulates or other source such as material transport and pile maintenance and can be determined by field observations in industrial sites. The dimensions of the surface S were defined arbitrarily by the authors as about ten times the stockpile surface area (Fig. 5). Fig. 5 then presents the two characteristic regions: (i) the stockpile vicinity is the surface taken into account to calculate the re-emission and (ii) the zone far away from the stockpile where the ratio u_s/u_r is approximately equal to 0.366 (undisturbed velocity profiles).

The second parameter to be chosen is the erosion threshold friction velocity for the surrounding regions. The USEPA guide gives values of u_t^* for several materials and conditions and among them the value for the ground surrounding a stockpile (cf. Table 13.2.5-2 in US-EPA [13]). For coal on the ground surface around the pile a value of 0.55 m/s is proposed. It can be compared to the value of 0.35 m/s that was used in the calculation of dust emission from the stockpile surface. The value for the stockpile surface was determined from wind-tunnel experiments (cf. Turpin and Harion [10]).

The other input values, aerodynamic particle size multiplier (k) and fastest mile of the wind velocity (u_{10}^+), remain unchanged and are equally used in both quantifications

on and around the stockpile. The aerodynamic particle size multiplier (k), as indicated by the USEPA model, assumes a value for each aerodynamic particle size (cf. Section 13.2.5.3 in USEPA [13]). The value of k equal to 0.5 was chosen to represent PM_{10} emissions.

Three values of the fastest mile of the wind velocity (u_{10-A}^+ , u_{10-B}^+ and u_{10-C}^+) were chosen to represent different situations of dust re-emission:

- no dust emission at all (u_{10-A}^+),
- dust emission over the whole region (u_{10-B}^+),
- no dust emission over the undisturbed area (surface boundary layer) and emission from the region disturbed by the stockpile (u_{10-C}^+).

For the third case (u_{10-C}^+), the wind erosion friction velocity has to be chosen lower than the erosion threshold velocity around the piles, i. e., $u^* \leq 0.55m/s$. Then considering Equation 3 which links the friction velocity and the fastest mile wind velocity, the value of u_{10}^+ can be defined:

$$u_{10}^+ \leq 10.38m/s \quad (5)$$

Finally, a smaller and a greater value than $u_{10-C}^+=10.38$ m/s were chosen to represent the two other cases above mentioned: $u_{10-A}^+=5.0$ m/s and $u_{10-B}^+=15.0$ m/s.

3.2 Dust emission estimation using different subarea discretisation levels

The original USEPA model proposes a distribution of the u_s/u_r ratio for stockpiles based on wind-tunnel measurements (Fig. 6). Previous numerical studies (cf. Badr and Harion [1] and Toraño et al [7]) were carried out to investigate the u_s/u_r distribution on the pile surface. However, the USEPA model proposes a maximum of four subareas of u_s/u_r , mainly due to the feeble velocity distribution detail obtained by the wind-tunnel experiments in which the model is based on. Contrarily, the CFD technique yields to a detailed velocity distribution and thus it is possible to enlarge the number of subareas used in the emission model. For example, Badr and Harion [1] and Turpin and Harion [10] presented seventeen subareas for oblong stockpiles obtained by CFD presented in Fig. 7 (also, see Table 1). By comparing Fig. 6 and Fig. 7, it can be seen that the distribution of u_s/u_r is quite similar in both cases, although the maximum values of u_s/u_r are slightly different and, furthermore, these differences increase as the stockpile orientation becomes aligned to the wind direction.

Table 2 synthesizes a comparison between dust emission quantification using these different discretisation levels. Although, both methods indicate an increment in dust emission from the perpendicular configuration to the stockpile oriented 30° , the more refined discretisation applied by Badr and Harion [1] and Turpin and Harion [10] permits better interpretation of the stockpile wind exposure. The maximum difference found was approximately 11.2% and most cases showed differences reaching a maximum value of 5%. These differences are more pronounced for $u_{10}^+ = 5.0$ m/s. The results obtained by using the USEPA discretisation method may underestimate dust emission due to the fact that the USEPA model also underestimates the maximum values of u_s/u_r on the piles surface.

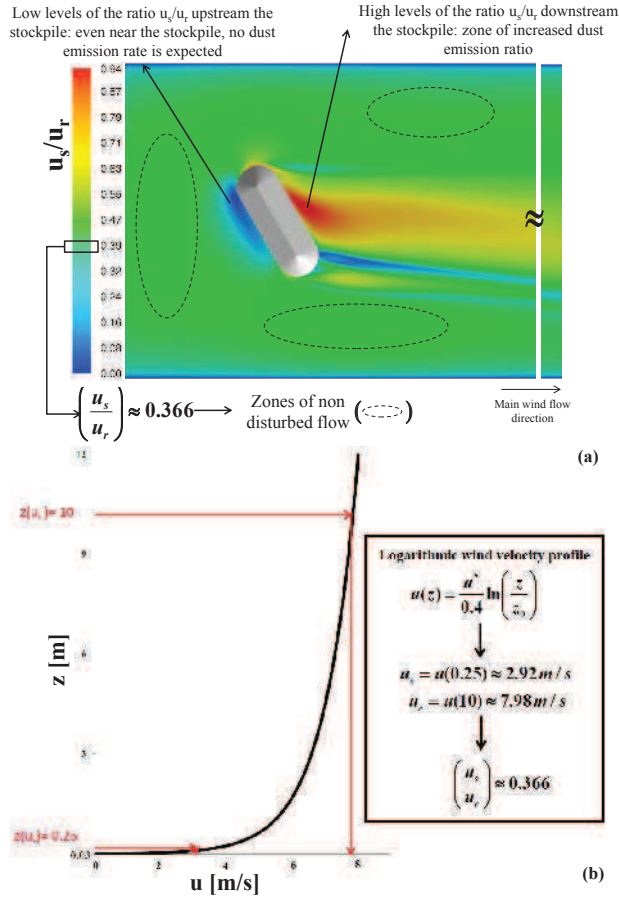


Fig. 4 (a) Typical contours of u_s/u_r on the horizontal plane parallel at 0.25 m above the ground surface (it corresponds to 0.00125 in the wind-tunnel and numerical scale). (b) Vertical logarithmic profile of wind velocity [6] that is used to calculate u_s/u_r in the undisturbed flow zones.

Table 2 Dust emission estimation for two different discretisation levels of u_s/u_r distribution.

u_{10}^+ m/s	Wind angle of incidence	Emission (kg/perturbation)		Difference (%)
		USEPA [13]	Reference works	
5.00	90°	0.7	0.8	7.4
	60°	1.4	1.5	9.2
	30°	1.4	1.6	11.2
10.38	90°	16.5	16.5	0.0
	60°	29.1	30.0	3.2
	30°	33.2	32.6	-1.7
15.00	90°	43.1	44.4	3.0
	60°	76.1	79.7	4.8
	30°	87.4	87.5	0.1

Reference works = Badr and Harion (2007) [1] and Turpin and Harion (2009) [10]

4 Results

4.1 Wind exposure of pile surface

Fig. 7 presents the distribution of u_s/u_r on the three piles' surfaces and features the influence of main wind direction. The scale of u_s/u_r values in the figure is the same

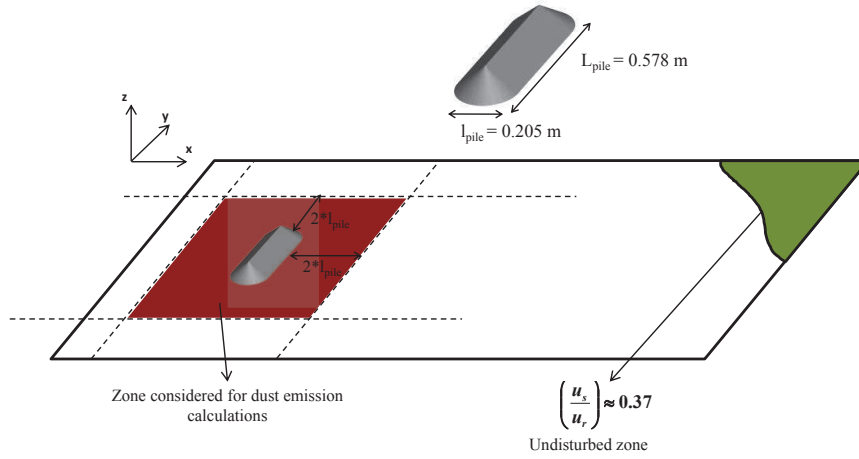


Fig. 5 Schematic representation of undisturbed zone away from the pile and zone considered for dust emission calculations including the stockpile and the ground surface where re-emission of settled particles may occurs (for perpendicular configuration).

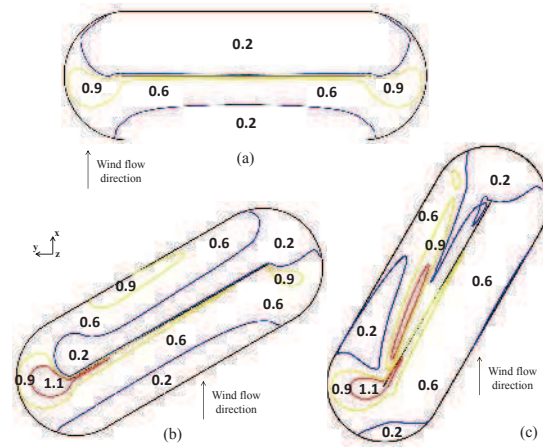


Fig. 6 Subdivision of the stockpile surface in four subareas corresponding to constant values of u_s/u_r as proposed by the USEPA for (a) perpendicular, (b) 60° and (c) 30° configurations.

for all orientations allowing a better visualization of the differences. In Fig. 7a, the stockpile is perpendicular to the wind direction and the maximum value of u_s/u_r is 0.98 which is the lowest among all investigated configurations. The highest levels of u_s/u_r are located on the pile crest and on both pile sides. In these regions, the flow is accelerated and detaches from the stockpile (Turpin and Harion [10]). The ratio u_s/u_r progressively increases with height on the windward wall. The minimum values of u_s/u_r are found on the leeward wall in the zone of recirculating flow.

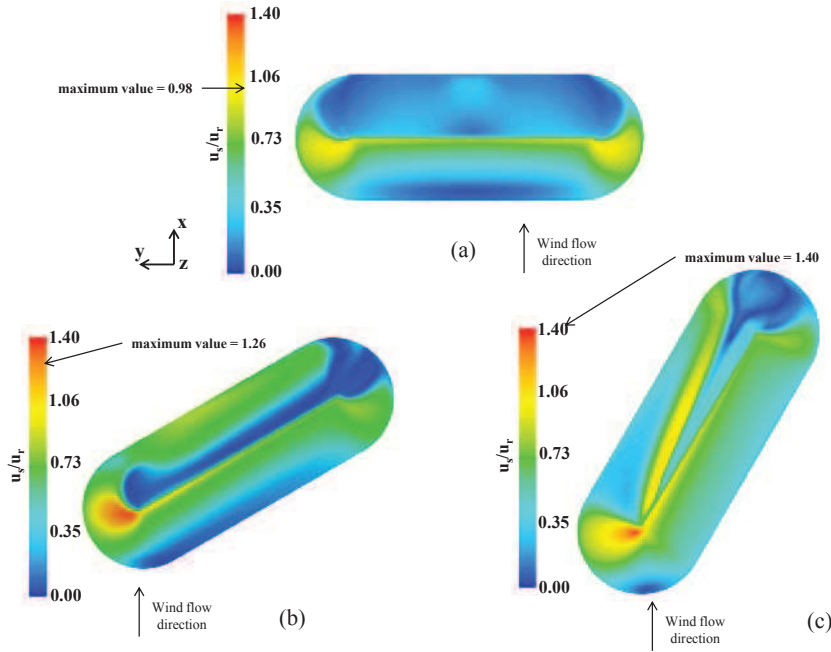


Fig. 7 Contours of u_s/u_r on the planes parallel to the stockpile surface at 0.25 m above the pile surface in real scale (it corresponds to 0.00125 in the wind-tunnel and numerical scale) for (a) perpendicular, (b) 60° and (c) 30° configurations.

The modification in the stockpile orientation deeply changes the u_s/u_r distribution, as is noticed in Figs. 7b and 7c. The u_s/u_r distribution patterns for the 60° configuration (Fig. 7b) shows that the highest levels of u_s/u_r are found on the left side of the windward wall (maximum value equal to 1.26) where an helical vortex arises and causes velocity augmentation (Turpin and Harion [10] and Furieri et al [5]). In this configuration, the helical vortex is also responsible for the high values of u_s/u_r on the leeward wall. The configuration 30° presents almost the same flow pattern as noticed for 60° except for some details downstream. The u_s/u_r distribution pattern for the 30° configuration (Fig. 7c) shows that the maximum values of the u_s/u_r are found on the pile crest and windward wall where large part of the surface exhibits values of u_s/u_r greater than 0.70 whereas for the perpendicular configuration it displays values between 0.10 and 0.50 and for the 60° configuration these values are in the range between 0.40 and 0.80.

4.2 Wind exposure of ground surface around a pile

Figs. 8a, 9a and 10a present u_s/u_r distribution on the ground around the stockpile for the whole domain. The zone near the stockpile considered in dust emission calculations (as defined in Fig. 5) is highlighted by means of dashed lines. Figs. 8b, 9b and 10b present the zones where friction velocity (u^*) is larger than the threshold friction velocity for the ground region ($u_t^* = 0.55$ m/s) for a situation in which u_{10}^+ is equal

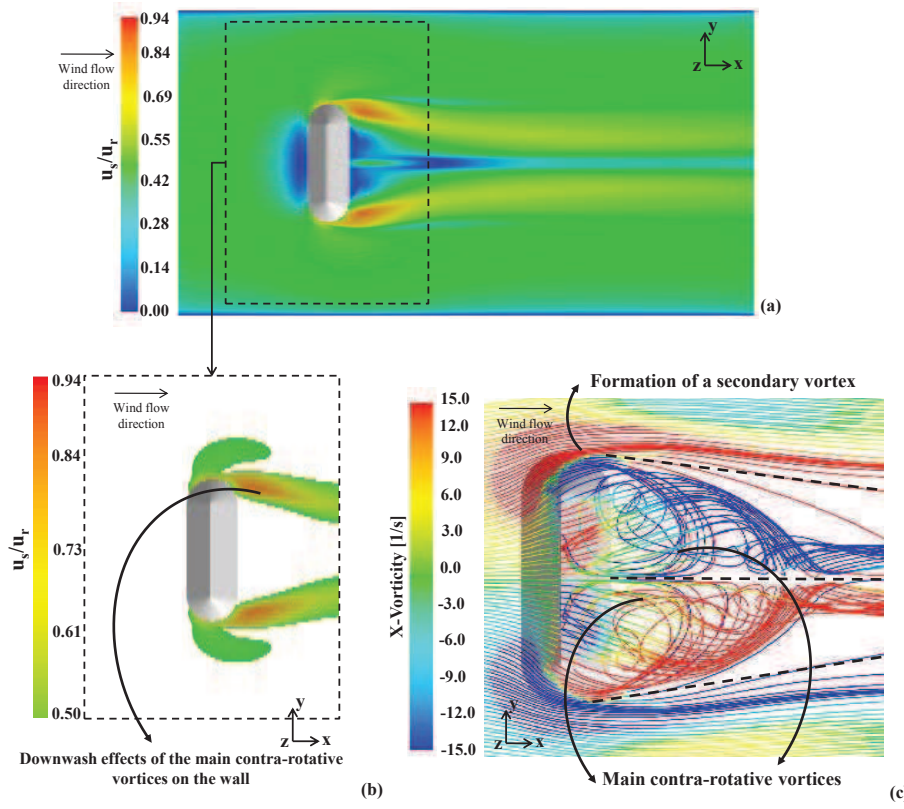


Fig. 8 Contours of u_s/u_r on the horizontal plane parallel at 0.25 m above the ground surface in real scale (it corresponds to 0.00125 in the wind-tunnel and numerical scale) for perpendicular configuration: (a) on the whole ground surface and (b) on the ground surface considered for dust emission calculations. (c) Streamlines coloured by the X-vorticity

to 10.38. These figures highlight only the contours of u_s/u_r larger than 0.50. From Equation 4, u_s/u_r values larger than 0.50 indicate a friction velocity larger than 0.57 m/s. Indeed, according to Equation 2, an emission event occurs as the friction velocity of the considered subarea is higher than 0.55 m/s which is the case for the highlighted regions. Finally, Figs. 8c, 9c and 10c represent the fluid flow streamlines over the stockpiles coloured by the streamwise component of the vorticity.

For the perpendicular configuration, the dust emission zones are located on both stockpile lateral sides as shown in Fig. 8. These are flow acceleration zones (Turpin and Harion [10] and Furieri et al [5]) where the flow structures formed due to the stockpile presence cause high levels of friction velocity and, consequently, particles take-off events. In the zone upstream the stockpile, as well as in the wake region, the friction velocity levels are lower and do not suggest the re-emission of settled dust. Fig. 8c shows main vortices developing. These vortices have opposite values of the X-vorticity meaning that they are contra-rotative. Moreover, the contours of the zones suggesting dust re-emission (Fig. 8b) indicate downstream the pile the downwash effects (fluid flow impinging vertically the ground causing high velocity gradient values) on the wall of these contra-rotative vortices. The lateral sides of each main vortex also

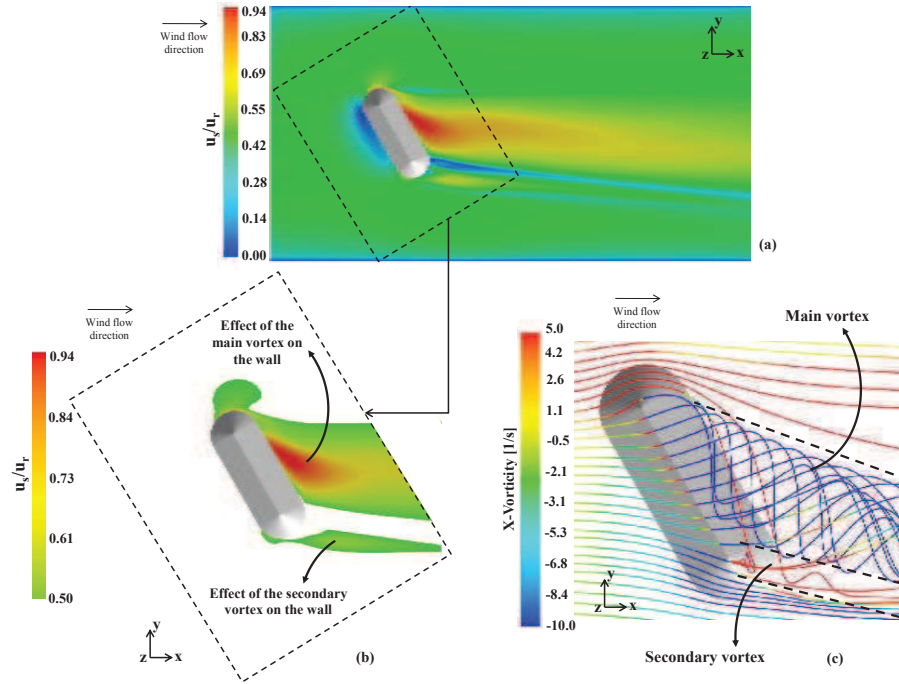


Fig. 9 Contours of u_s/u_r on the horizontal plane parallel at 0.25 m above the ground surface in real scale (it corresponds to 0.00125 in the wind-tunnel and numerical scale) for 60° configuration: (a) on the whole ground surface and (b) on the ground surface considered for dust emission calculations. (c) Streamlines coloured by the X-vorticity

present a secondary vortex, which is smaller and contra-rotative to the main vortex. The zones of formation of the secondary vortex are the flow acceleration.

Figs. 9a and 9b show the u_s/u_r distribution on the ground for the 60° configuration. The region of dust emission, in which the friction velocity is greater than the threshold friction velocity, is larger for this configuration. The main vortex formed downstream the pile and the intense velocity gradients near wall in this region downstream the pile (Turpin and Harion [10] and Furieri et al [5]) is the flow structure responsible for the high values of u_s/u_r that cause high wall shear stress. Fig. 9c show the single main vortex formed in this configuration. Also, in Fig. 9c, it is worth to note the secondary vortex with opposite values of X-vorticity which characterizes it as contra-rotative to the main vortex. Furthermore, the secondary vortex is responsible for a smaller zone of dust emission, highlighted in Fig. 9b.

Finally, Figs. 10a and 10b present the u_s/u_r distribution on the ground around the stockpile for the 30° configuration. Approximately, the values of u_s/u_r are in the range between 0.6 and 0.7, i.e. lower than those for the two other configurations investigated. In this orientation, as it was observed for 60°, there is a main vortex formed downstream the pile responsible for the zones of potential dust emissions. Figs. 10c shows the streamlines of this structure. The main vortex in this configuration is smaller and present lower effects on the ground than the one formed in the configuration 60°.

For all wind flow orientations, details about wall shear stress distribution, vortices, downwash and upwash zones are shown in the work of Furieri et al [5].

Table 3 Erodeable and non-erodeable areas for $u_{10}^+=10.38$ m/s on ($u_t^* = 0.35$ m/s) and around ($u_t^* = 0.55$ m/s) the stockpile.

u_s/u_r	u^* (m/s)	%			u_s/u_r	u^* (m/s)	%		
		On the stockpile					Around the stockpile		
		90°	60°	30°			90°	60°	30°
0.05	0.05	9.5	6.0	2.7	0.05	0.05	3.2	0.4	0.1
0.15	0.16	28.2	11.7	5.6	0.15	0.16	5.7	2.9	0.4
0.25	0.26	20.2	9.9	7.3	0.25	0.26	7.5	3.7	1.5
	Non-erodible	57.9	27.6	15.6	0.35	0.36	13.8	14.7	17.8
0.35	0.36	6.7	9.8	9.7	0.45	0.47	52.9	51.8	60.5
0.45	0.47	7.1	11.1	15.9		Non-erodible	83.1	73.5	80.3
0.55	0.57	7.4	13.0	20.3	0.55	0.57	8.6	10.5	10.1
0.65	0.67	6.7	13.9	15.3	0.65	0.66	6.5	11.2	5.8
0.75	0.78	5.9	12.2	10.9	0.75	0.77	1.8	3.4	3.8
0.85	0.88	5.4	7.5	5.4	0.85	0.88	0.0	1.4	0.0
0.95	0.99	2.9	2.3	3.5	0.95	0.99	0.0	0.0	0.0
1.05	1.09	0.0	1.4	2.4	1.05	1.10	0.0	0.0	0.0
1.15	1.19	0.0	0.9	0.6	1.15	1.21	0.0	0.0	0.0
1.25	1.30	0.0	0.3	0.3	1.25	1.32	0.0	0.0	0.0
1.35	1.40	0.0	0.0	0.1	1.35	1.43	0.0	0.0	0.0
1.45	1.50	0.0	0.0	0.0	1.45	1.54	0.0	0.0	0.0
1.55	1.61	0.0	0.0	0.0	1.55	1.65	0.0	0.0	0.0
1.65	1.71	0.0	0.0	0.0	1.65	1.76	0.0	0.0	0.0
	Erodible	42.1	72.4	84.4		Erodible	16.9	26.5	19.7

*Values in bold represent an accumulation of surface percentage

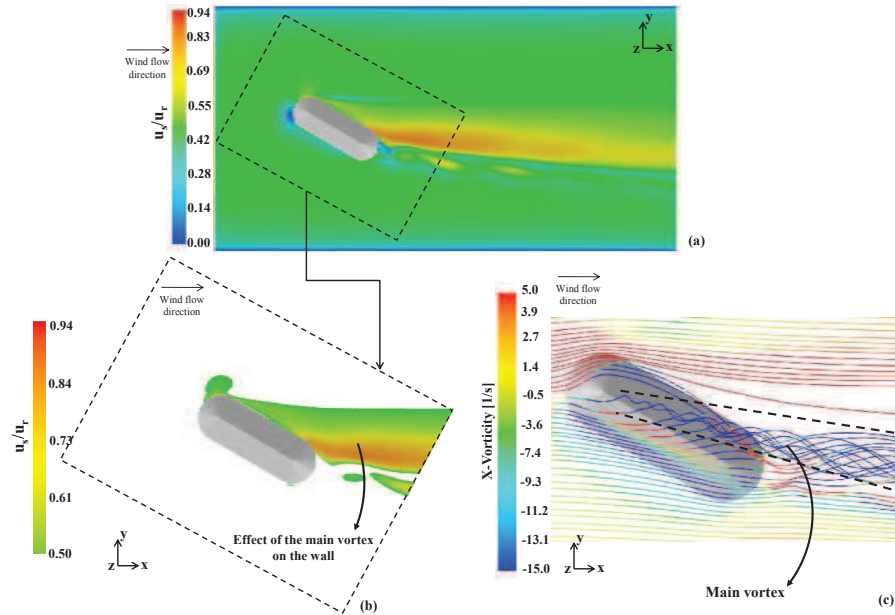


Fig. 10 Contours of u_s/u_r on the horizontal plane parallel at 0.25 m above the ground surface in real scale (it corresponds to 0.00125 in the wind-tunnel and numerical scale) for 30° configuration: (a) on the whole ground surface and (b) on the ground surface considered for dust emission calculations. (c) Streamlines coloured by the X-vorticity

4.3 Quantitative analysis of dust emissions

This section presents the results obtained by using the USEPA model previously presented in Section 3. Table 3 presents the percentage of erodeable and non-erodeable areas

Table 4 Dust emissions from stockpile surface and ground surface around the pile.

		Emissions (kg/perturbation)			Contribution (%)		
		u_{10}^+ (m/s)			u_{10}^+ (m/s)		
		5	10.38	15	5	10.38	15
Surface du tas	90°	0.8	16.5	44.4	100	67.7	34.2
	60°	1.5	30.0	79.7	100	57.1	32.8
	30°	1.6	32.6	87.5	100	71.8	41.1
Surface autour du tas	90°	0.0	7.9	85.2	0.0	32.3	65.8
	60°	0.0	22.6	163.5	0.0	42.9	67.2
	30°	0.0	12.8	125.6	0.0	28.2	58.9
Emissions globales	90°	0.8	24.4	129.6			
	60°	1.5	52.6	243.2			
	30°	1.6	45.4	214.1			

on and around the stockpile (based on the total area of the considered surface, see Fig. 5) that are calculated by summation of subareas for each u_s/u_r range (see Equation 1). The friction velocity was calculated using u_{10}^+ equal to 10.38 m/s as presented in Equation 5. The erodible area on the stockpile was found larger for the 30° configuration than for the other configurations, reaching about two times the value calculated for the perpendicular configuration. The results in Table 3 showed that the erodible area around the stockpile, for all configurations, is smaller than the erodible area on the stockpile surface. It can be explained by the fact that the threshold friction velocity is higher for the region around the stockpile and the ratio of u_s/u_r is higher on the stockpile surface. Thus, for the perpendicular configuration, the percentage of erodible area is equal to 42.1% on the stockpile and 16.9% around the pile. For the 60° and 30° configurations, respectively, these values are 72.4% and 26.5%, and 84.4% and 19.7%. In addition, the results presented in Table 3 shows that the highest percentage of erodible area on pile surface was found for the 30° configuration and around the pile the same trend was found for the 60° configuration. This large erodible area around the stockpile for the 60° configuration may be explained by the intense and larger main vortex formed downstream the pile close to the leeward wall and extended to the far wake region.

Table 4 synthesizes the overall data of dust emission estimation from stockpile surface and ground surface around the pile. The emission rates are calculated for different values of u_{10}^+ . For all the values of u_{10}^+ investigated, the stockpile emissions are higher for the 30°. For instance, if $u_{10}^+ = 10.38$, in this configuration the emission per perturbation is equal to 32.6 kg whereas for the 60° and 90° configurations it was found equal to 30.0 and 16.5 kg, respectively. The ground surface surrounding the pile gives the highest values of dust emissions for the 60° configuration (22.6 kg for $u_{10}^+ = 10.38$) while the other configurations it gives smaller values of dust emissions per perturbation (7.9 kg for 90° configuration and 12.8 kg for 30° configuration for the same fastest mile of the wind velocity). Table 4 illustrates the importance of re-emission by showing that the existence of silt particles on the ground around the pile and their emission due to the wind erosion cannot be neglected. For u_{10}^+ equal to 10.38 m/s, the contribution of re-emission is approximately 30% for the 90° and 30° configurations and reaches about 43% for the 60° configuration. For u_{10}^+ equal to 15 m/s, the contribution of re-emission doubles while for u_{10}^+ equal to 5 m/s, the re-emission is found to be negligible.

5 Conclusions

A quantitative investigation of particles re-emission from the regions surrounding stockpiles by using the USEPA methodology was presented. In order to estimate emissions rates from the ground surface around the stockpile, some input parameters have specific values to fit the conditions of this region: threshold friction velocity and the dimensions of the region where the re-emission may occur. The influence of the fastest mile of the reference velocity and pile orientation in relation to wind direction were investigated.

The value of k equal to 0.5 was chosen to represent PM_{10} emissions from both regions analysed. The threshold friction velocity equal to 0.55 m/s was applied for particles take-off from the ground surface around the pile and 0.35 m/s for emissions from the stockpile surface. The fastest mile of the reference velocity equal to 10.38 m/s was taken as the limit value for which there is no emission from the undisturbed region in the vicinity of the stockpile. Under these conditions the ground surface where re-emission can occur is delimited by u_s/u_r greater than 0.50.

The present investigation shows that (i) there exists a zone of particles take-off downstream the pile and its size depends on the incoming wind flow direction and (ii) the contribution of re-emission of dust particles settled around in global emissions is significant.

It was established that as the wind velocity increases, the contribution of re-emission also increases. In fact, among the wind velocities tested, for values lower than 5 m/s, no contribution of re-emission in the global emission was found. The dust emission from the pile surface is larger for 30° configuration. On the other hand, considering the ground surface around the pile, the 60° configuration is responsible for a greater emission rate. The contribution of the re-emission in the global emissions has indicated a maximum value of 43% for the 60° configuration for $u_{10}^+ = 10.38$ m/s. It can be concluded that for u_{10}^+ equal or greater than 10.38 m/s, re-emission from the ground surface around the pile must not be neglected or, as a consequence, the global emission from an open stockpile yard will be underestimated. Finally, the global emissions assumed a minimum value for the piles oriented perpendicular to the wind direction for all wind velocity investigated.

6 Acknowledgements

This work was carried out with the financial support of EDF R&D.

References

1. Badr T., Harion J.-L., 2007. Effect of aggregate storage piles configuration on dust emissions. *Atmospheric Environment* 41, 360-368.
2. Diego I., Pelegry A., Torno S., Toraño J., Menendez M., 2009. Simultaneous CFD evaluation of wind flow and dust emission in open storage piles. *Applied Mathematical Model* 33, 3197-3207.
3. Ferreira A., Lambert R., 2011. Numerical and wind tunnel modeling on the windbreak effectiveness to control the aeolian erosion of conical stockpiles. *Environmental Fluid Mechanics*. DOI 10.1007/s10652-010-9176-x.
4. FLUENT User's guide V6.3. <http://www.ansys.com/Products/Simulation+Technology/Fluid+Dynamics/ANSYS+Fluent>

5. Furieri B., Russeil S., Harion J-L., Santos J. M., 2012. Experimental surface flow visualization and numerical investigation of flow structure around an oblong stockpile. *Environmental Fluid Mechanics* (Accepted for publication).
6. Hsu S.A., Meindl E.A., Gilhousen D.B. 1994. Determining the Power-Law Wind-Profile Exponent under Near-Neutral Stability Conditions at Sea. *J. Appl. Meteor.* 33, 757-765.
7. Toraño J., Rodrigues R., Diego I., Rivas J. M., Pelegry A., 2007. Influence of the pile shape on wind erosion CFD emission simulation. *Applied Mathematical Modelling* 31, 2487-2502.
8. Toraño J., Torno S., Diego I., Menendez M., Gent M., 2009. Dust emissions calculations in open storage piles protected by means of barriers, CFD and experimental tests. *Environmental Fluid Mechanics* 9, 493-507.
9. Turpin C., 2010. Amélioration des modèles de quantification des émissions particulaires diffuses liés à l'érosion éolienne de tas de stockage de matières granulaires sur sites industriels. PhD Thesis, University of Valenciennes, Industrial Energy Department, Ecole de Mines de Douai.
10. Turpin C. Harion J.-L., 2009. Numerical modelling of flow structures over various flat-topped stockpiles height: implications on dust emissions. *Atmospheric Environment* 43, 5579-5587.
11. Turpin C., Harion J.-L., 2010. Effect of the topography of an industrial site on dust emissions from open storage yards, *Environmental Fluid Mechanics* 10, 677-690.
12. USEPA, 1985. Windbreak effectiveness for storage-pile fugitive-dust control. A wind Tunnel Study. Department of Marine, Earth and Atmospheric Sciences, North Carolina State University, EPA, NC 27695-8208.
13. USEPA, 2006. Miscellaneous Sources, Industrial Wind Erosion, AP-42, 5th edn, vol I, Chap 13.2.5, November 2006. <http://www.epa.gov/ttn/chief/ap42/ch13/final/c13/final/c13s0205.pdf>.
14. World Meteorological Organization. 2006. Guide to Meteorological Instruments and Methods of Observations. Seventh Edition.

4.1.3 Analysis of a rounded crest stockpile: influence on dust emissions

The present chapter intends to investigate the effect of a rounded shape of the oblong stockpile crest on dust emissions. Similar situations found in literature and previous analysis carried out in the present thesis, have motivated the numerical simulations of a rounded crest. Firstly, the work of Turpin and Harion (2009) [72], also concerning oblong stockpiles, has already presented a comparative analysis of different shapes of crest, notably various flat-topped stockpiles height. The work of Turpin and Harion (2009) [72] was based on a previous study of Badr and Harion (2007) [3], which for a similar geometry, showed that the crest line is the zone over the pile exhibiting the highest levels of near wall flow velocity distribution and consequently the highest dust emission rate. Hence, a suitable arrangement of the crest may limit the negative effects of the wind erosion of piles on storage yards of industrial sites. The flat-topping of the crest was tested in the work of Turpin and Harion (2009) [72] to check if this modification of the crest could reduce the rates of dust emissions from this region. But, for all tested cases, the numerical simulations of several flat-topped crests resulted in an overall increase of the total dust emissions.

The second motivation raised from the wind-tunnel experiments performed in this thesis with an oblong stockpile made of sand (cf. section 3.1.1 for more details). These experiments have suggested that at the wind-tunnel scale, and for the experimental sand pile configuration, the rounded form of the crest had a significant radius relative to the height of the pile of sand. The manner in which the piles were set up in the wind-tunnel is similar to that usually accomplished on real industrial sites (hopper). The crests are not normally sharpened as it is considered in simulations concerning oblong stockpiles.

At the real scale, the radius is very small relative to the height of the pile. However, it could be relevant to evaluate the influence on dust emission of a rounded form crest of an oblong stockpile, with a significant radius. Different radius of the rounded crest shape were then tested for different wind flow orientations and free stream velocities. Also, the stockpiles were designed to maintain some characteristics of the models with sharpened crest already simulated: angle of repose, width of the crest and volume of the pile.

The aims of this subsection are listed below:

- evaluation of the modifications noticed on the near wall flow distribution on the stockpile surface due to the rounded crest shape,
- simplified investigations of the air flow pattern surrounding the rounded shape of the crest and
- as a consequence of the two points above mentioned, perform the analysis of the dust emission by using the USEPA (2006) [75] methodology.

It is worth to note that all numerical simulations of the rounded form of the crest were done with the open-source CFD code *Code_Saturne*.

4.1.3.1 Tested configurations

The tested cases are presented in Figure 4.1 which shows two rounded crest geometries compared to the sharpened one. The main dimensions are highlighted in the figure for the three cases. The numerical model presents a scale ratio of 1:200. It can be noticed, in these images, the geometrical parameters of the stockpiles that have been kept, between the sharpened and rounded shapes: crest length $L_{crest} = 0.373m$ (maintain the same dimensions of the crest which is the zone of interest in these analysis), side slope $\alpha = 38^\circ$ (to simulate the same material, coal) and volume $V = 0.00364m^3$ (to compare the emissions from a same quantity of granular material).

As the above mentioned, there are identical dimensions between the tested configurations. Thus, others have to be changed to accomplish the same volume of stored material. In that way, stockpile length (L) and half-width (l) are larger as the value of (r_{pile}) increases. Indeed, r_{pile} is the parameter that defines the rounded shape of the crest. Figure 4.2 details the configuration where $r_{pile}=1$. The value of r_{pile} is given in *cm* and indicates the radius of a circle limited in the pile. Black dashed lines

represent the original sharpened crest. Thus, the volume comprised between the original shape and the limited circle is deleted from the pile. For the sake of understanding, $r_{pile}=2$ is also represented in the image. The rounded crest stockpile presents lower heights. For the extreme case that is tested in this subsection ($r_{pile} = 5$), the height is about 10% smaller. The dimensions of the pile are calculated after a routine that effectuate the minimisation between the volume of the rounded crest and the sharpened one. The value of l is obtained to minimize this difference and the others are taken from it.

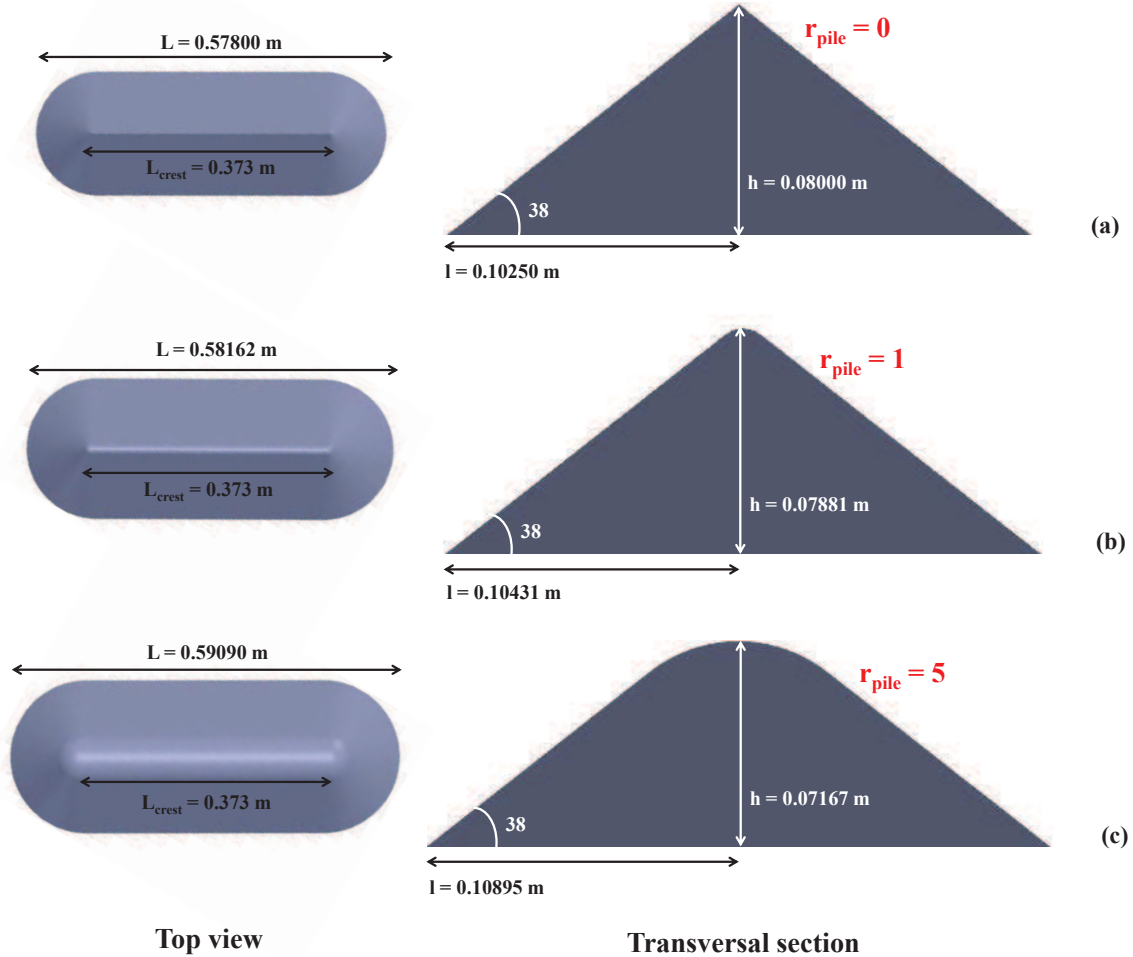


Figure 4.1: Tested configurations and different shapes of stockpile crests: (a) sharpened crest, (b) rounded crest with radius $r_{pile} = 1$ and (c) rounded crest with radius $r_{pile} = 5$

For the tested wind flow orientations (30° , 60° and 90°), two values of the parameter r_{pile} of the rounded crest were simulated: $r_{pile} = 1$ (Figure 4.1b) and $r_{pile} = 5$ (Figure 4.1c). $r_{pile} = 0$ means the sharpened crest (Figure 4.1a). The values chosen allow an analysis of the evolution of the aeolian erosion with the gradual modification of the crest rounded form. The wind direction that resulted in more modifications of the wind flow distribution on the crest (60°) is also simulated for $r_{pile} = 0.5$. This smallest value of $r_{pile} = 0.5$ was considered in numerical simulations to check if, even for a slight rounding of the crest, the near wall flow distribution presents important differences. The results are reported in following paragraphs.

The first part of the discussions in this chapter concerns the comparisons about the near wall flow distribution over the stockpile surface between sharpened and rounded crests. These comparisons are shown in Figures 4.3, 4.4 and 4.5, respectively presenting stockpiles oriented 30° , 90° and 60° . The near wall flow distribution is shown by means of u_s/u_r values over the pile surface. The parameter u_s/u_r , already presented in previously sections of the present thesis indicates the ratio between the near wall velocity u_s , calculated at 0.25 m (in real scale) from the surface of interest and the free stream velocity referent to the value at 10 m height, u_r . The parameter u_s/u_r was

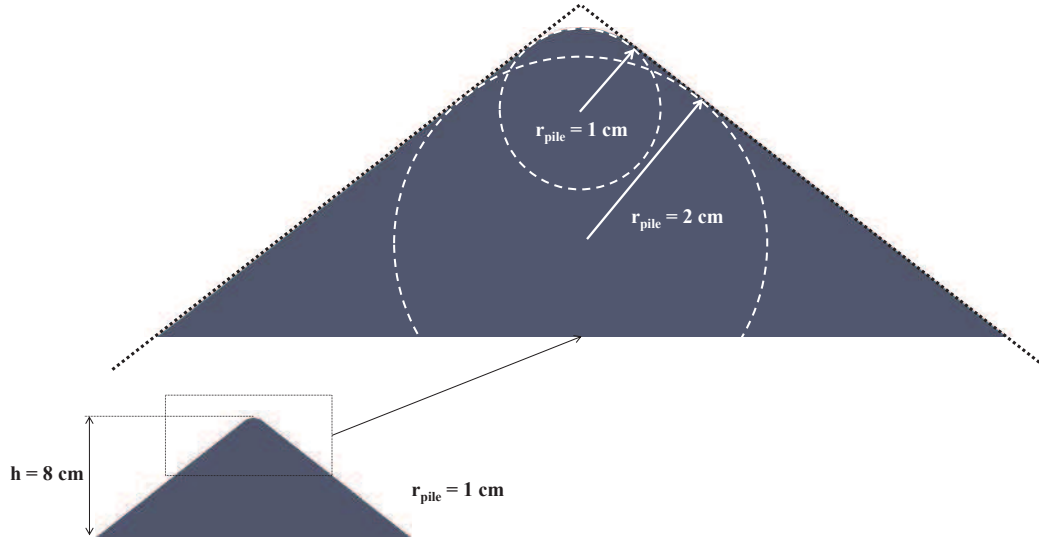


Figure 4.2: Definition of r_{pile}

chosen to perform the comparisons between each configuration as it is an input data of the USEPA used to estimate dust emissions (USEPA (2006) [75]).

4.1.3.2 Near wall flow topology over a rounded crest of an oblique and perpendicular stockpiles

Oblique - 30°

For 30°, Figures 4.3a, 4.3b and 4.3c are the results of near wall flow distribution for, respectively, a sharpened crest, a rounded with $r_{pile} = 1$ and a rounded with $r_{pile} = 5$. The near wall flow distribution is represented with the same scale to enable the visualization of differences between the configurations.

The numerical results have shown differences but an overall near wall flow pattern nearly the same. In Figures 4.3a, 4.3b and 4.3c three main regions have been highlighted:

- regions 1-a, 1-b and 1-c: stockpile crest and the detachment point,
- regions 2-a, 2-b and 2-c: leeward wall,
- regions 3-a, 3-b and 3-c: ineffective zone of the stockpile surface (the zone without effects on dust emissions)

Other regions have less importance on the final distribution: the windward wall and the impingement region (smaller shear over the wall).

In Figure 4.3b, about the rounded crest with $r_{pile} = 1$, some significant modifications are observed. The rounded crest (region 1-b) presents a significant increasing of u_s/u_r levels compared to region 1-a on the sharpened crest, from approximately 0.90 to 1.30. Due to the modification of the crest's shape (from sharpened to rounded) the fluid behaviour on the crest line is strongly altered. For the sharpened crest, the elevated levels of u_s/u_r are result of flow acceleration, normally observed on this kind of geometry. In the case of a rounded crest, the flow presents a different pattern of acceleration. The rounding of the crests causes the increasing of zones with strong velocity gradient and consequently higher levels of u_s/u_r .

For $r_{pile} = 1$, there are no significant modifications of the leeward wall flow pattern or the ineffective zone (respectively, regions 2-b and 3-b). The main vortex is differently formed and as a consequence has lower effects on the leeward wall of the rounded configuration. The ineffective

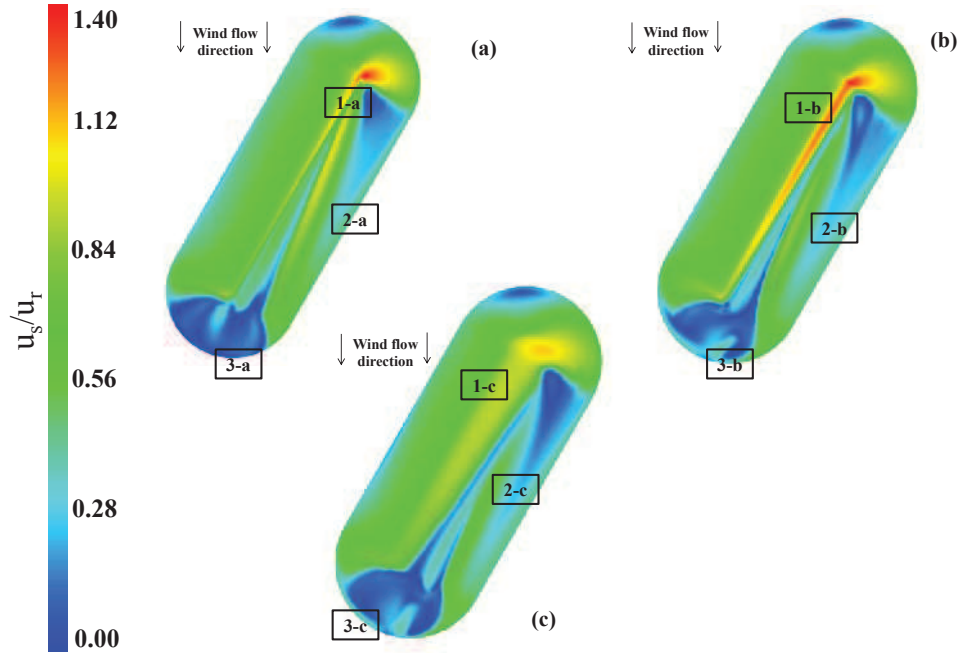


Figure 4.3: Numerical simulation results of the near wall flow distribution by means of the ratio u_s/u_r of a stockpile oriented 30° : (a) sharpened crest, (b) rounded crest with radius $r_{pile} = 1$ and (c) rounded crest with radius $r_{pile} = 5$

zone on the leeward wall is slightly augmented and the highest value observed over this zone is not greater than 1.00 while for the sharpened crest it overpasses this value.

Among the tested configurations the crest presented in region 1-c ($r_{pile} = 5$) has the lowest exposure levels. The maximum value of u_s/u_r is about 1.15 near the portion located more upstream the crest. However, the higher radius caused the formation of a crest having a higher surface of contact with the incoming wind flow at the top of the pile. In that case, even the weaker acceleration occurs over a greater zone which may represent in the quantifications a elevated dust emission rate. Regions 2-c and 3-c have smaller surfaces than those seen in Figure 4.3b but present the same features: ineffective zone and effects of the main downstream vortex.

Oblique - 90°

Besides the results of the pile oriented 30° , the investigation of an another oblique pile (60°) and a perpendicular pile is also the scope of the present work. The results corresponding to the perpendicular stockpile will be presented in this chapter before those of 90° . For 60° additional informations are given due to their more importance in near wall, air flow and dust quantification.

In that way, Figure 4.4 illustrates the near wall flow topology for the perpendicular stockpile. The main near wall flow features for this configuration are: the highest zones of wall friction values (or near wall velocity) are located on both stockpiles lateral sides (region 1-a) and over the entire crest equally distributed (region 2-a) and two zones of very low levels of velocity near the stockpile surface, close to the ground on the windward wall and on the leeward wall (3-a). The first ineffective zone on the pile is the stagnation region where the incoming flow is deviated in this region towards sides and top of the pile. Secondly, the leeward wall is inside the recirculation bubble formed downstream the pile.

The modification of the crest, firstly considering $r_{pile} = 1$, causes the increase of the maximum velocity ratio value from about 1.00 to approximately 1.15 (region 2-b). These high values are noticed over a significant region along the crest line. The others features, commonly observed on the sharpened crest, are also noticed on the rounded crest with $r_{pile} = 1$. The featuring of $r_{pile} = 5$ shows the formation of an extended zone of high values of u_s/u_r along the crest (regions 1-c and 2-c). However, its maximum value is reduced to approximately 0.95, the lowest among the crests tested.

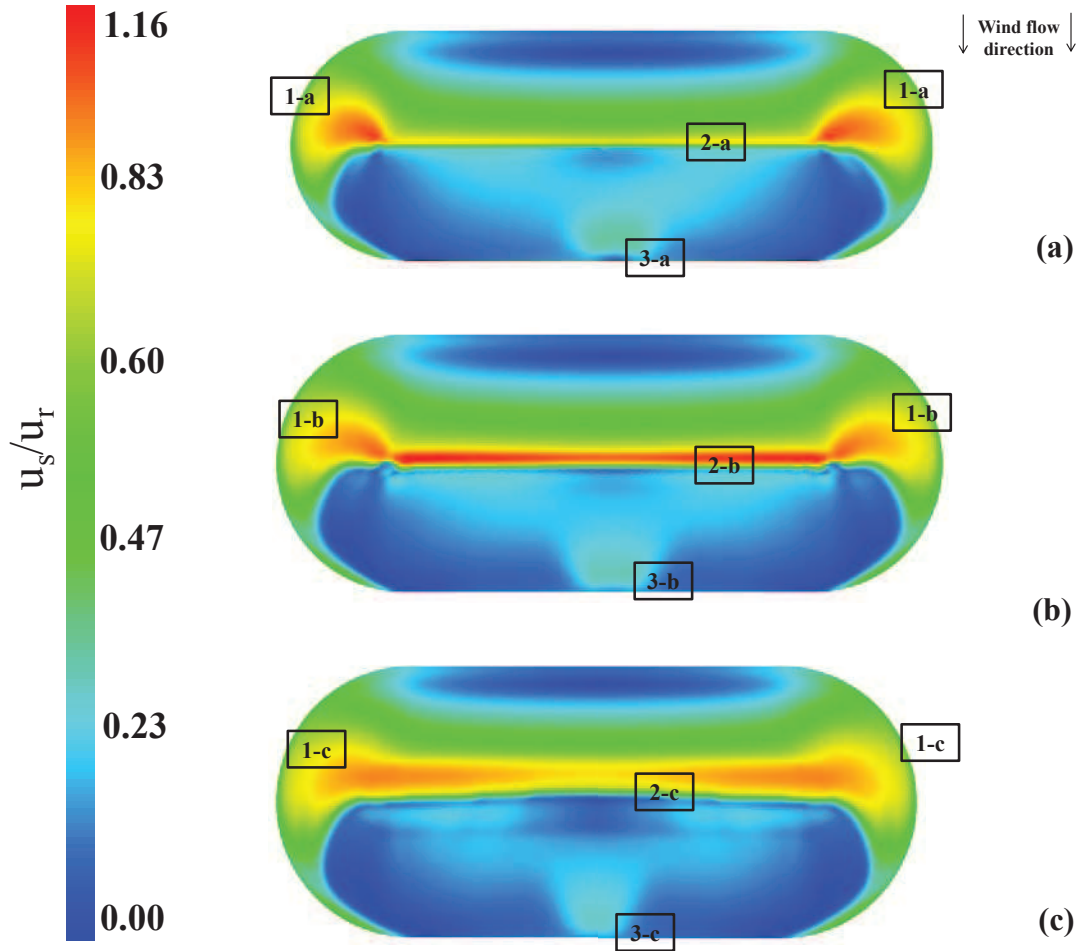


Figure 4.4: Numerical simulation results of the near wall flow distribution by means of the ratio u_s/u_r of a stockpile oriented 90° : (a) sharp crest, (b) rounded crest with radius $r_{pile} = 1$ and (c) rounded crest with radius $r_{pile} = 5$

Oblique - 60°

The near wall flow distribution of the stockpiles oriented 60° is shown in Figures 4.5a-4.5d. Modifications of the fluid flow pattern caused by the rounded shape of the crest are more clearly noticed for this wind flow direction. For this configuration, a third value was tested: $r_{pile} = 0.5$. The aim is to check the sensibility of the fluid flow pattern due to a slight rounding of the crest.

The sharp pile does not present a clear visualization, because of this scale, of the fluid flow pattern normally observed in other sections. Here, only a local augmentation of the levels of u_s/u_r is observed, the detachment point very upstream the crest line (near to mark 2-a). u_s/u_r level reaches 1.30 in this region. On region 3-a the main vortex presents its main effects in which high levels of u_s/u_r are noticed near the ground at the bottom of the wall. In a comparison between the four cases, regions 1-a to 1-d present very few differences. Only approaching the crest, the most considerable discrepancies are noticed. The zones of u_s/u_r greater than 0.75 slightly increases over regions 3-a to 3-d. The pattern of region 3 is highly modified for $r_{pile} = 5$.

Finally, the rounded crest causes a high increase of u_s/u_r values for a significant surface over the crest line. The distribution over the crest line, increases from values lower than 1.00 to maximums about 1.80. Figure 4.5b, which represents $r_{pile} = 0.5$, shows that, even for a small rounding of the crest line the u_s/u_r values are increased. The configuration with $r_{pile} = 1$ (Figure 4.5c) also presents the high levels near wall velocity distribution. Figure 4.5d ($r_{pile} = 5$) shows a maximum of about 1.30 for the values of the near wall velocity ratio. As for the other orientations, the maximum magnitude is not very high, but the surface of impact is the largest. For instance, in the configuration

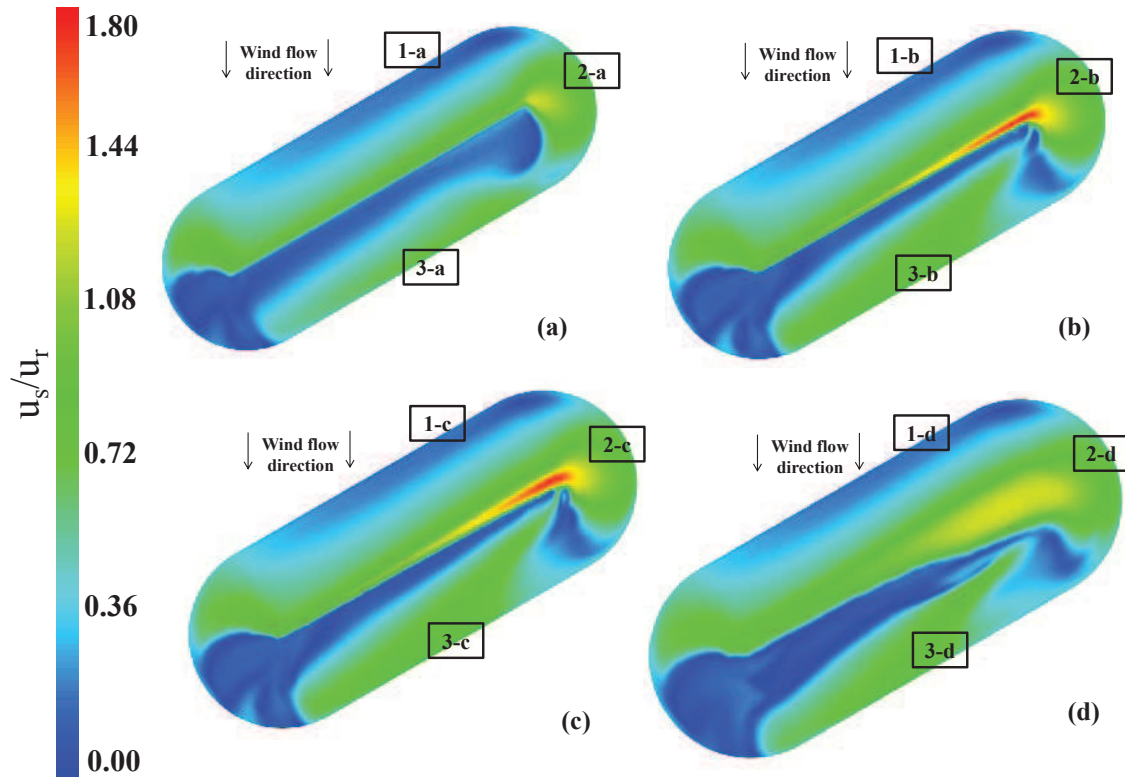


Figure 4.5: Numerical simulation results of the near wall flow distribution: ratio u_s/u_r of a stockpile oriented 60° : (a) sharp crest, (b) rounded crest with $r_{pile} = 1$ and (c) rounded crest with $r_{pile} = 5$

30° , $r_{pile} = 1$ presented a maximum of 1.40 and $r_{pile} = 5$ a maximum of 1.05.

A more detailed understanding of the way that the fluid flow is modified due to the different shapes of crest, is presented in Figure 4.6. In this figure, for the four tested cases of the 60° wind direction, the fluid flow is shown by means of contours of the longitudinal wind velocity over a plane XZ in the middle of the pile. The longitudinal velocity values are normalized by their values measured at the distance corresponding in the model scale to 10 m height in real scale ($U_{ref} = 5.26$ m/s). The fluid flow pattern near the stockpile peak (crest line) is magnified permitting a more detailed observation of the velocity distribution very near the crest.

The longitudinal fluid flow observed for the four tested configurations presented in Figures 4.6a-4.6d has similar characteristics. The most relevant discrepancies are found on: (i) the near wall of the crest line, (ii) the formation of the main vortex and (iii) its effects on the leeward wall. A representation of the main vortex is noticed in this plane by the negative velocity values downstream the pile. The smaller vortex is more attached to the leeward wall of the pile and presents more effects on this surface (highlighted arrow at the right of Figures 4.6). Moreover, on the leeward wall, the ineffective zone is smaller for the rounded crest piles. The rounding of the crest promotes a very less abrupt flow detachment. This situation is clearly observed in Figure 4.6a which is compared to the other Figures 4.6. In fact, the recirculation observed in Figure 4.6a means a flow that has been more accelerated due to the shape of the stockpile crest. Additionally, the colours of the contours near the leeward wall show a more accelerated flow in Figure 4.6d. The length of the main vortex is strongly reduced.

Zone B on the four sub-figures show the evolution of the downstream main coherent structure which correspond to the change in wind exposure downstream of the pile seen in Figure 4.6. For the sharp crest, the flow separation is located on the crest. The separation angle is very close to the side slope. For r_{pile} ranging from 0.5 to 5, the separation angle decreases and the separation is extruded downstream from the beginning of curvature of the pile surface.

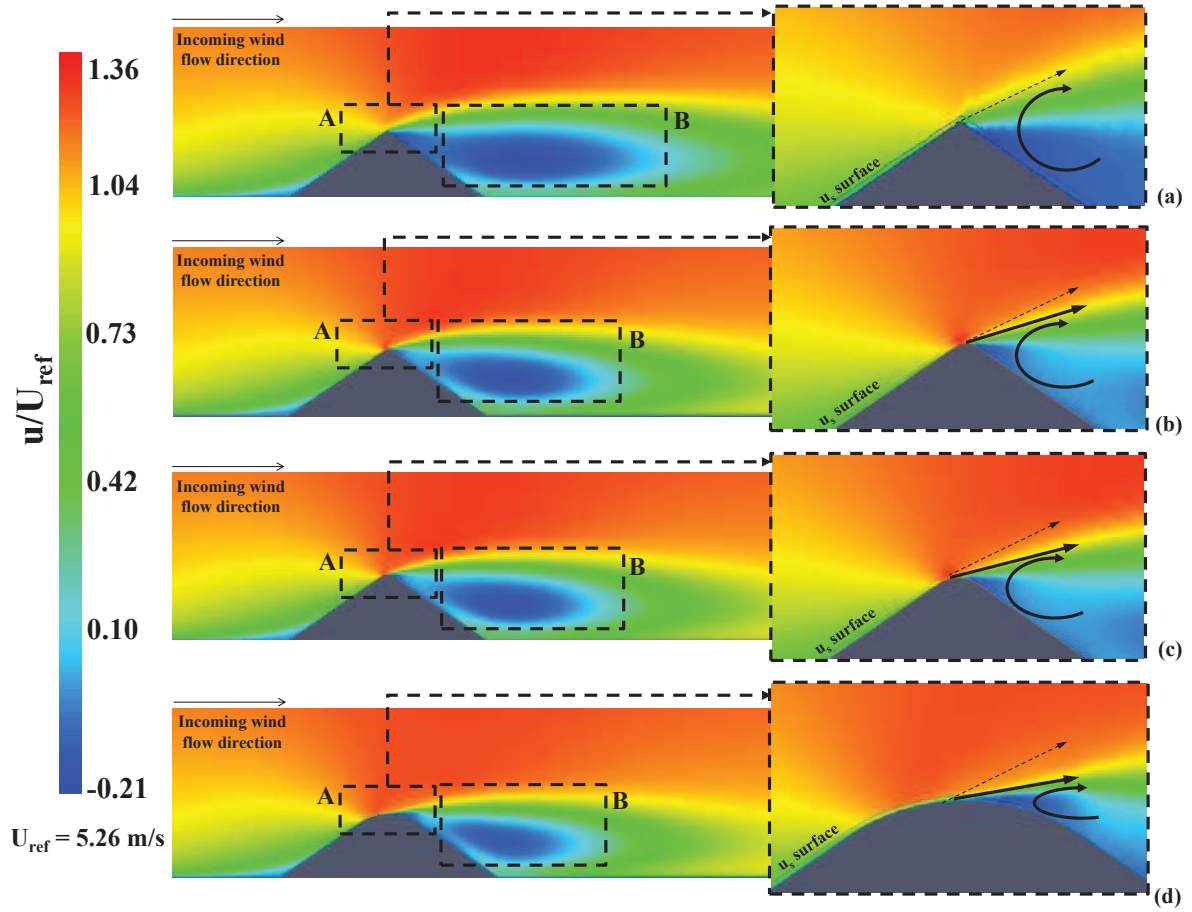


Figure 4.6: Contours of longitudinal wind velocity plotted over a XZ plane located at the computational domain center line for the stockpile oriented 60° (at right, detail of separation on the crest): (a) sharpened crest, (b) rounded with radius $r_{pile} = 0.5$, (c) rounded with radius $r_{pile} = 1$ and (d) rounded with radius $r_{pile} = 5$

4.1.3.3 Dust emission quantification

Table 4.1 summarizes the quantification of dust emissions from rounded crest stockpiles comparing to sharpened crests. The quantification was calculated using the USEPA (2006) [75] methodology. The dust emissions are shown in kg per perturbation and are calculated for three values of u_{10}^+ : 5, 10 and 15 m/s. It is worth to note that these estimations are presented in the real scale and are identically carried out as those already discussed in previous chapters.

The oblique configuration of stockpile oriented 30° shows a very slight reduction of the values of emissions for a rounded crest pile. The two rounded crest piles configurations have resulted in almost identical values of dust emissions. A link with the near wall velocity distribution should be done to a better understanding of the alteration in the quantification caused by the different crest shapes. The visualization of the pile oriented 30° indicates that the increasing of low level zones over the leeward wall has promoted the slightly reduction in the emission. The crest line is more eroded in Figure 4.3b which would result in more dust emitted. However, on the rounded crest piles the ineffective zones on the leeward wall is increased and the region near the crest (still on the leeward wall) is protected in these rounded configurations. The differences of dust quantification between rounded $r_{pile} = 1$ and $r_{pile} = 5$ are very low.

The emissions for the perpendicular orientation have shown a different behaviour. The dust emissions, contrarily to that observed for 30° , slightly increase as the crest becomes more rounded (from $r_{pile} = 1$ to $r_{pile} = 5$). For instance, the emissions corresponding to a fastest mile equal to 10 m/s results in 17.4, 18.7 and 20.6 kg per perturbation, respectively for, sharpened, $r_{pile} = 1$ and $r_{pile} = 5$. Differently to what is observed in the results of the pile oriented 30° , the leeward wall does

not present a different pattern of the ineffective zones due to the alterations of the rounded crest. In fact, the distribution on the leeward wall is very similar while over the crest the values of u_s/u_r are higher and involves a higher surface which defined more dust emitted. The emissions increase about 10% as the crest is modified for wind velocity equals to 10 m/s, and about 25% for 15 m/s.

Table 4.1: Dust emission quantification of two shapes of stockpile's crest: sharpened and rounded

		Emissions (kg)		
		$u_{10}^+ = 5 \text{ m/s}$	$u_{10}^+ = 10 \text{ m/s}$	$u_{10}^+ = 15 \text{ m/s}$
30°	Sharpened	1.8	33.8	89.9
	Rounded ($r_{pile} = 1$)	1.7	28.2	85.1
	Rounded ($r_{pile} = 5$)	1.7	28.8	85.4
90°	Sharpened	1.1	17.4	47.6
	Rounded ($r_{pile} = 1$)	1.4	18.7	54.2
	Rounded ($r_{pile} = 5$)	1.5	20.6	59.0
60°	Sharpened	1.5	24.7	73.8
	Rounded ($r_{pile} = 0.5$)	2.9	34.3	96.8
	Rounded ($r_{pile} = 1$)	2.8	34.0	96.2
	Rounded ($r_{pile} = 5$)	3.1	35.9	100.9

Finally, the dust emission quantification for the orientation 60° shown the highest differences between sharpened and rounded crest stockpiles. The dust emitted from the sharpened crest was found to be about the half of the value calculated for the rounded crest (results corresponding to $u_{10}^+ = 5 \text{ m/s}$). For other velocity values, the increasing noticed on the dust emitted values is lower but reaches about 40%. It is worth to note that, this important increased dust emissions quantified for this orientation are observed for the calculation performed with the lowest rounded crest analysed ($r_{pile} = 0.5$). The emissions for the others two tested values of r_{pile} are slightly higher for all velocities calculated. The increasing of emissions may be easily understood after a visualization of the near wall flow distribution (Figure 4.5). The crest shows very high velocity ratio values and, as shown in previous paragraphs, the leeward wall is exposed to higher velocities. For the pile with $r_{pile} = 5$ the eroded zone over the leeward wall is smaller, however, the crest shows eroded surfaces over a higher value of than the sharpened one.

4.1.3.4 Conclusions

The present chapter was carried out in order to analyse the implication on dust emissions of the modifications on the stockpiles crest. Motivated by previous studies that have checked the highly influence of the crest on dust emissions, the analysis presented herein aimed to investigate a shape of crest until now not tested in the terms carried out in this chapter: a rounded shape. The rounded crest was already observed on experimental models of oblong piles. The flow near the wall was found to be highly modified by the shape of crest.

The investigations have presented the zones over the stockpile surface more modified due to the rounded crest. For all orientations, the crest and leeward wall (for oblique configurations) are the regions highly changed due to the modification noticed of the crests. The numerical simulation results and dust emission quantification have shown that for all velocity values tested, the pile oriented 60° and rounded crest has presented the highest global dust emission values. Only for one tested configuration (30°), the dust emission results were very slightly reduced for a rounded crest compared with the sharpened configuration. The values increase for the perpendicular stockpile with rounded crest. However, the perpendicular orientation still presents the lowest levels among all tested configurations. The tested cases of the stockpile oriented 60°, which is not the worst atmospheric pollution situation for a sharpened crest, becomes it for the rounded crest for all velocity values tested.

4.2 Investigation of various arrangements of two successive stockpiles

4.2.1 Aeolian erosion of isolated and successive arrangements of oblong storage piles

The analysis of dust emissions from isolated piles has been published in the last few years. However, it has also been verified the strong influence of a nearby obstacle on the overall fluid flow distribution over that previously isolated. In this framework, this subsection presents the results and discussions about the influence of a second nearby stockpile on, firstly, the near wall flow distribution near the surface of interest (stockpile surface) and, secondly, on the global dust emissions. These results were then presented as an article entitled **"Aeolian erosion of isolated and successive arrangements of oblong storage piles"** to be submitted to the **"Applied Mathematical Modelling"** journal. The oblong stockpile was numerically simulated under three configurations: isolated and successive with two values for the gap between them. The meteorological conditions were evaluated by changing the incoming wind orientation and velocity magnitude. The numerical simulations for the results presented in this subsection were performed with an open-source CFD code called *Code_Saturne*. Finally, dust emissions were assessed by the widely used mathematical methodology proposed by USEPA (2006) [75].

1 Aeolian erosion of isolated and successive arrangements 2 of oblong storage piles

3 B. Furieri^{a,b}, S. Russeil^{a,b}, M. Milliez^c, J. L. Harion^{a,b}, J. M. Santos^d

4 ^a*Univ Lille Nord de France, F-59000 Lille, France*

5 ^b*EMDouai, EI, F-59500 Douai, France*

6 ^c*CEREA, EDF R&D, Ecole des Ponts ParisTech, Université Paris Est, F-78401
7 Chatou, France*

8 ^d*Universidade Federal do Espírito Santo, DEA, 29060-970 Vitória, ES, Brazil*

9 Abstract

10 The present work is focused on the investigation of overall emissions from
11 several arrangements of oblong stockpiles. Previous studies dealt with dust
12 emission quantification and wall flow topology concerning isolated oblong
13 piles. This paper aims to analyse the influence of a second successive pile
14 on global dust emissions on industrial sites, on which there is rarely a sin-
15 gle isolated pile. Dust emission rates are assessed by the US-EPA model
16 and fluid flow data is predicted by numerical simulations carried out with
17 the open-source Computational Fluid Dynamic (CFD) code *Code_Saturne*.
18 Orientation, free stream velocity and distance between piles are the param-
19 eters analysed in these investigations. Three scenarios conducted in these
20 investigations indicate that dust emission from two successive close stock-
21 piles is: (i) increased for the piles oriented 60°, (ii) slightly decreased for the
22 perpendicular piles and (iii) was not influenced by the interactions for the
23 orientation 30°. The analysis of the downstream stockpile shows that, as
24 the gap increases, the interactions have less impacts on dust emission. It is
25 also found that the isolated stockpile emits less dust than the upstream or
26 downstream pile in the successive configuration. Total emissions are found
27 to be approximately the same for the two distances between piles that have
28 been tested. This study provides to the industrial management several infor-
29 mation concerning the best arrangement of the piles in order to limit particle
30 emissions.

31 *Keywords:*

32 Aeolian erosion, Dust emission quantification, US-EPA methodology,

35 1. Introduction

36 In industrial sites worldwide, diffuse sources present a negative contri-
37 bution to the overall ambient air quality. The effects of wind erosion of
38 industrial granular materials on diffuse source emissions were subjects re-
39 cently studied by several authors (7; 10; 12; 14; 18). The aeolian erosion on
40 industrial sites must be surveyed and controlled, as it is requested by environ-
41 mental authorities. Three approaches are usually performed to survey and
42 manage emission from diffuse sources: field measurements, experimental sim-
43 ulations (in laboratories) or numerical calculations. Field measurements are
44 expensive and although wind tunnel measurements are in constant improve-
45 ment concerning the quality of techniques ((7; 8; 10; 13)), measurements
46 techniques are complex to perform and difficult to implement. Thus, math-
47 ematical methodologies are a suitable solution for the investigation of wind
48 flow impact on diffuse sources. Numerical simulations provide detailed in-
49 formation concerning the fluid flow that includes the most important input
50 data for the mathematical model of diffuse dust emission estimation: wind
51 velocity distribution near the surface of interest. A literature survey re-
52 veals numerous studies about experimental and numerical analysis of diffuse
53 sources (2; 3; 4; 5; 6; 9; 10; 18; 19).

54 Badr and Harion (2007) (2) investigated the effects of the stockpile config-
55 uration on dust emissions calculated by the USEPA methodology USEPA2006.
56 Numerical simulations were performed to improve the understanding of three-
57 dimensional flow processes occurring around stockpiles of varying shapes. An
58 optimal configuration emitting less dust was found. Later, Turpin and Har-
59 ion (2009) (18) carried out numerical simulations for several stockpile shapes.
60 The results of the flow field on the stockpiles surfaces were integrated in the
61 USEPA methodology. Results showed that flattening the stockpile crest did
62 not lead to a decrease of dust emissions. Indeed, the acceleration at the top
63 of the stockpile and on the lateral sides increases with the clipping height.
64 Recently, Furieri et al. (2012) (10) used experimental and numerical tech-
65 niques to evaluate the wind flow near the wall surrounding isolated oblong
66 stockpiles. The authors found airflow turbulent structures and areas of high
67 wall friction levels that may be linked to potential dust emission from the
68 ground surface around the piles. These authors presented discussions about

the fluid mechanics on and around isolated oblong piles and consequently the overall dust quantification. However, numerous works have shown that the fluid flow interactions occurring between nearby obstacles and surrounding buildings are very important and have a strong impact on the overall distribution of the fluid flow velocity near the surface (6; 19; 5). Furthermore, an isolated configuration of stockpile is rarely encountered in industrial sites. Stockpiles are usually arranged successively in parallel lines. However, these articles did not evaluate in details the near wall flow distribution and the main fluid flow structures formed due to the interactions between piles. Very recently, Cong et al (5) presented the effects of the arrangement of multiple stockpiles on the quantification of dust emissions. These authors focused on flat-topped and conical piles, however, oblong piles are more commonly found in industrial sites. The USEPA methodology was used in Cong et al (5) work to determine emission rate without further discussions about the fluid flow structures.

The present work aims the investigation of fluid flow structures around multiple oblong stockpiles and their influence on the global amount of emitted dust. This paper presents discuss the influence of the number of piles, the stockpile orientation in relation to the incoming wind flow direction and the distance between piles on dust emission rates calculated by using the USEPA methodology.

2. Mathematical methodology

2.1. Numerical simulation background

The numerical simulation performed in this work are based on the previous work carried out by Turpin and Harion (2009) (18) which has been validated by wind tunnel data. These authors investigated the influence of different crest shapes on the emission rates of an oblong isolated stockpile.

In the present work, the solution of the three dimensional equations of mass and momentum was computed with the open-source code (1) named Code-Saturne which is based on the co-located finite volume approach. The standard $k-\omega$ Shear Stress Transport (SST) model was used to account for turbulence effects. Figure 1(a) shows the computational domain and boundary conditions. The mesh is produced by an extrusion from triangular cells defined on the ground surface and pile walls (see Figure 1(b)) towards the top boundary of the computational domain. As required by the turbulence

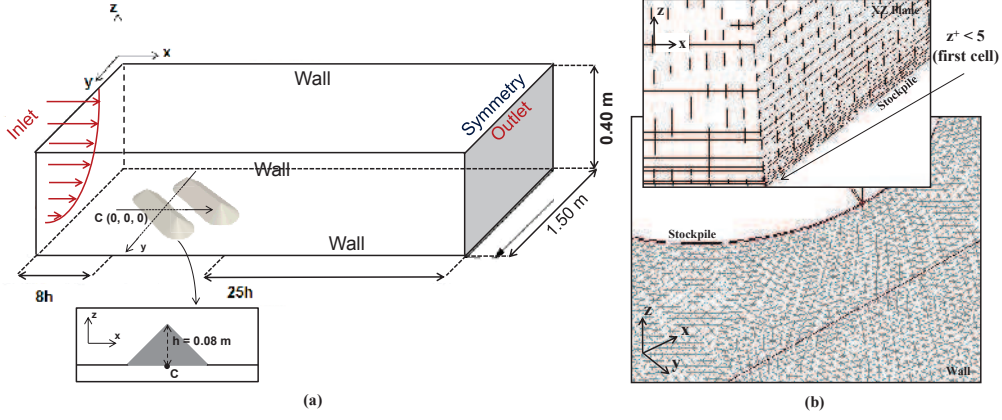


Figure 1: (a) Computational domain and (b) Meshing

model $k-\omega$ SST closure, there is a mesh refinement near the wall surface where $z^+ \leq 5$.

The modelled stockpile is an oblong stockpile with an angle of repose equal to 38° which is representative of coal piles commonly found in real industrial sites. The dimensions of the real stockpile were scaled-down by a factor of 1:200 to carry out the numerical simulations: 0.578 m (width), 0.205 m (length) and 0.08 m (height). Dimensions of upstream and downstream zones were set in the computational domain to ensure that the results are not influenced by the size of the domain (as performed by Turpin and Harion (2009) (18)). Spanwise and vertical dimensions of the domain are based on the dimensions of wind-tunnel in which Turpin and Harion (2009) (18) carried out the experimental work to validate the numerical simulations. In fact, the vertical dimension of the computational domain was set as half of the wind-tunnel height reducing computational cost. This condition has been tested and there is no influence on the obtained results. The inlet boundary conditions for velocity (u , v and w), turbulent kinetic energy (k) and specific dissipation rate (ω) were obtained from preliminary numerical simulations of a flow in a channel in which a periodic streamwise flow was set as boundary conditions at the inlet and outlet in order to produce a fully developed channel flow and the final converged flow field was set as the inlet condition for the simulation presented in this paper. The free stream velocity (u_r) was equal to 6.5 m/s. For the outlet boundary conditions, it was assumed that the flow is fully developed and for the upper boundary condition, symme-

try was imposed. Finally, smooth walls with no-slip conditions were set at domain lateral walls, as well as at stockpile and ground walls.

2.2. USEPA model for dust emission quantification

The USEPA model of dust emission quantification requires the following input data:

- particle size multiplier (taken as the average particles size) (k)
- threshold friction velocity (u_t^*)
- distribution of u_s/u_r on the surface of interest (u_r is the reference velocity at 10 m height from the ground and u_s is the velocity at 25 cm from the surface, both for real scale)
- number of perturbations (N)
- number of isosurfaces of u_s/u_r (M)
- the highest velocity value measured by an anemometer at a reference height for a period between perturbations (u_{10}^+)

The whole input data set is dependent on the characteristics of materials and the industrial site configuration. However, the distribution of the ratio u_s/u_r needs further investigation which can be pursued by means of numerical simulations. An experimental distribution of this parameter is given in the USEPA guide for isolated stockpile. Thus, numerical simulations were carried out using the open-source model *Code_Saturne* to obtain the u_s/u_r distribution on the surfaces of interest. A single pile perturbation was considered for the investigated configurations. A perturbation is defined in the USEPA guidance (20) as an intervention done in a storage pile yard for maintenance and transport of material.

Equation 1 is the fundamental formulation of USEPA methodology to calculate the emission rate (E). The pile surface is divided in subareas representing different levels of wind erosion exposure, each subarea being considered as a distinct source corresponding to a constant value of u_s/u_r . Thus, the summation in Equation 1 considers these subareas separately accounting for the respective fraction of subarea S .

$$E = k \sum_{i=1}^N \sum_{j=1}^M P_{ij} S_{ij} \quad (1)$$

where P is the erosion potential (g/m^2). The erosion potential P is calculated based on the friction velocity (u^*) and threshold friction velocity (u_t^*) as shown in Equation 2. For the disturbed fluid flow around stockpiles the USEPA model proposes Equation 3 to determine friction velocity.

$$\begin{cases} P = 58 (u^* - u_t^*)^2 + 25 (u^* - u_t^*) \\ P = 0 & \text{for } u^* \leq u_t^* \end{cases} \quad (2)$$

$$u^* = 0.10 \left(\frac{u_s}{u_r} \right) u_{10}^+ \quad (3)$$

The aerodynamic particle size multiplier (k) is different for each considered aerodynamic particle size (cf. Section 13.2.5.3 in USEPA guide (20)). The value of k equal to 0.5 was chosen to represent PM_{10} particles emissions (PM_{10} defines the particles in suspension presenting diameter less than 10 μm). The value of the threshold friction velocity equal to 0.35 m/s (representing an agglomeration of coal) was determined by wind-tunnel experiments (cf. (18)). Three different values of u_{10}^+ were investigated (5, 10 and 15 m/s) to simulate different atmospheric conditions. It is important to note that, according to (18), the u_s/u_r distribution does not vary for different values of u_r and thus, although for the numerical simulations u_{10}^+ is equal to u_r , it is not worth to run the simulations for different values of u_{10}^+ as these simulation would produce the same u_s/u_r distribution.

3. Results and discussions

The tested configurations were: one isolated stockpile, two parallel stockpiles with a gap equal to $1e$ and $2e$ ($e = 0.9h$ where h is the stockpile height), and three stockpiles orientations in relation to wind direction: 30° , 60° and 90° .

3.1. Wind exposure of pile surface and surrounding air flow

Figures 2 and 3 represent, respectively, the results of numerical simulations of the distribution of near wall flow velocity (u_s/u_r) and the flow

streamlines around the piles for the orientation 30° . The same results are presented in Figures 4 and 5 (60°) and Figures 6 and 7 (90°) for the orientation 60° and 90° , respectively. The wind exposure patterns on the piles surfaces for the three configurations are very similar. Figure 2 presents the distribution of u_s/u_r for one isolated pile (Figure 2a), two successive piles with a gap $1e$ (Figure 2b) and two successive piles with a gap $2e$ (Figure 2c). Figure 2d shows the contours of the longitudinal flow velocity on a XZ plan.

Figure 2a presents the near wall wind flow pattern for the isolated stockpile and shows high values of the ratio u_s/u_r near the crest with a maximum on the first detachment point, three zones with low values of u_s/u_r (impingement zone, upstream and on the bottom of the leeward wall) and traces of the main vortex on the leeward wall. Zone A indicated in Figures 2a, 2b and 2c presents the differences found in u_s/u_r distribution for these three configurations. The other zones present very similar distributions: (i) the impingement region and the line along the crest both presenting the highest levels of the ratio u_s/u_r , (ii) an unaffected region on the leeward and windward wall and (iii) the effect of the main vortex on the leeward wall (high wall friction).

Figure 2d shows a contour plot of the longitudinal wind velocity for the configuration in which the gap between piles is equal to $1e$. Point (I) indicates a recirculation (negative values of the X velocity very near the wall) and the effect on the upstream pile is the low levels of u_s/u_r . The fluid flow detachment is highlighted by point (II): the fluid flow is accelerated and causes much larger velocity values near the crest. Point (III) indicates a recirculation region and a larger zone of negative velocities near the zone A, downstream pile. The streamlines show that in the leeward side, the flow separates from the pile surface and creates this recirculation zone. The streamlines over the successive piles present behaviour than the ones around the isolated pile. In fact, it suggests that for this orientation (30°) the influence of the second pile may be neglected. The main vortex, which is the structure responsible for the erosion on the first stockpile, does not impinge on the second pile and the recirculation structures do not reduce the levels of u_s/u_r . These findings can be verified for both tested gaps.

The wall flow distribution and plot of longitudinal wind velocity for the piles oriented 60° are presented in Figures 4a to 4d. Zone B is characterized by low levels of u_s/u_r as the fluid impinging the windward wall flows towards the laterals and top stockpile walls. The deviation of the free stream flow impinging the stockpile causes the appearance of zones C and D. Zone C

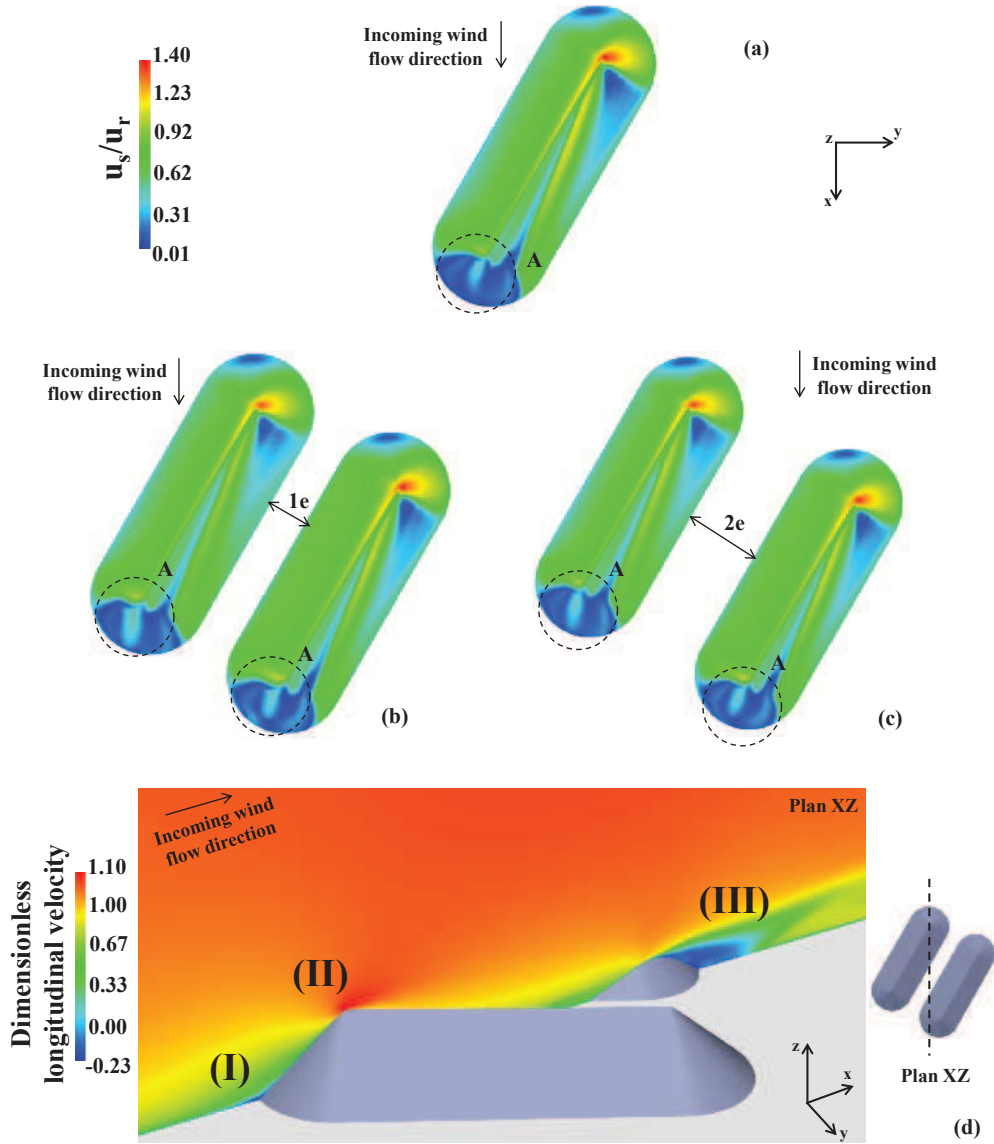


Figure 2: Wind flow exposure on the stockpile oriented 30°: (a) isolated stockpile, (b) two successive stockpiles with gap $1e$ and (c) two successive stockpiles with gap $2e$ (with $e = 0.9h$ where h is the stockpile height). (d) Plan of dimensionless longitudinal wind velocity

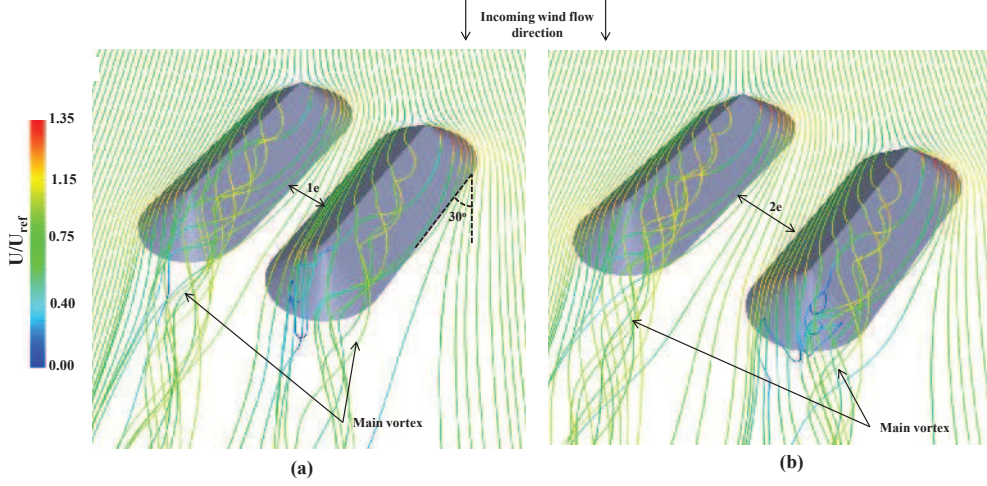


Figure 3: Streamlines coloured by the wind flow velocity magnitude for the orientation 30° : (a) two stockpiles with a gap equal to $1e$ and (b) two stockpiles with a gap equal to $2e$. (The velocity measured at 10m in real scale is chosen as the reference velocity $U_{ref} = 5.26$ m/s)

220 presents the highest levels of u_s/u_r . Each configuration for the piles oriented
 221 60° has different values of u_s/u_r in zone C where the interactions between
 222 successive piles are more significantly seen. Zones E and F can be observed in
 223 the leeward side of the stockpiles. Zone E is the region of ineffective erosion.
 224 Zone F presents the effects of the main vortex and a slight augmentation of
 225 u_s/u_r levels is perceived on the upstream piles for both configurations with
 226 two stockpiles. For this orientation (60°), there are differences of great signif-
 227 icance of wind exposure between the tested configurations: the interactions
 228 between the piles in this case show the most visible differences among all
 229 the tested orientations. The stockpiles with a gap $1e$ present the maximum
 230 levels of u_s/u_r in zone C (equal to 1.63). The isolated stockpile presents
 231 a maximum value of 1.40 in zone C which is lower than the configurations
 232 with multiple piles. The most pronounced variations of u_s/u_r in zone D are
 233 perceived in the downstream piles and the maximum value of u_s/u_r for the
 234 isolated pile is approximately equal to 1.02. In the first piles for the mul-
 235 tiple pile configurations, there is an augmentation of u_s/u_r to 1.30 in zone
 236 D while the second piles do not present significant modifications in zones
 237 D. The comparisons between isolated and successive piles indicated strong

238 modifications of zone D in the case where the piles have a gap equal to $1e$.
 239 Values of u_s/u_r reach 0.50 on most part of this region, whereas for an isolated
 240 pile or piles separated by $2e$ this value is lower than 0.20. Finally, zone F
 241 may be analysed for both upstream and downstream piles. For downstream
 242 piles this zone does not present significant modifications, only a slight reduc-
 243 tion of the ineffective zone. However, if the analysis is carried out for the
 244 upstream stockpiles for both tested gaps, one can notice the influence of the
 245 interactions between stockpiles on the near wall velocity distribution. The
 246 interaction corresponds to the main vortex. Zone F shows higher values of
 247 u_s/u_r in the first piles for the multiple piles configurations. A maximum of
 248 0.85 is found for the isolated pile and the downstream piles in the multiple
 249 pile configurations. The upstream piles result in u_s/u_r values greater than
 250 1.30.

251 Figure 4d presents the plots of longitudinal wind velocity for two XZ
 252 plans. The plan XZ 1 shows at point (I) the fluid flow acceleration on the
 253 pile crest and consequently the highest values of wind velocity. Point (II)
 254 indicates the main vortex of the upstream stockpile. The acceleration can
 255 also be seen near the crest of the downstream pile. Observing plan XZ
 256 2, the highlighted points (III) and (IV) represent the main vortices formed
 257 downstream each pile. Focusing on the first main vortex (between the piles),
 258 it is possible to notice its effects on the downstream pile (zone D).

259 High levels of u_s/u_r noticed for the orientation 60° , are seen in Figure 5.
 260 The main vortex formed downstream the first pile impinges the windward
 261 wall of the second pile. Moreover, this main vortex has more influence on
 262 the leeward wall of the upstream pile than the isolated one. The amount
 263 of disturbed fluid flow impinging the downstream pile is more significant for
 264 the gap equal to $1e$. The near wall flow velocity distribution for the three
 265 perpendicular cases tested is presented in Figure 6. The results of the near
 266 wall flow topology for two successive stockpiles (Figure 6 (b) and Figure 6
 267 (c)) show that the distribution of the near wall flow velocity does not present
 268 a symmetric pattern as it is expected for RANS numerical simulations of
 269 geometrical symmetric configurations. However, the configurations with two
 270 geometrical symmetric obstacles (as the two successive stockpiles) may result
 271 in non symmetrical results of the near wall flow distribution. This condition
 272 may be called bistability. The bistability was already investigated by few
 273 authors (15; 11). Both studies performed numerical and experimental simu-
 274 lations for an incoming wind flow oriented in angles around the perpendicular
 275 position. The authors have studied the fluid flow impinging symmetrical ge-

ometries and both found a bistable flow. Extra numerical simulations were performed to verify if the asymmetric results for the orientation 90° are valuable for the discussions and comparisons with other wind orientations. Thus, stockpiles oriented 89.5° and 90.5° were simulated (see Figure 8 for details of the near wall velocity distribution). For these numerical simulations, the fluid flow pattern of 90° is very near the orientation 89.5° and the main vortex impinges the windward wall of the downstream pile on the same side (black dashed line). For the configuration 90.5° , this structure is observed on the opposite side.

As the main aim of the present work is to quantify dust emission and the obtained results of dust emitted for the three orientations (90° , 90.5° and 89.5°) where lower than 3 %, the dust quantified for 90° will be taken hereafter for the comparisons with 30° and 60° . Finally, Figures 6 will be used for the discussions of the modification on the near wall flow topology.

The isolated stockpile oriented 90° (Figure 6a) presents the following main characteristics of the near wall velocity distribution: (i) the highest levels of u_s/u_r are found on the crest and on the sides of the piles, (ii) the recirculation zone downstream the pile causes the lowest levels of the ratio and (iii) on the lower part of the windward wall u_s/u_r values are near to zero and theses values increases the top and sides. The analysis of the two nearby stockpiles leads to the identification of several zones of surface protection (low levels of u_s/u_r). Zone G in the leeward wall is more representative on the piles separated by the gap $1e$. Also, the zones having high levels of u_s/u_r are smaller in these configurations. The analysis of the regions indicating the existence of ineffective zones over the wall, zone H shows up the differences on the near wall velocity distribution on the leeward wall. Here, on both piles it is increased the amount of surface with very low levels of u_s/u_r . The formation of a large recirculation zone is the main cause of this behaviour on these walls. The perpendicular stockpile streamlines (Figure 7) show the two strong recirculation zones formed between piles and on the leeward wall of the downstream pile. Some zones in where the fluid flow does not impinge the piles are also perceived.

3.2. Dust emissions quantification

The graphics presented in Figure 9 summarize the quantitative analysis of dust emission for all the configurations. The quantification of emitted dust (in kg per perturbation), calculated by the USEPA methodology previously presented, is shown in the plots divided into three categories: (i) piles

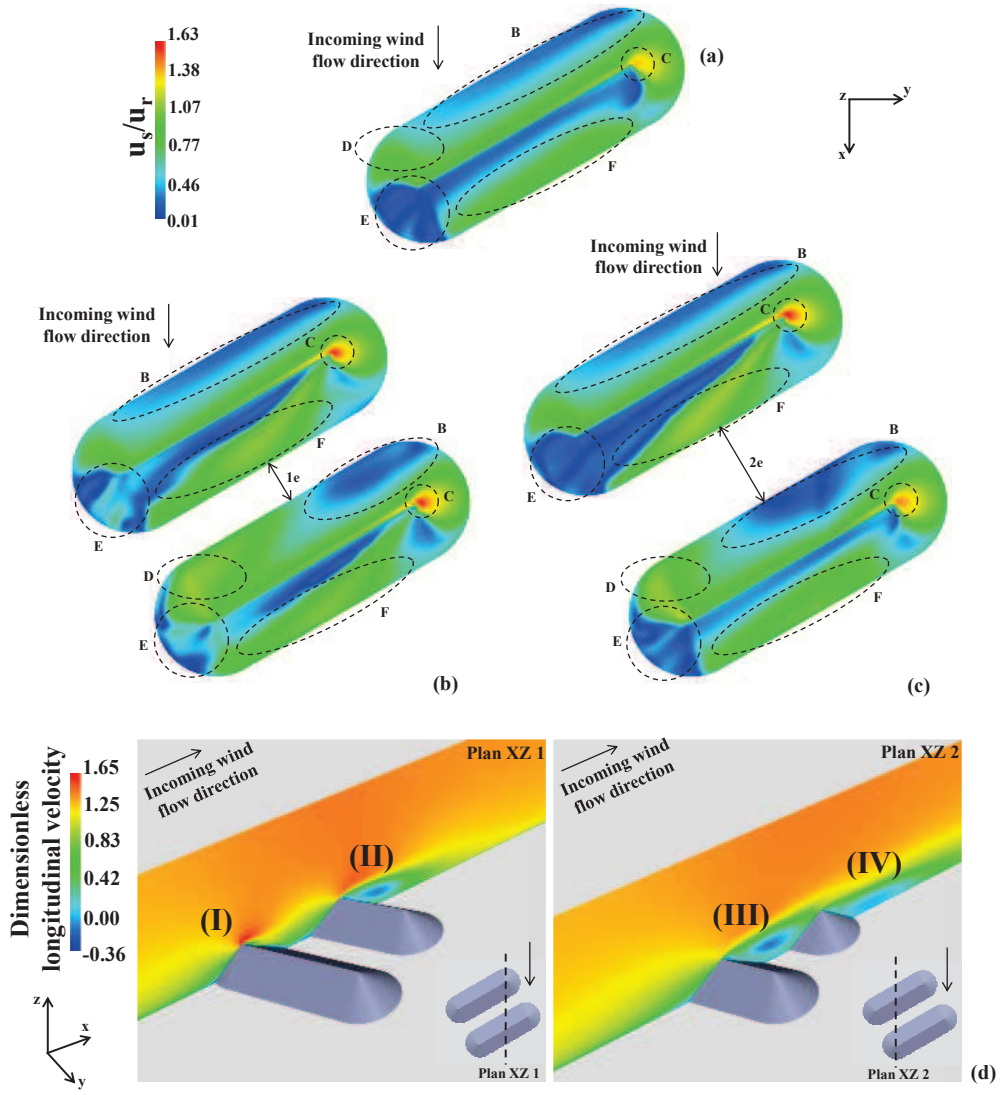


Figure 4: Wind flow exposure on the stockpile oriented 60°: (a) isolated stockpile, (b) two successive stockpiles with gap $1e$ and (c) two successive stockpiles with gap $2e$ (with $e = 0.9h$ where h is the stockpile height). (d) Plans of dimensionless longitudinal wind velocity

313 separated by the gap $1e$, (ii) piles separated by the gap $2e$ and (iii) isolated
 314 pile.

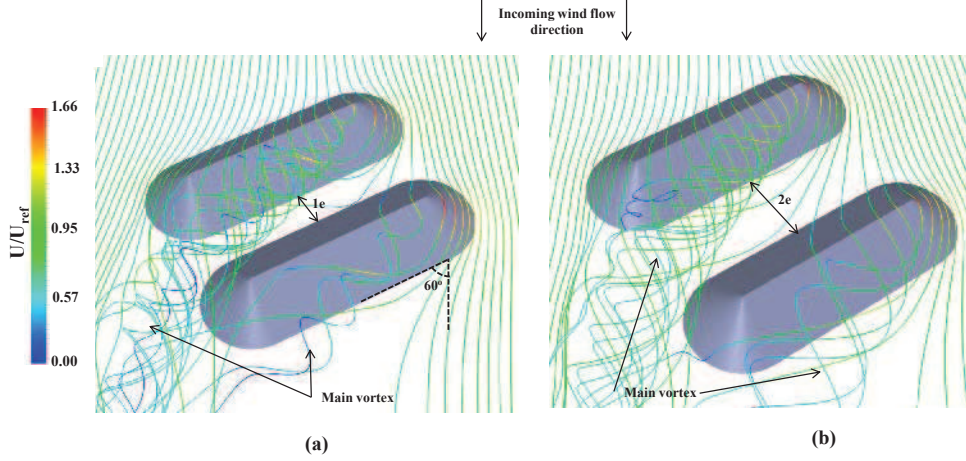


Figure 5: Streamlines coloured by the wind flow velocity magnitude for the orientation 60° : (a) two stockpiles with a gap equal to $1e$ and (b) two stockpiles with a gap equal to $2e$. (The velocity measured at 10m in real scale is chosen as the reference velocity $U_{ref} = 5.26$ m/s)

315 Firstly, a slightly reduction of the amount of emitted dust is assessed for
 316 two nearby stockpiles perpendicular to the main wind flow direction. More-
 317 over, the strong impact of a second parallel stockpile, seen for the orientation
 318 60° , and the low modifications of the fluid flow pattern, for 30° , are clearly
 319 noticed in the values of emitted dust presented in Figure 9.

320 The differences of percentage values between the dust quantification of
 321 the isolated pile and the two nearby stockpiles are presented hereafter. The
 322 piles oriented 30° indicate a maximum difference of 3.5% for the test with
 323 main wind velocity equal to 5 m/s and gap $1e$, compared to the isolated one.
 324 This slight reduction of emitted dust is mainly caused by the differences of
 325 the ratio u_s/u_r seen in zone A among the tested configurations. The levels
 326 of u_s/u_r with emission potential for this velocity are those more modified
 327 by the phenomena explained in zone A. Other values of velocity indicate
 328 differences close to 1%, which agree with the uniformity of the near wall
 329 velocity distribution for this orientation.

330 The highest differences are found for the configuration 60° which are
 331 higher than twice for the lowest velocity values tested and 55.0% for 10 m/s.
 332 This condition is extremely important as these values of wind velocity are
 333 the most observed in nature. For this configuration, the interactions between

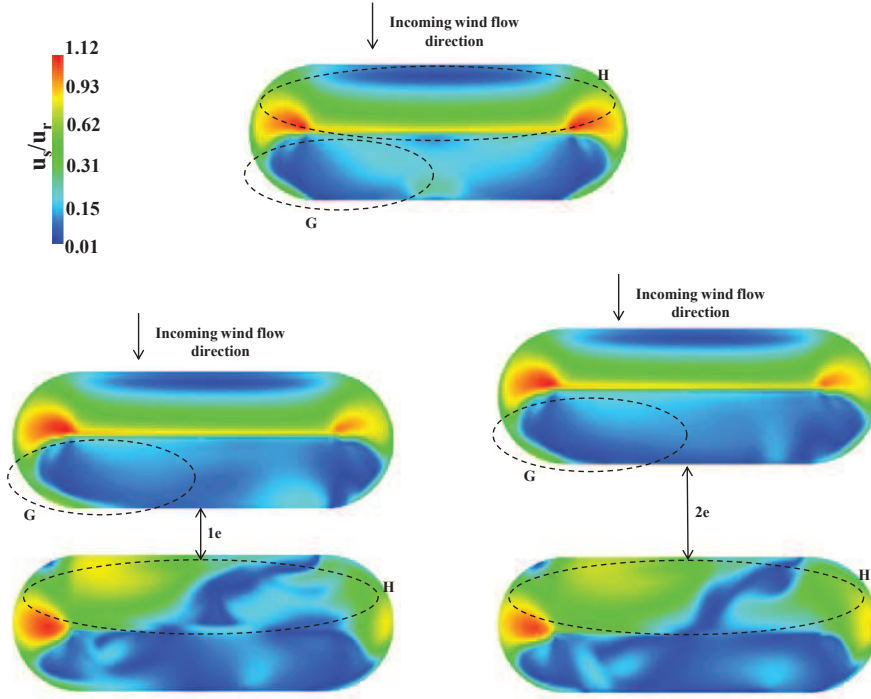


Figure 6: Wind flow exposure on the stockpile oriented 90° : (a) isolated stockpile, (b) two successive stockpiles with gap $1e$ and (c) two successive stockpiles with gap $2e$ (with $e = 0.9h$ where h is the stockpile height).

nearby stockpiles (stronger as the gap is smaller), are mainly responsible for the great increase in dust emissions noticed for all tested velocities. Even for a gap greater than approximately twice the pile height, the emissions are almost 10 % higher than for an isolated pile. In this way, there is a strong influence of the fluid flow pattern on dust emission which is strongly increased.

The perpendicular configuration shows that the comparison reaches a maximum of 22.7% also for 5 m/s. In this configuration, all the comparisons show negative percentage values as there is always a reduction of dust emitted between the isolated pile and the sum of two nearby stockpiles. The recirculation zones formed downstream the piles oriented 90° is the main reason for the reduction on the emitted mass.

The whole discussion performed in this section reveals the importance of

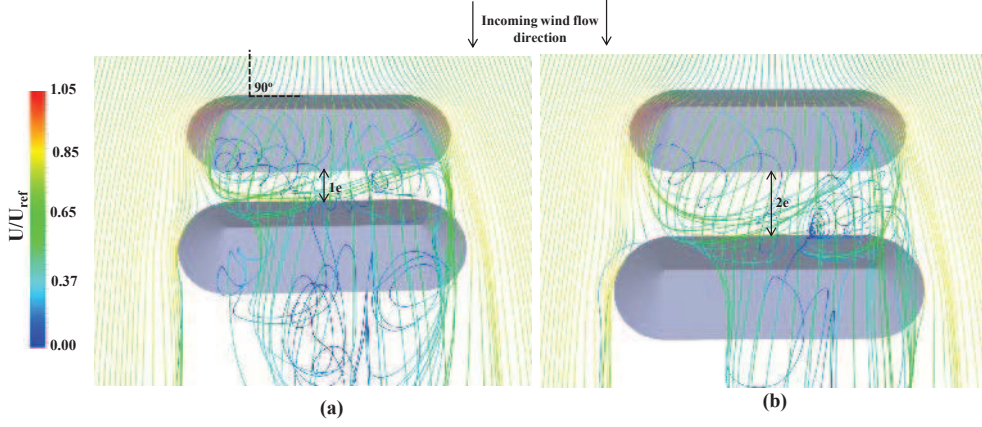


Figure 7: Streamlines coloured by the wind flow velocity magnitude for the orientation 90° : (a) two stockpiles with a gap equal to $1e$ and (b) two stockpiles with a gap equal to $2e$. (The velocity measured at 10m in real scale is chosen as the reference velocity $U_{ref} = 5.26$ m/s)

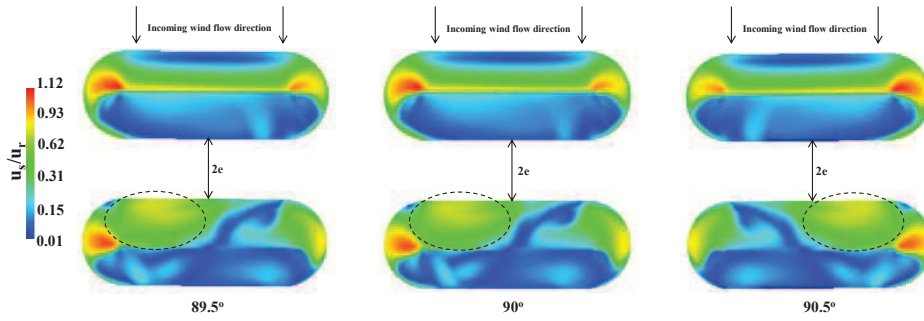


Figure 8: Wind flow exposure on two nearby stockpiles with gap $2e$ oriented 89.5° , 90° and 90.5°

347 investigating the interactions between wall-mounted obstacles. The results
 348 are a practical application for industrial sites. The quantification carried out
 349 for several arrangements assists the definition of a configuration presenting
 350 the best condition reducing the final global emission. For instance, accord-
 351 ing to the USEPA quantification previously presented, a pair of stockpiles
 352 with a gap approximately equal to the stockpile height and perpendicular
 353 to the most recurrent wind flow direction is preferable to reduce levels of
 354 atmospheric pollution from industrial sites with diffuse sources.

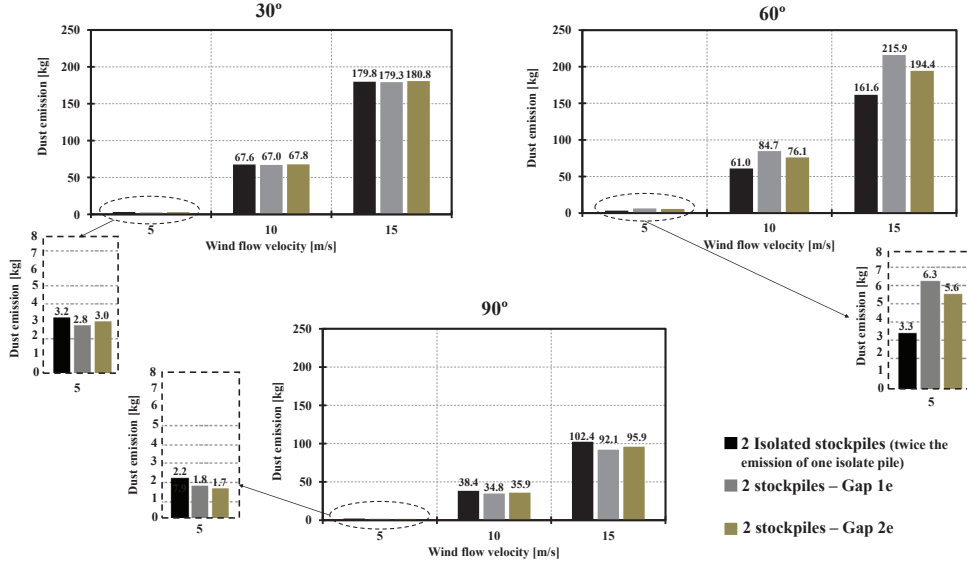


Figure 9: Quantification of dust emission for an isolated stockpile (black), two stockpiles separated by a gap 1e (grey) and two stockpiles separated by a gap 2e (yellow). $e = 0.9h$ where h is the stockpile height)

4. Conclusions

The present analysis of wall flow topology and dust emission quantification focused on oblong stockpiles found on industrial sites. The main objectives were: near wall flow topology, air flow visualization and effective quantification of emitted dust for several configurations and arrangements using the USEPA methodology. The numerical simulations were carried out with the CFD open-source code *Code_Saturne*.

Three stockpile arrangements were tested: one isolated stockpile, two nearby stockpiles with gap 1e and with gap 2e ($e = 0.9h$ where h is the stockpile height). The wall flow topology indicated significant conclusions assisted by the analysis of streamlines over the piles: (i) proximal values of near wall velocity distribution for all the cases of the configuration 30°, (ii) the streamlines of the piles oriented 30° shown that the main vortex formed downstream the first pile does not impinge the windward wall of the upstream stockpile for both gaps, (iii) the highest levels of u_s/u_r for each configuration (one pile or two piles) are always reached for the configuration 60°, (iv) the smaller the gap is the higher the levels of u_s/u_r for the configuration 60° are,

(v) streamlines of the configuration 60° have clearly shown that the main vortex impinges the downstream pile, (vi) the perpendicular configuration is characterized by the reduction on the values of u_s/u_r along the stockpile (mainly on the downstream stockpile).

The results of dust emission quantification are a consequence of the near wall fluid flow pattern. Thus, the quantification of the emission from twice the amount emitted by an isolated stockpile oriented 30° is approximately 67.6 kg for 10 m/s and, for the same velocity and orientation, the two successive stockpiles with gap $1e$ and $2e$ emit, respectively, 67.0 kg and 67.8 kg . The results of wall flow topology and dust emission quantification indicate the significance of the interactions existing between successive stockpiles for 60° and 90° . The adverse environmental effects, after a wind erosion event, may be minimized performing the arrangement of the piles on industrial sites. The objective is to orient the piles perpendicular the most usual wind flow direction which results in the lowest amount of dust emissions. For instance, for a free stream velocity equal to 10 m/s , 34.8 kg for gap $1e$ and 35.9 kg for gap $2e$ are emitted for the perpendicular stockpiles against 38.4 kg for twice the isolated pile. The main advice for industrial operators is to avoid the orientation in which the stockpiles are approximately 60° to the main wind flow direction. In this condition, the main vortex has strong effects on the successive pile increasing the amount of dust emitted (61.0 kg for the isolated pile and 84.7 and 76.1 kg for $1e$ and $2e$ also for 10 m/s).

5. Acknowledgements

This work was carried out with the financial support of EDF R&D.

References

- [1] Archambeau F., Mchitoua N., and Sakiz M., 2004. Code saturne: a nite volume code for the computation of turbulent incompressible flows industrial applications. *Int. J. Finite Volumes*, 1(1).
- [2] Badr T., Harion J-L., 2007. Effect of aggregate storage piles configuration on dust emissions. *Atmospheric Environment* 41, 360-368.
- [3] Cong, X.C., Chen, Z.L., Zhan, S.F., 2010. Experimental study of static dust emission of coal pile in the open air. *Journal of China University of Mining Technology* 39, 6849-6853.

- 405 [4] Cong, X.C., Cao, S.Q., Chen, Z.L., Peng, S.T., Yang, S.L., 2011. Im-
406 pact of the installation scenario of porous fences on wind-blown particle
407 emission in open coal yards. *Atmospheric Environment* 45, 5247-5253.
- 408 [5] Cong, X.C., Yang, S.L., Cao, S.Q., Chen, Z.L., Dai, M.X., Peng S.T.,
409 2012. Effect of aggregate stockpile configuration and layout on dust emis-
410 sions in an open yard. *Applied Mathematical Modelling*. In Press.
- 411 [6] Diego I., Pelegry A., Torno S., Toraño J., Menendez M., 2009. Simulta-
412 neous CFD evaluation of wind flow and dust emission in open storage
413 piles. *Applied Mathematical Model* 33, 3197-3207.
- 414 [7] Faria R., Ferreira A., Sismeiro J., Mendes J., Sousa J., 2011. Wind
415 tunnel and computational study of the stoss slope effect on the aeolian
416 erosion of transverse sand dunes. *Aeolian Research* 3, 303-314.
- 417 [8] Ferreira A., Oliveira R., 2009. Wind erosion of sand placed inside a rect-
418 angular box. *Journal of Wind Engineering and Industrial Aerodynamics*
419 97, 1-10.
- 420 [9] Ferreira A., Lambert R., 2011. Numerical and wind tunnel modeling
421 on the windbreak effectiveness to control the aeolian erosion of conical
422 stockpiles. *Environmental Fluid Mechanics*. DOI 10.1007/s10652-010-
423 9176-x.
- 424 [10] Furieri B., Russeil S., Santos J.M., Harion J.L., 2012. Experimental
425 surface flow visualization and numerical investigation of flow struc-
426 ture around an oblong stockpile. *Environmental Fluid Mechanics*. DOI
427 10.1007/s10652-012-9249-0.
- 428 [11] Herry B., Keirsbulck L., Labraga L., Paquet J-B., 2011. Flow bistability
429 downstream of three-dimensional double backward facing steps at zero-
430 degree sideslip. *Journal of Fluids Engineering* 133, 54501-54505.
- 431 [12] King J., Etyemezian V., Sweeney M., Buck B.J., Nikolich G., 2011.
432 Dust emission variability at the Salton Sea, California, USA. *Aeolian*
433 *Research* 3, 67-69.
- 434 [13] Neuman C., Nickling W., 1995. Aeolian sediment flux decay: non-linear
435 behaviour on developing deflation lag surfaces. *Earth Surface Processes*
436 *and Landforms* 20, 423-435.

- 437 [14] Ojelede M.E., Annegarn, H.J., Kneen, M.A., 2011. Evaluation of aeolian emissions from gold mine tailings on the Witwatersrand. *Aeolian Research* 3, 477-486.
- 438
- 439
- 440 [15] Syms G., 2008. Simulation of simplified-frigate airwakes using a lattice-Boltzmann method. *Journal of Wind Engineering and Industrial Aerodynamics* 96, 1197-1206.
- 441
- 442
- 443 [16] Toraño J., Torno S., Diego I., Menendez M., Gent M., 2009. Dust emissions calculations in open storage piles protected by means of barriers, CFD and experimental tests. *Environmental Fluid Mechanics* 9, 493-507.
- 444
- 445
- 446
- 447 [17] Toraño J., Rodrigues R., Diego I., Rivas J. M., Pelegry A., 2007. Influence of the pile shape on wind erosion CFD emission simulation. *Applied Mathematical Modelling* 31, 2487-2502.
- 448
- 449
- 450 [18] Turpin C. Harion J.-L., 2009. Numerical modelling of flow structures over various flat-topped stockpiles height: implications on dust emissions. *Atmospheric Environment* 43, 5579-5587.
- 451
- 452
- 453 [19] Turpin C., Harion J.-L., 2010. Effect of the topography of an industrial site on dust emissions from open storage yards, *Environmental Fluid Mechanics* 10, 677-690.
- 454
- 455
- 456 [20] USEPA, 2006. Miscellaneous Sources, Industrial Wind Erosion, AP-42, 5th edn, vol I, Chap 13.2.5, November 2006.
- 457
- 458 <http://www.epa.gov/ttn/chief/ap42/ch13/final/c13/final/c13s0205.pdf>.

4.2.2 Analysis of dust re-emission from the ground region surrounding successive stockpiles

Previous works have deeply studied the aeolian erosion over oblong storage piles:

- in section 4.1.1, wall and air flow pattern surrounding isolated stockpiles were presented. Delimitation of the potential zones of settled dust re-emission;
- in section 4.1.2, quantification of dust re-emission by means of the USEPA methodology (three incoming wind flow directions and three wind velocities) of an isolated stockpile and
- in section 4.2.1, the work discussed the influence of a second nearby stockpile on the near wall flow topology and consequently on the dust emission quantification. The complex fluid flow structures formed due to the presence of a successive pile has presented strong effects over the piles.

The ground region surrounding storage piles presents a strong impact on the overall atmospheric condition. The estimated amount of the settled dust re-emitted may not be neglected as it was shown in section 4.1.2. The results of the quantification of dust re-emission, presented in section 4.1.2, showed for a given wind flow condition that 67% of the overall emitted dust is subject of the re-emission from the ground region around stockpiles. Furthermore, the results in section 4.2.1, dealing with the complex structures formed between successive stockpiles and their influence on dust emission quantification, shown a considerable increase on the values of kg/m^2 for two successive stockpiles oriented 60° . The increase on dust emissions for the last mentioned configuration is about 45%.

In that way, the present subsection aims to proceed previous investigations, studying the influence of complex structures (formed due to the stockpile arrangement) on the fluid flow near the ground region surrounding piles. For that aim, the results and discussions are divided in three parts:

- a comparison between numerical contours of normalized wall shear stress and oil-film fluid flow visualization (cf. Chapter 2) is done for some tested cases;
- distribution of the near wall velocity surrounding the stockpiles by means of numerical simulations (cf. section 4.2.1 for details about modelling parameters), for all tested configurations, aiming the calculation of the ratio u_s/u_r and
- dust emission quantification (USEPA methodology).

4.2.2.1 Wall and air flow topology around successive stockpiles

The experimental technique of oil-film fluid flow visualization, applied on the wall around a stockpile model, intends to obtain a more suitable understanding of the flow featuring on this region. As extensively said in previous sections, this experimental approach offers a two-dimensional visualization with a good spatial resolution of the distribution of the wall friction which is associated to dust re-emission. The fluid flow visualization by this experimental technique is presented for the following configurations: 30° and gap $1e$ (Figure 4.7), 60° and gap $2e$ (Figure 4.10) and 90° and gap $2e$ (Figure 4.13). The objective is, for each flow orientation which presents a specific flow pattern, analyse more detailed, by means of this comparison, the near wall flow for at least one gap. The numerical near wall flow distribution for the other gaps is presented later in this subsection.

Therefore, Figure 4.7a presents numerical contours of normalized wall shear stress ($\tau_{ref} = 0.07Pa$ computed for the undisturbed region on the computational domain) and Figure 4.7b shows the last photograph taken during the experimental technique of surface flow visualization. The last photograph indicates the instant when the oil-film pattern does not present more modifications. The numerical results have shown a good agreement with the experimental technique. Indeed, the highlighted zones are very similar in both approaches.

Region 1 depicts the effects, on the ground surface, of the main vortex formed downstream the first stockpile. A strong friction on the wall is noticed in this highlighted region. The high wall

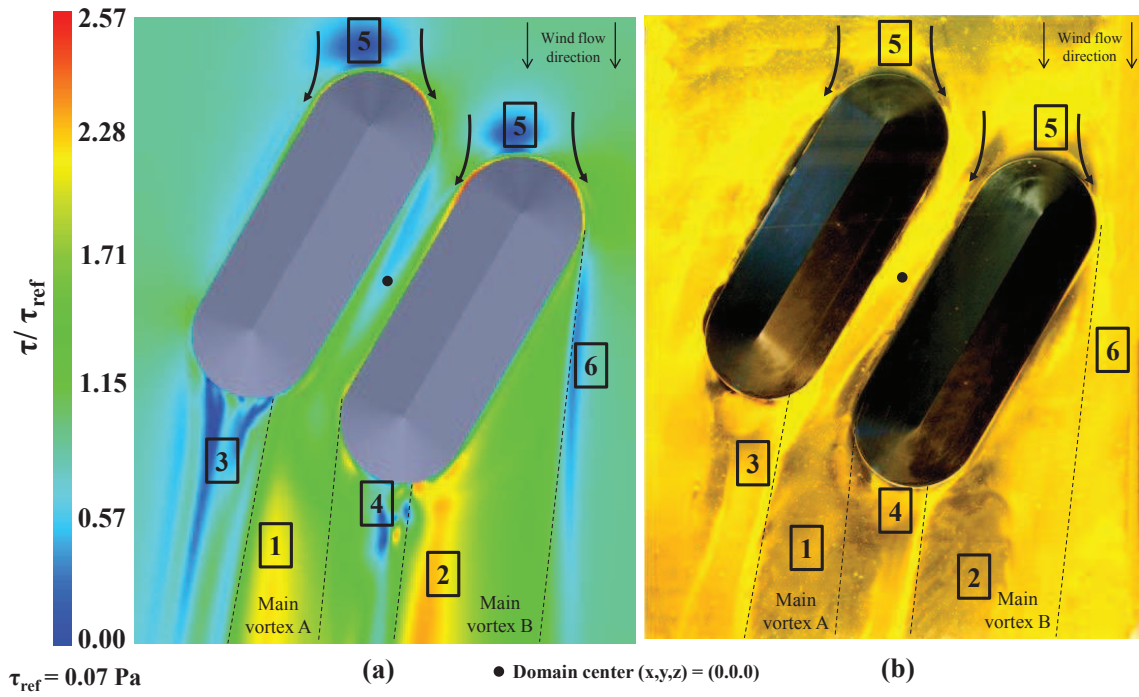


Figure 4.7: Numerical and experimental approaches of the wall shear stress evaluation on the ground region surrounding two successive stockpiles oriented 30° with a gap equal to $1e$ ($e = 0.9h$, h is the stockpile height): (a) numerical contours of normalized wall shear stress magnitude ($\tau_{ref} = 0.07 Pa$) and (b) photograph of oil-film surface flow visualization

friction caused by the main vortex is also identified in the photograph. The darkest regions indicate high wall friction: the oil-film is dislocated towards another region on the plate. Region 2 is also an example of high friction on the wall: effect of the main vortex formed downstream of the second pile. On the other hand, regions of intense yellow color represent an accumulation of the oil-film corresponding in the numerical results of low levels of wall shear stress. Regions 3, 4, 5 and 6 indicate the accumulation of the oil-film. Numerical results have shown for regions 3 and 4 the lowest levels of normalized wall shear stress (blue contours in Figure 4.7a). Region 5 is the impingement zone with low levels of wall shear stress. The incoming fluid flow is deviated towards the stockpile crest and lateral sides. The black arrows illustrate the flow acceleration perceived in this region: a local augmentation of the wall shear stress. The experimental photograph shows black areas near the stockpile as an effect of the flow acceleration. Section 4.2.1 presented streamlines between the successive piles and their effects on the piles. The analysis of streamlines shows the incoming fluid flow deviation and the formation of the main vortices on both stockpiles. Finally, Region 6 shows an ineffective zone on the ground downstream the second pile, right of the main vortex. In the first pile, this region is concentrated between the piles.

The dashed lines on Figure 4.7 delimit the effects areas of the main vortices on the wall: main vortex A formed on the upstream pile and main vortex B formed on the downstream pile. These vortices are also highlighted in Figure 4.8. Figure 4.8 presents the evolution of the spanwise component of the wall shear stress and the streamlines on a YZ plane. Between the zones under the effects of the main vortices ($-3.75 < y/h < -1.25$ and $0.00 < y/h < 2.00$) there is a smaller vortex ($-1.25 < y/h < 0.00$) resulted from the modification of the main vortex A by the downstream pile. The smaller vortex does not present an important effect on the surface. The normalized wall shear stress levels are not higher than 0.75.

On the regions modified by the main vortices, downwash zones are noticed. These structures, highlighted over the streamlines, are responsible for high velocity gradient values near the wall which consequently results in high wall shear stress values ($\tau_{yz}/\tau_{ref} = 1.10$ for the main vortex A and $\tau_{yz}/\tau_{ref} = 1.31$ for the main vortex B). The peak of wall shear stress observed in the main vortex A is slightly smaller than the peak in the zone affected by the main vortex B caused by the interaction

of the main vortex A with the downstream pile. In fact, the main vortex A does not impinge the downstream pile, however it is slightly modified by its presence (cf. section 4.2.1 for more details about the streamlines surrounding the stockpiles). Settled particles are re-emitted as a result of upwash zones. For instance, the streamlines in Figure 4.8, show an upwash zone is noticed at y/h approximately equal to -3.75. Accordingly, surface flow visualization shows at this transversal location an intense yellow color which is related to an accumulation of the coating.

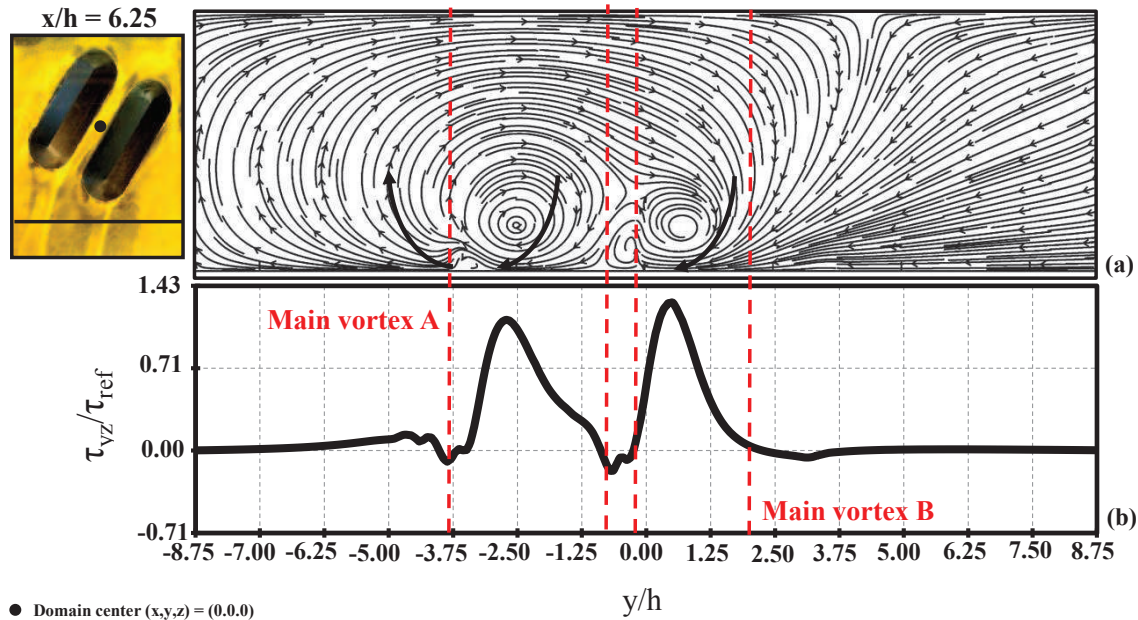


Figure 4.8: Numerical results of the air flow topology surrounding the successive stockpiles oriented 30° : (a) streamlines over a transversal (YZ) plane and (b) plot of normalized spanwise wall shear stress ($\tau_{ref} = 0.07 Pa$)

Figure 4.9 shows the near wall velocity distribution, by the means of the ratio u_s/u_r , for the three tested arrangements. A better comprehension of the modifications caused by the successive pile may be seen in these contours. Also, the influence of the gap between the piles on this distribution is analysed using Figures 4.9b and 4.9c.

The pattern of the fluid flow distribution near the wall for the isolated stockpile indicates four main zones:

- region 1, effect of the main vortex,
- region 2, effect of the secondary vortex,
- region 3, ineffective zone downstream the pile (lowest levels of u_s/u_r),
- region 4, wind flow impingement and
- region 5, ineffective zone in the right of the main vortex.

Figures 4.9b and 4.9c show that some of these structures are strongly modified by the presence of a successive stockpile. In fact, only the region 4 does not present significant differences. Figure 4.9b (gap $1e$), indicates the contours of the main vortex on the near wall (Region 1). The main vortex is highly modified compared to the isolated configuration. A smaller area of the region 3 for the downstream pile (low levels of shear stress) is also noticed.

In conclusion, the analysis carried out in previous paragraphs indicated that the arrangement of piles orientated 30° presents more significant modifications of near wall flow topology on the ground surface than on the surface of the pile. Indeed, the results presented in section 4.2.1 have shown that the modifications on the pile are very small. This condition is observed for both tested gaps.

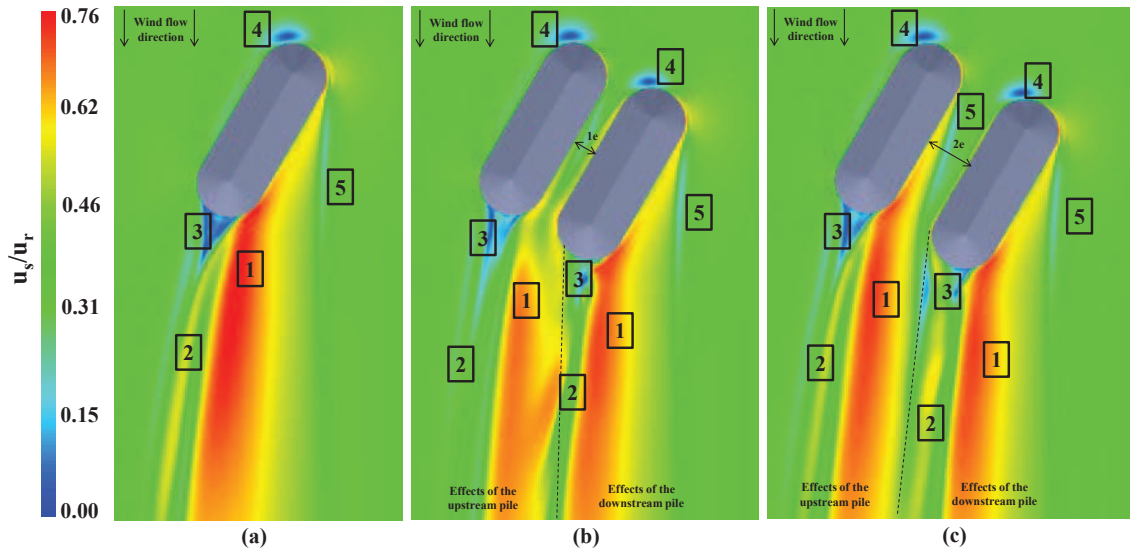


Figure 4.9: Near wall flow velocity distribution in terms of the ratio u_s/u_r of the configuration 30° : (a) isolated stockpile, (b) two successive stockpiles with a gap $1e$, (c) two successive stockpiles with a gap $2e$ ($e = 0.9h$, h is the stockpile height)

However, the results of wall flow topology around the piles are sensibly different between the three tested arrangements. The effects of the main vortex A (formed upstream) are highly modified by the downstream stockpile. Furthermore, the areas called region 3, for the downstream piles, are completely different in both configurations with two stockpiles.

Results for the orientation 60° are presented in Figures 4.10, 4.11 and 4.12. The configuration with a gap equal to $2e$ was chosen for this orientation to discuss numerical wall shear stress and oil-film fluid visualization. Among all the tested configurations, the effects noticed on the wall flow topology are the strongest for this orientation. Figure 4.10 presents the numerical contours of normalized wall shear stress and the experimental photograph of oil-film surface flow visualization. In Figure 4.10, four regions were highlighted:

- region 1 is the effect of the main vortex formed on the upstream pile (main vortex A) and on the downstream pile (main vortex B),
- region 2 is the effect of the secondary vortex which is modified due to the presence of a downstream pile,
- region 3 the ineffective zone, indicates low levels of wall shear stress on the ground region situated between the main vortices and
- region 4 is the impingement region.

It is worth to note that, a very good agreement is observed between the visualizations shown in Figures 4.10a and 4.10b. Region 1 presents the highest levels of normalized wall shear stress: a peak of approximately 4.30 is computed. The higher friction existent in the orientation 60° may be noticed comparing Figure 4.10 and Figure 4.7 (30° , maximal value: 2.57). Indeed, the zones of intense black color are greatly more visible for the orientation 60° (regions 1 in Figure 4.10). Moreover, the equivalent region highlighted on the photograph has, as expected, an intense black color which means a zone of high friction over the surface. The main vortex strongly affects the velocity distribution in the wake. However, due to the presence of the second stockpile, the values of wall shear stress become more intense in the gap between the piles. The main vortex A is deviated caused by the downstream pile and intensifies the effects on the ground surface. Lastly, the main vortex B is similar to the structure formed around the isolated pile.

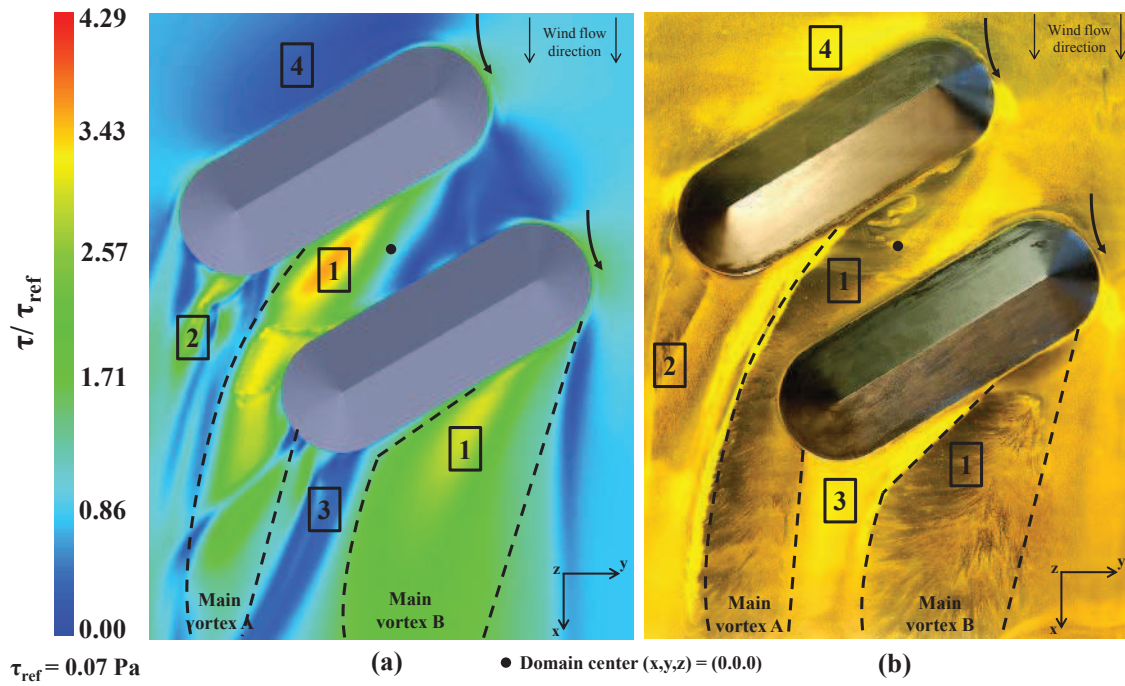


Figure 4.10: Numerical and experimental approaches of the wall shear stress evaluation on the ground region surrounding two successive stockpiles oriented 60° with a gap equal to $1e$ ($e = 0.9h$, h is the stockpile height): (a) numerical contours of normalized wall shear stress magnitude ($\tau_{ref} = 0.07 \text{ Pa}$) and (b) photograph of oil-film surface flow visualization

The important effects of the secondary vortex, which is a structure normally found in the isolated configuration, is not noticed in Figure 4.10. Region 2 is the effect on the wall of a modified secondary vortex. The region 2 in the photograph shows small modification of the initial pattern of the oil-film. For the downstream pile, there is only the main vortex. The secondary one is replaced by the main vortex A, formed upstream. The photograph of the experimental technique shows, in region 3, an accumulation of the oil-film. The accumulation in this region is an expected pattern. This region is situated between the two main vortices, in a zone of very small wall friction. The numerical results also show this pattern: the normalized wall shear stress over this region is less than the unity. The region 4 on the upstream pile does not present any modifications compared to the region seen in the isolated pile configuration. Additionally, the flow acceleration is equally observed in both piles and highlighted by the black arrows. Dashed lines on Figure 4.10 delimit the regions of the effects of the main vortices A and B on the wake.

Details about the main vortices A and B, and their effects on the ground region responsible for the particle take-off, are illustrated in Figure 4.11. Figure 4.11a depicts the streamlines over a spanwise plane. Figure 4.11b is a plot of the normalized spanwise component of wall shear stress. Both images are located at the same transversal position $x/h = 3.75$. Two main structures are highlighted in Figure 4.11: main vortices A and B. Main vortex A is modified by the presence of the downstream stockpile. While main vortex B indicates a maximum value of shear stress $\tau_{yz}/\tau_{ref} = 2.60$, the peak for the main vortex A is smaller, about $\tau_{yz}/\tau_{ref} = 1.80$. Furthermore, in the right and left sides of the main vortex A smaller structures causing augmentations of the levels of τ_{yz}/τ_{ref} are noticed. The evolution of the spanwise shear stress of the main vortex B is about the same observed in the isolated stockpile (see section 4.1.1 for more details about the air flow topology of the isolated stockpile). The black arrows represent upwash and downwash zones. The two peaks of normalized spanwise shear stress observed in Figure 4.11a are linked to the downwash zones highlighted in Figure 4.11b. Finally, there is an upwash zone for approximately y/h between -3.75 and 5 .

Figure 4.12 shows numerical contours of u_s/u_r for all the tested arrangements of stockpiles oriented 60° to the main wind flow direction. The four regions previously listed in Figure 4.10 are highlighted in Figure 4.12. The highest levels of u_s/u_r are found over the gap between successive

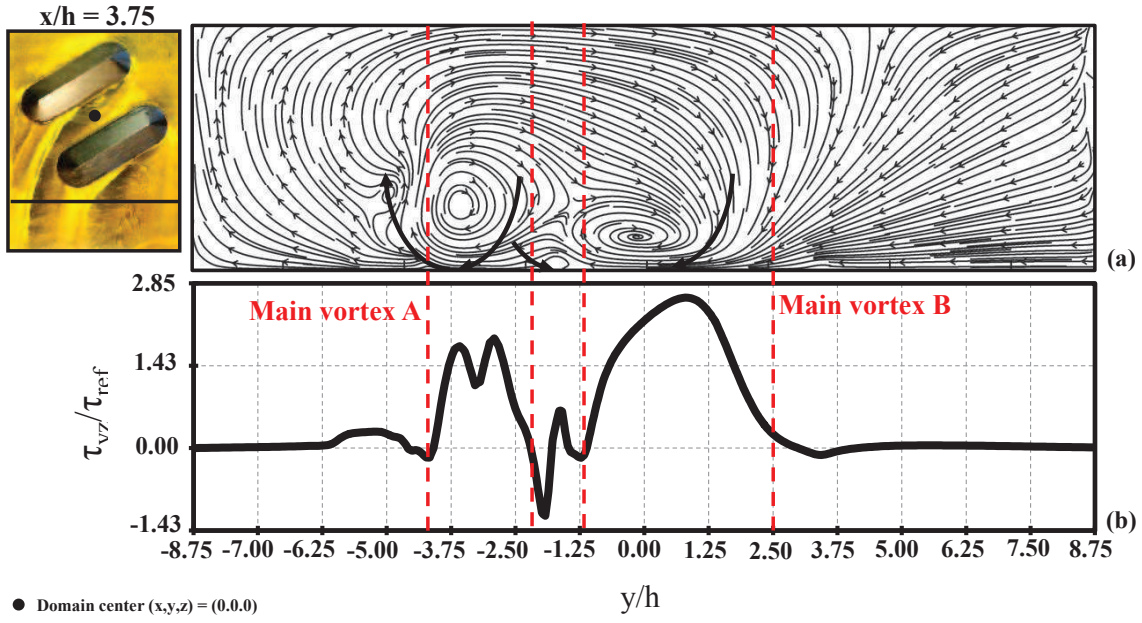


Figure 4.11: Numerical results of the air flow topology surrounding the successive stockpiles oriented 60° : (a) streamlines over a transversal (YZ) plane and (b) plot of normalized spanwise wall shear stress ($\tau_{ref} = 0.07Pa$)

stockpiles. As the piles are arranged with a larger gap (represented herein by the isolated stockpile), the effects of the main vortex on the ground are stronger. The fact of being nearby in the configuration $1e$, sensibly changes the main vortex A (formed on the upstream stockpile) which causes more impact on the stockpile surface than on the ground around the pile. The practical effects of these distributions will be discussed hereafter by the USEPA quantification of dust emissions.

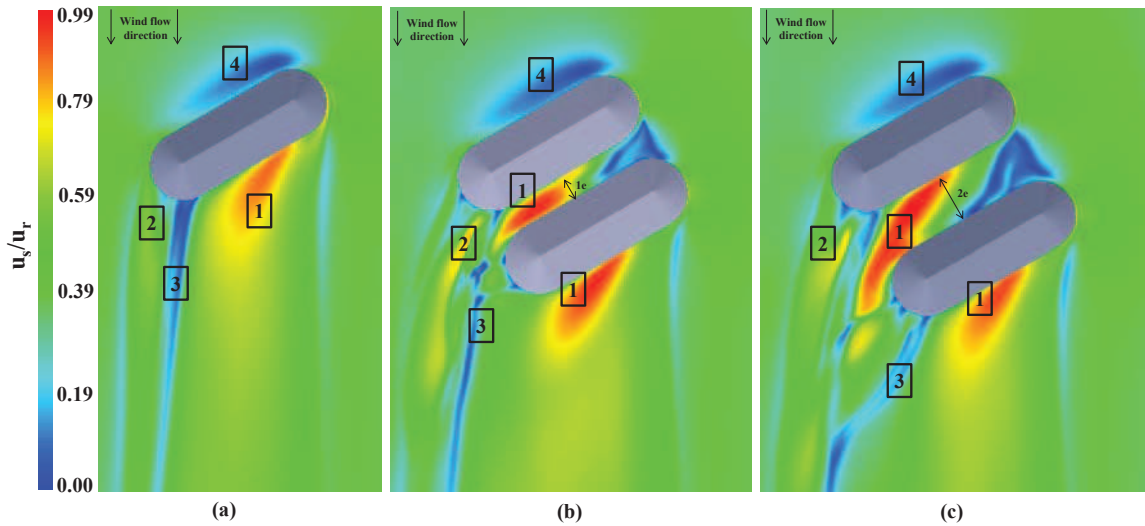


Figure 4.12: Near wall flow velocity distribution in terms of the ratio u_s/u_r of the configuration 60° : (a) isolated stockpile, (b) two successive stockpiles with a gap $1e$, (c) two successive stockpiles with a gap $2e$ ($e = 0.9h$, h is the stockpile height)

Figures 4.13, 4.14 and 4.15 present numerical and experimental results for the perpendicular inflow. The numerical simulations results of the perpendicular orientation contain the effects of the bi-stability. More detailed information about the bi-stability of the fluid flow is presented in section 4.2.1 (the numerical simulation results presented in the section 4.2.1 are the same as those shown in the current section). The analogies found out between normalized wall shear stress and

the experimental surface flow visualization are presented in Figure 4.13. The acceleration regions are defined by the black arrows on the sides of the windward wall of the upstream stockpile. Furthermore, three regions are highlighted in this configuration: the main vortex A (region 1), the main vortex B (region 2) and a recirculation zone in the wake (region 3).

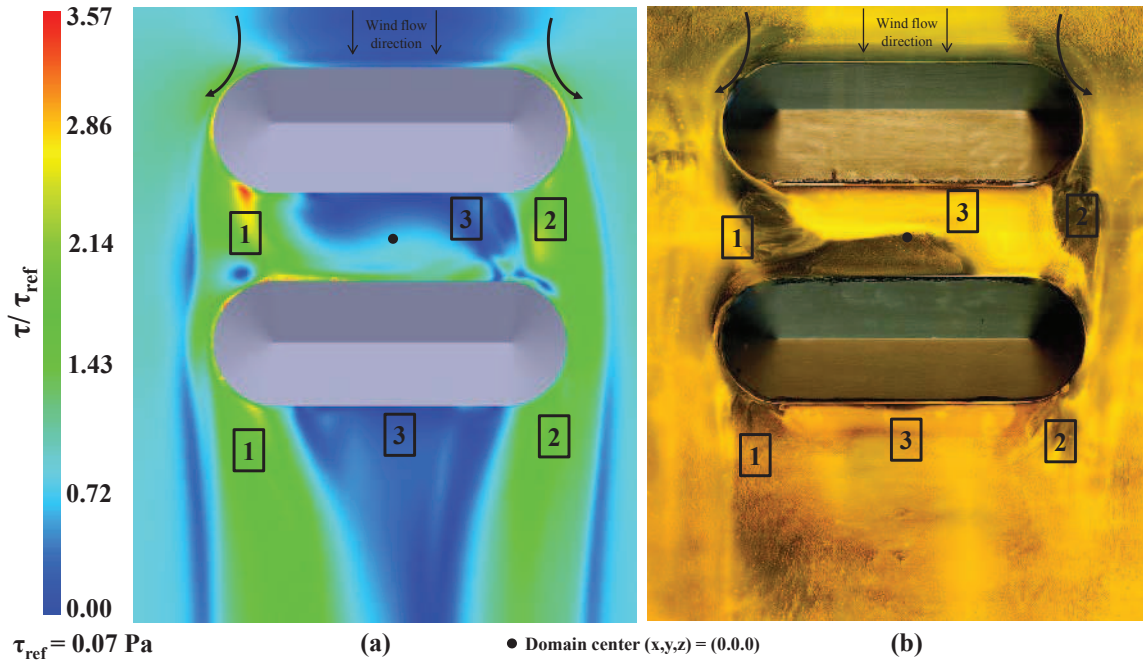


Figure 4.13: Numerical and experimental approaches of the wall shear stress evaluation on the ground region surrounding two successive stockpiles perpendicular to the incoming wind flow with a gap equal to $1e$ ($e = 0.9h$, h is the stockpile height): (a) numerical contours of normalized wall shear stress magnitude ($\tau_{ref} = 0.07 Pa$) and (b) photograph of oil-film surface flow visualization

The main vortex A presents stronger effects on the wall than the main vortex B. In addition, in the distribution of oil-film, the zone of intense black color is more intense on the right side of the piles (region 1). This condition is also caused by the bi-stability of the fluid flow around stockpiles. The zones of low wall shear stress shown by the numerical contours are well noticed on the photograph of experimental visualization (regions 3). A comparison with the isolated pile results (cf. section 4.1.1) of normalized shear stress shows a reduction of these values around the piles. The zones of more concentrated values of wall shear stress, noticed on the isolated configuration, are less present in this case.

In Figure 4.14, presenting streamlines and spanwise wall shear stress evolution, the bi-stability of the flow is easily recognized. For instance, the main vortex A presents a peak of $\tau_{yz}/\tau_{ref} = -2.14$ while the main vortex B expected to be symmetric presents the same peak equal to 1.43. The upwash zone, normally placed in the middle line of the domain is dislocated to the left (following the flow direction). At the streamlines plane a great main vortex is noticed beside a small one.

Figure 4.15 shows the comparison of near wall flow distribution in terms of the ratio u_s/u_r for the three arrangements of perpendicular stockpiles. The main conclusion of this image is that the zones of low ratio u_s/u_r and consequently no take-off are greater where there is a successive stockpile.

4.2.2.2 Dust emission quantification

The quantification of dust re-emissions on the surrounding areas was carried out by using the USEPA methodology [75]. Table 4.2 compiles the data of mass of dust re-emission per area of the surface being analysed. Table 4.3 summarizes the contribution of the re-emission on the overall emissions in real industrial site scale. For more details about the methodology of dust re-emission quantification implemented hereafter, cf. section 4.1.2.

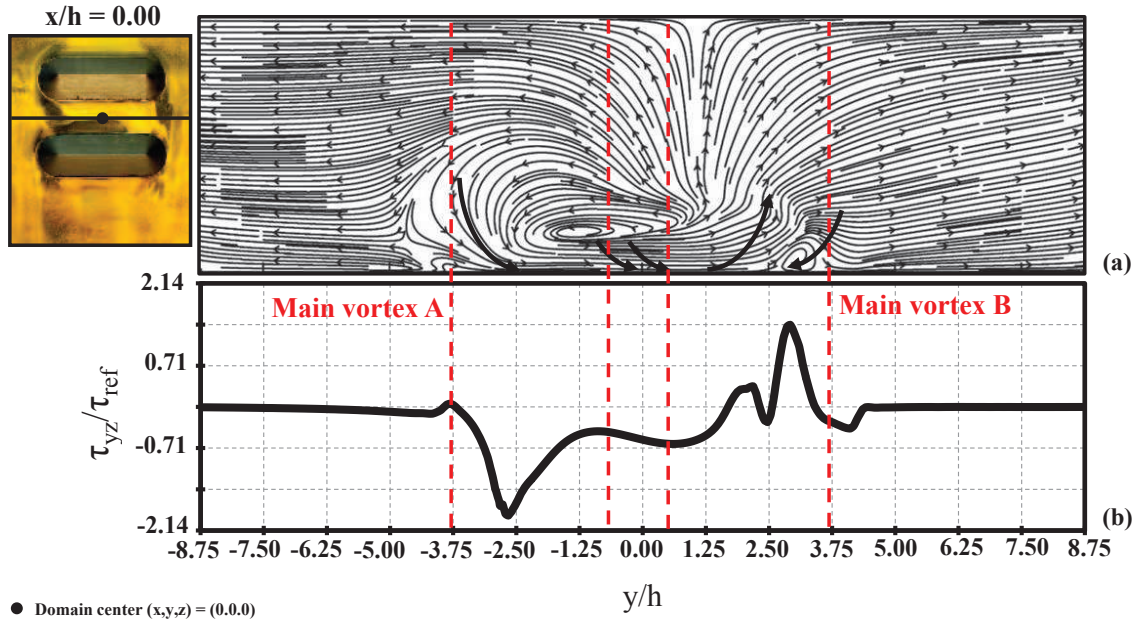


Figure 4.14: Numerical results of the air flow topology surrounding the perpendicular successive stockpiles: (a) streamlines over a transversal (YZ) plane and (b) plot of normalized spanwise wall shear stress ($\tau_{ref} = 0.07 Pa$)

The area of the surface of interest surrounding the stockpiles changes for each tested configuration. For this reason, the quantification of dust re-emission was chosen to be presented in units of g/m^2 which normalizes the data (isolated pile, $52998 m^2$; two piles gap 1e, $64031 m^2$ and two piles gap 2e, $68219 m^2$ in real scale). The surface around the pile was chosen arbitrarily as it was done in section 4.1.2. The isolated pile case characterizes a situation on industrial sites where successive piles present a very high gap between them.

The choice of the tested values of u_{10}^+ is explained in section 4.1.2. For the smallest wind velocity ($u_{10}^+ = 5 m/s$) there is no emission of settled dust on the surrounding areas for all tested configurations. On the other hand, for the results of intermediate tested wind velocity ($u_{10}^+ = 10.38 m/s$) the re-emission reaches $2.87 g/m^2$ for two stockpiles oriented 60° with a gap equal to 2e. Events of very high velocity values of the incoming flow ($u_{10}^+ = 15 m/s$) result in the increase of approximately ten times the values of dust re-emission rate.

The orientation 60° presents for all velocities the highest values of re-emitted dust on the surrounding areas. In addition, the gap between piles has few influence on the analysis of dust re-emission for the orientations 60° and 90° for all wind velocities tested. On the other hand, for the orientation 30° , the re-emission is very sensible to the modification of the gap which indicates a difference about 19% for a given velocity. The re-emission increases for the configuration with two nearby stockpiles (compared with the isolated stockpile) for the oblique orientations, 30° and 60° while for the perpendicular orientation there is a decrease.

Table 4.2: Dust emissions per perturbation in g/m^2 for the tested cases: on and around the stockpiles

		Emissions (g/m^2)		
		$u_{10}^+ = 5 m/s$	$u_{10}^+ = 10.38 m/s$	$u_{10}^+ = 15 m/s$
Around the stockpiles	One pile 30°	0.0	0.15	1.63
	Two piles 30° 1e	0.0	0.22	1.95
	Two piles 30° 2e	0.0	0.26	2.12
	One pile 60°	0.0	0.34	2.52
	Two piles 60° 1e	0.0	0.44	2.83
	Two piles 60° 2e	0.0	0.47	2.87
	One pile 90°	0.0	0.16	1.63
	Two piles 90° 1e	0.0	0.11	1.52
	Two piles 90° 2e	0.0	0.12	1.56

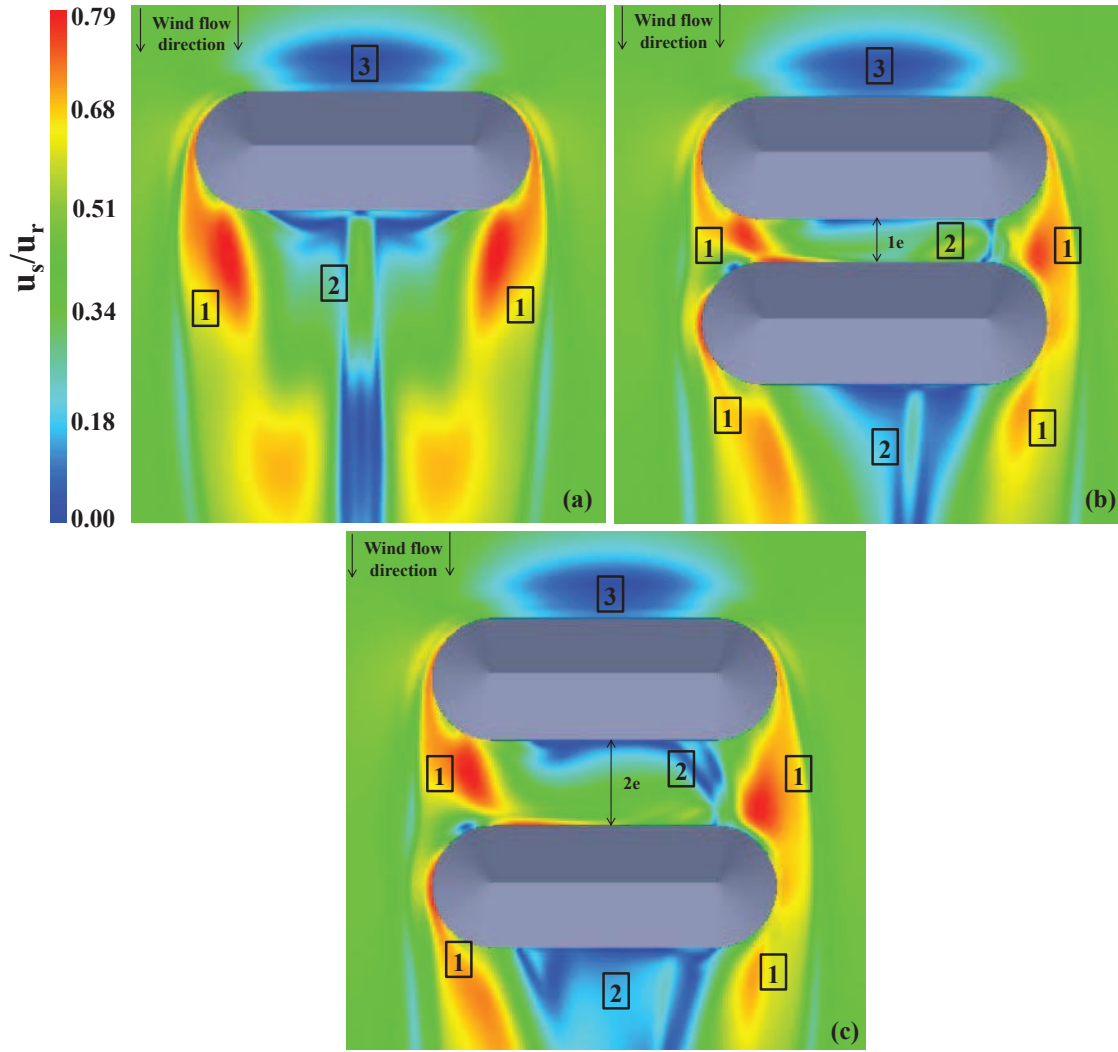


Figure 4.15: Near wall flow velocity distribution in terms of the ratio u_s/u_r of the perpendicular configuration: (a) isolated stockpile, (b) two successive stockpiles with a gap $1e$, (c) two successive stockpiles with a gap $2e$ ($e = 0.9h$, h is the stockpile height)

The information presented in Table 4.3 determines the importance of the re-emission of settled particles on the overall emissions of yards of granular material agglomeration. The contribution of the ground region shows that for the smallest velocity there is no re-emission and it increases if the velocity increases. The other two velocities have shown that the re-emission is more important for the isolated stockpile and the two tested gaps have shown a very small influence on the value of the contribution of the surrounding region. For the intermediate tested velocity, $u_{10}^+ = 10.38$ m/s, the maximum importance of the region surrounding the pile is found for the isolated pile oriented 60° : 38.9 %. The results for the greatest velocity present, also for the isolated pile oriented 60° , the maximum value found for the contribution of the surrounding stockpile equal to 63.8 %.

4.2.2.3 Conclusions

The quantification of dust re-emission was not considered in any previous work concerning the aeolian erosion of successive diffuse sources. A complete analysis of the fluid mechanics of the incoming flow disturbed by the stockpiles arrangements has shown for all tested configurations air flow structures promoting zones of re-emission of settled particles.

The most important practical application is the comparative analysis of dust emission between different velocities, orientations and arrangements. The fluid flow over a stockpile or a group of stockpiles oriented 60° presented huge vortices with great effects on the ground. This arrangement

Table 4.3: Contribution in percent of the ground region surrounding stockpiles

		Contribution of the surrounding region (%)		
		$u_{10}^+ = 5 \text{ m/s}$	$u_{10}^+ = 10.38 \text{ m/s}$	$u_{10}^+ = 15 \text{ m/s}$
Contribution Around the Pile	One pile 30°	0.0	20.2	47.4
	Two piles 30° 1e	0.0	16.7	40.4
	Two piles 30° 2e	0.0	18.0	43.9
	One pile 60°	0.0	38.9	63.8
	Two piles 60° 1e	0.0	25.1	46.2
	Two piles 60° 2e	0.0	29.6	49.6
	One pile 90°	0.0	30.0	62.2
	Two piles 90° 1e	0.0	16.3	50.2
	Two piles 90° 2e	0.0	17.9	51.7

has to be avoided on industrial sites. However, if this orientation must be set operators must separate the piles the maximum. Finally, the perpendicular orientation shown, for all configurations, the lowest emission rates. In this orientation there is no main vortex acting around the pile which is the structures responsible for the elevated rates of dust emission for the other orientations and successive stockpiles promotes an ineffective zone. On some industrial sites, the amount of dust re-emitted from the ground is being considered in the final quantification of emissions.

Résumé en français - Conclusions

Cette thèse a été consacrée à l'étude de l'érosion éolienne des tas de stockage de matières granulaires sur les sites industriels. Les caractéristiques globales de l'écoulement turbulent sur des tas de stockage et les caractéristiques locales de l'écoulement sur des éléments de rugosité, qui représentent les particules de la matière granulaire, sont les principaux résultats obtenus à l'aide d'approches expérimentales (soufflerie) et numériques.

Les visualisations pariétales de l'écoulement à l'aide de la technique du film d'huile ont contribué à répondre au manque d'informations concernant la topologie de l'écoulement proche paroi autour de tas de stockage et ont fourni des indications qualitatives qui ont contribué à une validation partielle des simulations numériques présentant plusieurs zones potentielles de réémissions de particules. Ces zones au sol entourant les tas sont généralement chargées de particules fines sur les sites industriels.

Pour le cas d'un tas de stockage impacté par un écoulement de vent perpendiculaire, des zones d'accélération sur chaque côté du tas sont observées. Elles induisent des zones de fort frottement pariétal qui présentent donc un potentiel élevé de réémission de particules. Les tas orientés à 30° et 60° par rapport au vent incident ont présenté les valeurs les plus élevées de la contrainte pariétale dans leur sillage. Ce résultat est lié à la formation et au développement d'un tourbillon quasi longitudinal en aval du tas. Des configurations de tas de stockage oblongs et successifs ont été également étudiées. Les configurations testées (un tas isolé et deux tas proches avec des distances différentes entre les deux tas) ont montré les effets de la complexité des structures d'écoulement formées par l'interaction entre les tas.

La quantification de la réémission de particules dans le voisinage des tas de stockage par la méthode USEPA qui dépend de la distribution de vitesse proche paroi (u_s/u_r) entourant les piles, a été prédite par simulations numériques. La contribution de la réémission de particules déposées autour des tas est dans certaines configurations particulièrement importante: par exemple, les réémissions représentent jusqu'à 43% du total émis au global pour un tas orienté 60° pour une vitesse de vent de 10 m/s. Les émissions globales d'un site industriel peuvent aussi être grandement sous-estimées si ces émissions supplémentaires environnantes ne sont pas prises en compte. La quantification de différents arrangements de tas successifs a également été réalisée. Les résultats montrent que la disposition des tas orientés 60° par rapport à la direction principal du vent doit être évitée sur les sites industriels. L'incidence sur les émissions de particules des modifications de la crête des tas a été réalisée pour un tas isolé.

Les mesures continues en soufflerie de la masse émise ont été réalisées dans le but d'évaluer l'influence des particules non-érodibles pour un tas de stockage isolé et perpendiculaire par rapport au vent. Le sable testé présente une granulométrie bimodale. Deux taux de couverture (10 et 20%) et trois vitesses de l'écoulement libre (6, 7 et 8 m/s) ont été testés. Les résultats ont montré une décroissance temporelle du flux de masse émise du fait de la présence de particules non-érodibles. La valeur de masse émise à partir de pesées différentielles est la plus élevée pour la vitesse la plus élevée et le plus faible taux de couverture. L'agglomération des particules non-érodibles sur la surface érodible provoque la diminution de la quantité de particules émise. D'autres expériences en soufflerie pour des tas de stockage obliques ont montré une forte érosion sur la crête et la formation d'un tourbillon fortement érosif sur la paroi.

Les investigations menées sur l'influence des particules non-érodibles ont conduit à des résultats importants pour la quantification d'émissions de particules sur les sites industriels. La technique expérimentale de mesure en continu menée dans cette thèse est originale. Elle a conduit à des perspectives intéressantes. De plus, ces résultats expérimentaux ont été utilisés pour proposer une

amélioration de la méthodologie de l'USEPA. Un manque remarqué dans cette méthodologie réside dans le fait que les différentes proportions de particules non-érodibles présentes dans des agglomérats de matières granulaires naturels ne sont pas explicitement prises en compte. Ainsi, il a été proposé une modification de la formulation du potentiel d'érosion qui intègre ce paramètre.

L'analyse de l'influence locale de la présence de particules non-érodibles a été effectuée avec des simulations numériques. L'évolution de la vitesse de frottement moyennée est analysée pour un domaine partiellement couvert par des éléments de rugosité de distribution poly-dispersée. Une formulation mathématique associe le frottement sur les parois et les paramètres géométriques des éléments de rugosité pour un lit de particules avec des diamètres et des hauteurs égales (condition rarement rencontrée pour des matériaux granulaires réels). Les résultats ont montré que la formulation originale [71], initialement développée pour des éléments de rugosité mono-dispersés (diamètre et hauteurs identiques), reste valable pour les distributions de particules poly-dispersées utilisées dans cette thèse.

Conclusions and Perspectives

Conclusions

This thesis was dedicated to investigate the wind erosion of granular material storage piles commonly found on industrial sites. Turbulent flow patterns over storage piles and local turbulent flow characteristics over roughness elements which represent granular material particles are the main results obtained by means of experimental (wind-tunnel) and numerical approaches.

The oil-film surface flow visualization contribute to fulfil the lack of wall flow topology informations and provided partial validation of numerical simulations presenting several potential zones of particles re-emission. These should not be neglected if the ground surrounding the piles is charged with silt particles which is commonly the case on industrial sites. For the stockpile impinged by a perpendicular incoming flow the acceleration zones on each lateral side indicate high wall friction and high potential of dust re-emission. Stockpiles oriented 30° and 60° to the main incoming wind flow presented the highest values of wall shear stress in the near wake, caused by a strong main longitudinal vortex. Successive oblong stockpiles were also studied. The tested arrangements (one isolated stockpile and two nearby stockpiles with different gaps) showed the effects of complex fluid flow structures formed due to interactions between piles.

The quantification of dust re-emission by means of the USEPA methodology which depends on the near wall flow distribution (u_s/u_r) surrounding the piles was predicted by numerical simulations. The contribution of re-emission of settled dust particles is found to be significant: for instance, a value of 43% (ratio between dust re-emission and global emissions) is obtained for the 60° configuration for a velocity about 10 m/s. The global emission from a open stockpile yard may be underestimated if these additional surrounding emissions are not taken into account. The quantification with arrangements of successive stockpiles was also carried out. The arrangement of stockpiles arranged 60° has to be avoided on industrial sites. The implication on dust emissions of the modifications of the stockpile crest was carried out for an isolated pile. The rounded crest oriented 60° has presented the highest global dust emission values. Only for one tested configuration (30°), the dust emission results were very slightly reduced for a rounded crest compared to the sharpened configuration.

The wind-tunnel continuous measurements of the emitted mass primarily investigated the influence of non-erodible particles for an isolated and perpendicular stockpile. The tested sand had a bimodal granulometry. Two cover rates 10 and 20% and three free stream velocities (6, 7 and 8 m/s) were tested. The results showed a temporal decrease of the emitted mass flux due to the presence of non-erodible particles. The mass balance value was the highest for the highest velocity and lowest cover rate. The agglomeration of non-erodible particles on the erodible surface causes the diminution of the amount of particles taking-off towards the free stream flow. Further wind-tunnel experiments for oblique stockpiles have shown a strong erosion on the crest and the formation of a huge main vortex impacting on the leeward wall. Cover rate and wind velocity magnitude showed influence on the temporal decrease but with lower importance than for the perpendicular orientation.

The investigations about non-erodible particles showed results of great significance on the dust emission behaviour on industrial sites. The original experimental technique carried out in this thesis lead to some interesting perspectives which are described in the next section. Moreover, these experimental results were used to propose improvements to the USEPA methodology. A lack noticed in this methodology lies in the fact that the various proportions of non-erodible particles found in natural granular materials are not explicitly taken into account. Thus, we propose a modification of

the erosion potential parameter which is now modified to be dependent on the amount of non-erodible particles.

The local analysis of non-erodible particles was carried out by means of numerical simulations. The mean friction velocity evolution on the erodible fraction is analysed for a domain partially covered by roughness elements. A mathematical formulation associating wall friction and roughness elements geometrical parameters had been set for a bed of particles with equal diameters and heights (condition rarely encountered in nature). The present numerical analysis enables to state that the original formulation [71] is still valid for poly-dispersed roughness elements distributions. The emerging height and the diameter of the non-erodible particles have a strong influence on the erosion potential of an erodible surface.

Associated with these works it may seem appropriate to consider the perspectives presented in the following section.

Perspectives

The main suggestions for future works include numerical and experimental analysis of the effects of non-erodible particles. In addition, there are also scope for further investigations concerning the aeolian erosion of oblong stockpiles (isolated, successive and on industrial situations).

The discussions about the agglomeration of non-erodible particles over an oblong stockpile model surface gave a lot of information regarding their influence on dust emissions. Even if the results shown in this thesis for a bimodal size distribution have greatly extended the understanding of the influence of non-erodible particles on emissions, the wind-tunnel experiences of sand particles should be extended.

The implementation of the existent data to improve the most used methodology of dust quantification showed the necessity to adapt the experiments to the actual conditions found in nature. For the tested bimodal granulometry, the two modes keep their properties, i. e., erodible and non-erodible, for all the tested wind velocities. In this framework, it is suggested, at first, to carry out experiments with a new particle size distribution. It could be very interesting to add a third mode between the two previous. This range of particles sizes would then be non-erodible for low velocities and become erodible as the velocity increases. This would provide relevant measurements being closer to real size distributions of granular materials on industrial sites. Figure 4.16 (take-off criterion) illustrates the new cases with three modes of size distribution. The velocities 9 and 10 m/s were inserted in the graphic to be tested in future works. For instance, the zone between black arrows illustrate the erodible fraction for 7 m/s . Otherwise, the zone between red arrows shows the erodible fraction for 9 m/s . It is worth to note that, the third mode becomes erodible for the higher velocity.

Additionally, the experimental simulation of successive stockpiles are also of great interest for future works. Numerical simulations have shown that the interactions between successive stockpiles present strong influence on the final pattern of near wall flow distribution on the stockpile surface. It is of great interest to visualize the influence of the complex structures formed between nearby stockpiles on their surfaces.

The second main suggestion for future works corresponds to the local analysis of non-erodible particles. While the numerical simulations of poly-dispersed distributions of roughness elements have given important results on non-erodible particles influence, further numerical simulations are proposed for future works, namely, the implementation of Large Eddy Simulation (LES) analysis. LES allow an access to accurate data on turbulence quantities.

The RANS steady simulations carried out previously present only the mean field. LES are then expected to complete the current study on the evolution of the friction velocity based on the geometrical characteristics of the elements on the underlying surface. These simulations would assess more precisely the wind friction velocity. Also, future works should study in greater detail the vortical structures formed around the non-erodible particles and the evolution of the production of turbulence with the gradual increase of the erodible surface cover.

Large eddy simulations have already been started. The subgrid-scales model chosen was the

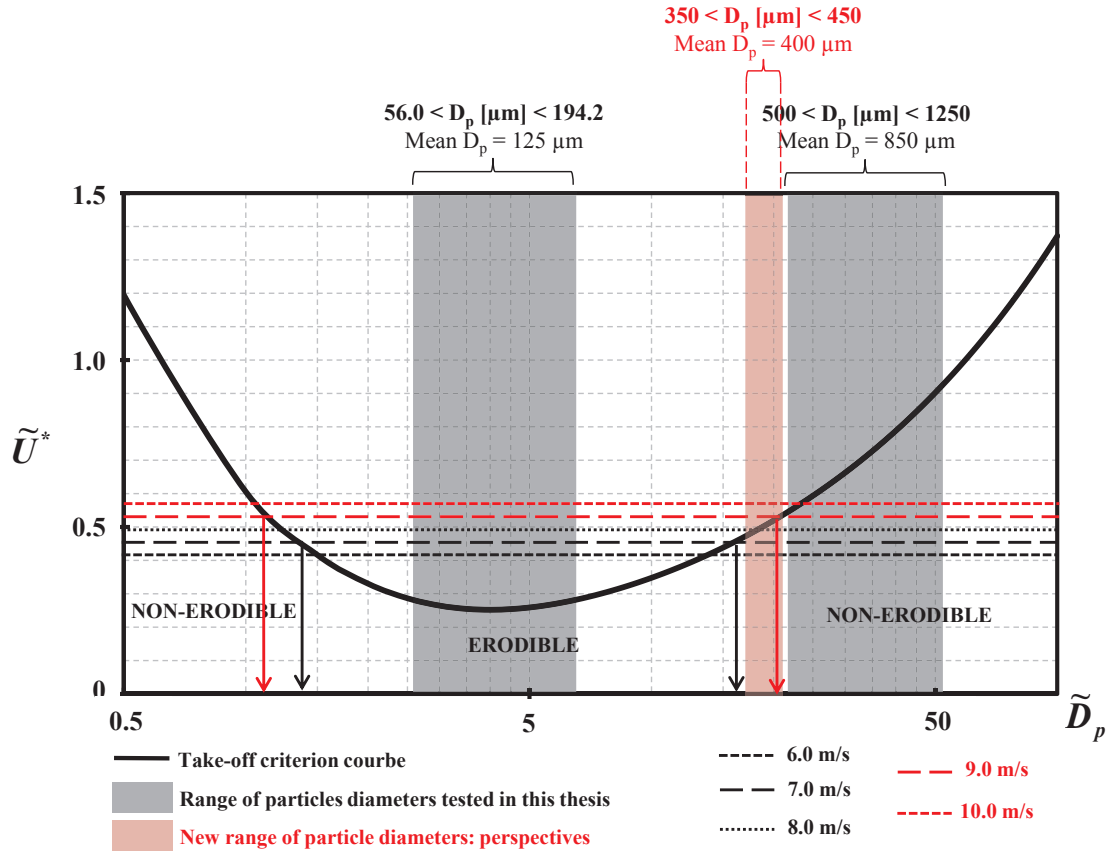


Figure 4.16: New particle size distribution to be tested in future works

dynamic model, which is the one mostly tested by other authors using *Code_Saturne*. The mesh is highly refined near the wall ($z^+ < 1$ for the first mesh). Further analysis about the best modelling of the subgrid-scales should be carried out. First results are presented illustrating our interest in these simulations. The results do not yet present the needed levels of convergence. Thus, it was decided to present only the current results illustrating the progress of the numerical simulations. Figure 4.17 presents instantaneous contours (four time-steps) of wall shear stress normalized by the value found in previous RANS numerical simulations of a smooth domain ($\tau_{ref} = 0.158 \text{ Pa}$).

These contours show peaks of high wall shear stress for all the time-steps. The mean distribution (computed by RANS simulations) presents the maximum value of the normalized wall shear stress approximately equal to 2.8. The black dashed lines highlight those zones of high wall shear stress values which reaches 11.1. It may indicate that some zones seen as low friction in RANS simulations may present for several time-steps peaks of very high friction.

Some LES numerical simulations are currently running for a mono-dispersed distribution of particle diameters and heights. Other configurations are aimed for future works with the objective to create a database of turbulence description for several roughness elements distributions. The simulations will be assessed and validated by comparisons with direct numerical simulations published for homogeneous roughness (Orlandi and Leonardi (2006) [56]). Other configurations are aimed for future works creating then a data base of turbulence description for several roughness elements distributions.

It is also thought to perform some experiments to validate the numerical study. These measures will help to characterize the influence of the presence of non-erodible particles on the turbulence near the wall. Experiments are intended to be carried out in wind tunnel using 3D PIV in horizontal planes positioned below the non-erodible particles. Random distributions, i.e., mono-and poly-dispersed, will be tested.

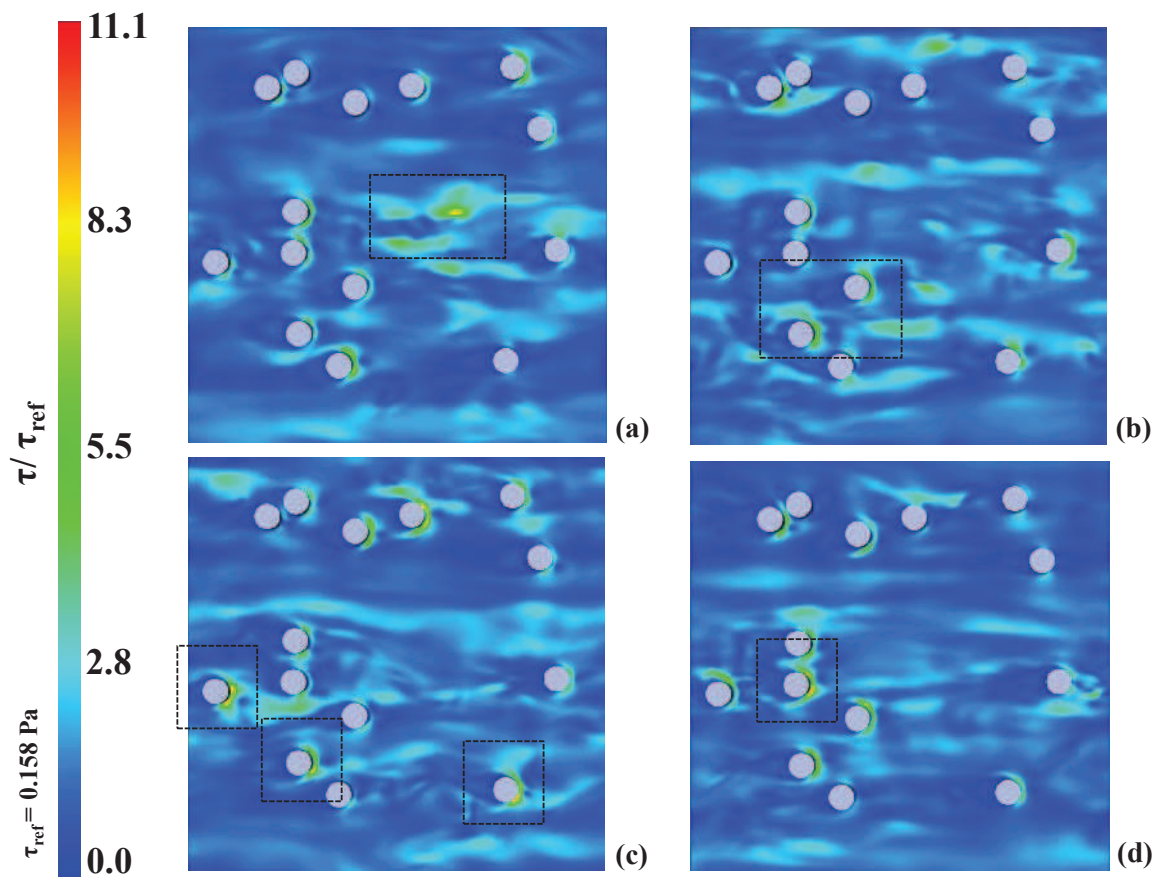


Figure 4.17: Instantaneous contours of wall shear stress on the underlying surface surrounding cylindrical roughness elements.

Bibliography

- [1] T. Badr. *Quantification des Émissions atmosphériques diffuses de particules produites par Érosion Éolienne*. PhD thesis, University of Valenciennes, France, 2007.
- [2] T. Badr and J.L. Harion. Numerical modelling of flow over stockpiles: Implications on dust emissions. *Atmospheric Environment*, 39(30):5576 – 5584, 2005.
- [3] T. Badr and J.L. Harion. Effect of aggregate storage piles configuration on dust emissions. *Atmospheric Environment*, 41(2):360 – 368, 2007.
- [4] R.A. Bagnold. The physics of blown sand and desert dunes. *Progress in Physical Geography*, 18:91–96, 1941.
- [5] R.F. Blackwelder and J.H. Haritonidis. Scaling of the bursting frequency in turbulent boundary layers. *J. Fluid. Mech.*, 316:285–306, 1983.
- [6] J. Blasek. *Computational Fluid Dynamics: Principles and Applications*. Elsevier, 2001.
- [7] B. Blocken, T. Stathopoulos, and J. Carmeliet. Cfd simulation of the atmospheric boundary layer: wall function problems. *Atmospheric Environment*, 41(2):238 – 252, 2007.
- [8] R.A. Bowling. A theoretical review of particle adhesion. *Mttal, K.L. (Ed.), Particles on Surface 1: Detection, Adhesion and Removal*, pages 129–142, 1988.
- [9] S. Brown, W.G. Nickling, and J.A. Gillies. A wind tunnel examination of shear stress partitioning for an assortment of surface roughness distributions. *Journal of Geophysical Research*, 113, 2008.
- [10] I. Burton. The quantitative revolution and theoretical geography. *The Canadian Geographer*, 7:151–162, 1963.
- [11] C.E.I Byrne and A.E. Holdo. Effects of increased geometric complexity on the comparison between computational and experimental simulations. *Journal of Wind Engineering and Industrial Aerodynamics*, 73:159–179, 1998.
- [12] S.K. Carney, B.P. Bledsoe, and D. Gessler. Representing the bed roughness of coarse-grained streams in computational fluid dynamics. *Earth Surface Processes and Landforms*, 31:736–749, 2005.
- [13] I.I.Y. Castel. A simulation model of wind erosion and sedimentation as a basis for management of a drift sand area in the netherlands. *Earth Surface Processes and Landforms*, 32:602–611, 2006.
- [14] P. Chassaing. *Turbulence en mécanique des fluides*. Cepadue Editions, 2000.
- [15] W.S. Chepil. Dynamics of wind erosion. *Soil Sci*, 60:305–480, 1945.
- [16] P.Y. Chou. On velocity correlations and the solutions of the equations. *Quarterly of Applied Mathematics*, 3:38, 1945.
- [17] F. Clauser. Turbulent boundary layers in adverse pressure gradients. *AIAA Journal Special Supplement*, 21:91–108, 1954.

- [18] X.C. Cong, S.Q. Cao, Z.L. Chen, S.T. Peng, and S.L. Yang. Impact of the installation scenario of porous fences on wind-blown particle emission in open coal yards. *Atmospheric Environment*, 45(30):5247 – 5253, 2011.
- [19] J. Cousteix. *Turbulence et couche limite*. Cepadues, 1989.
- [20] F. Curbani. Estudo da dispersão de poluentes na atmosfera ao redor de um prédio isolado através da simulação das grandes escalas. Master's thesis, Universidade Federal do Espírito Santo, Brazil, 2004.
- [21] I. Descamps. *Erosion Éolienne d'un lit de particules à large spectre granulométrique*. PhD thesis, University of Valenciennes, France, 2004.
- [22] I. Descamps, J.-L. Harion, and B. Baudoin. Taking-off model of particles with a wide size distribution. *Chemical Engineering and Processing: Process Intensification*, 44(2):159 – 166, 2005.
- [23] O. Desreumaux and J.P. Bourez. Préparation de bouillies pour visualisation pariétales sur maquette de sous-marin à cepra 19. *Technical report of the Fluid Mechanics Institut of Lille (IMFL), France*, 89, 1989.
- [24] I. Diego, A. Pelegry, S. Torno, J. Tora no, and M. Menendez. Simultaneous cfd evaluation of wind flow and dust emission in open storage piles. *Applied Mathematical Modelling*, 33(7):3197 – 3207, 2009.
- [25] O. Duran, P. Claudin, and B. Andreotti. On aeolian transport: Grain-scale interactions, dynamical mechanisms and scaling laws. *Aeolian Research*, 3(3):243 – 270, 2011.
- [26] R. Faria, A.D. Ferreira, J.L. Sismeiro, J.C.F. Mendes, and A.C.M. Sousa. Wind tunnel and computational study of the stoss slope effect on the aeolian erosion of transverse sand dunes. *Aeolian Research*, 3(3):303 – 314, 2011.
- [27] A. Ferreira and R. Lambert. Numerical and wind tunnel modeling on the windbreak effectiveness to control the aeolian erosion of conical stockpiles. *Environmental Fluid Mechanics*, 11:61–76, 2011.
- [28] A.D. Ferreira and R.A. Oliveira. Wind erosion of sand placed inside a rectangular box. *Journal of Wind Engineering and Industrial Aerodynamics*, 97(1):1 – 10, 2009.
- [29] J.H. Ferziger and M. Peric. *Computational Methods for Fluid Dynamics*. Springer, 2002.
- [30] J.M. Foucaut. *Etude théorique et expérimentale des phénomènes d'envol et de saltation de particules dans une couche limite turbulente*. PhD thesis, University of Lille, France, 1994.
- [31] B. Furieri, S. Russeil, J.-L. Harion, and J. Santos. Experimental surface flow visualization and numerical investigation of flow structure around an oblong stockpile. *Environmental Fluid Mechanics*, 2012.
- [32] Y. Gao and W.K. Chow. Numerical studies on air flow around a cube. *Journal of Wind Engineering and Industrial Aerodynamics*, 93(2):115 – 135, 2005.
- [33] D. Gillette and P. Stockton. The effect of nonerodible particles on wind erosion of erodible surfaces. *Journal of Geophysical Research*, 94:12885–12893, 1989.
- [34] T. Guiming. Surface oil flow technique and liquid crystal thermography for flow visualization in impulse wind tunnels. *Acta Mechanica Sinica*, 10:220–226, 1994.
- [35] J.L. Harion, C. Evrard, B. Furieri, V. Lecocq, A. Guinard, C. Ranty, O. Michel, and G. Alac. Amélioration et validation de la méthode de quantification des émissions diffuses de particules de plein air sur sites. ADEME-ARMINES-LECES-ArcelorMittal, Convention ADEME-ARMINES 08-74-C0128., 2010., 2010.

- [36] R. Hosker. Dispersion in the vicinity of buildings. *Second Joint Conference on Applications of Air Pollution Meteorology and Second Conference on Industrial Meteorology*, pages 92–107, 1980.
- [37] J. Iversen and B. White. Saltation threshold on earth, mars and venus. *Sedimentology*, 29:111–119, 1982.
- [38] J. Jimenez and P. Moin. The minimal flow unit in near wall turbulence. *J. Fluid. Mech.*, 225:213–240, 2000.
- [39] W.P. Jones and B.E. Launder. The prediction of laminarization with a two-equation model of turbulence. *Int. Journal of Heat and Mass Transfer*, 15:301–314, 1972.
- [40] P.S. Klebanoff and F.W. Diehl. Some features of artificially thickened fully developed turbulent boundary layer with zero pressure gradient. *Natl. Advisory Comm. Aeronat.*, 2475, 1951.
- [41] N. Lancaster, W.G. Nickling, C.K. McKenna-Neuman, and V.E. Wyatt. Sediment flux and airflow on the stoss slope of a barchan dune. *Geomorphology*, 17:55 – 62, 1996.
- [42] B. Launder and D. Spalding. The numerical computation of turbulent flows. *Computer methods in Applied Mechanics and Engineering Software*, 3:269 – 289, 1974.
- [43] W.C. Leeuw, H.G. Pagendarm, F.H. Post, and B. Walter. Visual simulation of experimental oil-flow visualization by spot noise images from numerical flow simulation. *Sixth Eurographics workshop on visualization in scientific computing*, 50:150–165, 1995.
- [44] H.C. Lim, T.G. Thomas, and I.P. Castro. Flow around a cube in a turbulent boundary layer: Les and experiment. *Journal of Wind Engineering and Industrial Aerodynamics*, 97(2):96 – 109, 2009.
- [45] I. Livingstone, G.F.S. Wiggs, and C.M. Weaver. Geomorphology of desert and dunes: A review of recent progress. *Earth Science Reviews*, 80:239–257, 2007.
- [46] M.V. Lopez, J.M.D. Herrero, G.G. Hevia, R. Gracia, and D.E. Buschiazso. Determination of the wind-erodible fraction of soils using different methodologies. *Geoderma*, 137:407–411, 2007.
- [47] H. Ludwig and W. Tillmann. Investigation of the wall-shearing stress in turbulent boundary layer. In *NACA Technical Memorandum*, 1950.
- [48] C. McKenna-Neuman, N. Lancaster, and W. Nickling. Relations between dune morphology, air flow, and sediment flux over reversing dunes. *Sedimentology*, 44:1103–1113, 1997.
- [49] F. Menter. Two-equation eddy-viscosity turbulence models for engineering applications. *AIAA Journal*, 32:1598–1605, 1994.
- [50] R.N. Meroney, B.M. Leidl, S. Rafailidis, and M. Schatzmann. Wind-tunnel and numerical modeling of flow and dispersion about several building shapes. *Journal of Wind Engineering and Industrial Aerodynamics*, 81:333 – 345, 1999.
- [51] J.P. Merrison. Sand transport, erosion and granular electrification. *Aeolian Research*, 4(0):1 – 16, 2012.
- [52] A. Mollinger and F. Nieuwstadt. Measurement of the lift force on a particle fixed to the wall in the sublayer of a fully developed turbulent boundary layer. *J. Fluid. Mech.*, 316:285–306, 1996.
- [53] V.Y. Mosharov and N. Radchenko. Method of gas or liquid flow visualization on an object surface, 2009.

- [54] C. Neuman and W. Nickling. Aeolian sediment flux decay: non-linear behaviour on developing deflation lag surfaces. *Earth Surface Processes and Landforms*, 20:423–435, 1995.
- [55] J. Nikuradse. Regularity of turbulent flow in smooth pipes. *Forsch. Arb. Ing.-Wes*, 356, 1932.
- [56] P. Orlandi and S. Leonardi. Dns of turbulent channel flows with two- and three-dimensional roughness. *Journal of Turbulence*, 7:1–22, 2006.
- [57] D.R. Parsons, I.J. Walker, and G.F.S. Wiggs. Numerical modelling of flow structures over idealized transverse aeolian dunes of varying geometry. *Geomorphology*, 59:149 – 164, 2004.
- [58] M. R. Raupach, D. A. Gillette, and J. F. Leys. The effect of roughness elements on wind erosion threshold. *Journal of Geophysical Research*, 98:3023–3029, 1993.
- [59] K. Sada and A. Sato. Numerical calculation of flow and stack-gas concentration fluctuation around a cubical building. *Atmospheric Environment*, 36(35):5527 – 5534, 2002.
- [60] J.M. Santos. *Flow and Dispersion Around Isolated Buildings*. PhD thesis, University of Manchester Institute of Science and Technology, Department of Chemical Engineering, Institute of Science and Technology, 246 p., 2000.
- [61] J.M. Santos, N.C. Reis Jr., E.V. Goulart, and I. Mavroidis. Numerical simulation of flow and dispersion around an isolated cubical building: The effect of the atmospheric stratification. *Atmospheric Environment*, 43(34):5484 – 5492, 2009.
- [62] G. Sauermann, J.S. Andrade, L.P. Maia, U.M.S. Costa, A.D. Araujo, and Hermann H.J. Wind velocity and sand transport on a barchan dune. *Geomorphology*, 54:245–255, 2003.
- [63] H. Schlichting. *Boundary Layer Theory*. McGraw-Hill Book Compagny, 1968.
- [64] F. Schultz-Grunow. The frictional resistance of rotating disk in enclosures. *Journal of Applied Mathematical and Mechanics*, 15:191–204, 1950.
- [65] J. Shabbir, W. Shih, A. Liou, and A. Zhu. A new k-epsilon eddy viscosity model for high reynolds number turbulent flows-model development and validation. *Computer fluids*, 3:227–243, 1995.
- [66] Y. Shao. Physics and modelling of wind erosion. *Atmospheric and Oceanographic Sciences Library*, 2008.
- [67] R.F. Shi, G.X. Cui, Z.S. Wang, C. Xu, and Z. S. Zhang. Large eddy simulation of wind field and plume dispersion in building array. *Atmospheric Environment*, 42:1083–1097, 2008.
- [68] G. Sterk. Flattened residue effects on wind speed and sediment transport. *Soil Science Society of America Journal*, 64:852–858, 2000.
- [69] J. Torano, S. Torno, I. Diego M. Menendez, and M. Gent. Dust emissions calculations in open storage piles protected by means of barriers, cfd and experimental tests. *Environmental Fluid Mechanics*, 9:493–507, 2009.
- [70] C. Turpin. *Amélioration des modèles de quantification des émissions particulaires diffuses liées à l'érosion éolienne de tas de stockage de matières granulaires sur sites industriels*. PhD thesis, University of Valenciennes, France, 2010.
- [71] C. Turpin, T. Badr, and J.-L. Harion. Numerical modeling of aeolian erosion over rough surfaces. *Earth Surface Processes and Landforms*, 2009.
- [72] C. Turpin and J.-L. Harion. Numerical modeling of flow structures over various flat-topped stockpiles height: Implications on dust emissions. *Atmospheric Environment*, 43(35):5579 – 5587, 2009.

- [73] C. Turpin and J.-L. Harion. Effect of the topography of an industrial site on dust emissions from open storage yards. *Environmental Fluid Mechanics*, 2010.
- [74] USEPA. Introduction to ap 42. In *USEPA proceedings*, 1995.
- [75] USEPA. *Miscellaneous Sources, Industrial Wind Erosion, AP-42*, 2006.
- [76] H.K. Versteeg and W. Malalasekera. *An introduction to computational fluid dynamics - The finite volume method*. Pearson Education Limited, Harlow, 2nd edition, 2007.
- [77] C.M. Weaver and G.F.S. Wiggs. Field measurements of mean and turbulent airflow over a barchan sand dune. *Geomorphology*, 128:32–41, 2011.
- [78] B.R. White. Two-phase measurements of saltating turbulent boundary layer. *Intl. J. of Multi-phase Flow*, 8:459–473, 1982.
- [79] G.F.S. Wiggs, I. Livingstone, and A. Warren. The role of streamline curvature in sand dune dynamics: evidence from field and wind tunnel measurements. *Geomorphology*, 17:29 – 46, 1996.
- [80] D. Wilcox. *Turbulence modeling for CFD*. Springer, 1998.
- [81] I.G. Wilson. Aeolian bedforms - their development and origins. *Sedimentology*, 19:173–210, 1972.
- [82] H. Zhao, G.S. Castle, I.I. Inculet, and A.G. Bailey. Bipolar charging of poly-disperse polymer powders in fluidized beds. *IEEE Trans. Ind. Appl.*, 39:612, 2003.
- [83] A. Zimon. Adhesion of dust and powder. *Plenum Publishing Corporation*, 1982.

EROSION ÉOLIENNE DE TAS DE STOCKAGE DE MATIÈRES GRANULAIRES SUR SITES INDUSTRIELS : AMÉLIORATION DES MÉTHODES DE QUANTIFICATION DES ÉMISSIONS

Résumé: L'érosion éolienne des matières granulaires (minerais, charbons, ...) est un des facteurs influençant grandement la qualité de l'air dans l'environnement proche de nombreux sites industriels. L'objectif principal de ce travail est l'amélioration des méthodologies de quantification des émissions des sources diffuses, notamment à partir d'une meilleure prise en compte de l'exposition éolienne des sources que sont les tas de stockage et des répartitions granulométriques des matières présentes sur les sites de stockage. Les observations sur sites industriels montrent que les régions proches des tas de stockage de matières granulaires sont chargées de particules de granulométries plutôt fines. Celles-ci sont susceptibles d'être remises en suspension par les structures tourbillonnaires générées par le vent incident. Ainsi, ces zones d'envol potentiel ont fait l'objet d'analyses afin de quantifier leur contribution aux émissions globales. Une technique de visualisation d'écoulement pariétal, associée à des simulations numériques tridimensionnelles, ont été mises en œuvre pour mieux comprendre ces structures de l'écoulement. Les matières granulaires sont un mélange de particules érodibles et non-érodibles. Le caractère érodible étant lié aux propriétés des particules (principalement granulométrie et masse volumique), ainsi qu'à la vitesse du vent incident. Dans ce cadre, deux types d'études ont été menées: des essais expérimentaux d'envol de particules dans une soufflerie et des simulations numériques tridimensionnelles avec un logiciel open-source de mécanique des fluides (*Code_Saturne*). Une technique originale a ainsi été développée pour quantifier, par une pesée en continue, l'influence des particules non-érodibles sur le flux massique envolé. En parallèle, le comportement des particules sur la surface est analysé à l'aide de clichés photographiques. L'analyse de l'effet des particules non-érodibles au niveau local est réalisée grâce à des simulations numériques pour des configurations poly-dispersées. Les résultats présentés dans ce mémoire constituent de premiers éléments pouvant possiblement contribuer à l'amélioration des modèles actuels de quantification des émissions de particules par une meilleure intégration et pris en compte de la présence de particules non-érodibles pour les matières présentant de larges spectres granulométriques.

Mots clés: érosion éolienne, émissions diffuses, tas de stockage, simulations numériques, soufflerie, particules non-érodibles

Abstract: Wind erosion of granular materials (ores, coal, ...) is one of the factors that greatly influence the quality of the air in the immediate vicinity of many industrial sites. The main objective of this work is the improvement of methodologies for quantifying emissions from diffuse sources. It may be carried out by a better consideration of wind exposure on the sources (storage piles) and larger size distributions of granular materials present at the storage sites. Observations show that areas near storage piles of granular materials on industrial sites are loaded with silt particles. These particles may be re-emitted by vortex structures. Thus, these areas of potential particles take-off were analyzed to quantify their contribution to global emissions. A wall flow visualization technique associated with three-dimensional numerical simulations have been implemented. Granular material is a mixture of erodible and non-erodible particle. The erodible character may be associated to particle properties (mainly size and density), as well as the ambient wind speed. In this context, two types of studies were conducted: experimental tests of particles take-off in a wind-tunnel and numerical simulations with a three-dimensional open-source fluid dynamics code (*Code_Saturne*). An original technique has been developed to quantify, by a continuous weighing, the influence of non-erodible particles of the mass flow. In parallel, the behaviour of particles on the surface is analyzed using photographs. The analysis of the effect of non-erodible particles at local level is achieved through numerical simulations for poly-dispersed configurations. The results presented in this thesis are the first elements that can potentially contribute to the improvement of current models of quantification of particulate emissions through a better integration of the presence of non-erodible particles for materials with large particle size spectra.

Keywords: wind erosion, fugitive emissions, storage piles, numerical simulations, wind-tunnel, non-erodible particles